Novel III-V Active Regions by Metal-Organic Vapor Phase Epitaxy for Semiconductor Laser Diodes

by

Honghyuk Kim

A preliminary report submitted in partial fulfillment of
the requirements for the degree of

Doctor of Philosophy
(Electrical and Computer Engineering)

Under the supervision of Prof. Luke J. Mawst

At the
University of Wisconsin-Madison
2020

Date of final oral examination: 12/18/2019

The dissertation is submitted to the following members of the final oral committee:
- Luke J. Mawst, Professor, Electrical and Computer Engineering
- Thomas F. Kuech, Professor, Chemical and Biological Engineering
- Dan Botez, Professor, Electrical and Computer Engineering
- Padma Gopalan, Professor, Material Science and Engineering

Novel III-V Active Regions by Metal-Organic Vapor Phase Epitaxy for Semiconductor Laser Diodes

Honghyuk Kim
Under the Supervision of Professor Luke J. Mawst
At the University of Wisconsin-Madison

This work summarizes the epitaxial growth by metal-organic vapor phase epitaxy (MOVPE) and the subsequent device characterizations for III-V semiconductor laser diodes, emitting in the near infrared wavelength range, which employ novel active regions consisting of either dilute $GaAs_{1-x}Bi_x$ based quantum well (QW) or $In_xGa_{1-x}As$-based quantum dots (QDs) formed by nanopatterning. The incorporation of the Bi atoms into the host GaAs matrix can lead to the rapid reduction in the band gap energy (E_g) and an increase in the spin-orbit splitting (Δ_{SO}), which are believed to potentially suppress hot-hole driven Auger recombination and intervalence band absorption (IVBA) in the telecom wavelength regions (λ~0.98-1.55μm). The substantial reduction in the band gap energy is primarily explained by the perturbation between the valence band edge of the host GaAs matrix and the Bi impurity level . This origin of the band gap reduction therefore leads to a relatively large valence band offset at the GaAs and $GaAs_{1-z}Bi_z$ heterointerface, while resulting in a relatively small conduction band offset, especially within the dilute concentration regime (%Bi < ~5%). In addition, Bi atoms exhibit a low solubility within a host GaAs matrix, requiring the epitaxial growth to be performed in a non-typical condition such as a low growth temperature (~400°C) and a near stoichiometric V/III gas phase molar flow ratio (~1). These growth conditions can lead to a high degree of unintentional carbon incorporation as well as a high density of point defects and defect complexes within the $GaAs_{1-z}Bi_z$ epitaxial layer, thereby degrading the luminescent properties. Therefore, a careful optimization of both the growth parameters and the heterostructure design is necessary for the application of the $GaAs_{1-z}Bi_z$ film to the optoelectronic devices such as laser diodes and solar cells, which is a subject investigated in this work. Moreover, the impacts of the post growth thermal annealing on the

luminescent properties of $GaAs_{1-z}Bi_z$ based QWs, evaluated by either photoluminescence or the laser device performances, are present in this thesis.

In addition, the MOVPE process allows for the epitaxial deposition of a thin layer by the chemical interaction between the heated substrate and the chemical species decomposed from the reactant gases within a cold-wall reactor. Thus, the MOVPE process is well suited to perform selective area epitaxy (SAE) where the local growth of an epitaxial layer is carried out through patterned amorphous dielectric masks such as SiO_2 or Si_3N_4. In a conventional QD active region, the QDs are formed on an inherent two-dimensional wetting layer, which prevents the full 3-dimentional carrier confinement to the QD, and thus presents challenges for realizing the predicted ideal characteristics of the QD laser such as large differential gain for high speed modulation, low temperature sensitivities in the lasing wavelength and ultra-low threshold current densities. By contrast, nanopatterning and selective SAE offer a more controllable pathway for QD formation, allowing the QD size to be decoupled from the strain state of the material. This process results in the formation of dense arrays of wetting-layer-free QDs, although the challenges stemming from surface state formation and efficient carrier injection into the QDs have remained problematic issues. In this work, the $In_xGa_{1-x}As$-based QD active region lasers grown on either GaAs or InP substrate were demonstrated, where the QDs are formed by block copolymer (BCP) lithography and the subsequent SAE, that results in the QD density of $\sim 8 \times 10^{10}$cm^2. Improved luminescent properties such as an increase in the PL intensity (at room temperature) and a substantial reduction in the threshold current density (at 80K) were obtained by *in situ* etching prior to the SAE of $In_{0.3}Ga_{0.7}As$ QDs on GaAs substrate. In addition, an enhanced carrier injection into the InAs QDs in the presence of an adjacent QW is experimentally demonstrated. Furthermore, the growth and the characteristics of $In_{0.8}Ga_{0.2}As$ QD active region lasers grown on InP substrate are present in this work, which resulted in a relatively low threshold current density of 1.6 kA/cm^2 with the emission wavelength of 1.67 μm near room temperature.

Acknowledgement

During my Ph.D study, I have been privileged to be able to get involved in the various research topics ranging from the crystal growth by metal organic vapor phase epitaxy (MOVPE) to fabrication and characterization of III-V semiconductor based optoelectronic devices. This might have not been possible without the guidance and commitment of my advisor, Prof. Luke Mawst throughout my graduate study. I deeply appreciate him for his support, motivation and encouragement, by which I was able to learn how to critically and scientifically think. I am also grateful for giving me the valuable opportunities to attend many academic conferences where I was able to learn new perspectives on various research areas and social networking skills.

The works on the dilute bismide alloy presented in this thesis benefited from the intensive collaborative research performed within the framework of Material Research Science and Engineering Centers (MRSEC) at University of Wisconsin-Madison. In particular, I would like to appreciate Prof. Thomas Kuech, one of the collaborators through MRSEC, for his valuable inputs and suggestions on the crystal growth by MOVPE as well as his insights on the material characterizations, which compose a major part of this thesis. Also, Prof. Susan Babcock's inputs on the nano/microscopic characterization through the collaborative work in MRSEC, without doubt, greatly influenced my Ph.D study on the dilute bismide alloy, which helped me gain an insight on how to design a series of experiments. In addition, I sincerely thank Prof. Dan Botez for his advices on the device physics and characterizations. I must admit that I learned a lot from him not only about the device physics, but also about how to efficiently manage a research project and how to think scientifically in interpreting a set of experimental data, as I was lucky enough to get partially involved in his QCL-related projects over the years. I am also thankful for Prof. Padma Gopalan for her contribution to the development and characterization of the patterned quantum dot

(QD) lasers, which employed block copolymer lithography. Her inputs and supports were essential in demonstrating patterned QD lasers operating at room temperature, which set a milestone that allowed for further detailed characterizations.

In addition, it was such a pleasure to be able to work with talented Ph.D students in Mawst/Botez group throughout my Ph.D study. I deeply appreciate Dr. TaeWan Kim and Dr. Jeremy Kirch for teaching me the technical aspects of Thomas Swan MOVPE system. Also, I am grateful for Dr. Chun-Chieh Chang and Dr. Colin Boyle for training me in device fabrication in WCAM. At the same time, I want to express my sincere gratitude to Dr. Chris Sigler, Dr. Ayushi Rajeev, Kevin Oresick, Benjamin Knifer, and Jae Ha Ryu for inspiring technical discussion and idea that we shared. Not only that, but I also appreciate my colleague Ph.D students and Post-docs in the other research groups. I am thankful for Dr. Kamran Forghani in Kuech group for training me in PL measurement and providing me insights on the growth of dilute bismide. The technical discussion with Dr. Yingxin Guan in Kuech group was also an essential part of this work. I also deeply appreciate Wei Wei in Padma Group for his excellent contribution for developing various types of block copolymer mask and preparing the patterned sample in a short period of time.

Our collaborators at *Aerospace Corporation* (Dr. Yongkun Sin), at *Ajou University* (Prof. Jaejin Lee), and at *Microlink* device (Dr. Rao Tatavarti) are also gratefully acknowledged.

Last but not least, none of the works during my Ph.D study would have been possible without the unconditional support and love of my dear family, J.Y. Kim, Y.J. Hwang, and E.H. Kim, to whom I dedicate this dissertation.

Table of Contents

Chapter 1. Introduction

Chapter 2. MOVPE and related characterization

Chapter 3. Design considerations of QW and QD-based laser diode

Chapter 4. $GaAs_{1-z}Bi_z$ QW Active Region Laser Diodes

Chapter 5. Patterned QD Active Region Laser Diodes

Chapter 6. Future works

Chapter 7. Appendix

List of Figures

List of Tables

Chapter 1. Introduction

1. 1. Overview

Semiconductor diode lasers have been widely used in daily life as a compact coherent light source, enabling the fast and efficient data transfer via optical fiber communication systems, and leading to the development of various consumer products (such as CD/DVD/Blu-ray Disc technology, barcode scanner, high resolution printouts, and laser pointers).

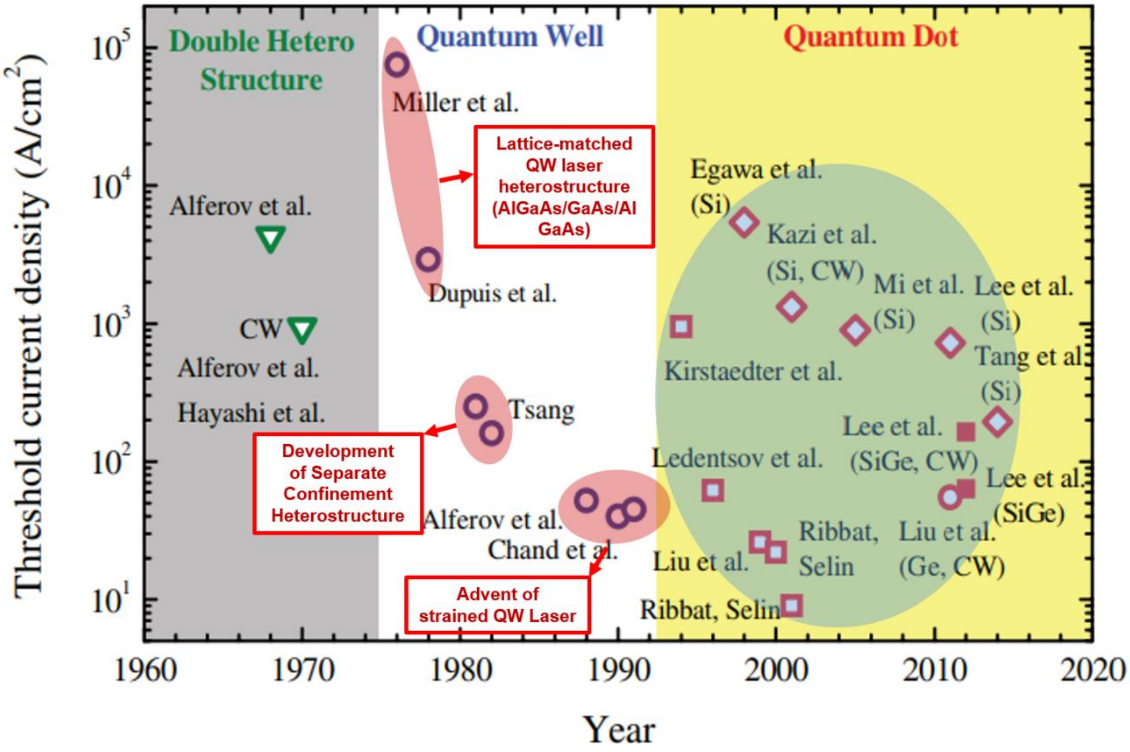

Fig. 1-1 *The historical development of heterostructure lasers showing the record threshold current densities at the time of publication. CW indicates that the threshold current values were obtained under continuous operation (after reference [2]).*

The first reported electrically injected semiconductor laser operated at liquid nitrogen temperature (77K) and was composed of a PN junction of the single crystalline GaAs where the depletion region forms an active region for the population inversion, one of the requirements for the lasing action together with the cavity, under a forward bias [1]. Since then, ongoing improvement in the device performance has been reported as significant advances in both the crystal growth techniques and heterostructure designs have been introduced, as schematically shown in Fig. 1-1. The advent of the *p*-*i*-*n* double heterostructure has made the semiconductor laser diodes truly practical, leading to two Nobel prize awards in physics in the year of 2000 [3-4]. Unlike the homojunction-based devices, where carriers are swept within the depletion region under a forward bias, the higher band gap energy of the cladding layers allows for the carrier confinement within the intrinsic (*i*) active region, which then greatly increases the probability of the injected electrons and hole to recombine [3]. In addition, the cladding layers, which has a higher band gap energy, generally have a lower index of refraction than that of the intrinsic active region, which makes it possible to confine optical energy density in the transverse direction [3].

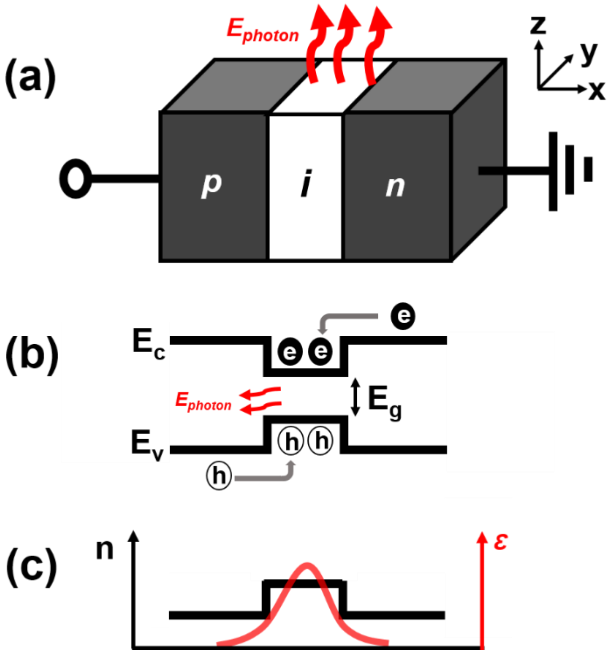

Fig. 1-2 *Aspects of the p-i-n double-heterostructure laser diode: (a) a schematic of the material structure; (b) a band gap diagram showing the conduction and valence band offsets vs. transverse distance; and (c) the refractive index profile (n) and the corresponding transverse optical energy density profile ($\mathcal{E}$) for a mode traveling along the laser cavity direction*

Since its invention by Nelson in 1963 [5], liquid phase epitaxy (LPE) had been a major crystal growth technique, which had led to many important first demonstrations of optoelectronic devices such as the first continuous wave lasing at room temperature from GaAs/AlGaAs *p*-*i*-*n* DH structure laser diodes [6-7] or *p*-*i*-*n* photodiodes [8]. LPE is a solution-based crystal growth technique where a bulk substrate (e.g., single crystal GaAs) is brought into contact with a supercooled melt (e.g., liquid phase GaAs), from which an epitaxial film precipitates on the bulk substrate. While this growth technique has been successfully employed for the epitaxial growth of various high crystalline quality III-V semiconductor layers such as GaP, AlGaAs, InGaAs, InGaAsP, and InGaAsSb [6-11], it is not well suited for growing thin structures, because of lack of precise control and uniformity in the thickness, especially over a large substrate. The controllable growth of thin layers with high uniformity and fidelity was realized after the invention of molecular beam epitaxy (MBE) [12] and metal organic vapor phase epitaxy (MOVPE) [13] in late 1960s, leading to the demonstration of quantum well-based laser diodes [14], which take advantage of quantum size effect (QSE). QSE and the subsequent quantized energy level arising from the reduced dimensionality of the semiconductor leads to the significant reduction of the required amount of current density to reach the population inversion. The MBE process is a form of evaporation where the thermal reaction of beams of atoms and molecules with the substrate takes place at an appropriate temperature in an ultrahigh vacuum [12]. On the other hand, MOVPE is a process where an epitaxial layer is deposited by the chemical interaction between the heated substrate and the chemical species decomposed from the reactant gases within a cold-wall reactor [15]. Both crystal growth techniques have successfully led to the development of the QW-based laser diodes with the dramatically improved device performance, together with the introduction of the separated confinement heterostructure (SCH) [16], which enhances carrier funneling into the QW and effectively increases the optical overlap over the QW area, leading to an improved device performance as will be discussed later.

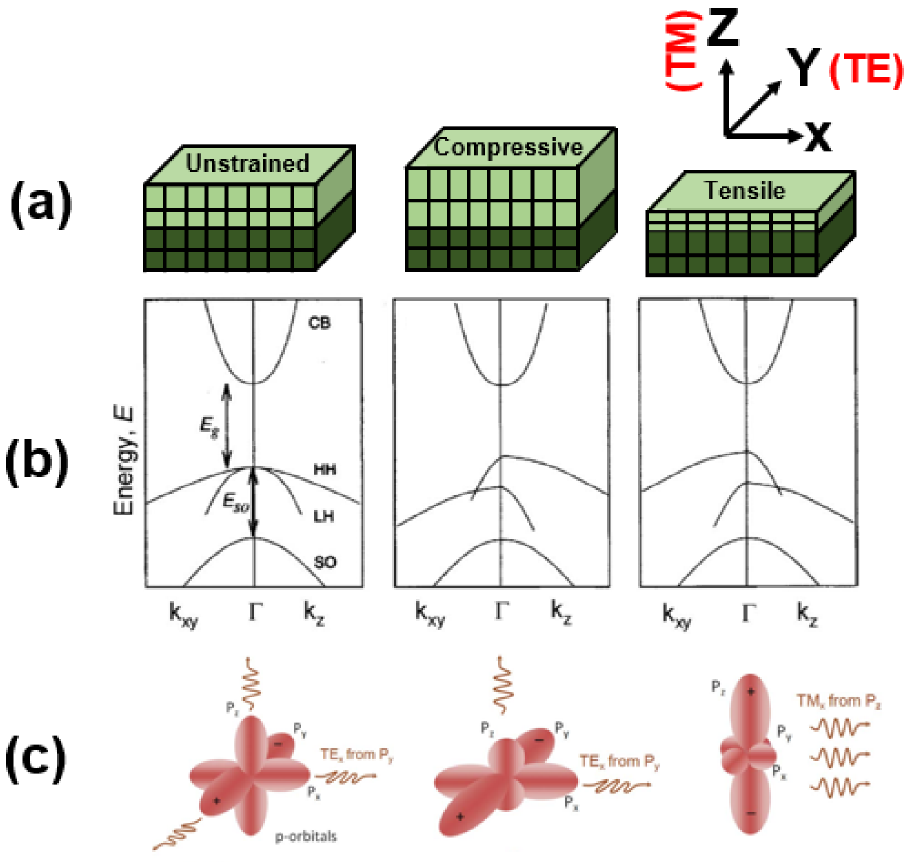

Fig. 1-3 *(a) Schematic diagram showing the effects of biaxial strain on the crystal symmetry, (b) E-k diagram of a bulk epitaxial layer depending on the biaxial strain status where the degeneracy (heavy hole and light hole) at the valence band maximum at Γ valley is split under the biaxial strain, and (c) hole distribution in three p-orbitals (P_x, P_y, and P_z) depending on the biaxial strain status. (after reference [17])*

Further improvement in the performance of the QW laser diodes was realized by employing pseudomorphically grown “strained” quantum wells within the active region. As schematically shown in Fig 1-3 (b), the tetragonal distortion of the lattice by the presence of the biaxial strain split the degeneracy at the valence band maximum at Γ valley, allowing for the population inversion to be achieved at a lower injected carrier density [17-19]. In addition, the broken cubic symmetry also induces non-symmetric hole distribution among the three p-orbitals, as schematically shown in Fig 1-3 (c), which can closely match to the symmetry of the laser beam polarization within the laser cavity, eventually leading to an enhanced optical gain [20].

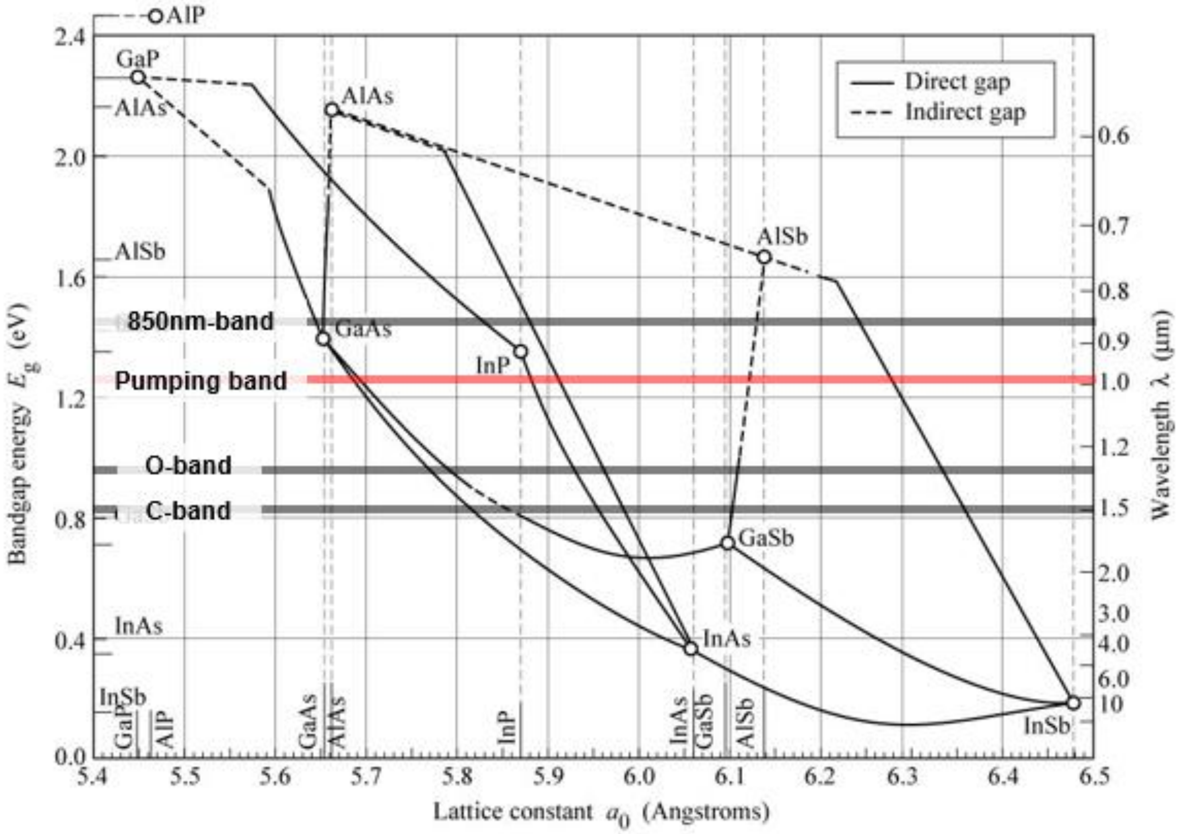

Fig. 1-4 *Energy gap vs. lattice constant of III-V compound semiconductors where the ternary compounds are defined by curves that connect the illustrated binary alloys*

Fig. 1-4 presents the band gap energies and the lattice parameters of important III-V compound semiconductors with important wavelengths, which includes fiber-optic communication bands at

0.85 (850nm-band), 1.3 (O-band), and 1.55 µm (C-band), as well as 0.98 µm (pumping band) for pumping Er-doped fiber amplifiers (EDFA) [21]. High performance strained QW lasers on GaAs substrate have effectively been used for the wavelength ranging from visible (e.g., 634 nm emitting tensile strained InGaP QW laser on GaAs substrate) to the near infrared regime (e.g., 980 nm emitting compressively strained InGaAs QW on GaAs substrate) [22-23]. On the other hand, for the emission wavelength near telecom O-band or C-band, InP has been primarily used as a substrate as it allows for the multinary alloys, such as AlInGaAs or InGaAsP QW to be grown with the desired degree of biaxial strain [24-25]. The higher price of InP substrate, as well as its fragility which limits the maximum wafer size, have led to a higher manufacturing cost of the semiconductor lasers, emitting near the telecom C and O-band wavelength regime. In addition, the unaviliablity of a material combination, which leads to a high index contrast as in GaAs/AlAs pairs on GaAs substrate, has limited the production of vertical cavity surface emitting laser (VCSEL) on InP substrate, which can also result in a significantly lower manufacturing cost, in comparison to that of edge emitting device geometry. Therefore, there have been significant research interests in developing a novel material system on GaAs substrate whose emission wavelength can be reached at near telecom O and C-band, which cannot be readily realized by using conventional strained InGaAs QW active region on GaAs substrate owing to the catastrophic strain relaxation beyond the critical thickness, *i.e.*, the thickness after which the misfit dislocations are generated [26]. As a means to enable the wavelength extension, the growth of metastable III-alloy, such as dilute nitride alloy, by either MBE or MOVPE has drawn much attention, as the incorporation of N can rapidly reduce the band gap energy of the host GaAs matrix by the nitrogen impurity level perturbed with the conduction band minima of the host GaAs, which is explained by the framework of conduction band anti-crossing model (CBAC) [27-28]. The laser diodes employing the dilute-nitride active region, such as the heavily compressive strained InGaAs(N) QWs, have successfully demonstrated the laser emission near the telecom O-band along with low threshold current densities [29]. However, these dilute-nitride-based devices tend to suffer from large N- and C-related non-radiative defects [30-31], especially within the as-grown material, as well as Auger recombination, which plays a major role in the fundamental carrier loss mechanism in telecom C and O-band emitting semiconductor laser diodes [32-33]. For this reason, the dilute-Bi alloy, such as GaAsBi, has recently drawn much attention as an alternative to the dilute nitride alloy, due to a rapid reduction in the band gap energy (E_g), as well as an increase in spin-orbit splitting energy (Δ_{so}) with increasing Bi within the dilute-Bi alloy, thus having potential for the reduced Auger loss [34-35] at the point where Δ_{so} is greater than E_g. However, these potential benefits can only be realized when a substantially high Bi incorporation is achieved. Also, the non-typical growth parameters involved in incorporating Bi into the host GaAs matrix can often result in unintentional impurity incorporation as well as the formation of point defect and its defect complexes. Therefore, in this work, the growth of GaAsBi-based QW on GaAs substrate by MOVPE, as well as impact of the post-growth thermal annealing, have been investigated. Also, the impact of the QW heterostructure design for the laser diode active region was investigated.

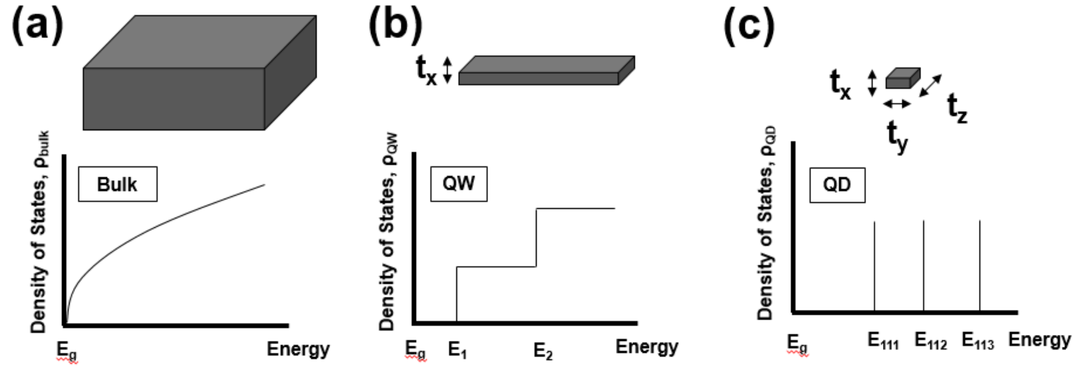

$$\rho_{bulk} = \frac{(2m^*/\hbar^2)^{3/2}}{2\pi^2}\sqrt{E}$$

$$\rho_{QW} = \frac{m^*}{\pi\hbar^2 t_x}\sum_{l}\theta(E - E_l)$$

$$\rho_{QD} = \frac{2}{t_x t_y t_z}\sum_{l,m,n}\delta(E - E_{l,m,n})$$

Fig. 1-5 *Density of state of a semiconductor within (a) bulk, (b) QW, and (c) QD structure*

Fig. 1-5 schematically represents the density of state of a semiconductor within bulk, QW, and QW structure. Similar to the advantage achievable from QW-based active region in comparison to the bulk counterpart, the further reduced dimensionality in the volume of the quantum dot (QD) active region within the laser diodes have been predicted to lead to the formation of delta function like density of state (DOS) and potential for ultra-low transparency current density (i.e., the injected carrier density at which the amount of absorption and emission within the medium are same), low linewidth enhancement factors, and temperature insensitive device performance. However, the realization of all the predicted advantages has remained challenging, as schematically presented in Fig. 1-1 where the early demonstrated QD lasers did not show superior performance to that of the state-of-art QW laser [36-37].

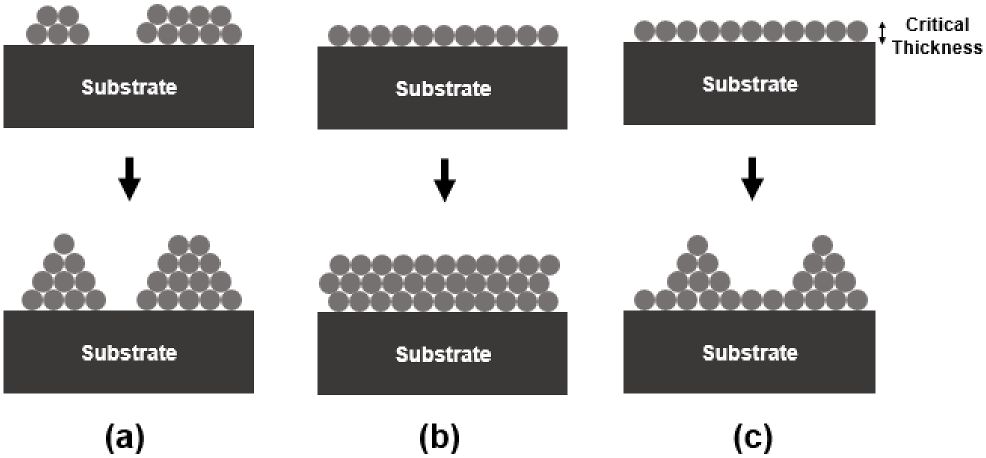

Fig. 1-6 (a) Volmer-Weber (island growth) mode: adatom cohesive force is stronger than surface adhensive force, (b) Frank-van der Merwe (layer-by-layer) mode: surface adhensive force is stronger than adatom cohesive force, and (c) Stranski-Krastanov (layer plus island growth) mode: Until the critical thickness, FM mode. At the critical thickness, transition to VW mode occurs.

The crystal growth mode can be classified into three categories: Volmer-Weber (VW), Frank van der Merwe (FM), and Stranski- Krastanov (SK) mode, as schematically shown in Fig. 1-5. In VW mode, the adatom cohesive is stronger than the surface adhensive force, leading to formation of island. On the other hand, in FM growth mode, the surface adhensive force is stronger than the adatom cohesive force leading to layer by layer growth, which is suitable for the growth of the QW and bulk layer. By contrast, when an epitaxial layer with a sufficient strain energy is grown on a lattice-mismatched substrate, the growth is initially dominated by FM growth mode until reaching the critical thickness, after which the eventual transition from FM mode to VW mode takes place. This growth mode is called SK growth mode shown in Fig. 1-6 (c) . As a result, SK growth mode leads to the formation of coherent islands on a thin wetting layer whose thickness corresponds to the critical thickness [38]. The conventional QD active regions are composted of InAs QDs on GaAs substrate grown by SK growth mode where the QD formation is driven by the strain energy from a large lattice mismatch between GaAs and InAs [39]. While the narrow band gap energy of the InAs QDs made it possible to achieve the telecom O-band emission on GaAs substrate, the presence of this inherent wetting layer has been identified to prevent a full 3-dimensional carrier confinement within the QDs, making it difficult to realize the predicted ideal performances of the QD active region-based laser diodes [40]. In addition, the randomness in the QD nucleation site and the subsequent variation in the volume distribution have led to "inhomogeneous broadening" in the density of state of the QD ensembles, which has been attributed to another limiting factor for realizing ideal characteristics [41]. On the other hand, nanopatterning and subsequent selective area epitaxy (SAE) growth offer a more controllable pathway for QD formation, allowing the QD size to be decoupled from the strain state of the material and reducing the degree of randomness in the QD nucleation site, although the non-radiative defects introduced during the formation of nanopatterns have remained as problematic issues [42] .

1. 2. Organization of this thesis

Together with the background issues identified aforehand, the work presented in this thesis is directed towards the development of novel active regions for the semiconductor laser diodes.

In chapter 2, the brief theoretical background of the MOVPE process, which was exclusively used for the crystal growth in this work, will be given together with introducing relevant *in situ* and *ex situ* analysis techniques, such as real-time reflectance measurement, high-resolution x-ray diffraction (HR-XRD), Van der Pauw Hall measurement, and photoluminescence.

In chapter 3, the hetero-epitaxial design criteria for the high performance QW and QD active region laser diodes will be considered, in which internal and external device parameters that determine the device performance will be discussed in detail.

In the following chapter, the growth of novel metastable GaAsBi alloy by MOVPE, impact of the post-growth thermal annealing, QW heterostructure design, and the application to the laser diodes will be given, together with an analysis of the observed device characteristics.

Then, in chapter 5, the development of quantum dot active region laser diodes on either GaAs or InP substrate using the nanopatterns defined by block copolymer lithography will be discussed. In particular, the efforts on reducing the processing-related damages by *in situ* etching prior to the QD growth as well as enhancement of the carrier injection into the QD active region by the adjacent heterostructure will be addressed.

Finally, the possible future works on GaAsBi-based QW active region lasers will be discussed in chapter 6, in order to realize its predicted potential advantages and to achieve a further extension in the lasing wavelength. Also, alternative approaches to form QD active region lasers, while utilizing the nanopatterns by diblock copolymer lithography, will be suggested with the preliminary theoretical/experimental results. In addition, the experimental test set-up for extracting internal device parameters of the QD lasers will be presented.

Reference

[1] Hall, Robert N., et al. "Coherent light emission from GaAs junctions." *Physical Review Letters* 9.9 (1962): 366.

[2] Wu, Jiang, et al. "Quantum dot optoelectronic devices: lasers, photodetectors and solar cells." *Journal of Physics D: Applied Physics* 48.36 (2015): 363001.

[3] Alferov, Zhores I. "Nobel Lecture: The double heterostructure concept and its applications in physics, electronics, and technology." *Reviews of modern physics* 73.3 (2001): 767.

[4] Kroemer, Herbert. "Nobel Lecture: Quasielectric fields and band offsets: teaching electrons new tricks." *Reviews of modern physics* 73.3 (2001): 783.

[5] Nelson, Herbert. "Epitaxial growth from the liquid state and its application to the fabrication of tunnel and laser diodes." *RCA review* 24.4 (1963): 603-615.

[6] Z. Alferov, V.M. Andreev, D.Z. Garbuzov, Y.V. Zhilyaev, E.P. Morozov, E.L. Portnoi, V.G. Trofim, “Investigation of the influence of heterostructure parameters on the threshold current of lasers and obtaining a cw lasing regime at room temperature” Fiz. Tekh. Poluprovodn. 4, 1826 (1970) [So. Phys. Semicond. 4, 1573 (1971)

[7] Hayashi, I., et al. "Junction lasers which operate continuously at room temperature." *Applied Physics Letters* 17.3 (1970): 109-111.

[8] Burrus, C. A., A. G. Dentai, and T. P. Lee. "InGaAsP pin photodiodes with low dark current and small capacitance." *Electronics Letters* 15.20 (1979): 655-656.

[9] Brantley, W. A., et al. "Effect of dislocations on green electroluminescence efficiency in GaP grown by liquid phase epitaxy." *Journal of Applied Physics* 46.6 (1975): 2629-2637.

[10] Sankaran, R., R. L. Moon, and G. A. Antypas. "Liquid phase epitaxial growth of InGaAs on InP." *Journal of Crystal Growth* 33.2 (1976): 271-280.

[11] Nahory, R. E., et al. "Efficient $GaAs_{1-x}Sb_x/Al_yGa_{1-y}As_{1-x}Sb_x$ double heterostructure LED's in the 1-μm wavelength region." *Applied Physics Letters* 27.6 (1975): 356-357.

[12] Cho, Al Y., and J. R. Arthur. "Molecular beam epitaxy." Progress in solid state chemistry 10 (1975): 157-191.

[13] Manasevit, Harold M. "Single-crystal gallium arsenide on insulating substrates." *Applied Physics Letters* 12.4 (1968): 156-159.

[14] Dupuis, Russell D., et al. "Room-temperature laser operation of quantum-well $Ga_{(1-x)}Al_xAs$-GaAs laser diodes grown by metalorganic chemical vapor deposition." *Applied physics letters* 32.5 (1978): 295-297.

[15] Kuech, T. F. "Metal-organic vapor phase epitaxy of compound semiconductors." *Materials Science Reports* 2.1 (1987): 1-49.

[16] Tsang, W. T. "Extremely low threshold (AlGa)As graded-index waveguide separate-confinement heterostructure lasers grown by molecular beam epitaxy." *Applied Physics Letters* 40.3 (1982): 217-219.

[17] Adams, A. R. "Strained-layer quantum-well lasers." *IEEE Journal of Selected Topics in Quantum Electronics* 17.5 (2011): 1364-1373.

[18] Adams, A. R. "Band-structure engineering for low-threshold high-efficiency semiconductor lasers." *Electronics Letters* 22.5 (1986): 249-250.

[19] Yablonovitch, Eli, and E. Kane. "Reduction of lasing threshold current density by the lowering of valence band effective mass." *Journal of Lightwave Technology* 4.5 (1986): 504-506.

[20] Ahn, Doyeol, and Chuang Shun-Lien. "Optical gain in a strained-layer quantum-well laser." *IEEE journal of quantum electronics* 24.12 (1988): 2400-2406.

[21] Coldren, Larry A., Scott W. Corzine, and Milan L. Mashanovitch. *Diode lasers and photonic integrated circuits*. Vol. 218. John Wiley & Sons, 2012.

[22] Chang-Hasnain, C. J., R. Bhat, and M. A. Koza. "High performance 634 nm InGaP/InGaAlP strained quantum well lasers." *Electronics Letters* 27.17 (1991): 1553-1555.

[23] Mawst, Luke J., et al. "8 W continuous wave front-facet power from broad-waveguide Al-free 980 nm diode lasers." *Applied Physics Letters* 69.11 (1996): 1532-1534.

[24] Ohnoki, N., et al. "Record high characteristic temperature (To= 122 K) of 1.55 µm strain-compensated AlGaInAs/AlGaInAs MQW lasers with AlAs/AlInAs multiquantum barrier." *Electronics Letters* 35.1 (1999): 51-52.

[25] Garrod, T., et al. "50% continuous-wave wallplug efficiency from 1.53 µm-emitting broad-area diode lasers." *Applied Physics Letters* 105.7 (2014): 071101.

[26] Matthews, J. W., and A. E. Blakeslee. "Defects in epitaxial multilayers: I. Misfit dislocations." *Journal of Crystal growth* 27 (1974): 118-125.

[27] Weyers, Markus, Michio Sato, and Hiroaki Ando. "Red shift of photoluminescence and absorption in dilute GaAsN alloy layers." *Japanese Journal of Applied Physics* 31.7A (1992): L853.

[28] O’Reilly, E. P., A. Lindsay, and S. Fahy. "Theory of the electronic structure of dilute nitride alloys: beyond the band-anti-crossing model." *Journal of Physics: Condensed Matter* 16.31 (2004): S3257.

[29] Tansu, Nelson, Jeng-Ya Yeh, and Luke J. Mawst. "High-performance 1200-nm InGaAs and 1300-nm InGaAsN quantum-well lasers by metalorganic chemical vapor deposition." *IEEE Journal of selected topics in quantum electronics* 9.5 (2003): 1220-1227.

[30] Kim, T. W., et al. "Properties of ‘bulk’ GaAsSbN/GaAs for multi-junction solar cell application: Reduction of carbon background concentration." *Journal of Crystal Growth* 393 (2014): 70-74.

[31] Dhar, S., et al. "Detailed studies on the origin of nitrogen-related electron traps in dilute GaAsN layers grown by liquid phase epitaxy." *Semiconductor science and technology* 20.12 (2005): 1168.

[32] Fehse, Robin, et al. "A quantitative study of radiative, Auger, and defect related recombination processes in 1.3-µm GaInNAs-based quantum-well lasers." *IEEE Journal of selected topics in quantum electronics* 8.4 (2002): 801-810.

[33] Yeh, Jeng-Ya, Nelson Tansu, and Luke J. Mawst. "Temperature-sensitivity analysis of 1360-nm dilute-nitride quantum-well lasers." *IEEE Photonics Technology Letters* 16.3 (2004): 741-743.

[34] Sweeney, S. J., and S. R. Jin. "Bismide-nitride alloys: promising for efficient light emitting devices in the near-and mid-infrared." *Journal of applied physics* 113.4 (2013): 043110.

[35] Batool, Z., et al. "The electronic band structure of GaBiAs/GaAs layers: Influence of strain and band anti-crossing." *Journal of Applied Physics* 111.11 (2012): 113108.

[36] Kirstaedter, N., et al. "Low threshold, large T_0 injection laser emission from (InGa) As quantum dots." *Electronics Letters* 30.17 (1994): 1416-1417.

[37] Kamath, K., et al. "Room-temperature operation of $In_{0.4}Ga_{0.6}As$/GaAs self-organised quantum dot lasers." *Electronics Letters* 32.15 (1996): 1374-1375.

[38] Ledentsov, N. N., et al. "Direct formation of vertically coupled quantum dots in Stranski-Krastanow growth." *Physical Review B* 54.12 (1996): 8743.

[39] Joyce, P. B., et al. "Optimizing the growth of 1.3 μm InAs/GaAs quantum dots." *Physical Review B* 64.23 (2001): 235317.

[40] Matthews, Daniel Richard, et al. "Experimental investigation of the effect of wetting-layer states on the gain–current characteristic of quantum-dot lasers." *Applied Physics Letters* 81.26 (2002): 4904-4906.

[41] Yamaguchi, Koichi, Kunihiko Yujobo, and Toshiyuki Kaizu. "Stranski-Krastanov growth of InAs quantum dots with narrow size distribution." *Japanese Journal of Applied Physics* 39.12A (2000): L1245.

[42] Coleman, James J., Jonathan D. Young, and Akash Garg. "Semiconductor quantum dot lasers: a tutorial." *Journal of Lightwave Technology* 29.4 (2010): 499-510.

Chapter 2. MOVPE and Related Characterization

2. 1. Crystal Growth by Metal Organic Vapor Phase Epitaxy (MOVPE)

The MOVPE is a form of a cold wall chemical vapor deposition, which utilizes metalorganic compounds and hydrides for the precursors [1]. Metalorganic (MO) compounds consist of metal atoms with a number of alkyl radicals attached. Table 2-1 shows some of the widely used MOs with their key properties, which were used in this present study.

Table 2-1 Physical properties of commercially available metalorganic (MO) sources for MOVPE

Chemical	Abbreviation	Formula	Melting Temp (°C)	Vapor pressure (P in Torr, T in K)	Note
Trimethyl-aluminum	TMAl	$(CH_3)_3Al$	15.4	log(P)=8.224-2134.83/T	Common
Trimethyl-gallium	TMGa	$(CH_3)_3Ga$	-15.8	log(P)=8.07-1703/T	Common
Triethyl-gallium	TEGa	$(C_2H_5)Ga$	-82.3	log(P)=8.083-2162/T	Common, Low C
Trimethyl-indium	TMIn	$(CH_3)_3In$	88	log(P)=10.52-3014/T	Common
Diethyl-zinc	DEZn	$(C_2H_5)_2Zn$	-28	log(P)=7.802-1560/T	P-doping source for P-terminating material
Carbon-tetrabromide	CBr_4	CBr_4	88-90	log(P)=7.7774-2346.14/T	P-doping source for As-terminating material
Trimethyl-bismuth	TMBi	$(CH_3)_3Bi$	-107.7	log(P)=8.05-1807.5/T	Bi precursor used in this study
Tertiarybutyl-arsine	TBAs	$(C_4H_9)AsH_2$		log(P)=7.5-1562.3/T	Primary substitute for AsH_3, low temperature growth

The MOVPE process involves a pyrolysis reaction of the vapors of a volatile organometallic compound and a gaseous hydride, as shown in the following simplest case

$$R_nA + DH_n \longrightarrow AD + nRH \qquad (2.1)$$

where R is an organic radical of some unspecified form but generally of lower order, such as methyl- or ethyl-radical and A and D are the constituent species for the deposited solid.

As such, the common example of this reaction includes the growth of GaAs and $Al_xGa_{1-x}As$:

$$(CH_3)_3Ga + AsH_3 \longrightarrow GaAs + 3CH_4 \qquad (2.2)$$

$$x(CH_3)_3Al + (1-x)(CH_3)_3Ga + AsH_3 \longrightarrow Al_xGa_{1-x}As + 3CH_4 \qquad (2.3)$$

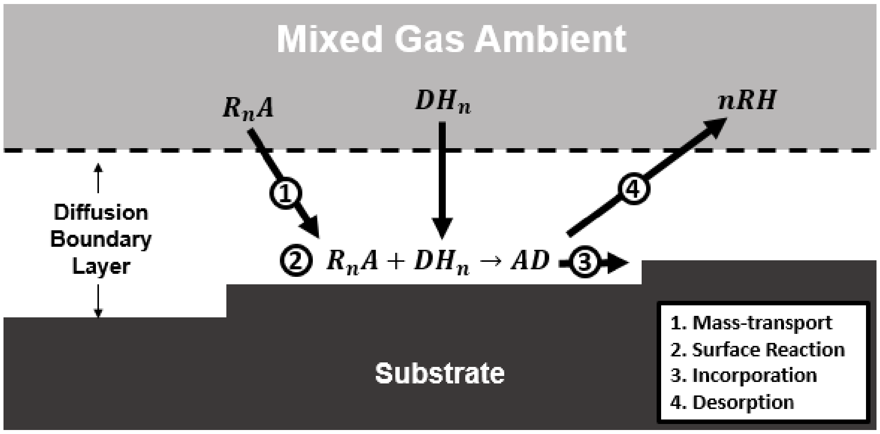

Fig. 2-1 *Schematic representation of the chemical processes taking place near the substrate surface.*

Fig. 2-1 shows the growth process taking place near the surface of the substrate as described by the reaction equation (2.1). The entire growth process is composed of mass-transport of reactants to surface, surface reaction, incorporation and the desorption of reaction products [2]. The growth ambient generally has a nonstoichiometric, excess, and uninterrupted group V species gas flows over the metal alkyl, which can compensate for the much greater volatility of the column V atoms in the desired solid films. In addition, the substrate temperature is typically held at a temperature higher than the pyrolysis temperature of the metal alkyl ensuring its rapid decomposition at the growth surface [2]. When these conditions are satisfied, the growth rate is limited by the mass transport of the group III reactant to the growth surface, and generally has a weak temperature dependence of the growth rate, as defined by the mass transport limited regime shown in Fig. 2-2. Therefore, the growth of most III-V semiconductor alloys takes place within this mass transport limited regime as it allows for the better control of the thickness and compositional uniformity across the entire wafer. By contrast, novel metastable alloys such as GaAsN and GaAsBi requires the growth to be performed within the reaction rate limited regime with a near stoichiometric V/III V/III ratio due to the low solubility of N or Bi within the host GaAs [4-5], which is investigated for $GaAs_{1-z}Bi_z$ alloy in Chapter 4.

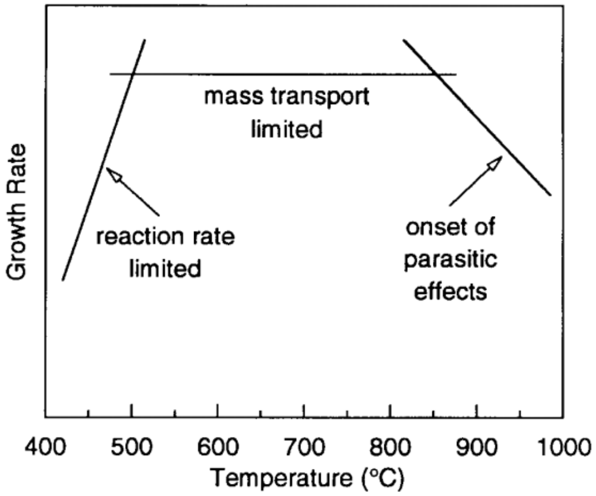

Fig. 2-2 *Growth rate as a function of temperature showing the three distinct growth-rate regime (after reference [3])*

III-V compound semiconductors and alloys grown by MOVPE process widely involve the use of hydrides, such as arsine (AsH_3) or phosphine (PH_3) for the column V species. In practice, the toxicity of these gases requires that special attention to be given to the safe transport, handling, and storage of these gases. For these safety reasons, there also has been considerable attention given to the use of MO sources for both the column III and V species, in which case the reaction equation becomes either

$$R_nA + R'_nB \longrightarrow AB + nRH + nR'H \tag{2.4}$$

or

$$R_nA + R'_nB \longrightarrow AB + nRR' \tag{2.5}$$

One of the interesting features of this MO-based column V species is that some of them exhibit significantly higher pyrolysis efficiency at a lower growth temperature than that of conventional hydride, as shown in Fig. 2-2.

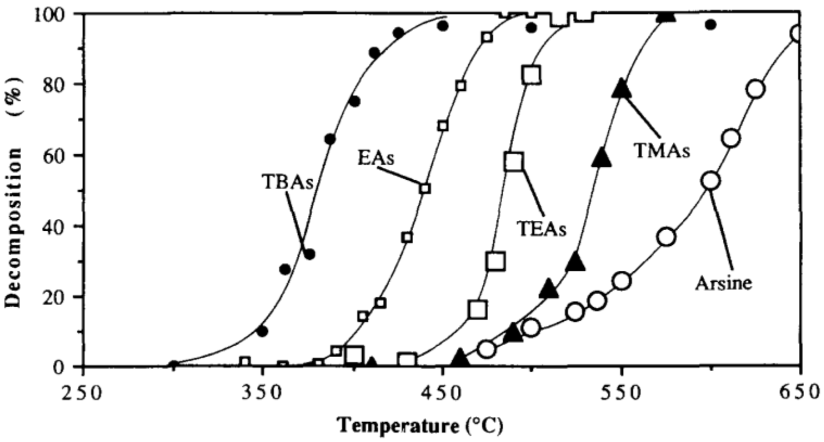

Fig. 2-3 *Percent pyrolysis versus temperature for several As-precursors, where the measurements were made in the same quartz reactor under nominally the same condition (After reference [6])*

This higher pyrolysis efficiency of the MO-based As-precursors, especially for TBAs, has allowed for the homogeneous growth of As-based metastable alloys such as GaAsN and GaAsBi at a reduced growth temperature (400~520 ºC) [4-5]. On the other hand, this low growth temperature, in return, can often result in the incorporation of significant amount of unintentional carbon impurities, as the volatile hydrocarbon radicals are not completely desorbed at the growth front. This unintentional background carbon has been shown to reduce the minority carrier lifetime [7], which can limit the device performance. The choice of column III MO source was shown to affect the unintentional carbon incorporation at a relatively low growth temperature. The methyl radicals have a relatively high desorption energy of ~38.6 – 43kcal/mol, leading to a low desorption rate at low temperatures [8-9]. Therefore, in an effort to reduce the unintentional carbon incorporation, the use of TEGa has been a preferred choice, rather than TMGa, when growing Ga-containing III-V alloy by MOVPE at a relatively low growth temperature.

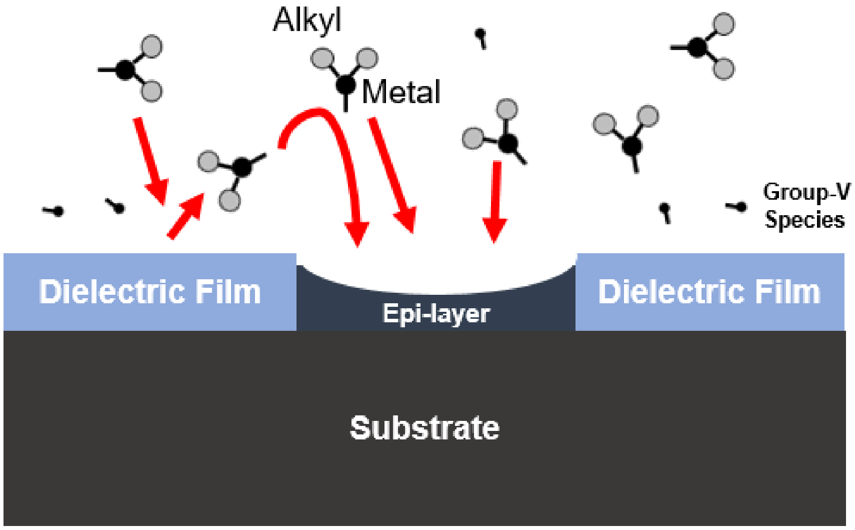

Fig. 2-4 *Chemical reaction model for the selective area epitaxy*

Another interesting aspect of the MOVPE process is that the dependency on the chemical reaction and surface diffusion of chemical species makes it possible to perform selective area epitaxy (SAE) where the local growth of epitaxial layer is carried out through patterned amorphous dielectric masks such as SiO_2 or Si_3N_4. In SAE, the epitaxial growth is inhibited in regions of the sample that are covered by the dielectric film, thus growth occurs only in unmasked area. The generally accepted proposition for the mechanism of the SAE is by the desorption of molecules or atoms impinging on the mask [10-11]. Then, the desorbed molecules collide with molecules in the gas phase, and are redirected towards the sample surface, where they desorb again if they strike the mask, but stick if they strike the openings in the mask, thus giving rise to a thickness enhancement of the selective deposits. In this process, growth precursors from the masked areas also diffuse to the exposed semiconductor surface. This diffusion increases the concentration of precursors near the masked area resulting in a growth rate enhancement in that area [12]. The SAE process is enhanced if the incoming reagents are not fully decomposed to the elemental species, since the sticking coefficients of Al, Ga, and In on SiO_2 or Si_3N_4 are not small at the typical growth temperatures, making the main reason for the lack of selectivity in the other types of crystal growth techniques such as solid source MBE or gas source MBE where elemental group III sources are used. Depending on the geometry of the dielectric mask, ternary and quaternary alloys typically can also shift in composition owing to the different gas phase diffusion and sticking coefficients of the precursor materials [13].

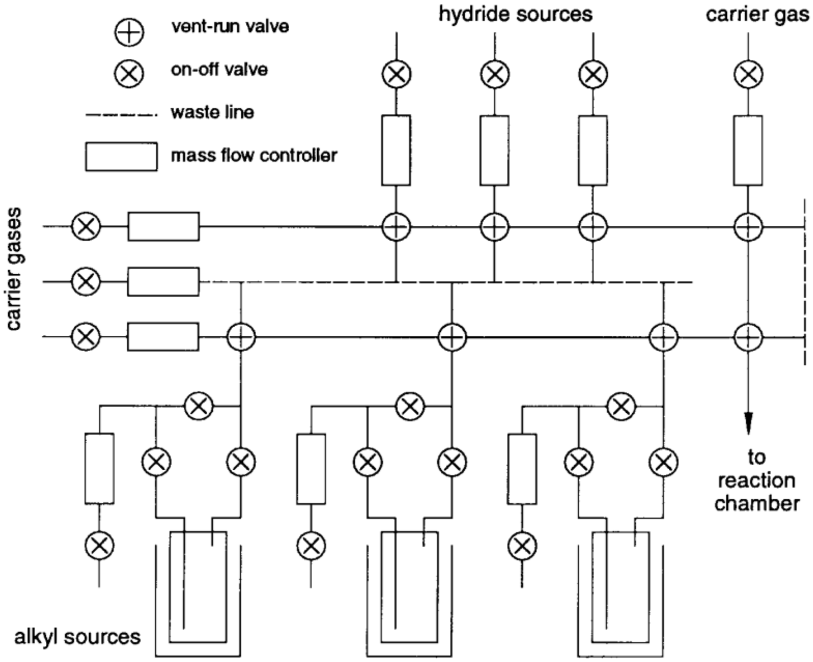

Fig. 2-5 *Schematic diagram of an MOVPE reactor delivery system gas panel, illustrating gas delivery modules, alkyl delivery modules, and the vent/run configuration (after reference [3])*

As schematically illustrated, the gas manifold contains the computer-controlled valves, mass flow and pressure controllers, and tubing that regulate and direct the flows and pressures of all reactants. Gas manifolds are designed in a vent/run configuration, where reactant flows are established in a line that goes directly to vent prior to their introduction into the reaction chamber. This establishment of flows helps reduce transient flow effects and allows the pressure of the MO cylinder to reach a constant steady state value. The reactant flows are then simply switched from the vent line to the line that goes to the reaction chamber (“run” line) in order to initiate the epitaxial growth. The pressure balancing between the vent and run legs is of importance to prevent either forward or backward flow surges during switching due to the pressure differences between the vent and run lines. These can result in the compositional variation at interfaces. This pressure balancing is accomplished through the use of electronically controlled needle valves using differential pressure measurements of the vent and run lines as feedback.

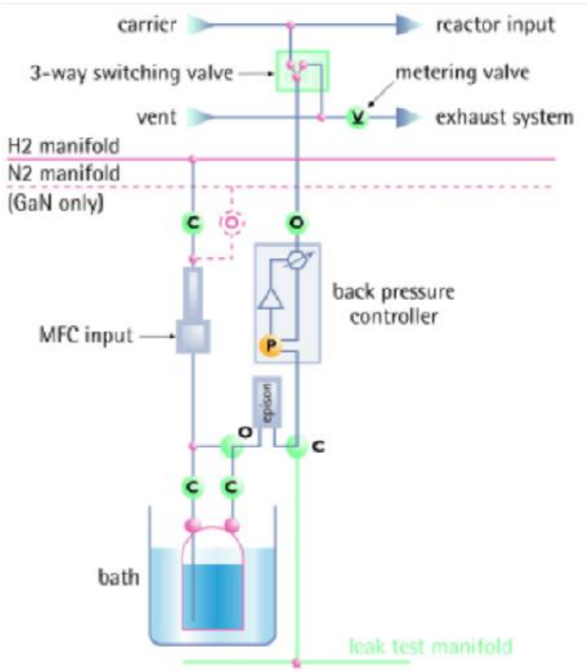

Fig. 2-6 *Schematic diagram of a typical bubbler arrangement*

The typical container for the MO source is in the form of a bubbler, as schematically represented in Fig. 2-6. Carrier gas (typically H_2) is passed through the bottom of the material via a dip tube [14]. Then the carrier gas transports the source material into the vent/reaction chamber. Assuming thermodynamic equilibrium between the condensed source and the vapor, the molar flow, v, can be written:

$$v = (P_v f_v / kT_{std}) P_{std} / P_{cyl} \tag{2.6}$$

where v is the molar flow in moles/min, P_v is the vapor pressure of the MO species at the bath temperature, f_v is the volume flow rate of the carrier gas through the bubbler in l/min, k is the gas constant, T_{std}=273ºC, P_{std}=1 atm, and P_{cyl} is the total pressure in the MO cylinder.

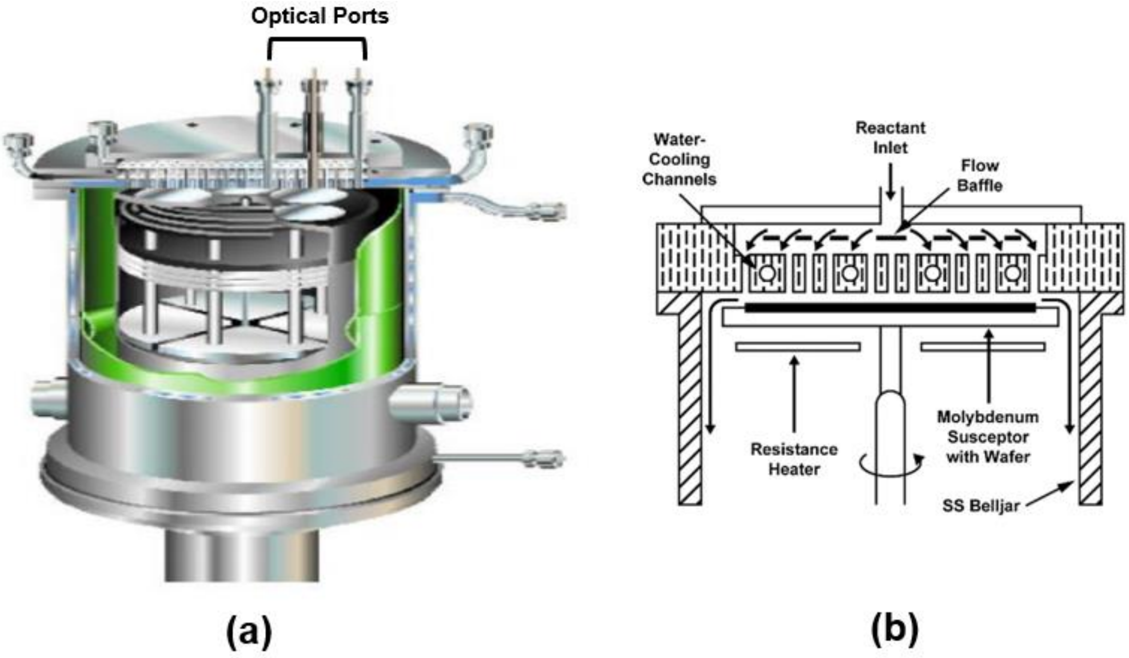

Fig. 2-7 *(a) Schematic diagram of Thomas Swan 3 x 2" reactor with close-coupled showerhead (CCS) configuration, and (b) Cross-sectional view of the CCS-based reactor (after reference 16).*

The reaction chamber is where the thermal decomposition, reaction, and deposition occur. Various types of reaction chamber designs have been introduced, such as vertical, horizontal, and barrel reactors [2], to ensure good uniformities in both substrate temperature and gas flow near the substrate. In this study, Thomas Swan 3 x 2" reactor with the close-coupled showerhead configuration was used for the crystal growth. In this configuration, the gases are introduced into the reactor through separate openings in the water-cooled showerhead to achieve an even distribution of the process gases. The substrates lie on a rotating susceptor (~100 rpm), which is heated by a resistive heater, to further enhance the uniformity in the gas mixture in a close proximity to the substrate surface [15-16], resulting in an improved deposition uniformity, as schematically shown in Fig. 2-7 (b).

2. 2. *in situ* characterization during MOVPE process

The real-time diagnostic tool (reflection high energy electron diffraction – RHEED), commonly employed in the MBE process, cannot be readily used in MOVPE because of the required high vacuum ($< 10^{-5}\,Torr$) in the electron diffraction process. For this reason, considerable attention has been given toward developing metrology which utilizes the optical reflectometry based on the Fabry-Perot interference.

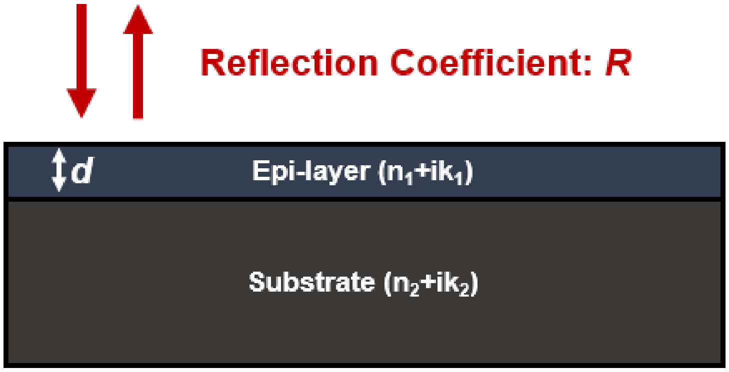

Fig. 2-8 *Fabry-Perot interference by two layers having distinct complex refractive indices*

A light beam at normal incidence to the layer surface gets partially reflected at the surface because of the difference in the refractive indices between epitaxial layer ($N_1 = n_1 + ik_1$) and the substrate ($N_2 = n_2 + ik_2$), as schematically represented in Fig. 2-8. Then the normal incidence reflection coefficient R for this bi-layer system can be given by

$$R = R_a R_a^* \tag{2.7}$$

where

$$R_a = \frac{r_{01}+r_{12}\exp(-2id\beta)\exp(\alpha d)}{1+r_{01}r_{12}\exp(-2id\beta)\exp(\alpha d)} \tag{2.8}$$

and $r_{ij} = (N_i - N_j)/(N_i + N_j)$ are the individual interface amplitude reflection coefficients, α is the absorption coefficient ($\alpha = 4\pi k_1/\lambda$), β is the phase angle ($\beta = 2\pi n_1/\lambda$), and λ is the wavelength of the light source.

The reflectivity R in this bi-layer system oscillates with a thickness period of $\lambda/2n_1$ and a damping factor due to absorption in the overlayer, which is governed by k_1 [17]. Then, the simultaneous determination of the growth rate and the composition in high accuracy is possible in real time, by fitting the experimental reflectivity data to equation (2.7) with the pre-determined complex refractive indices. Fig. 2-9 shows the *in situ* reflectance measured during the growth of GaAs/ $Al_xGa_{1-x}As$ on a 2” (001) GaAs substrate within the 3x2” Thomas Swan CCS reactor equipped with *LayTec’s EpiTT*^{TM}, which shows the Al composition of 53.9 ± 3.1%, which is in good agreement with the target 55%.

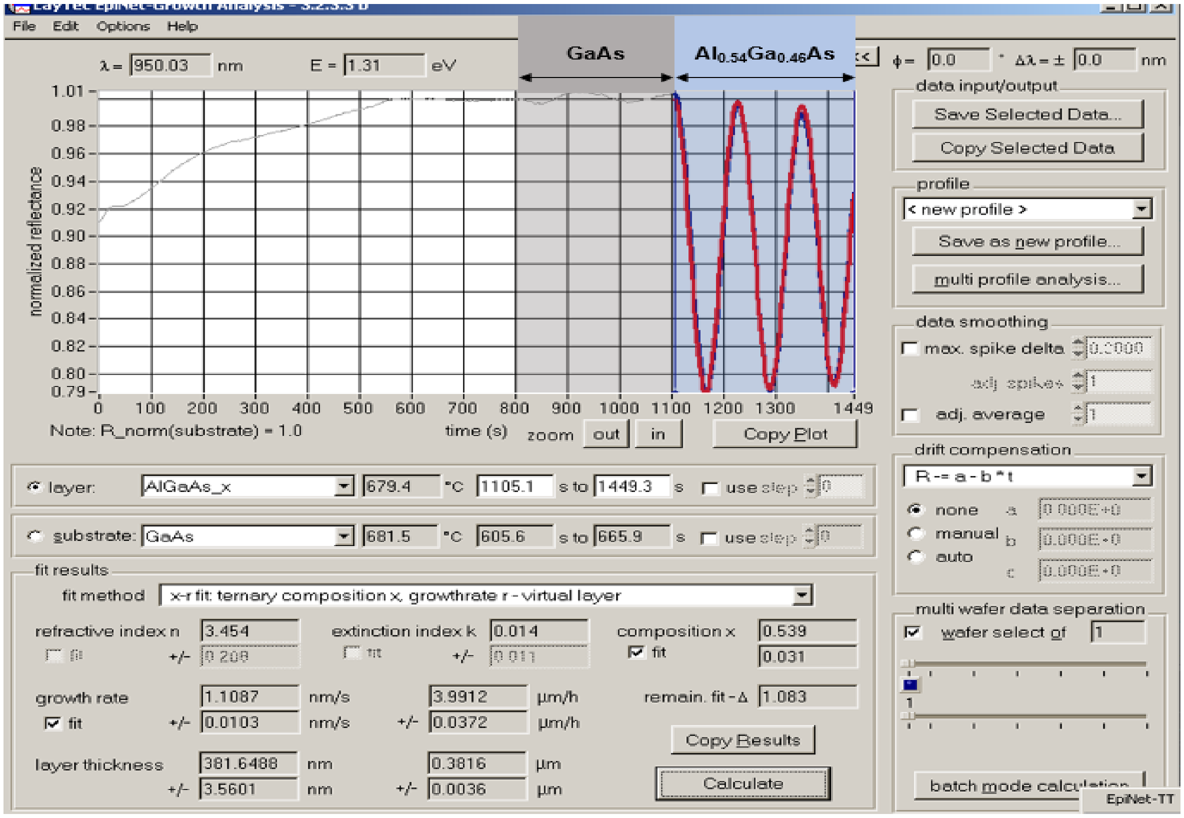

λ = 950.03 nm E = 1.31 eV

ϕ = 0.0 ° Δλ = ± 0.0 nm

Note: R_norm(substrate) = 1.0

profile: < new profile >

☐ max. spike delta 0.2000

adj. spikes 1

☐ adj. average 1

drift compensation: R -= a - b * t

● none a 0.000E+0

○ manual b 0.000E+0

○ auto c 0.000E+0

☑ wafer select of 1

● layer: AlGaAs_x 679.4 °C 1105.1 s to 1449.3 s ☐ use step 0

○ substrate: GaAs 681.5 °C 605.6 s to 665.9 s ☐ use step 0

fit results

fit method: x-r fit: ternary composition x, growthrate r - virtual layer

refractive index n 3.454 ☐ fit +/- 0.208

extinction index k 0.014 ☐ fit +/- 0.011

composition x 0.539 ☑ fit 0.031

growth rate 1.1087 nm/s 3.9912 µm/h

☑ fit +/- 0.0103 nm/s +/- 0.0372 µm/h

remain. fit - Δ 1.083

layer thickness 381.6488 nm 0.3816 µm

+/- 3.5601 nm +/- 0.0036 µm

Fig. 2-9 *Measured in situ reflectance during the growth of GaAs/*$Al_{0.54}Ga_{0.46}As$ *on GaAs substrate, where fitted curve is indicated in red, showing the extracted Al composition of 53.9±3.1%, which is in close agreement with target 55%.*

This *in situ* reflectance can be also used to diagnose and investigate the surface roughening or coarsening in real time, which are frequently employed for the growth of GaN-based MOVPE on mismatched substrate such as sapphire or Si [18]. In addition, the etch rate during *in situ* etching process can be accurately measured by the real time reflectometry, as *in situ* etching is the reverse process of the deposition of an epitaxial layer [19].

2. 3. *ex situ* characterization for the epitaxial layer grown by MOVPE

2. 3. 1. High-resolution X-ray diffraction

The *in situ* characterization by measuring the reflectivity cannot be readily applied for the identifying the composition and thickness of the nanostructures such as a strained QW, because obtaining at least a half period, corresponding to $\lambda/4n_1$, in the oscillation is necessary to obtain the growth rate, which can often exceed the critical thickness of the strained epitaxial layer. In addition, predetermination for the complex refractive index is not trivial. Therefore, *ex situ* measurement such as high-resolution x-ray diffraction is often used to accurately extract the growth rate and the composition of the strained epitaxial layer, which has a finite critical thickness for the relaxation.

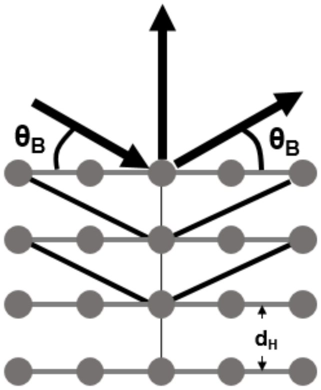

Bragg's Law:

$$\boldsymbol{2d_H sin\theta_B = n\lambda}$$

Fig. 2-10 *Diffraction of x-rays by a section of a crystal with lattice planes spaced a distance d_H apart.*

Based on the Bragg's law, shown in Fig. 2-10, the lattice constant of a cubic structure is directly proportional to the spacing d of any particular set of lattice planes. Therefore, by measuring the Bragg angle θ_B for this set of planes, d_H can be determined, and thus the lattice constant (a) can be calculated. In addition, the angular separation of the peaks ($\Delta\theta$) can be related to the lattice mismatch through the differential form of the Bragg equation with respect to θ. For symmetric geometry, where the diffraction planes are parallel to the sample surface, the following relation is obtained.

$$(\varDelta a\ /\ a)_{\perp} = -cot\theta_{B}\varDelta\theta \qquad (2.9)$$

where $(\varDelta a\ /\ a)_{\perp}$ represents the lattice strain perpendicular to the crystal surface (out-of-plane), which is related to the relaxed lattice mismatch $(\varDelta a\ /\ a)_{Relaxed}$ by

$$(\varDelta a\ /\ a)_{Relaxed} = (\varDelta a\ /\ a)_{\perp}[(1-v)/(1+v)] \qquad (2.10)$$

assuming the in-plane strain to be zero, and v is Poisson's ratio for the layer material.

The relaxed lattice mismatch can be found by using Vegard's law, $a_{A_{1-x}B_x} = (1-x)a_{A_{1-x}} + xa_{B_x}$. Therefore, by measuring the peak separation, the composition of a strained alloy can be accurately measured, and vice versa. In addition, the interaction between incident and reflected x-ray waves through the whole epitaxial layer can be attributed to the diffraction patterns, resulting in Pendellosung fringes, $\varDelta\theta_P$. The known relation between the angular spacing of the $\varDelta\theta_P$ and the thickness L of the whole epilayer is [20]

$$L = \lambda|\gamma_h|/\varDelta\theta_P \sin{(2\theta_B)} \qquad (2.11)$$

where $\gamma_h = sin(\theta_B + \alpha)$ and α is the angle between the sample surface and diffraction plane, leading to the following simplified relation for symmetrical geometry

$$L = \lambda / 2\Delta\theta_P \cos(\theta_B) \tag{2.12}$$

The equation (2.11) and (2.12) are applicable to a strained superlattice having a period of T, in which case the whole epitaxial layer thickness L is replaced by the superlattice period T, and the oscillation spacing is replaced by the angular distance between the satellite peaks. Therefore, the strained superlattice periodicity as well as the layer thickness can be accurately measured. In addition, the interfacial abruptness can be qualitatively assessed by the contrast in the Pendellosung fringe.

2. 3. 2. Photoluminescence

Luminescence is the term used to describe the non-equilibrium emission of radiation. Photoluminescence (PL) measurement is a non-destructive spectroscopic technique which utilizes the spontaneous emission of light from a material under optical excitation. The typical setup for the PL measurements includes a laser source for the photoexcitation, collimating lens, spectrometer, photodetector, and often lock-in amplifier to collect a small signal, as schematically shown in Fig. 2-11. The sample is occasionally kept in a temperature-variant cryostat in order to perform the temperature dependent PL measurements, which can provide insight into the carrier dynamics associated with thermally activated recombination process.

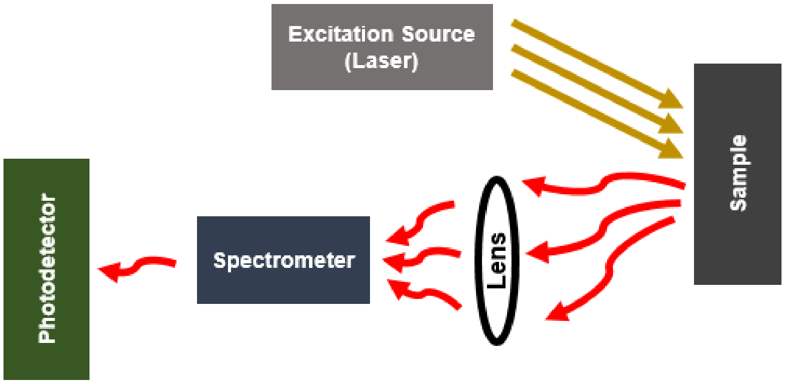

Fig. 2-11 *Typical experimental setup for PL measurements*

When light of sufficient energy, i.e., photon energy higher than the bandgap of the sample, from the excitation source is incident on a sample, photons are absorbed, and electronic excitations are created by electron-hole pair generation process. Eventually, these excess electron-hole pairs relax, and the electrons returns back to the ground state. If radiative relaxation occurs, the emitted light is called PL, as schematically represented in Fig. 2-12 (a).

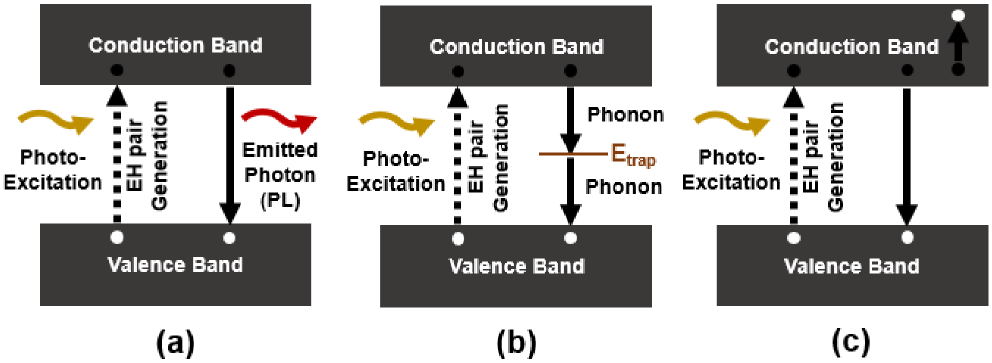

Fig. 2-12 *(a) Band-to-band Radiative recombination, (b) Nonradiative recombination via an intermediate state (*E_{trap}*), and (c) Nonradiative recombination via Auger process*

The resulting PL spectrum provides the transition energy such as band gap energy of a semiconductor material. On the other hand, a rapid non-radiative recombination via either midgap states, in the presence of a high concentration of surface states, impurities and defect states, or Auger process can also take place.

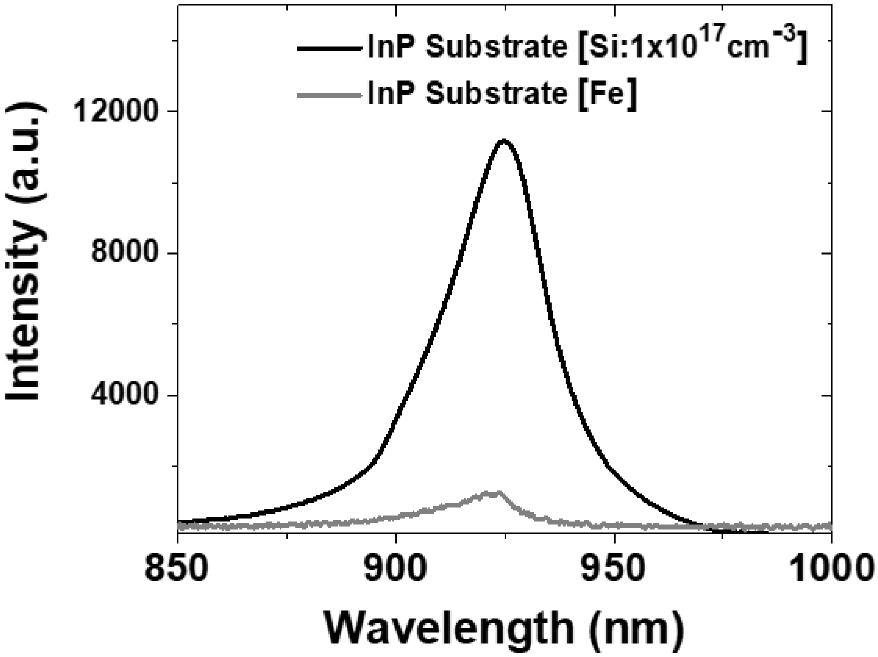

Fig. 2-13 *PL spectra of either Si-doped InP or Fe-doped InP substrates measured at the same condition* ($\lambda_{excitation} = 532nm$) *at room temperature.*

Therefore, the PL measurement can be used to qualitatively estimate the radiative efficiency ($\eta_{rad} = \frac{number\ of\ photons\ emitted}{number\ of\ photons\ absorbed}$) of the material, which is an important parameter for realizing high-performance optoelectronic devices. Fig. 2-13 presents PL spectra of two types of InP substrates (either Si-doped or Fe-doped), which shows the PL peak position corresponding to the band gap energy of InP (0.923nm). Si is a shallow donor while Fe acts as a deep acceptor in InP, which forms a midgap state, resulting in the observed difference in the PL intensity.

2. 3. 3. Hall Measurement by Van der Pauw Resistivity Measurement

Hall measurement employing Van der Pauw method provides information about electrically active impurities (carriers) and mobility in a practical manner. The van der Pauw method involves applying a current and measuring voltage using four small contacts on the circumference of a flat homogeneous isotropic square sample. This method is useful for measuring small samples because geometric spacing of the contacts is of less importance. Using this method, the resistivity can be derived from a total of eight measurements that are made around the periphery of the sample with the configurations shown in Fig. 2-14.

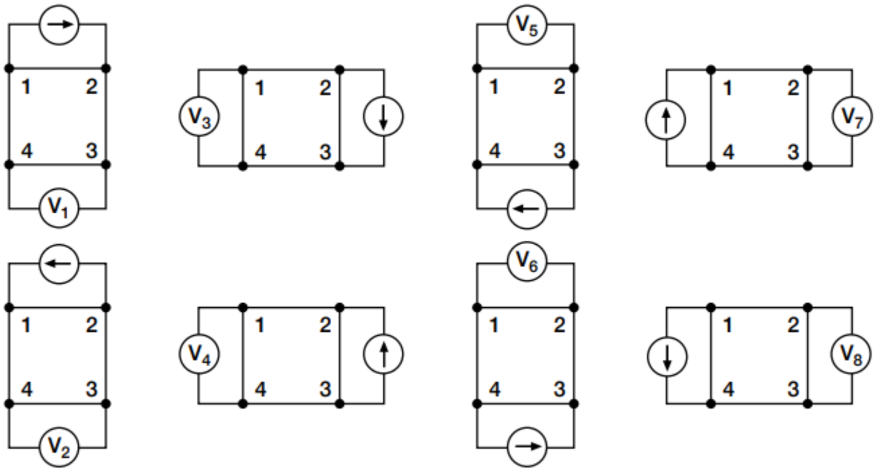

Fig. 2-14 *Van der Pauw Resistivity Conventions*

Once all the voltage measurements are made, the sheet resistivity (R_s) can be numerically found by the following relation

$$\exp(-\pi R_A/R_s) + \exp(-\pi R_B/R_s) = 1 \tag{2.13}$$

where R_A and R_B are as follows,

$$R_A = (\frac{V_{34}}{I_{21}} + \frac{V_{43}}{I_{12}} + \frac{V_{12}}{I_{43}} + \frac{V_{21}}{I_{34}})/4 \quad \text{and} \quad R_B = (\frac{V_{41}}{I_{32}} + \frac{V_{14}}{I_{23}} + \frac{V_{23}}{I_{14}} + \frac{V_{32}}{I_{41}})/4$$

By applying positive (P) and negative (N) magnetic fields with the direction normal to the surface of the sample and subsequently measuring the difference of the voltages ($\bar{V}_{ij}$), the overall Hall voltage can be obtained by the following relation:

$$V_H = \left(\frac{\Delta V_{13}+\Delta V_{24}+\Delta V_{31}+\Delta V_{42}}{8}\right) \quad (2.14)$$

where $\Delta V_{ij} = V_{ij,P} - V_{ij,N}$

Equation (14) can be further simplified by the measurement consistency following current reversal, leading to the following relation,

$$V_H = \left(\frac{\Delta V_{13}}{2}\right) = \left(\frac{\Delta V_{24}}{2}\right) = \left(\frac{\Delta V_{31}}{2}\right) = \left(\frac{\Delta V_{42}}{2}\right) \quad (2.15)$$

Therefore, the sheet carrier density ($n_S = n \times d$) can be calculated by balancing the electric field with the Lorentz force, i.e.,

$$n_s = IB/q|V_H| \quad (2.16)$$

when $V_H = \left(\frac{\Delta V_{13}}{2}\right)$ is measured with I=I_{24}. Similarly, the Hall mobility (μ_{Hall}) is given by

$$\mu_{Hall} = \frac{|V_H|}{R_S I B} = 1/(q n_s R_S) \quad (2.17)$$

2. 4. Summary

In this chapter, the crystal growth mechanism by MOVPE and the related crystal growth techniques required to realize the growth of laser heterostructure have been reviewed. The choice of precursors depending on the growth condition was considered in detail, as novel III-V metastable alloys often exhibit a very little solubility in typical growth temperature range (600-800°C), which requires the crystal growth to be performed at lower growth temperature (400-500 °C). The use of TBAs as an As-precursor together with TEGa as a Ga-precursor is preferred for the crystal growth near this low growth temperature owing to it superior decomposition efficiency as well as potentially lower carbon incorporation. In addition, the *in situ* and *ex situ* metrology including real-time reflectance, HR-XRD, PL and Hall measurement were reviewed, which were used in this study to characterize MOVPE-grown materials and to realize the laser heterostructure.

Reference

[1] Manasevit, Harold M. "Single-crystal gallium arsenide on insulating substrates." *Applied Physics Letters* 12.4 (1968): 156-159.

[2] Kuech, T. F. "Metal-organic vapor phase epitaxy of compound semiconductors." *Materials Science Reports* 2.1 (1987): 1-49.

[3] Coleman, James J. "Metalorganic chemical vapor deposition for optoelectronic devices." *Proceedings of the IEEE* 85.11 (1997): 1715-1729.

[4] Volz, Kerstin, et al. "MOVPE growth of dilute nitride III/V semiconductors using all liquid metalorganic precursors." *Journal of Crystal Growth* 311.8 (2009): 2418-2426.

[5] Oe, Kunishige, and Hiroshi Okamoto. "New semiconductor alloy $GaAs_{1-x}Bi_x$ grown by metal organic vapor phase epitaxy." *Japanese journal of applied physics* 37.11A (1998): L1283.

[6] Stringfellow, G. B. "Fundamental aspects of vapor growth and epitaxy." Journal of crystal growth 115.1-4 (1991): 1-11.

[7] Fushimi, Hiroshi, and Kazumi Wada. "Degradation mechanism in carbon-doped GaAs minority-carrier injection devices [HBTs]." *IEEE Transactions on Electron Devices* 44.11 (1997): 1996-2001.

[8] Lacklison, D. E., et al. "RHEED studies of MOMBE growth using TMGa or TEGa with As_2." *Journal of crystal growth* 120.1-4 (1992): 50-56.

[9] McCaulley, J. A., R. J. Shul, and V. M. Donnelly. "Kinetics of thermal decomposition of triethylgallium, trimethylgallium, and trimethylindium adsorbed on GaAs (100)." *Journal of Vacuum Science & Technology A: Vacuum, Surfaces, and Films* 9.6 (1991): 2872-2886.

[10] Kayser, O. "Selective growth of InP/GaInAs in LP-MOVPE and MOMBE/CBE." *Journal of crystal growth* 107.1-4 (1991): 989-998.

[11] Colas, E., et al. "Lateral and longitudinal patterning of semiconductor structures by crystal growth on nonplanar and dielectric-masked GaAs substrates: application to thickness-modulated waveguide structures." *Journal of crystal growth* 107.1-4 (1991): 226-230.

[12] Cotta, M. A., et al. "Scanning force microscopy measurement of edge growth rate enhancement in selective area epitaxy." *Applied physics letters* 62.5 (1993): 496-498.

[13] Fujii, Takuya, and Mitsuru Ekawa. "Origin of compositional modulation of InGaAs in selective area metalorganic vapor phase epitaxy." *Journal of applied physics* 78.9 (1995): 5373-5386.

[14] Hersee, S. D., and J. M. Ballingall. "The operation of metalorganic bubblers at reduced pressure." *Journal of Vacuum Science & Technology A: Vacuum, Surfaces, and Films* 8.2 (1990): 800-804.

[15] Wang, Christine A. "Early history of MOVPE reactor development." *Journal of Crystal Growth* 506 (2019): 190-200.

[16] Vernon, S. M., et al. "Close-spaced MOCVD reactor for 1%-uniformity growth of In-containing materials on 4" substrates." *Proceedings of 1994 IEEE 6th International Conference on Indium Phosphide and Related Materials (IPRM)*. IEEE, 1994.

[17] Farrell, Trevor, John V. Armstrong, and Philip Kightley. "Dynamic optical reflectivity to monitor the real-time metalorganic molecular beam epitaxial growth of AlGaAs layers." *Applied physics letters* 59.10 (1991): 1203-1205.

[18] Benzarti, Z., et al. "Study of Surface and Interface Roughness of GaN-Based Films Using Spectral Reflectance Measurements." *Journal of Electronic Materials* 44.10 (2015): 3243-3252.

[19] Rebey, A., et al. "*in situ* reflectance monitoring of the growth and etching of AlAs/GaAs structures in MOVPE." *Journal of crystal growth* 261.4 (2004): 450-457.

[20] Tapfer, L., and K. Ploog. "Improved assessment of structural properties of Al_xGa_{1-x} As/GaAs heterostructures and superlattices by double-crystal x-ray diffraction." *Physical Review B* 33.8 (1986): 5565.

[21] van der Pauw, Leo J. "A method of measuring the resistivity and Hall coefficient on lamellae of arbitrary shape." *Philips technical review* 20 (1958): 220-224.

Chapter 3. Design Considerations for QW and QD-based Laser Diodes

3. 1. Optical Waveguide Theory

In Chapter 1, the optical confinement within the DH structure-based laser diode has been briefly discussed, which was attributed to the one of the reasons for its success in the realization of practical devices operating at room temperature. In an edge emitting laser diode geometry, this optical confinement in the transverse direction can be mathematically described by Maxwell's equations.

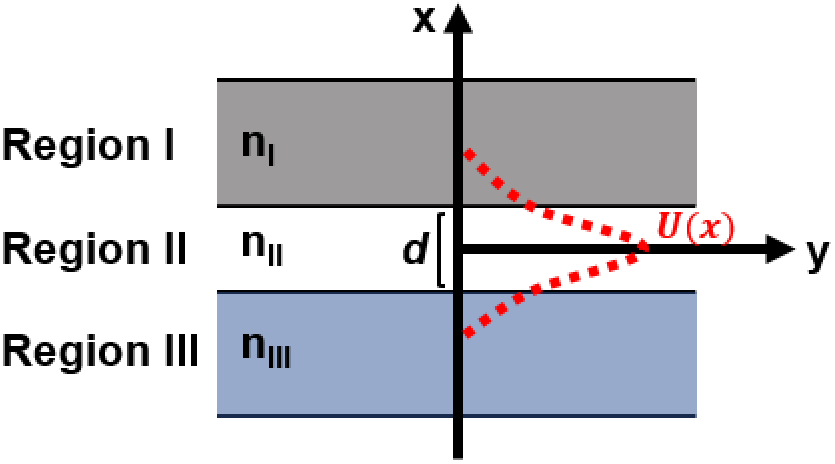

Fig. 3-1 *Schematic diagram of a three-layer heterostructure waveguide where the x-direction is defined as the transverse direction and the y-direction corresponds to the direction of propagation*

Shown in Fig. 3-1 is the schematic diagram of a three-layer structure, forming a positive index profile in the transverse direction (*i.e.*, $n_I = n_{III} < n_{II}$), which is commonly employed in the DH structure. The electric fields of the supported modes within this structure will be confined to the waveguide core region (Region II) with evanescent tails within the cladding layers (Region I and III) as a result of the positive index profile. This supported electric fields can be described by time-independent Helmholtz wave equation:

$$\nabla^2 U(x) + [n^2 k_0^2 - \beta^2] U(x) = 0 \tag{3.1}$$

where $U(x,y)$ is the transverse amplitude, $n = \sqrt{(\varepsilon/\varepsilon_0)}$ is the complex refractive index, $k_0 = 2\pi/\lambda$ is the free space wave number and β is the complex propagation constant.

The real part of β is inversely related to the phase velocity and from this relation, an effective propagation constant is defined as $\beta_{eff,m}$ for each of the supported mode within the waveguide structure. This effective propagation constant is related to the free space wave number scaled by an effective refractive index, β=$k_0 n_{eff,m}$ [1]. The continuity of $U(x)$ at the boundary leads to the boundary condition at the heterojunction as such $U_{I_{at\ x=d/2}} = U_{II_{at\ x=d/2}}$ and $\frac{d}{dx} U_{I_{at\ x=d/2}} = \frac{d}{dx} U_{II_{at\ x=d/2}}$, and similarly between Region II and III. Therefore, in the case of symmetric refractive index profile (n_I=n_{III}), the general solutions of equation (3.1) in each region are obtained as such:

$$\text{Region I: } U_I(x) = Be^{-\gamma x} \tag{3.2}$$

$$\text{Region II: } U_{II}(x) = \begin{cases} Acos(k_x x) & Symmetric\ case \\ Asin(k_x x) & Asymmetric\ case \end{cases} \tag{3.3}$$

$$\text{Region III: } U_{III}(x) = Be^{\gamma x} \tag{3.4}$$

where γ = $k_x$tan ($\frac{k_x 2}{d}$) for symmetric case and γ = $-k_x$cot ($\frac{k_x 2}{d}$) for asymmetric case.

Plugging these general solutions into equation (3.1) yields k_x and γ as such:

$$k_x{}^2 = k_0{}^2 n_{II}{}^2 - \beta^2 \quad (3.5)$$

$$\gamma^2 = \beta^2 - k_0{}^2 n_I{}^2 \quad (3.6)$$

where the effective refractive index can be found numerically using the following relation:

$$\frac{k_0 d}{2}\sqrt{n_{II}{}^2 - n_{eff}{}^2} = \tan^{-1}\left(\sqrt{\frac{n_{eff}{}^2 - n_I{}^2}{n_{II}{}^2 - n_{eff}{}^2}}\right) + (m-1)\frac{\pi}{2} \quad (3.7)$$

Then, the transverse confinement factor (Γ) can be calculated using the relation above, which is defined as the fraction of the optical energy that is confined in the active region of the laser diodes.

$$\Gamma = \frac{\int_{-d/2}^{d/2} |U(x)|^2 dx}{\int_{-\infty}^{\infty} |U(x)|^2 dx} \quad (3.8)$$

Γ is an important parameter in designing laser heterostructure as it is directly proportional to the modal gain that is related to the threshold current density, as will be shown later in this chapter. Therefore, typical high-performance laser heterostructures are designed in a way that the transverse optical confinement factor is maximized.

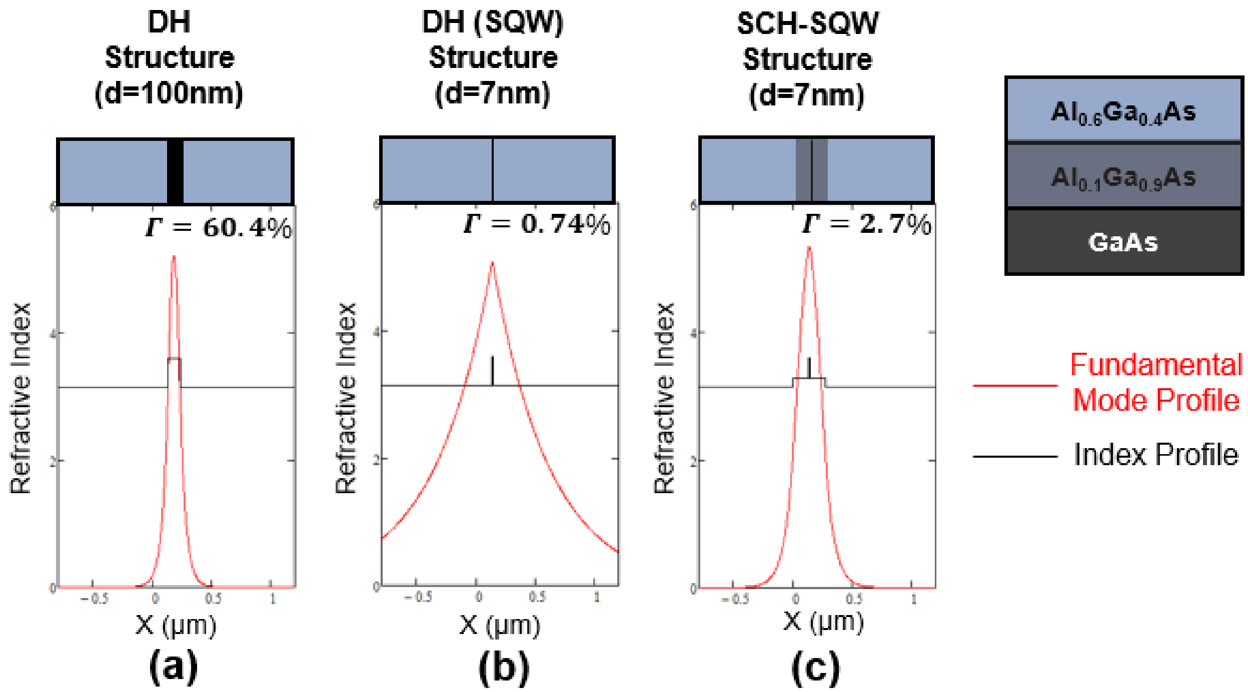

Fig. 3-2 *Simulated transverse fundamental modes (m=0) for examples of heterostructure active region: (a) p-i-n DH structure (100nm-thick GaAs sandwiched by* $Al_{0.6}Ga_{0.4}As$ *cladding layers), (b) p-i-n DH structure employing a single QW (SQW) region (7nm-thick GaAs sandwiched by* $Al_{0.6}Ga_{0.4}As$ *cladding layers), and (c) Separate-confinement-heterostructure (SCH) employing a SQW region (7nm-thick GaAs sandwiched by* $Al_{0.1}Ga_{0.9}As$ *SCH and* $Al_{0.6}Ga_{0.4}As$ *cladding layers)*

Shown in Fig. 3-2 are the simulated transverse fundamental modes (m=0) for various types of heterostructure active region. As the thickness of the *i*-region is reduced, a rapid reduction in the optical confinement factor takes place, as shown in the Fig. 3-2 (a) and (b). This was the main reason for the early demonstrations of the QW active region lasers exhibited similar or even higher threshold current densities than those of *p-i-n* DH structure active region lasers, as discussed in Chapter 1. However, by introducing the separate confinement heterostructure as schematically shown in Fig. 3-2 (c), the optical confinement factor of the QW active region lasers has significantly improved, leading to a superior device performance than those of the *p-i-n* DH structure-based lasers [2-3]. It must be noted that the optical confinement factor of the QW active region lasers, which employs SCH structure, is still significantly lower than that of *p*-*i*-*n* DH structure-based lasers. However, this lower optical confinement factor of the QW active region laser is compensated by the advantages including higher material gain coefficients and lower transparency current density, which arise from the reduced dimensionality, as will be discussed later in this chapter.

3. 2. Current injection in Laser Diodes

"LASER" stands for "Light Amplification by Stimulated Emission of Radiation". Therefore, in lasers, light amplification is achieved via stimulated emission process as schematically shown in Fig 3-3 (b).

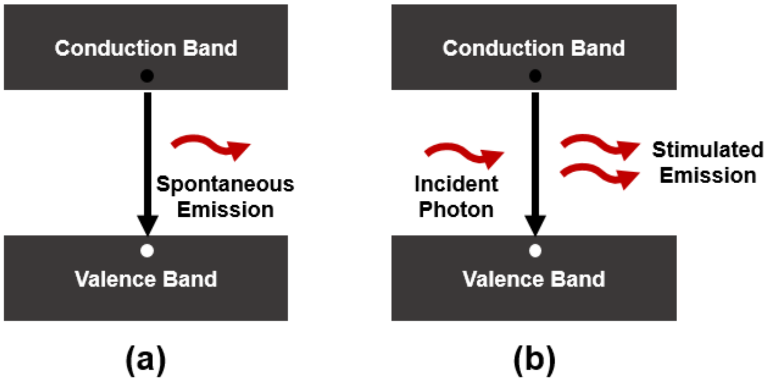

Fig. 3-3 *Light emission process: (a) by spontaneous emission and (b) by stimulated emission*

Spontaneous emission process occurs when an electron radiatively recombines with a hole in the absence of interaction with an external photon. On the other hand, stimulated emission process takes places when an incident photon perturbs an electron-hole pair, which induces photon emission that has a same phase and amplitude as the incident photon. In a laser, light from this stimulated emission process is efficiently extracted in a resonant cavity. Typical geometry of the resonant cavity employed in in-plane semiconductor laser diodes is schematically represented in Fig. 3-4 where the cavity is formed by the cleaved facets.

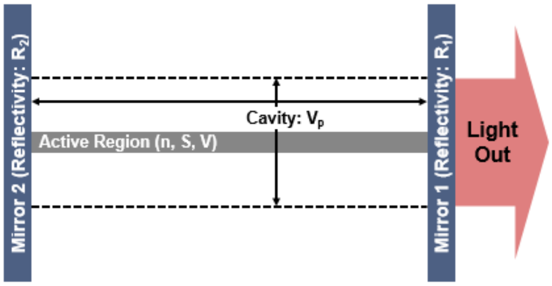

Fig. 3-4 *Schematics of in-plane, edge-emitting laser illustrating the active (V) and cavity (V_p) volumes where n is the carrier density, and S is photon density.*

The carrier concentration in the active region is determined by the rate equation

$$\frac{dn(t)}{dt} = \eta_i \frac{J(t)}{qd} - R(n) - v_g g(n) S(t) \tag{3.9}$$

where the first term on the right-hand side accounts for carrier injection into the active region with a thickness d. The unit charge q is $1.6 \times 10^{-19} C$.

The injection efficiency of carriers into the active region is η_i, which is the percentage of electrons and holes transporting into the active region after surviving the carrier losses due to recombination outside the active regions and/or leakage of carriers out of the active region. $R(n)$ represents both radiative and nonradiative carrier recombination processes. The last term is related to the carrier loss owing to stimulated emission process when the laser cavity has a photon density S(t), which is the number of photons per unit volume. These photons encounter a gain of g(n) [1/cm] while propagating with the group velocity v_g of light, $v_g=c/n_g$, where ng is the group index and c is the seed of light in free space. The recombination rate, $R(n)$ is given by

$$R(n) = An + Bn^2 + Cn^3 = \frac{n}{\tau} \tag{3.9}$$

where τ is carrier lifetime, A is known as the monomolecular recombination coefficient accounting for the defects or monocarrier type recombination, B is the radiative recombination coefficient, and C accounts for nonradiative Auger recombination processes.

Under the steady-state condition before the stimulated emission start to occur, equation (3.9) can be expressed as

$$\frac{\eta_i J}{qd} = An + Bn^2 + Cn^3 = \frac{n}{\tau} \tag{3.10}$$

which can be then used at the threshold

$$\frac{\eta_i J_{th}}{qd} = n_{th} + B{n_{th}}^2 + C{n_{th}}^3 = \frac{n_{th}}{\tau} \tag{3.11}$$

Since n_{th} typically clamps above threshold due to the rapid stimulate emission process, the equation (3.10) can be substitute into equation (3.9), yielding the following relation for the above-threshold case,

$$\frac{dn(t)}{dt} = \eta_i \frac{J-J_{th}}{qd} - v_g gS, \qquad (J > J_{th}) \tag{3.12}$$

where the steady state photon density (S) can be given as follows,

$$S = \frac{\eta_i (J - J_{th})}{q v_g g_{th} d}, \qquad (Steady - state) \qquad (3.13)$$

Then, the output power above the threshold can be expressed by multiplying the stored optical energy density ($S \times h\nu \times V_p(cavity\ volume)$) by the energy loss rate through the mirrors ($v_g \alpha_m = 1/\tau_m$), and using $\Gamma = V_p/V$,

$$P_0 = \eta_i \left(\frac{\alpha_m}{<\alpha_i> + \alpha_m}\right) \frac{h\nu}{q} (J - J_{th}) \, , \qquad (J > J_{th}) \qquad (3.14)$$

where α_i internal loss associated with the free-carrier absorption while α_m is the mirror loss term defined as $\alpha_m = \frac{1}{2L} \ln \left(\frac{1}{R_1 R_2}\right)$.

By defining $\eta_d = \eta_i \left(\frac{\alpha_m}{<\alpha_i> + \alpha_m}\right)$, which is the external differential quantum efficiency, the equation (3.14) can be further simplified.

$$P_0 = \eta_d \frac{h\nu}{q} (J - J_{th}) \, , \qquad (J > J_{th}) \qquad (3.15)$$

In contrast, the output power below the threshold current density can be similarly derived [1],

$$P_0 = \eta_r \eta_i \left(\frac{\alpha_m}{<\alpha_i> + \alpha_m}\right) \frac{h\nu}{q} \beta_{sp}(J) \, , \qquad (J < J_{th}) \qquad (3.16)$$

where η_r is the radiative efficiency defined as $\frac{Bn^2}{An+Bn^2+Cn^3}$, and β_{sp} is the spontaneous emission factor, defined as the percentage of the total spontaneous emission coupled into the lasing mode.

This typical P_0 as a function of injected J relationship is schematically shown in Fig. 3-5 (a). The inverse of the external differential quantum efficiency, ${\eta_d}^{-1}$ can be expressed as

$$ {\eta_d}^{-1} = {\eta_i}^{-1}[1 + \frac{\alpha_i L}{\ln\left(\frac{1}{R}\right)}] \tag{3.17} $$

Therefore, a plot of ${\eta_d}^{-1}$ versus the cavity length L shows a linear relation with the intercept ${\eta_i}^{-1}$ at L=0, as shown in Fig. 3-5 (b), which makes it possible to experimentally extract η_i and α_i.

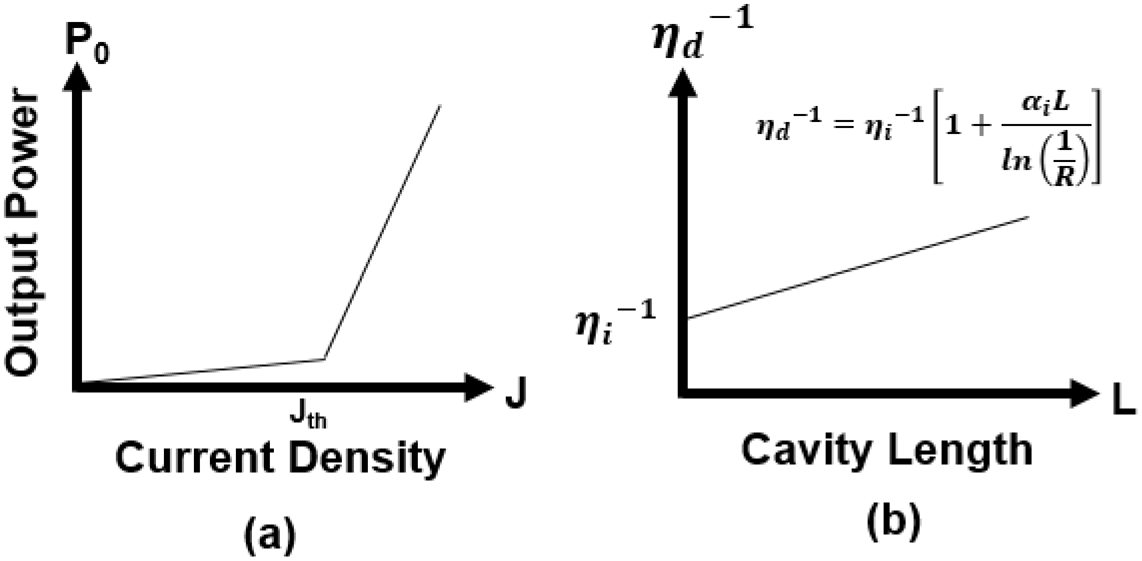

***Fig. 3-5** (a) The typical P_0 versus input current density (J) relation of the laser diodes, (b) A plot of the inverse external differential quantum efficiency (${\eta_d}^{-1}$) versus the laser cavity length, L. The intercept with the vertical axis gives the injection efficiency ${\eta_i}^{-1}$ while the slope gives the internal loss, α_i.*

The extracted η_i by this cavity length dependent measurement yields the value obtained above threshold, which is expressed as $\eta_{i\_above\ threshold}$ thereafter. This $\eta_{i\_above\ threshold}$ can be very distinct from the η_i values at threshold ($\eta_{i\_at\ threshold}$) and below-threshold ($\eta_{i\_below\ threshold}$) as pointed out by prior studies [4-5].

Once α_i is found, the threshold modal gain (Γg_{th}) can be calculated from the devices with the varying cavity length (L) using the following relation,

$$\Gamma g_{th} = \alpha_i + \alpha_m = \alpha_i + \frac{1}{2L}\ln\left(\frac{1}{R_1 R_2}\right) \tag{3.18}$$

The obtained threshold modal gain (Γg_{th}) can be, then, used to extract the modal gain coefficient (Γg_0) by fitting the data points to the following exponential curve.

$$J_{th} = \frac{J_{tr}}{\eta_{i\_at\ threshold}} \exp\left(\frac{\Gamma g_{th}}{\Gamma g_0}\right) \tag{3.19}$$

A caution needs to be taken here because $\eta_{i\_above\ threshold}$ value obtained from the cavity length dependent measurement by the relation (3.17) should not be applied for the $\eta_{i\_at\ threshold}$ term in equation (3.19) when trying to obtain the transparency carrier density (J_{tr}).

The transparency carrier density (J_{tr}) can be expressed as follows.

$$J_{tr} = \frac{q N_{tr} L_z}{\tau} \tag{3.20}$$

where N_{tr} is transparency carrier density and L_z is the active region thickness.

As expressed in equation (3.20), the direct proportionality of L_z with respect to J_{tr} has led to a significant reduction in the transparent current density (J_{tr}) as the active region was reduced from the bulk scale (~100nm) to usual quantum well thickness (5 ~ 10nm).

The transparency carrier density, *i.e.*, the number of injected carriers at which the rate of absorption of light exactly balances the rate of emission, can be achieved when the quasi-Fermi level energy separation (E_{fc}-E_{fv}) is equal to the transition energy of the active region. The total number of electrons (or holes) can be calculated by integrating the product of the density of state functions and the Fermi distribution function. Neglecting the contributions from higher subbands which are effectively cut off by the Fermi functions [6] and using the density of state presented in Fig 1-5, the electron density at the transparency condition of the bulk *p*-*i*-*n* DH laser can be numerically and/or analytically calculated as follows,

$$N_{DH}^{tr} = \frac{(2m_e^*)^{3/2}}{4\pi^2\bar{h}^3}\int_{\varepsilon_1}^{\infty}\frac{\sqrt{E_c-\varepsilon_1}\,dE_c}{e^{(E_c-\varepsilon_1)/kT}+1} = 2\left(\frac{\pi m_e^* kT}{2\pi^2\bar{h}^2}\right)^{3/2}\frac{4}{3\sqrt{\pi}}\Delta^{3/2} \qquad (3.21a)$$

where $m_e{}^*$ and $m_h{}^*$ are the effective mass for electron and hole, respectively, k is the Boltzmann constant (1.38064852 × 10-23 $\mathrm{m^2kgs^{-2}K^{-1}}$), h is Planck constant (6.62607004 × $10^{-34}\mathrm{m^2kg/s}$). Δ is numerically solved using the following relation,

$$\frac{4}{3\sqrt{\pi}}\Delta^{3/2} = \left(\frac{m_h{}^*}{m_e{}^*}\right)^{3/2} e^{-\Delta} \qquad (3.21b)$$

For GaAs, the effective masses of electron and holes are ${m_e}^* = 0.067m_0$ and ${m_h}^* = 0.5m_0$, which leads to Δ and $N_{DH,GaAs}^{tr} = 9 \times 10^{17} cm^{-3}$. Similarly, the transparency carrier densities of the semiconductor active region with the reduced dimensionality can be analytically found as follows,

$$N_{QW}^{tr} = \frac{{m_e}^*}{L_z \pi \bar{h}^2} \int_{\varepsilon_1}^{\infty} \frac{dE_C}{e^{(E_C - \varepsilon_1)/kT} + 1} = \frac{{m_e}^* kT}{L_z \pi \bar{h}^2} \times 1.43 \qquad (6{m_e}^* \approx {m_h}^*) \qquad (3.22a)$$

$$N_{QW}^{tr} = \frac{{m_e}^*}{L_z \pi \bar{h}^2} \int_{\varepsilon_1}^{\infty} \frac{dE_C}{e^{(E_C - \varepsilon_1)/kT} + 1} = \frac{{m_e}^* kT}{L_z \pi \bar{h}^2} \times \ln(2) \qquad ({m_e}^* \approx {m_h}^*) \qquad (3.22b)$$

$$N_{QD}^{tr} = \frac{2}{L_y L_x L_z} \int_{\varepsilon_1}^{\infty} \frac{\delta(E_C - \varepsilon_1) dE_C}{e^{(E_C - \varepsilon_1)/kT} + 1} = \frac{1}{L_y L_x L_z} \qquad (3.23)$$

$N_{QW,GaAs}^{tr}$ from the relation (3.22b) can be calculated to be $4.6 \times 10^{17} cm^{-3}$ assuming the L_z=10nm, while the relation (3.22a) yields $N_{QW,GaAs}^{tr} = 9.2 \times 10^{17} cm^{-3}$, which is similar to the calculated $N_{DH,GaAs}^{tr} = 9 \times 10^{17} cm^{-3}$. This result suggests the simply reducing the dimension of the active region does not yield a significant reduction in the transparency carrier density, while the reduction in the effective mass (${m_h}^*$) of the hole can result in the reduction in the N_{QW}^{tr} by a factor of two. This reduction in the effective hole mass can be achieved by introducing the biaxial strain, as schematically presented in Fig. 1-3 in Chapter 1. The transparency carrier densities of either DH structure or QW has the temperature dependency, which, in turn, is partially responsible for the temperature sensitivity in the threshold current density (J_{th}). The temperature dependency of the threshold current density can be characterized by using the relation,

$$J_{th}(T) = J_0 e^{\frac{T}{T_0}} \qquad (3.24)$$

where $J_{th}(T)$ is the threshold current density measured at the heat sink temperature of T.

The obtained T_0 by fitting the curve (3.24) is called a characteristic temperature coefficient for the threshold current density, which is a figure of merit to determine the temperature sensitivity of the laser's threshold current density.

Similarly, the temperature dependency of the external differential efficiency (η_d) can be described using the relation below,

$$\eta_d(T) = \eta_{d,0} e^{-\frac{T}{T_1}} \tag{3.25}$$

The measurement of these characteristic temperatures, T_0 and T_1, allow for the qualitative assessment of the carrier confinement within the active region of the semiconductor lasers during the laser operation.

Reference

[1] Coldren, Larry A., Scott W. Corzine, and Milan L. Mashanovitch. *Diode lasers and photonic integrated circuits*. Vol. 218. John Wiley & Sons, 2012.

[2] Dupuis, Russell D., et al. "Room-temperature laser operation of quantum-well $Ga_{(1-x)}Al_xAs$-GaAs laser diodes grown by metalorganic chemical vapor deposition." *Applied physics letters* 32.5 (1978): 295-297.

[3] Tsang, W. T. "Extremely low threshold (AlGa)As graded-index waveguide separate-confinement heterostructure lasers grown by molecular beam epitaxy." *Applied Physics Letters* 40.3 (1982): 217-219.

[4] Smowton, Peter M., and Peter Blood. "The differential efficiency of quantum-well lasers." *IEEE Journal of Selected Topics in Quantum Electronics* 3.2 (1997): 491-498.

[5] Tansu, Nelson, and Luke J. Mawst. "Current injection efficiency of InGaAsN quantum-well lasers." *Journal of applied physics* 97.5 (2005): 054502.

[6] Yariv, Amnon. "Scaling laws and minimum threshold currents for quantum-confined semiconductor lasers." *Applied physics letters* 53.12 (1988): 1033-1035.

Chapter 4. $GaAs_{1-z}Bi_z$ QW Active Region Laser Diodes

4. 1. Introduction

Recently, $GaAs_{1-z}Bi_z$ alloys have drawn much attention as it was shown both experimentally and theoretically that a small amount of Bi incorporation into GaAs induces a rapid reduction in the band gap (E_g) (62-84meV per Bi mole fraction) and an increase in spin-orbit splitting (Δ_{SO}) with increasing Bi concentration [1-4]. $GaAs_{1-z}Bi_z$ quantum well (QW) active regions are an alternate approach to dilute-nitride QWs for achieving lasers in the telecom wavelength regions (λ~1.3-1.55 μm) on GaAs substrates. Such QW active regions are easily incorporated into existing GaAs-based vertical cavity surface emitting laser (VCSEL) architectures employing high-index contrast distributed Bragg reflector (DBR) mirrors. Furthermore, it was predicted that Δ_{SO} can be larger than E_g when the Bi mole fraction exceeds 10% [1]-[7], revealing a potential of this material to suppress a dominate Auger recombination mechanism, which has been considered as one of the significant carrier loss pathways in InP-based telecom wavelength devices.

A great deal of efforts has been directed towards the pseudomorphic growth of dilute-bismide alloys on GaAs substrates by metalorganic vapor phase epitaxy (MOVPE) or molecular beam epitaxy (MBE) in order to realize near-IR emitting devices. The origin of the rapid band gap reduction has been attributed to the localized interaction between the Bi resonant level and the valence band of GaAs within a valence band anti-crossing model [8]. However, this interaction results in a relatively small conduction band offset at the GaAs/$GaAs_{1-z}Bi_z$ hetero-junction, particularly at low Bi mole fraction. Therefore, it is necessary to choose the proper barrier material in order to enhance the electron confinement in the conduction band of the $GaAs_{1-z}Bi_z$ active region. In this chapter, the origin of the bandgap reduction by the incorporation of the Bi atoms into the GaAs host matrix is reviewed in great detail. In addition, the issues with the carrier confinement within the Bi-containing active region will be discussed together with the theoretical calculation based on the density functional theory (DFT). Also, the growth of $GaAs_{1-z}Bi_z$ and the impact of the post-growth thermal annealing on the will be given in details. Finally, the characteristics of the laser diodes employing $GaAs_{1-z}Bi_z$ QW active region will be present in this chapter.

4. 2. Origin of Band Gap Reduction in $GaAs_{1-z}Bi_z$

The origin of the band gap reduction within $GaAs_{1-z}Bi_z$ has been explained within the framework of the valence band anticrossing (VBAC) model, which predicts the localized Bi-related states hybridized with the valence band of the host GaAs matrix [8-10]. This hybridization results in the creation of valence subbands E_{HH+}, E_{LH+}, E_{SO+}, E_{HH-}, E_{LH-}, E_{SO-}, as schematically shown in Fig. 4--1.which lead to the reduced band gap energy E_g. (HH, LH and SO refer to heavy hole, light hole, and spin orbit splitting band, respectively)

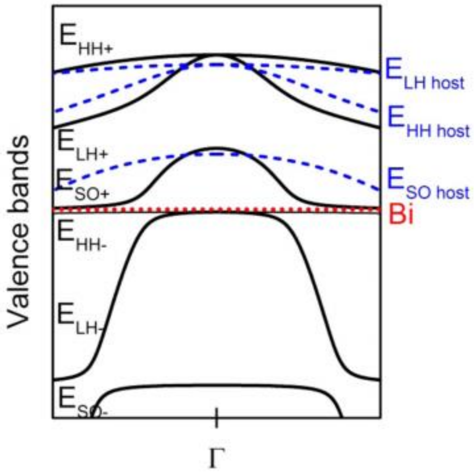

Fig. 4-1 *Schematic diagram showing valence band anticrossing effect at Γ-valley (after reference [10])*

By the approximation of the VBAC model, the variation of the band gap energy of the unstrained $GaAs_{1-z}Bi_z$ can be expressed as

$$E_g^{unstrained}(GaAs_{1-z}Bi_z) = E_g^{unstrained}(GaAs) - \frac{\Delta E_{MN}}{2}\left[\sqrt{1+4\left(\frac{C_{MN}}{\Delta E_{MN}}\right)^2 z} - 1\right] \quad (4.1)$$

where $E_g^{unstrained}(GaAs)$ is the band gap energy of unstrained GaAs, ΔE_{MN} is the energy separation between the resonant bismuth level and valence band maximum of GaAs, and C_{MN} is the coupling parameter in $GaAs_{1-z}Bi_z$, ΔE_{MN} ~-0.183 eV and C_{MN} ~ 1.13 based on a prior theoretical study employing tight binding model [6].

Together with the band gap reduction, the interaction of host E_{so} with Bi-related states also is shown to lead to a non-linear increase in the Δ_{so} (spin-orbit splitting energy: energy separation between valence band edge and E_{so}) with increasing Bi composition, as shown in Fig 4-2, which presents both the experimental and theoretical data.

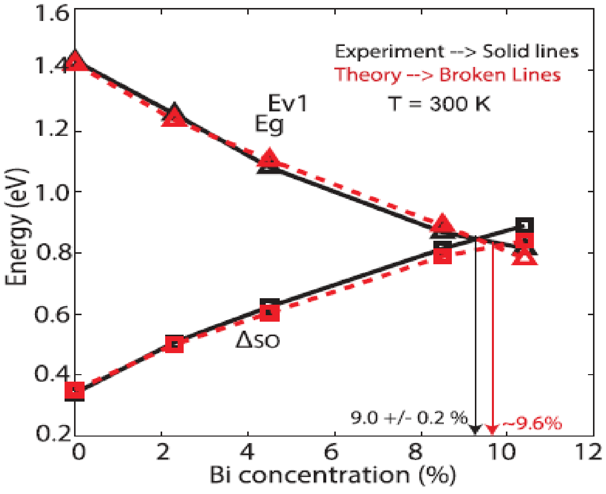

Fig. 4-2 *Comparison of the experimental and theoretical values of the energy gap E_g and spin-orbit-splitting energy Δ_{so} (after reference [12])*

This band gap reduction (~80meV/%Bi) is significantly higher than the band gap reduction that can be obtained by using conventional InGaAs alloy (~15mV/%In) [10].

Therefore, the increase in Δ_{so} together with the decrease in E_g has shown a promise for the suppression of hot-hole driven Auger recombination (CHSH auger recombination process) and intervalence band absorption (IVBA) at the Bi composition higher than 9~10% (z=0.1 in $GaAs_{1-z}Bi_z$). This IVBA and CHSH Auger process, schematically represented in Fig. 4-3., has been identified as a major carrier loss mechanism limiting efficiency of the conventional InGaAs or InGaAsN based QW laser emitting near telecom O- and C-band [13-14].

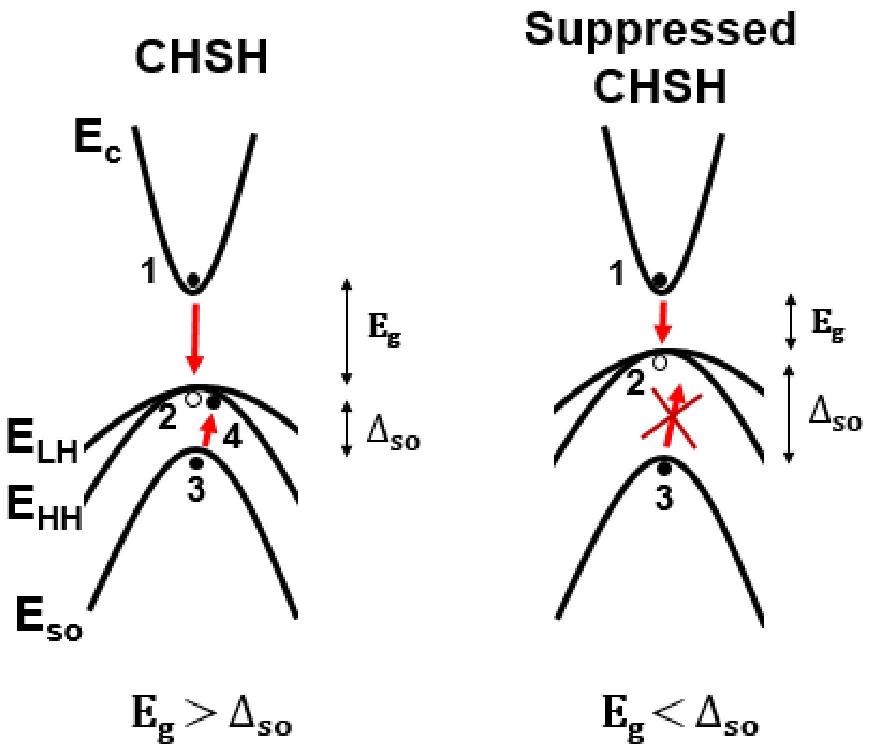

Fig. 4-3 *Schematic diagram showing the suppressed CHSH Auger process*

4. 3. Carrier confinement within $GaAs_{1-z}Bi_z$ QW Active Region with Strain-Balancing

The origin of this rapid band gap bowing effect owing to the interaction between the localized Bi resonant level and the valence band of GaAs has been shown to lead to a large valence band offset (~55meV/%Bi) and a relatively small conduction band offset (~15meV/%Bi) at the $GaAs_{1-x}Bi_x$/GaAs heterojunction, particularly at low Bi mole fraction [12], as schematically shown in Fig. 4-4, especially when the compressive strain of $GaAs_{1-z}Bi_z$ is taken into account.

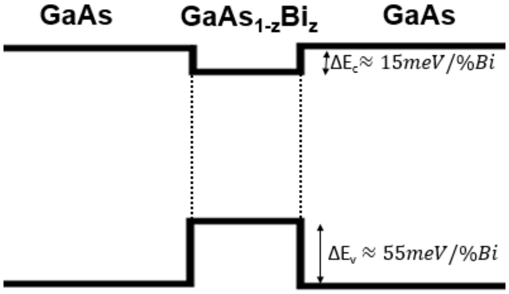

Fig. 4-4 *Schematic energy band diagram of a $GaAs_{1-z}Bi_z$/GaAs QW active region*

Especially at a low Bi mole fraction ($z < 0.03$), the ΔE_C is insufficient to effectively confine the electrons within the $GaAs_{1-z}Bi_z$ QW, which can lead to strong sensitivity of the device performance to heat-sink temperature. Therefore, for the application where the both electron and hole confinement is required, such as an active region within a laser diode structure, it is necessary to choose a higher bandgap material as an electron barrier especially at a low Bi mole fraction ($z < 0.03$). The first successful operation of an electrically injected $GaAs_{1-z}Bi_z$ single quantum well (SQW) laser with the lasing wavelength of 947 nm was reported by *Ludewig et al* [15]. Subsequently, there have been several other reports of diode lasers employing $GaAs_{1-z}Bi_z$ in the active region, confirming the potential of this material as a light-emitting source in near-IR region

[16-18]. In these prior studies, $Al_xGa_{1-x}As$ was used as a barrier material for low Bi-content QWs to improve the electron confinement in the conduction band and reduce thermally activated carrier leakage from the QW. Employing $Al_{0.12}Ga_{0.88}As$ as a barrier material for a $GaAs_{0.978}Bi_{0.022}$QW leads to a higher conduction band offset, ΔE_C= 133meV [18]. On the other hand, the use of tensile strained $GaAs_{1-y}P_y$ QW barrier provides a pathway for achieving both tight carrier confinement and the strain compensation.

To determine band offsets associated with $GaAs_{1-y}P_y$ and $GaAs_{1-z}Bi_z$, the density functional theory (DFT) simulations were employed as discussed in detail elsewhere [19].

To obtain ΔE_V of a heterojunction A/B where A and B are the two compounds forming the heterojunction, the macroscopic electrostatic potential (MEP) along [001] of A/B was calculated first [20]. To reduce the effects of using a specific finite-sized supercell, the average MEP of several A/B with different P and Bi atom configurations was used. Then the relative position of valance band maximum (VBM) in A/B was determined according to the VBM positions relative to MEP in the bulk of A and B. Finally, ΔE_C was calculated based on the ΔE_V and band gap difference of A and B, i.e., $\Delta E_C = \Delta E_g - \Delta E_V$. The band gaps of $GaAs_{1-y}P_y$ and $GaAs_{1-z}Bi_z$ strained to GaAs(001) were calculated using the following relationships, which were derived from previous DFT calculations and experimental fits [21].

$$E_g\left(GaAs_{1-y}P_y\right) = 1.42 + 0.811y - 0.118y^2 - 0.059y^3 \tag{4.2}$$

$$E_g(GaAs_{1-z}Bi_z) = 1.42 - 6.429z + 9.293z^2 + 14.224z^3 \tag{4.3}$$

The validity of our calculations was supported by the good agreement with previous experimental measurement [22] for $GaAs_{1-y}P_y$/GaAs (y=0.292) and reasonable agreement with an estimation based on tight-binding calculation [11] for $GaAs_{1-z}Bi_z/GaAs$ (z=0.042), as compared in Table 4-1. Selected compositions of the $GaAs_{1-y}P_y$ /$GaAs_{1-z}Bi_z$ heterojunction were calculated and results are shown in Table 4-1.

Table 4-1. Band offset values of different heterojunctions. Positive values of ΔE_V and ΔE_C for heterojunction A/B refer to an increase in the valence band energy and a decrease in the conduction band energy, respectively.

	$GaAs_{1-y}P_y$ / GaAs		GaAs / $GaAs_{1-z}Bi_z$		$GaAs_{1-y}P_y/GaAs_{1-z}Bi_z$		
(y, z)	(0.292, 0)	(0.292, 0)*	(0, 0.042)	(0, 0.042)†	(0.297, 0.016)	(0.297, 0.031)	(0.292, 0.042)
ΔE_C [meV]	182	150	95	72	231	265	280
ΔE_V [meV]	43	45	158	231	96	155	198

*Experimental data in Ref [22]; †Estimation based on tight-binding calculation of strained $GaAs_{1-z}Bi_z$, [11]

These theoretical results indicate that a properly chosen $GaAs_{1-y}P_y$ barrier can provide band offsets much greater than the thermal energy of room temperature even for the $GaAs_{1-z}Bi_z$ system with small Bi incorporation, as schematically presented in Fig 4-5 (a).

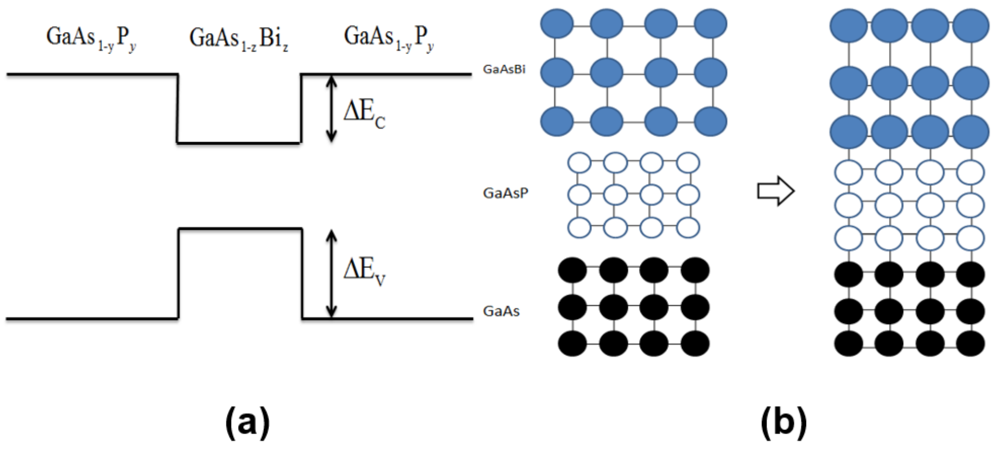

Fig. 4-5 *Schematic energy band diagram of (a) $GaAs_{1-y}P_y$ /$GaAs_{1-z}Bi_z$/$GaAs_{1-y}P_y$ QW active region, and (b) Schematic of strain accommodation in the corresponding heterostructure*

The $GaAs_{1-y}P_y$ as a barrier material for a $GaAs_{1-z}Bi_z$ active region lattice-matched to a GaAs substrate can be used to form strain-compensated QW structures, as mentioned earlier. The pseudomorphic growth of $GaAs_{1-y}P_y$ on GaAs substrate results in the tensile strain while the compressive strain is induced from $GaAs_{1-z}Bi_z$, as illustrated in Fig 4-5 (b). This compressive strain from the $GaAs_{1-z}Bi_z$ can be compensated for by employing $GaAs_{1-y}P_y$ barriers, resulting in a low- or zero- average strain for the active region. *N.J. Ekins-Daukes et al*. derived an expression [23] for the average strain energy,

$$U_{av} = \frac{\left(t_1 A_1 \varepsilon_1{}^2 + t_2 A_2 \varepsilon_2{}^2 + t_3 A_3 \varepsilon_3{}^2\right)}{t_1 + t_2 + t_3} \tag{4.4}$$

$$A_i = C_{11,i} + C_{12,i} - \frac{2C_{12,i}{}^2}{C_{11,i}} \tag{4.5}$$

where the coefficient C_{11} and C_{12} are elastic constants, t is the thickness and ε is the strain, and i is the index for each layer as depicted in Fig 2(b).

By linearly interpolating the binary elastic constants summarized in Table 4-2, C_{11} and C_{12} are estimated for $GaAs_{1-z}Bi_z$ and $GaAs_{1-y}P_y$ with various mole fractions of Bi and P.

Table 4-2: Elastic Constants

	GaBi [24]	**GaAs**	**GaP**
C_{11}[GPa]	81.6	118.89	140.05
C_{12}[GPa]	28.1	53.75	62.03
a[Å]	6.33	5.6533	5.4505

Ref [24]: Estimation based on extrapolation of experimental $GaAs_{1-z}Bi_z$ lattice constant

To balance the strain induced within the $\mathrm{GaAs_{1-y}P_y/GaAs_{1-z}Bi_z/GaAs_{1-y}P_y}$structure, the average in-plane stress, $\frac{\partial \mathrm{U_{av}}}{\partial \varepsilon_{\mathrm{GaAs_{1-y}P_y}}}$, needs to be zero, leading the following expression for the required barrier thickness.

$$\mathrm{t_{GaAs_{1-y}P_y}} = \frac{-\mathrm{t_{GaAs_{1-z}Bi_z} A_{GaAs_{1-z}Bi_z} \varepsilon_{GaAs_{1-z}Bi_z} a_{GaAs_{1-y}P_y}}}{2\mathrm{A_{GaAs_{1-y}P_y} \varepsilon_{GaAs_{1-y}P_y} a_{GaAs_{1-z}Bi_z}}} \qquad (4.6)$$

Fig. 4-6 presents the relationship between the thickness of the $\mathrm{GaAs_{1-y}P_y}$ barrier necessary to have a heterostructure with a zero stress for various P and Bi concentrations. It is possible to construct a strain balanced multiple quantum well structure consisting of alternating $\mathrm{GaAs_{1-z}Bi_z}$ /$\mathrm{GaAs_{1-y}P_y}$ layers, maximizing the carrier collection efficiency while using the Al-free material as a carrier confining barrier.

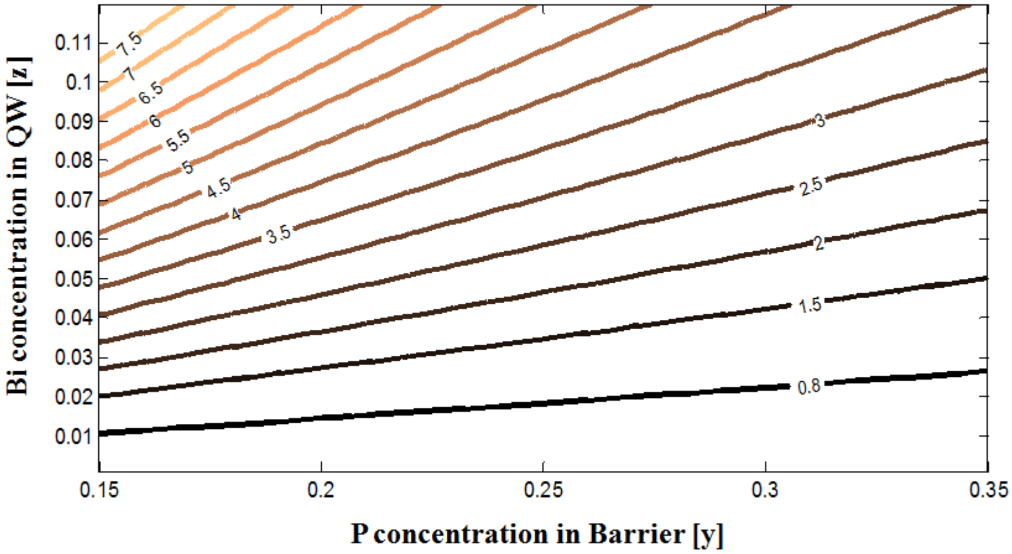

Fig. 4-6 *The* $\mathrm{GaAs_{1-y}P_y}$ *barrier thickness in nm for strain-balancing for various Bi and P concentration within the well and barrier respectively for a 7 nm thick* $\mathrm{GaAs_{1-z}Bi_z}$ *SQW.*

4. 4. MOVPE of GaAs$_{1-z}$Bi$_{z}$ Multiple Quantum Well

The metastable GaAs$_{1-x}$Bi$_{x}$ alloy exhibits a large miscibility gap with a very low Bi solubility in GaAs [25], although it was shown this solubility can be altered in the presence of the strain state as shown in Fig. 4-7. This restriction compels the growth of GaAs$_{1-x}$Bi$_{x}$ to be performed with non-typical growth parameters, involving the low growth temperature around 400 ℃ and near-stoichiometric V/III flux ratio for MBE and gas-phase ratio for MOVPE for the Bi incorporation into the host GaAs matrix [24,26]. In turn, the growth under the near-stoichiometric condition at such a low temperature can result in point defects and its associated defect complexes, which can act as non-radiative recombination centers within the materials [27]. In addition, particularly for the MOVPE growth, the low growth temperature can lead to high unintentional background carbon contamination as the hydrocarbon radicals from the metal-organic precursors, which are not effectively removed from the growth front, leads to an increased carbon incorporation [26]. This unintentional background carbon has been shown to reduce the minority carrier lifetime [28]. For these reasons, the growth parameters should be carefully optimized for the MOVPE growth of device quality GaAs$_{1-x}$Bi$_{x}$ films.

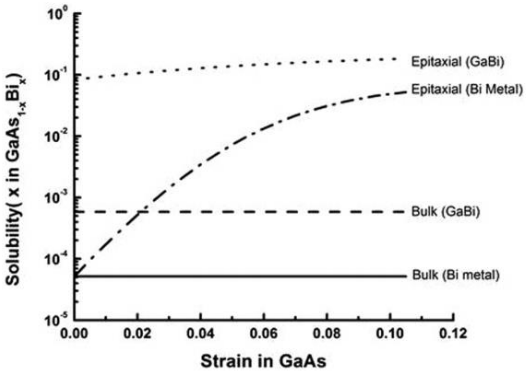

Fig. 4-7 *Solubility of Bi in GaAs versus the strain in the GaAs lattice parameter at 400°C under Ga-rich conditions using both Bi metal and GaBi as the reference state for Bi (After reference [29])*

The material growth in this study was performed, using a close-coupled-showerhead vertical reactor with a rotating susceptor. The growth was monitored *in situ* by the optical reflectance system by Laytec's EpiTT™. For the $GaAs_{1-x}Bi_x$ growth, triethyl-gallium (TEGa) was used as group III precursors while tertiarybutyl-arsine(TBAs), and trimethyl-bismuth (TMBi) were used for group V precursors. For the growth optimization, samples consisting of 5 period MQW (5x $GaAs_{1-x}Bi_x$/GaAs) were grown on nominally exact (001) semi-insulating GaAs substrates with varying growth temperature (T_{growth}) and varying TMBi/V gas phase ratio. All precursors were fed into the reactor simultaneously. After the $GaAs_{1-z}Bi_z$ QW growth, the growth temperature was raised to 630℃ under arsine/H_2 ambient, and the GaAs barrier was grown with trimethyl-gallium (TMGa) and arsine (AsH_3). The growth parameters are summarized in the Table 4-3.

Table 4-3. Growth Parameters used for the material optimization

Material	**Pressure [Torr]**	**Growth Temp. [℃]**	**TEGa [µmol/min]**	**TMBi/TBAs**	**V/III Ratio**
QW ($GaAs_{1-z}Bi_z$)	50	400~440	133	0.023~0.036	1.31
Barrier (GaAs)	100	630	TMGa used [55µmol/min]	N/A	60~70

This temperature ramping was employed in previous studies, and is thought to lead to evaporation of the surface-segregated Bi on the growing $GaAs_{1-x}Bi_x$ film [15, 30]. The Bi incorporation as a function of the growth temperature was investigated by varying only the growth temperature from 400 to 440 ℃ while maintaining other growth parameters including TEGa molar flow (133µmol/min), TMBi/TBAs = 0.036, reactor pressure ($P_{reactor}$=50Torr), and V/III ratio (V/III=1.31). Presented in Fig. 4-8 (a) are the HR-XRD spectra, which possess a sharp contrast in both pendellosung oscillations and the satellite peaks for all samples. These XRD measurements suggest that even with temperature ramping between well and barrier, it is possible to achieve an abrupt $GaAs_{1-x}Bi_x$/GaAs heterointerface, which agrees well with the previous reports. [15,30].

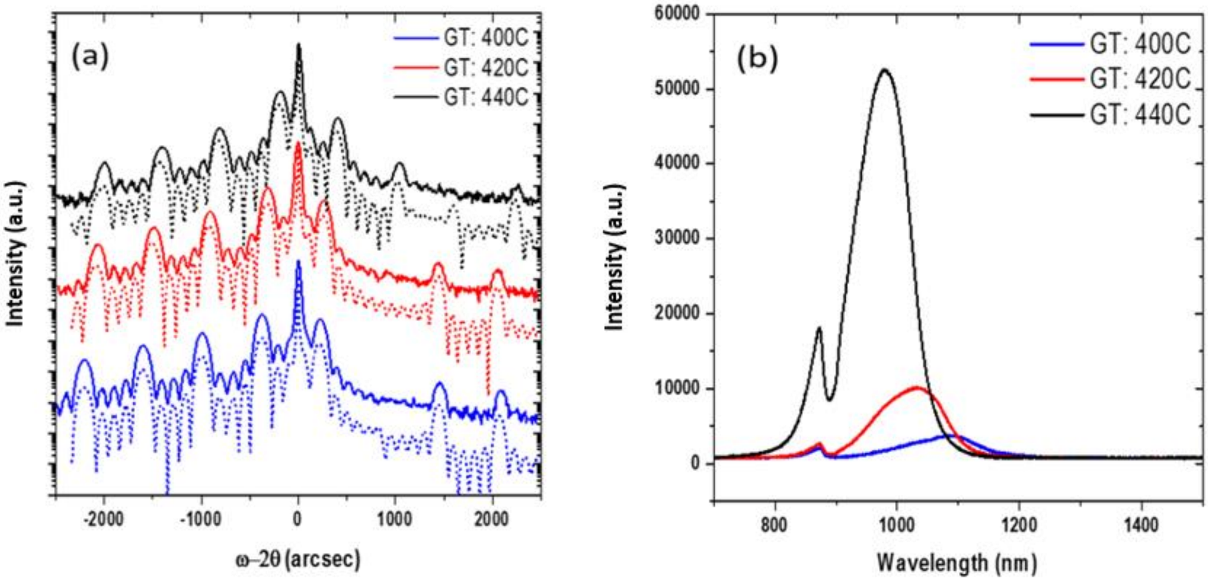

Fig. 4-8 *(a) HR-XRD ω-2θ measured around GaAs (004) reflection. Dynamic XRD simulations are indicated by the dotted lines for each sample. (b) Photoluminescence measured at room temperature*

Assuming a GaBi zincblende lattice constant of 0.633nm, the GaBi mole fractions of each sample was found from comparing the x-ray spectra to the XRD dynamic simulations at a point of best fit to the experimental HR-XRD data [24]. The structural details of each sample derived from the XRD simulations are summarized in Table 4-4.

Table 4-4. Structure Details and $GaAs_{1-x}Bi_x$ growth rate as a function of growth temperature

Growth Temperature [℃]	**Structure Details from the HR-XRD dynamic simulation**	**$GaAs_{1-z}Bi_z$ Growth Rate [nm/sec]**	**PL Peak Position [eV]**
400	**5x $GaAs_{0.957}Bi_{0.043}/GaAs$ (9/22nm)**	**0.036**	**1.114**
420	**5x $GaAs_{0.966}Bi_{0.034}/GaAs$ (10/22nm)**	**0.067**	**1.2**
440	**5x $GaAs_{0.974}Bi_{0.026}/GaAs$ (9/22nm)**	**0.1**	**1.261**

The PL measurements, shown in Fig. 4-8 (b), indicate a rapid increase in the PL intensities and spectral blueshifts as the T_{growth} increases. This result can possibly be attributed to a combination of effects including a decrease in the Bi-related defect concentration as a result of the reduced Bi incorporation, reduction in other point defects and defect complexes associated with near-stoichiometric growth, and a lower background carbon concentration resulting from a higher T_{growth}. Our observations agree well with the study by *Ludewig et al* [31], although it should be noted that their quantum well structures were grown by the pulsed MOVPE growth mode.

A study of the effect of gas-phase TMBi/V ratio on the luminescence properties of the $GaAs_{1-x}Bi_x$ QWs was carried out. For this study, only the TMBi molar flow was adjusted while fixing other growth parameters such as TEGa molar flow (133μmol/min), TBAs molar flow (174μmol/min), T_{growth} (440℃), and $P_{reactor}$ (50Torr). Shown in Fig. 4-9 (a) are the HR-XRD measurements and their corresponding dynamic simulations, which indicate a reduction in the growth rate as TMBi/V ratio increases.

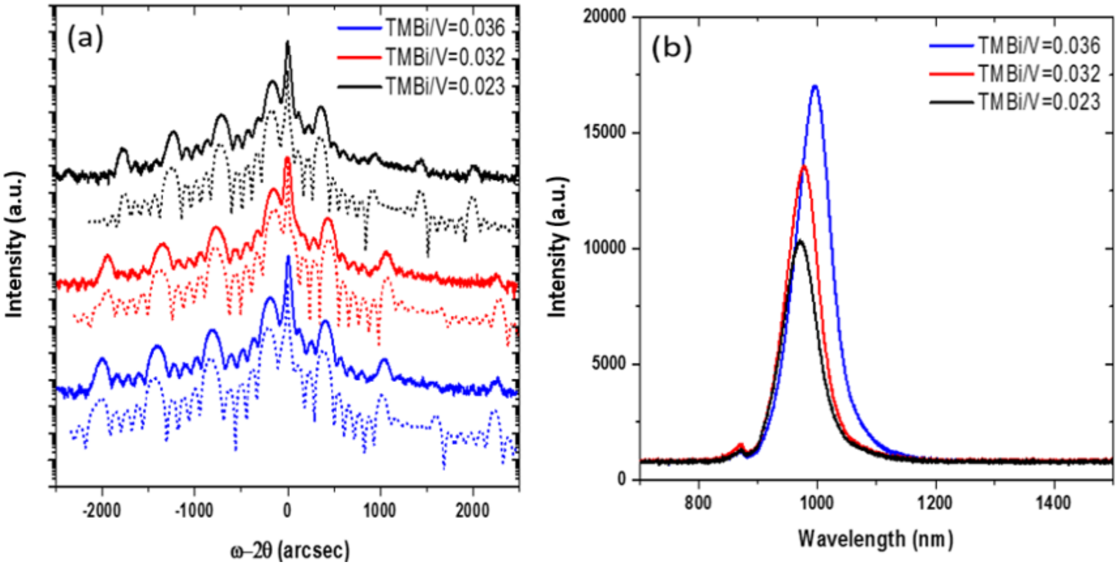

Fig. 4-9 *(a) HR-XRD ω-2θ measured around GaAs (004) reflection. Dynamic XRD simulations are indicated by the dotted lines for each sample. (b) Photoluminescence measured at room temperature*

Table 4-5 summarizes the structure details and their growth rates of each samples, deduced from the fitting of the XRD dynamic simulation to the experimental HR-XRD data. This decrease in growth rate is most likely due to the segregated Bi at the growth front, which can block surface sites, preventing the incorporation of Ga, as previously reported elsewhere [26].

Table 4-5. Structure Details and $GaAs_{1-z}Bi_z$ growth rate as a function of TMBi/V molar flow rate

TMBi/V Molar flow Ratio	Structure Details from the HR-XRD dynamic simulation	$GaAs_{1-z}Biz$ Growth Rate [nm/sec]	PL Peak Position [eV]
0.023	**5x $GaAs_{0.983}Bi_{0.017}$/GaAs (12/23nm)**	**0.134**	**1.28**
0.032	**5x $GaAs_{0.975}Bi_{0.025}$/GaAs (7/23nm)**	**0.105**	**1.27**
0.036	**5x $GaAs_{0.974}Bi_{0.026}$/GaAs (9/22nm)**	**0.1**	**1.261**

The *in situ* reflectance taken during the growth while varying TMBi/V is shown in Fig. 4-10. When TMBi/V ratio of either 0.023 (Fig.4-10 (a)) or 0.032 (Fig.4-10 (b)) were used, a monotonic increase in the reflectance intensity was observed. By contrast, when an increased TMBi/V ratio of 0.036 was used, the saturated reflectance, which appears as the plateau, was observed, as shown in the Fig. 4-10 (c). This observation is attributed to the reduction in the growth rate in the presence of the excess Bi segregated at the growth front. As a result, the sample surface with TMBi/V=0.036 contained Bi containing droplets, while the other samples exhibit a droplet-free surface.

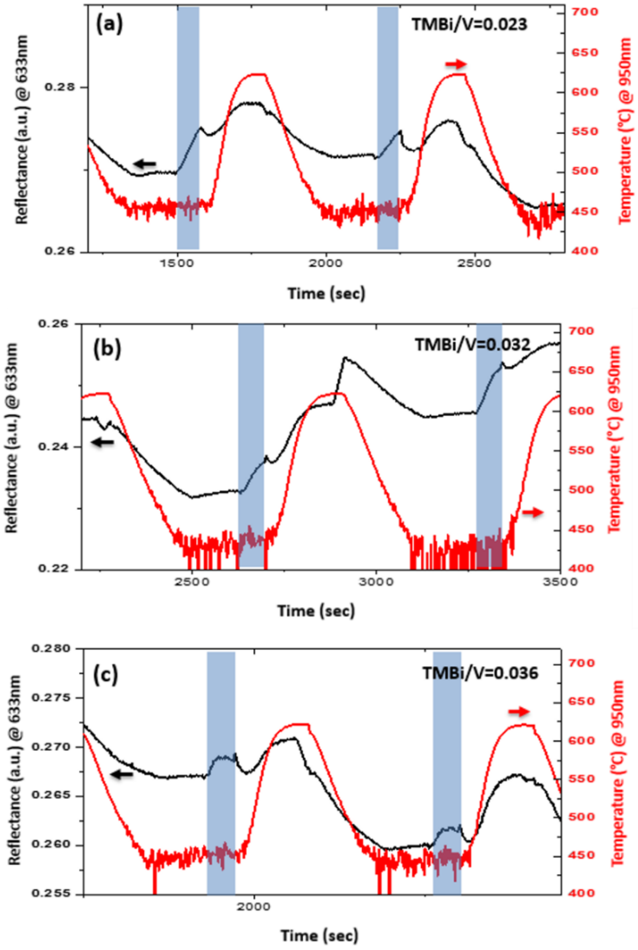

Fig. 4-10 *Reflectance measured in situ during the growth. The shaded area corresponds to the growth of* $GaAs_{1-z}Bi_z$ *QWs. (a) in situ reflectance during the growth with TMBi/V=0.023, (b) in situ reflectance during the growth with TMBi/V=0.032, and (c) in situ reflectance during the growth with TMBi/V=0.036*

It should be noted that the small decrease in the TMBi/V ratio from 0.036 to 0.032 does not significantly decrease the GaBi mole fraction in the solid phase, as shown in Fig 4-11.

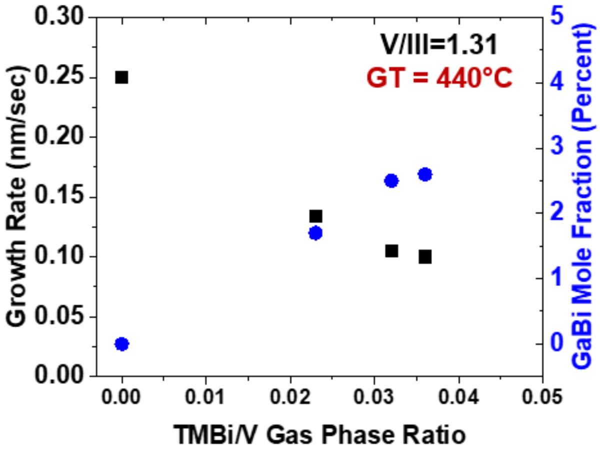

Fig. 4-11 *Growth rate and GaBi mole Fraction as a function of TMBi/V gas phase ratio*

Based on the trend deduced from the growths of TMBi/V=0.023 and 0.032, the expected solid GaBi mole fraction with TMBi/V=0.036 is 2.8% while the measured solid GaBi mole fraction is 2.6%. This implies that the growths under the TMBi/V of 0.032 to 0.036 take place within the "saturated regime", where solid GaBi mole fraction in the growing layer is independent of the input TMBi/V ratio above a certain ratio [32], as shown in Fig. 4-12.

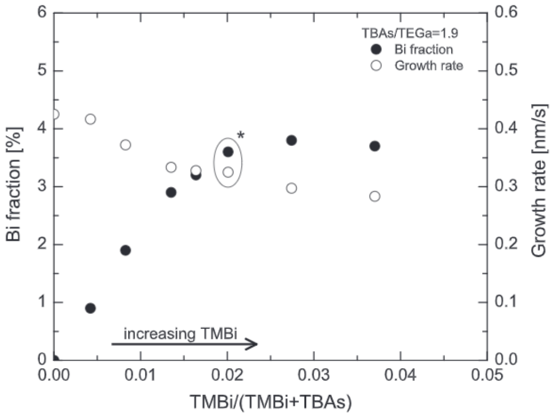

Fig. 4-12 *Growth rate and GaBi mole Fraction as a function of TMBi/V gas phase ratio (After reference [32])*

The reduction in the background carbon concentration observed when using a high TMBi/V ratio has also been reported, and again has been ascribed to an effect of the surface segregated Bi, blocking surface reaction sites [33]. Our observation of an increased PL intensity from the samples with the higher TMBi ratio, shown in Fig. 4-9(b), could be attributed to this effect.

To investigate the effect of the $GaAs_{0.8}P_{0.2}$ barrier on the luminescence properties, a 5x $GaAs_{0.975}Bi_{0.025}$ / $GaAs_{0.8}P_{0.2}$ (8/15nm) structure was grown in the similar manner to the samples grown with GaAs barriers, *i.e.*, temperature ramping to a higher growth temperature was used when growing the $GaAs_{0.8}P_{0.2}$ barrier after the growth of the $GaAs_{0.975}Bi_{0.025}$ QW. For the growth of $GaAs_{0.8}P_{0.2}$, TMGa, AsH_3 and Phosphine(PH_3) were used as precursors with the V/III gas phase ratio of 150. From the PL measurements, shown in Fig. 4-13 (a), it was found that the sample with the $GaAs_{0.8}P_{0.2}$ barrier exhibits and improved PL intensity with a slight blueshift, most likely due to the higher electron confinement in the QW resulting from higher ΔE_c, as mentioned earlier.

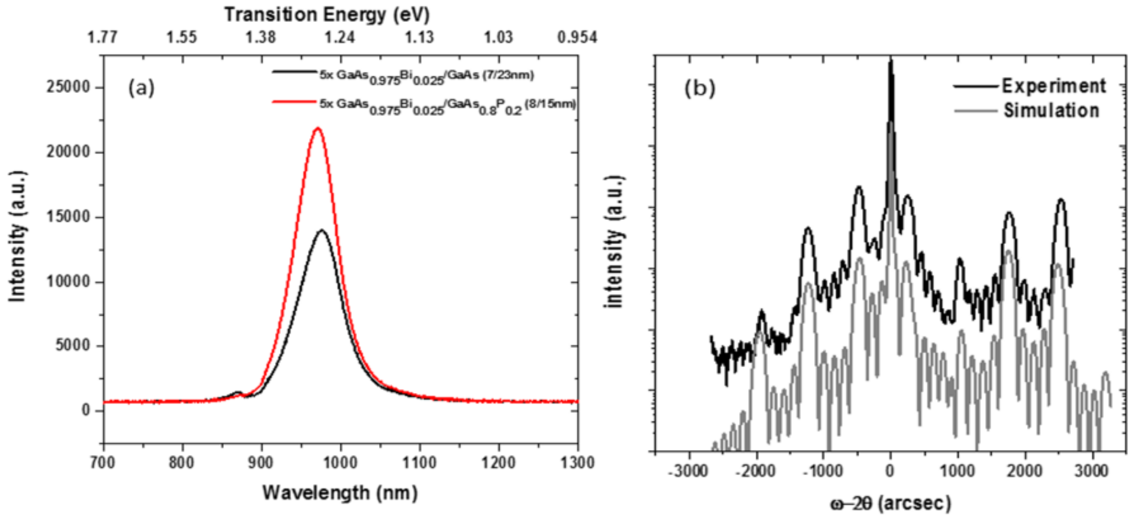

Fig. 4-13 *(a) RT-PLs from the 5-period MQW samples with GaAs and $GaAs_{0.8}P_{0.2}$ barriers, (b) HR-XRD measurement and the dynamic simulation for the 5x $GaAs_{0.975}Bi_{0.025}$ / $GaAs_{0.8}P_{0.2}$ MQW sample*

4. 5. Impact of Post-Growth Thermal Annealing

The post-growth thermal annealing at a higher temperature than the growth temperature has been often employed for the metastable alloys such as dilute nitride [34-35] or dilute bismide alloys, in order to improve the luminescent properties. Table 4-6 summarizes the prior studies that reported the impact of post-growth thermal annealing at the elevated temperature by either rapid thermal annealing (RTA) or *in situ* annealing within the MOVPE reactor.

Table 4-6. Summary of prior studies on the impact of post-growth thermal annealing

Report	Material	Method	Increases in PL intensity at RT	XRD Fringes
Mohmad *et al*[36]	**MBE grown $GaAs_{1-z}Bi_z$ (2<z<6.5%)**	**RTA**	**3x (2%~4%) @ 700°C 2x (6.5%) @ 600°C under N_2 for 30sec**	**Interface degrades when annealed at 700°C**
Grant *et al*[37]	**MBE grown $GaAs_{1-z}Bi_z$ (z~5.5%)**	**RTA**	**2x @ 500°C under N_2 for 30sec**	**Interface degrades when annealed at 750°C**
S. Mazzucato *et al*[38]	**MBE grown $GaAs_{1-z}Bi_z$ (z~2.3%)**	**RTA**	**~1.5X @ 750°C Under N_2 for 30sec**	**N/A**
Z. Chine *et al*[39]	**MOVPE grown $GaAs_{1-z}Bi_z$ (x~3.5%)**	***in situ***	**Maximum @ 600°C under H_2/AsH_3 for 15min (Low Temp. PL at 10K)**	**N/A**
H. Kim *et al*[40]	**MOVPE grown $GaAs_{1-z}Bi_z$ (x~3.5%)**	***in situ***	**~5x increase in RT-PL intensity**	**Interface degrades when annealed at higher than 700°C**

While there is no consensus on the absolute optimum post growth annealing condition, many studies indicate the post growth annealing at the temperature higher than 700°C can induce the the degraded interface, evidenced by XRD fringes [36-37,40] and occasionally the formation of Bi-rich precipitate as shown in Fig. 4-14.

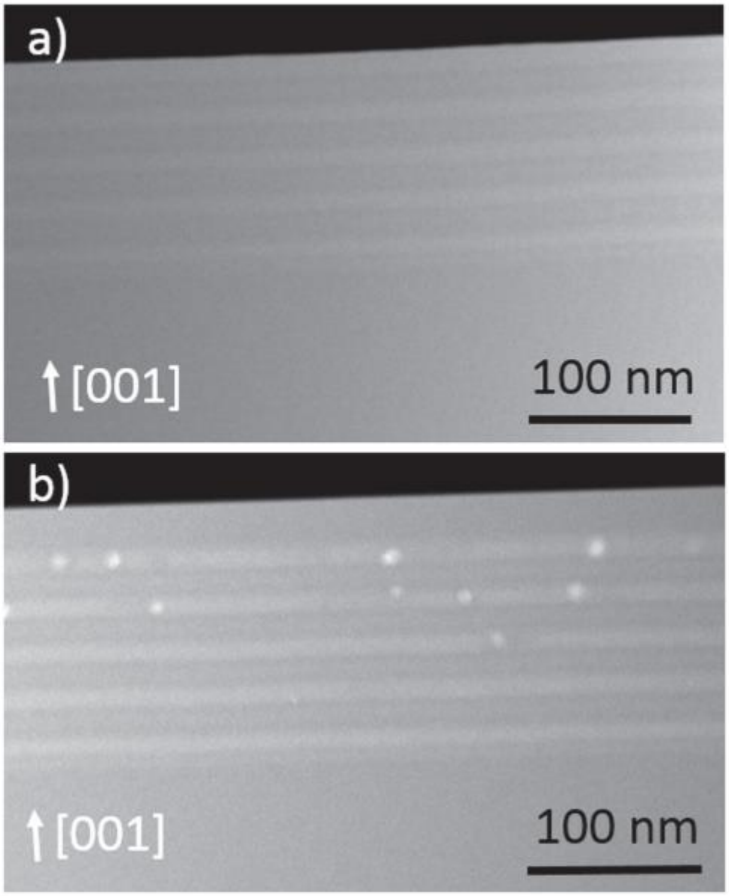

Fig. 4-14 *High angle annular dark field STEM image of the* $GaAs_{1-z}Bi_z/GaAs$ *superlattice (a) as-grown and (b) following a 45 min in situ anneal under* H_2/AsH_3 *ambient (After reference [41])*

While the exact role of this Bi-rich cluster in the optoelectronic device performance is unknown yet, this Bi-rich cluster can possibly lead to the increased scattering/absorption loss when present within the active region of the laser diodes. Therefore, we used the post-growth annealing condition at 630°C, which is empirically known not to cause either degradation at the interface or the formation of the Bi-rich precipitates.

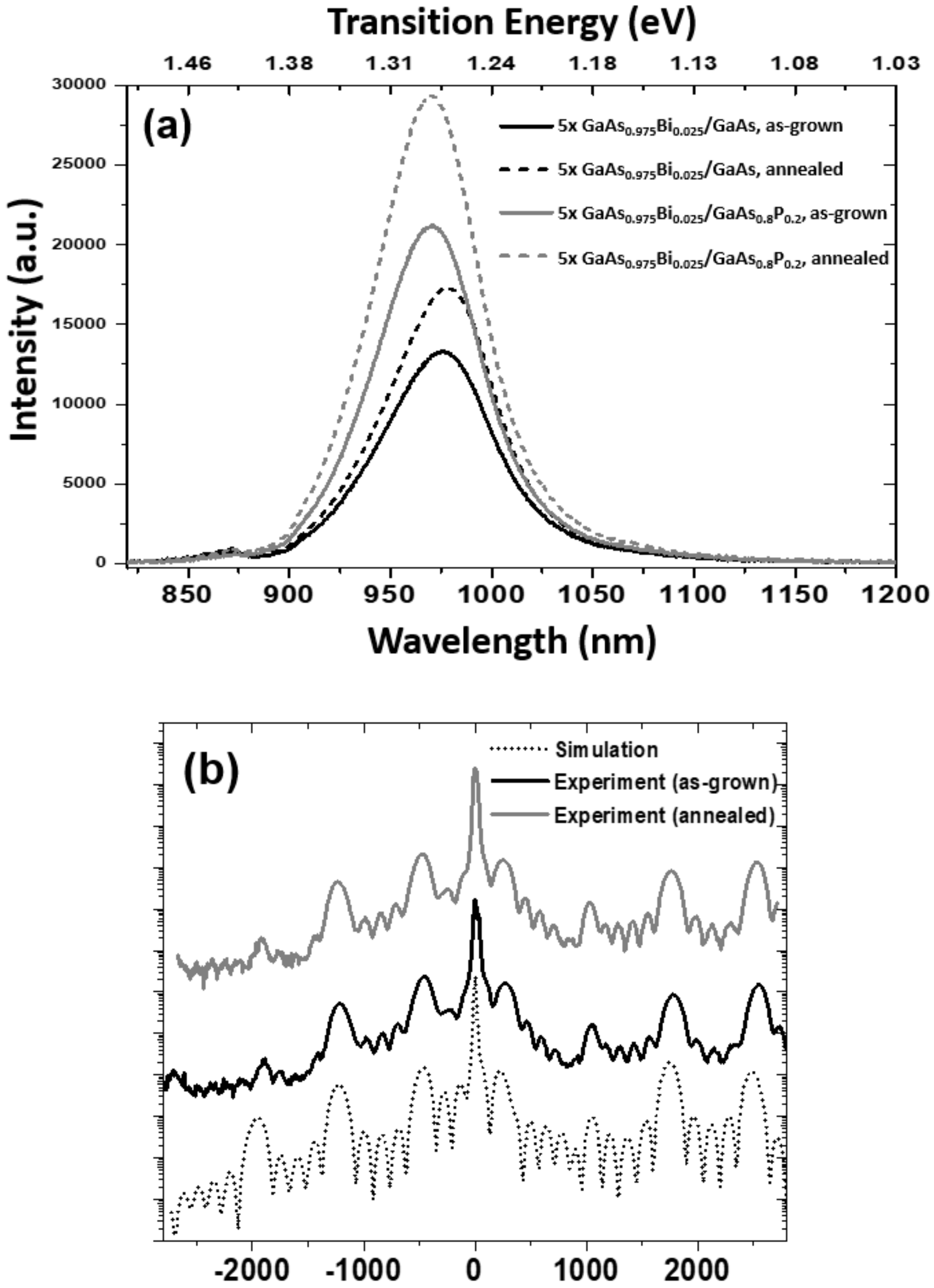

Fig. 4-15 *(a) RT-PLs from the 5-period* $GaAs_{0.975}Bi_{0.025}$ *MQW samples with GaAs and* $GaAs_{0.8}P_{0.2}$ *barriers before and after in situ anneal for 40 min at 630 °C under* H_2/AsH_3 *ambient, (b) the corresponding HR-XRD measurement and the dynamic simulation for the 5x* $GaAs_{0.975}Bi_{0.025}$ / $GaAs_{0.8}P_{0.2}$ *MQW sample before and after in situ anneal for 40 min at 630 °C under* H_2/AsH_3 *ambient*

Fig. 4-15 (a) presents the PL spectra at room temperature taken from 5-period $GaAs_{0.975}Bi_{0.025}$ MQW samples with GaAs and $GaAs_{0.8}P_{0.2}$ barriers before and after the *in situ* annealing for 40 min at 630 °C under H_2/AsH_3 ambient. Regardless of the type of the barrier, 1.5-fold increase in the RT-PL intensity was observed after annealing. The XRD spectra, shown in Fig. 4-15 (b), suggests no apparent degradation in the interfacial abruptness or compositional variation after the annealing.

4. 6. Growth and Characterization of $GaAs_{0.975}Bi_{0.025}$ QW Active Region Laser

After investigating growth condition as described in the previous section, the laser diode structures were grown on nominally exact n^+ GaAs substrates as shown in Fig. 4-16 (a). For a laser structure, it is important to have abrupt interfaces between QWs and barriers, without the Bi droplets, which could lead to current leakage paths or increased optical loss within the laser cavity. Therefore, in order to avoid the droplet formation, a TMBi/V = 0.032 was chosen for the growth of QW active region. Trimethyl-aluminum (TMAl), TMGa, and AsH_3 were used for the (Al)GaAs growth within the laser structures. Disilane (Si_2H_6) was used as a n-dopant while carbon tetrabromide (CBr_4) was used for p-dopant in the $Al_{0.65}Ga_{0.35}As$ upper cladding layer, and diethyl-zinc (DEZn) was used for heavily doped p+ GaAs contact layer. To investigate the effect of the high bandgap $GaAs_{1-y}P_y$ barrier on the electronic and optical properties, one laser diode structure was grown without P (y=0), while another laser diode was grown with y=0.2 within the $GaAs_{1-y}P_y$ barrier. The transverse optical confinement factor for this structure was calculated to be 2.4%.

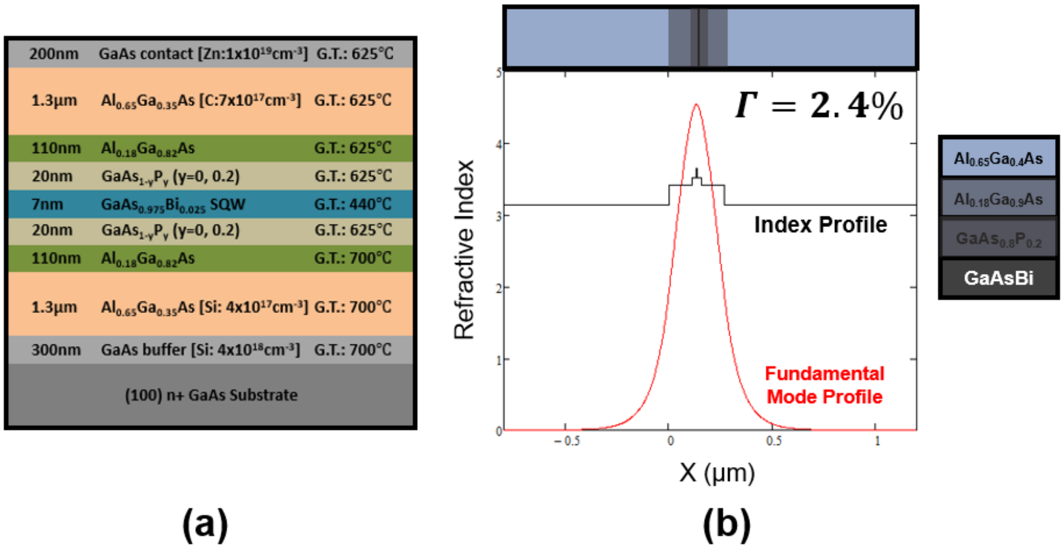

Fig. 4-16 *(a) Complete laser diode structure where the growth temperature is denoted as G.T. and GaBi mole fraction within SQW is 2.5% (x=0.025) and (b) Calculation of the transverse optical confinement factor for the corresponding structure*

After the laser structure growth, the wafers were cleaved and one of each sample were subjected to an additional *in situ* annealing within the MOVPE reactor under H_2/AsH_3 (AsH3=3.8mmol/min) for 25min.

25µm-wide ridge waveguide lasers were fabricated by a standard photolithographic process from both the as-grown and annealed samples. The wet etching using H_3PO_4:H_2O_2:H_2O = 3:1:20 was carried out to form the etched ridge waveguide structure, using a patterned photoresist mask. 200nm-thick SiN_x was deposited by plasma-enhanced chemical vapor deposition for the electrical passivation. The wafer was subsequently thinned down to 150µm. Contact layers consisting of Ti/Pt/Au (25/50/300nm) were e-beam evaporated on the top surface to form the ohmic contact to p+ GaAs. Contact to the n-type region was made to the backside of the wafer using a Ni/AuGe/Ni/Au (5/100/35/200nm) contact metallurgy. The contact metals were alloyed at 400°C for 30 sec using Rapid Thermal Annealing (RTA). Devices were measured *as-cleaved* (*i.e.*

no facet coatings) at room temperature and 80K under pulsed current operation. The electroluminescence (EL) data was collected using a grating diffractometer and Si photodetector while the output power from one facet were measured using InGaAs photodiode.

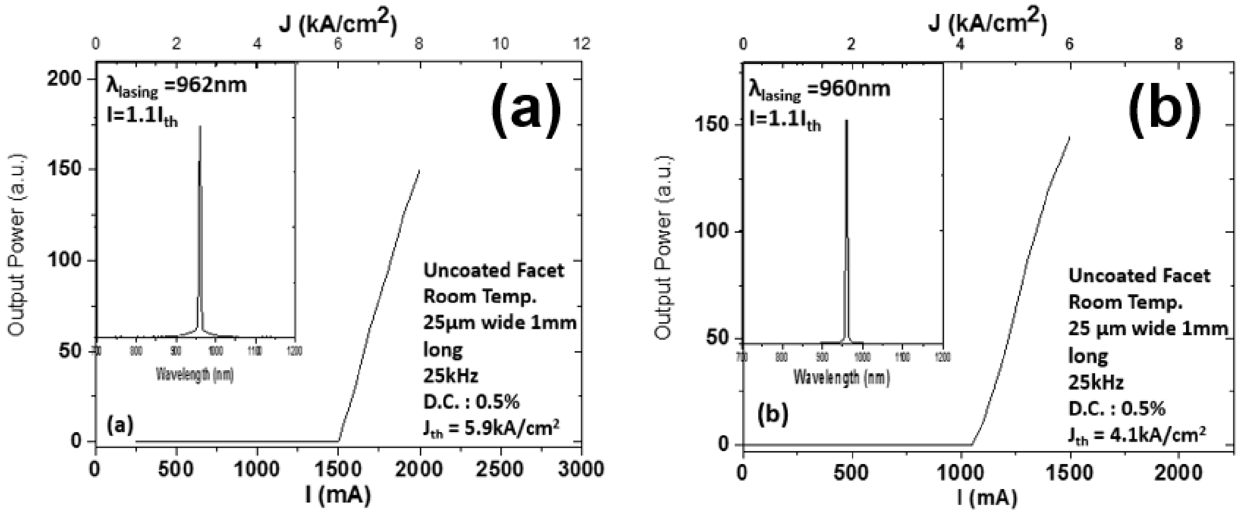

Fig. 4-17 *(a) PI and the spectrum (inset) of as-grown laser diode device employing* $GaAs_{0.975}Bi_{0.025}/GaAs_{0.8}P_{0.2}$*, (b) PI and the spectrum (inset) of annealed laser diode device employing* $GaAs_{0.975}Bi_{0.025}/GaAs_{0.8}P_{0.2}$

Both electroluminescence (EL) and light output vs. current input (PI) were measured from both annealed and as-grown laser diode devices employing $GaAs_{0.975}Bi_{0.025}/GaAs_{0.8}P_{0.2}$ active region, as shown in Fig. 4-17, which exhibit conventional threshold current (I_{th}) behavior and the narrowed full-width-half-max (FWHM) above the threshold current. A significant reduction in the threshold current density (J_{th}) was observed from the device with *in situ* annealing, as compared to the as-grown devices. However, the J_{th}=4.1kA/cm^2 from the annealed device was still higher than the previously lowest reported value of J_{th} = 1~1.1kA/cm^2 [15]. It should be noted that the GaBi mole fraction within the SQW laser structure employed in the previous study [15] was z=0.022 while the current devices employ z=0.025 which results in a longer lasing wavelength (λ_{lasing}=962nm vs.

947nm). Therefore, the higher J_{th} observed here could be attributed to a higher concentration of Bi-related defects. The reduction in J_{th} after annealing is most likely a result of a reduction in the point defect concentration within the GaAs$_{0.975}$Bi$_{0.025}$ SQW, which corresponds to the PL measurement shown in Fig. 4-15 (a).

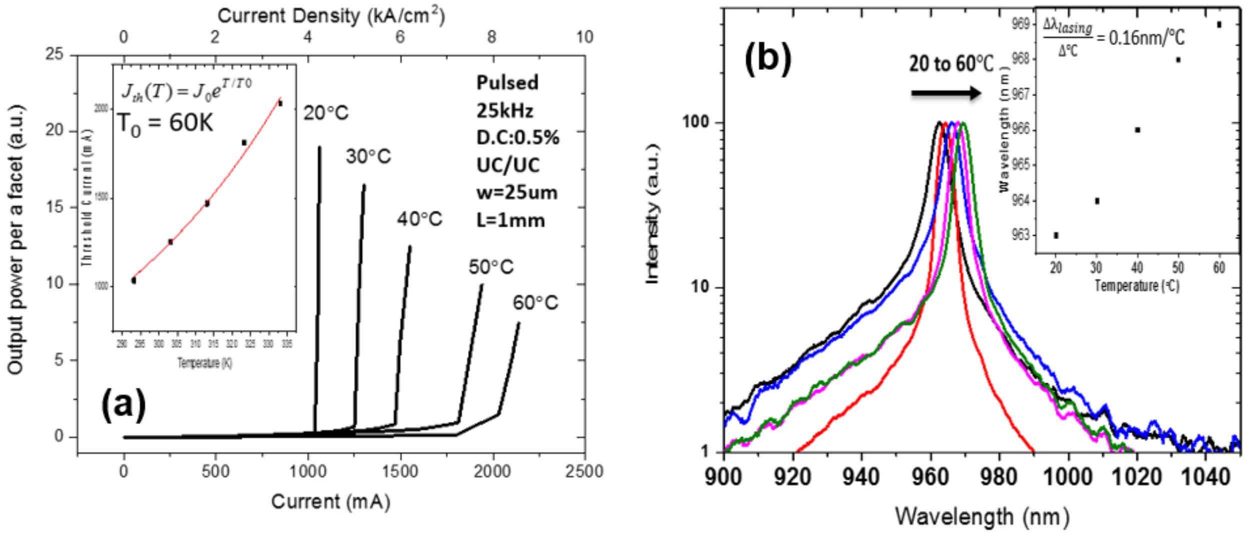

Fig. 4-18 *(a) The PI curves obtained from the annealed GaAs$_{0.975}$Bi$_{0.025}$/GaAs$_{0.8}$P$_{0.2}$ device, and (b) the spectral shifts measured at $I=1.1\times I_{th}$ as a function of heat sink temperature from 20 to 60 ℃*

The characteristic temperature, T_0, was measured from 20 to 60 ℃ from the devices with GaAs$_{0.8}$P$_{0.2}$ barriers fabricated from the annealed material as shown in Fig. 4-18 (a). The measured $T_0 \approx$ 60K, which was lower than that of the reported value ($T_0 \approx 100$K) [18] suggests that a higher P content in the GaAs$_{1-y}$P$_y$ barrier is necessary to effectively suppress the thermionic leakage [42]. It is worthwhile mentioning that the spectral shift as a function of varying temperature, $\frac{\Delta\lambda_{lasing}}{\Delta°C}$, was measured as 0.16nm/K, and was close to the reported value for bulk-like MBE grown dilute bismide lasers (0.17nm/K) [43]. These values are significantly lower than hat of conventional strained InGaAs QW laser emitting similar wavelength (vs. 0.35nm/K) [44]. This low temperature sensitivity of the lasing wavelength has been theoretically predicted in a prior study [45] and agrees well with the reported experimental temperature dependency of the $GaAs_{1-x}Bi_x$ band gap [46].

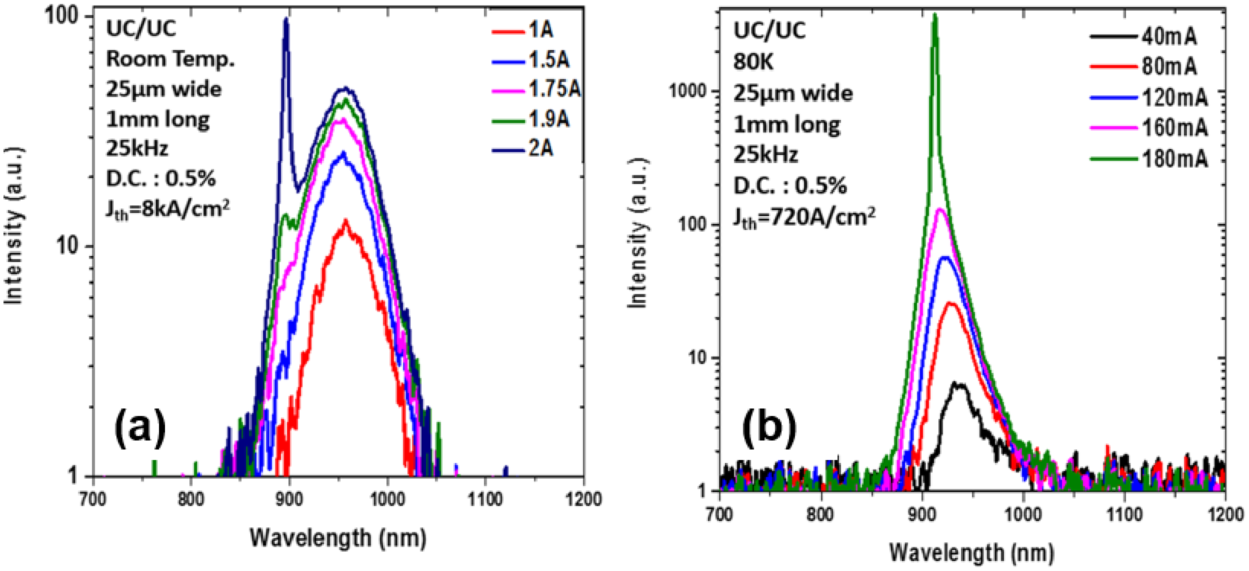

Fig. 4-19 *Spectra of the annealed $GaAs_{0.975}Bi_{0.025}$/GaAs devices measured at (a) room temperature, (b) 80K as a function of driving current*

For the devices with GaAs barriers, a lasing emission at higher transition energy, corresponding to 1.39eV, was observed at room temperature. At low drive current, the EL peak was positioned at lower transition energy, as shown in Fig. 4-19 (a). This result suggests that excessive band-filling and thermionic leakage exist within the QW structure. Similar behavior was observed by *I. Marko et al*, where they experimentally demonstrated that this higher transition energy emission corresponds to the e1-lh1 (light hole) transition [18]. In contrast, as presented in Fig. 4-19 (b), the measured spectrum at 80K on the devices with GaAs barriers does not exhibit excessive band filling. The measured threshold current density at 80K was J_{th}=720A/cm^2. While this value is quite high, it is smaller than the previously reported $J_{th}\approx$1.4kA/cm^2 measured at 20K from the device employing GaAs barriers in ref. 18. The observed lower J_{th} (J_{th}=720A/cm^2 vs. 1.4kA/cm^2 in ref. 18) at a higher operating temperature (80K vs. 20K in ref. 18) could be partially ascribed to the higher optical confinement factor, 2.4%, in our study compared to ~1.6% in ref. 18. Also, it should be noted that at 80K, the electron thermal energy corresponds to 6.89meV, which is significantly smaller than the conduction band offset at the heterointerface of $GaAs_{0.975}Bi_{0.025}$/GaAs. Therefore, one can expect minimal thermionic leakage at 80K. This suggests that a significant carrier loss via non-radiative recombination exists within the $GaAs_{1-x}Bi_x$ SQW, contributing to the relatively large measured J_{th} (720A/cm^2) at 80K.

4. 7. Growth and Characterization of $GaAs_{0.965}Bi_{0.035}$ QW Active Region Laser

In the previous section, the effects of the MOVPE growth parameters in incorporation of Bi into the host GaAs matrix have been discussed. Higher Bi incorporation was achieved by either employing a lower growth temperature or increasing TMBi/V gas phase ratio to some extent until reaching the “saturated regime”. In particular, the higher luminescent properties were observed from the material grown at the relatively high TMBi/Vi ratio. Therefore, in order to obtain a highly luminescent $GaAs_{1-z}Bi_z$ QW with a higher GaBi mole fraction, the growth condition needs to be optimized at a low growth temperature with adjusted TMBi/V and V/III ratio. This is in contrast to the typical MOVPE growth condition in “mass-transport limited regime” where only adjustment of molar flow is necessary to adjust the composition in the solid phase. It was also shown in the previous section that *in situ* reflectance measurement can be utilized to find the “saturated regime”, by which the reduction of the growth rate, as an evidence of the saturation of Bi incorporation, can be monitored in real time. Therefore, in this section, the growth of a GaAs$_{1-z}$Bi$_z$ quantum well active region with a higher GaBi mole fraction is investigated, by utilizing the characterization techniques mentioned above. The growth was carried out by reducing growth temperature to 430°C with a reduced V/III ratio as summarized in Table 4-7.

Table 4-7. Growth Parameters used for the material optimization

Material	Pressure [Torr]	Growth Temp. [℃]	TEGa [μmol/min]	TMBi/TBAs	V/III Ratio
QW (GaAs$_{1-x}$Bi$_x$)	50	430	186	0.007~0.036	0.84
Barrier (GaAs)	100	630	TMGa used (55μmol/min)	N/A	65

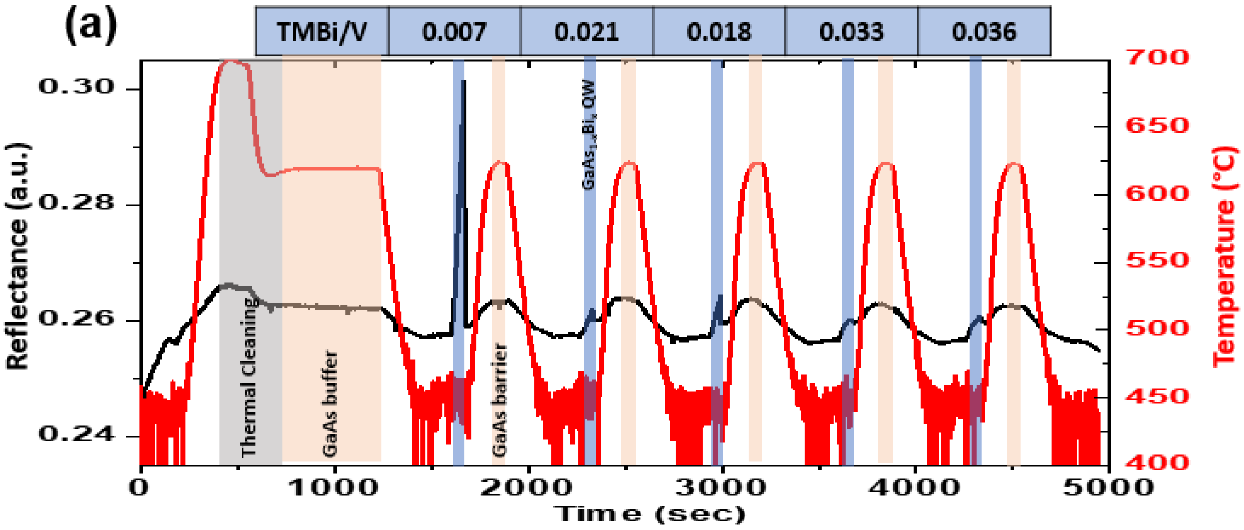

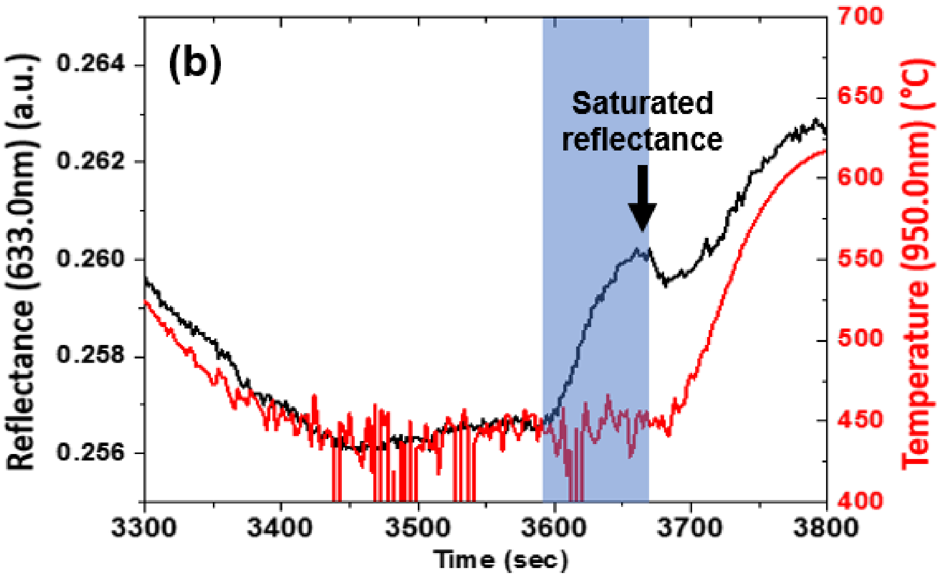

Fig. 4-20 *(a) in situ reflectance measured during the growth of* $GaAs_{1-z}Bi_z$ *MQW structure with varying TMBi/V ratio, and (b) in situ reflectance measured during the growth of* $GaAs_{1-z}Bi_z$ *QW at TMBi/V ratio of 0.033*

Fig. 4-20 presents *in situ* reflectance during the growth of $GaAs_{1-z}Bi_z$ MQW structure with varying TMBi/V ratio from 0.007 to 0.036. Similar to the prior observation discussed in the previous section, the saturated reflectance, which indicates saturation in the growth rate, was observed when the TMBi/V exceeds 0.033. In order to extract the GaBi mole fraction within the $GaAs_{1-z}Bi_z$ QW grown at this saturated regime, 5 period MQW structures were grown at the TMBi/V ratio of either 0.033 or 0.036 as shown in Fig. 4-21.

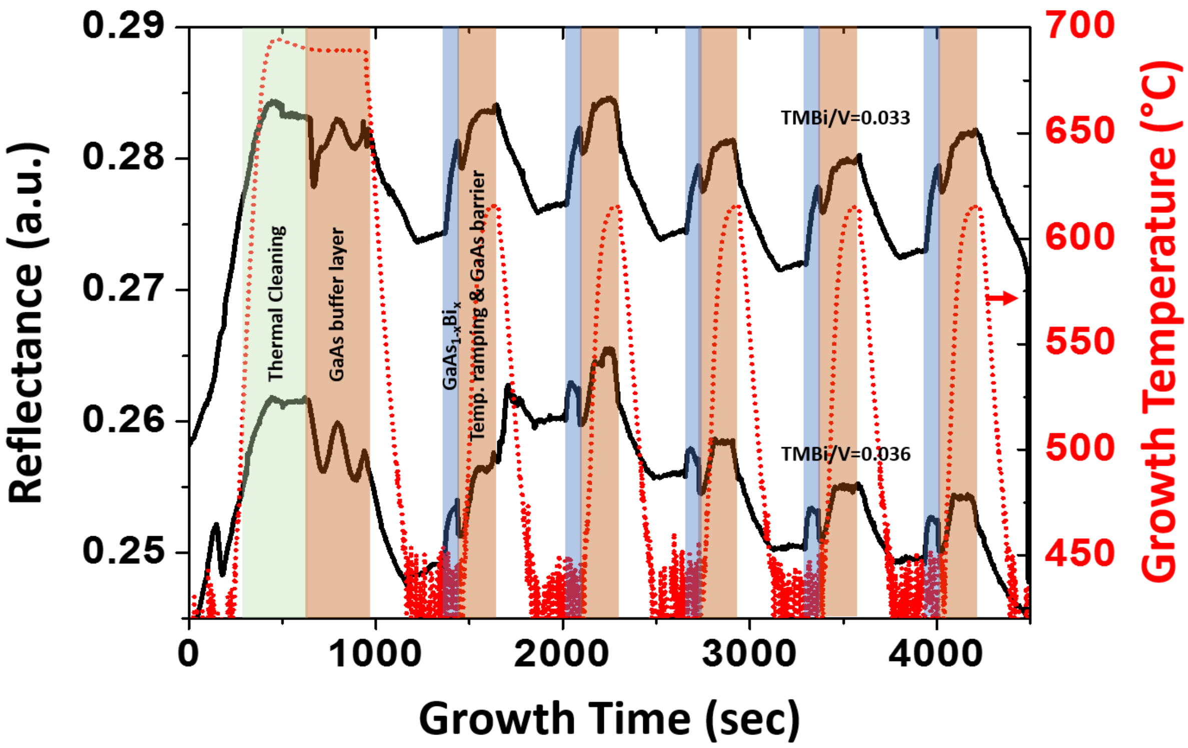

***Fig. 4-21** in situ reflectance during the growth. The shaded areas in different colors indicate the growth of each layer. The upper black curve is the in situ reflectance of the growth with TMBi/V=0.033 while the lower black curve corresponds to TMBi/V=0.036*

The clear evidence of the growth rate saturation by the reflectance intensity during the $GaAs_{1-x}Bi_x$ growth was observed when TMBi/V was 0.036, in contrast to that observed for TMBi/V=0.033. This is a strong indication of a reduced growth rate or suppression of growth under a high TMBi/V ratio (TMBi/V=0.036 in this case), which results from the segregated excess Bi at the growth front blocking the incorporation sites [32]. As a result, the MQW sample grown with TMBi/V=0.036 contains Bi-related droplets on the surface, which reduces overall reflectance intensity, while the sample grown with TMBi/V=0.033 or lower exhibit a droplet-free surface.

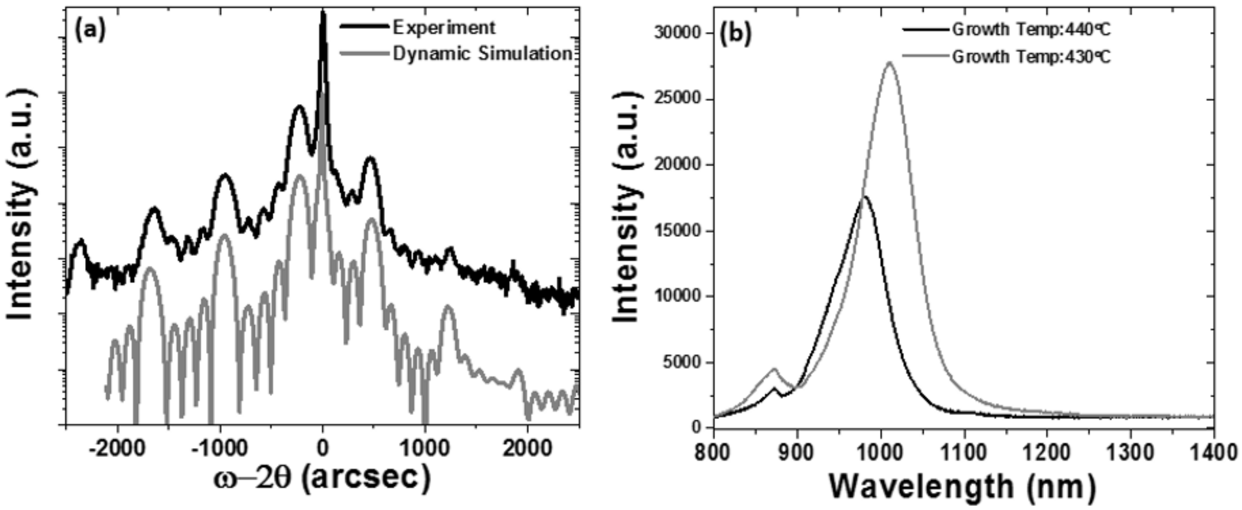

Fig. 4-22 *(a) HR-XRD measurement and the dynamic simulation for the 5x GaAs1-xBix/GaAs MQW structure grown with TMBi/V=0.033 where the thickness of a Bi-containing well and GaBi mole fraction were extracted to be 7nm and x=0.035, respectively, assuming* a_{GaBi}*=0.633nm (b) RT-PLs from the identical structures grown at 440°C (5x* $GaAs_{0.975}Bi_{0.025}$*/GaAs (7/22nm) grown by the same growth condition in section 4.5 and 430°C (5x* $GaAs_{0.965}Bi_{0.035}$*/GaAs (7/20nm) growth condition in table 4-7).*

Assuming a GaBi zincblende lattice constant, a_{GaBi}, of 0.633nm [24], the GaBi mole fraction and thickness of a Bi-containing well were extracted by comparing the measured XRD spectra to the dynamic simulation at a point of the best fit, which are summarized in Table 4-8.

Table 4-8. Structure Details and $GaAs_{1-x}Bi_x$ ***growth rate found from HR-XRD***

Growth Temp. [°C]	**TMBi/V**	**Structure Details**	**$GaAs_{1-x}Bi_x$ Growth Rate [nm/sec]**	**PL Peak Position (nm)**
430	**0.033**	**5x $GaAs_{0.965}Bi_{0.035}$/GaAs (7/20nm)**	**0.08**	**1015**

The RT-PL measurement indicates that the luminescence spectrum of the 5x $GaAs_{0.965}Bi_{0.035}$/GaAs (7/20nm) sample exhibits a higher PL intensity and a longer peak wavelength compared to the sample which was discussed in the previous section, most likely resulting from the further optimized growth condition such as adjusted V/III and TMBi/V ratio. In addition, Secondary ion mass spectroscopy (SIMS) measurements indicate that the carbon and oxygen concentrations within the $GaAs_{0.965}Bi_{0.035}$ QW are $5\text{~}6\times10^{17}$ and below $5\times10^{15}cm^{-3}$, respectively, which is indicative of growth within the “saturation regime” as the carbon concentration of GaAs grown under a similar condition is generally in excess of $10^{19}cm^{-3}$ [26].

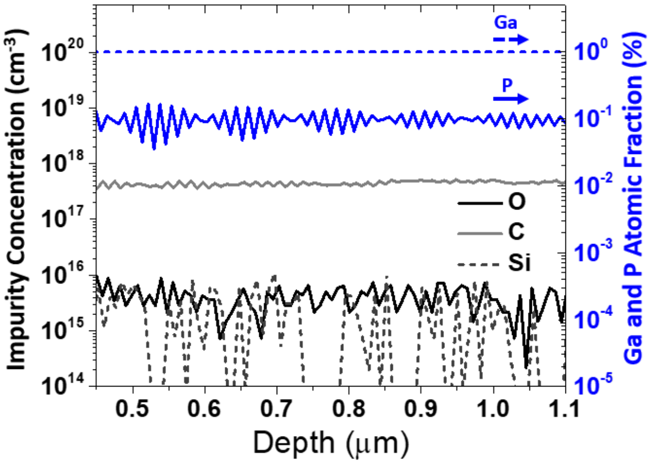

Fig. 4-23 *Secondary ion mass spectroscopy measurement from a strain compensated 50 period* $GaAs_{0.965}Bi_{0.035}/GaAs_{0.75}P_{0.25}$ *(7/3nm) structure*

Therefore, we chose this growth condition for the laser diode active region, which is schematically depicted in Fig 4-24. For the growth of the upper layers of the device structure, a lower growth temperature, 630°C was used to avoid any possible Bi out-diffusion and formation of Bi-rich precipitate as discussed in the prior section. In addition, a 1 nm-thick GaAs interlayer between $GaAs_{0.965}Bi_{0.035}$ and $GaAs_{0.75}P_{0.25}$ layer was inserted as a strain buffer layer [47] and to further protect the QW surface during the temperature ramping.

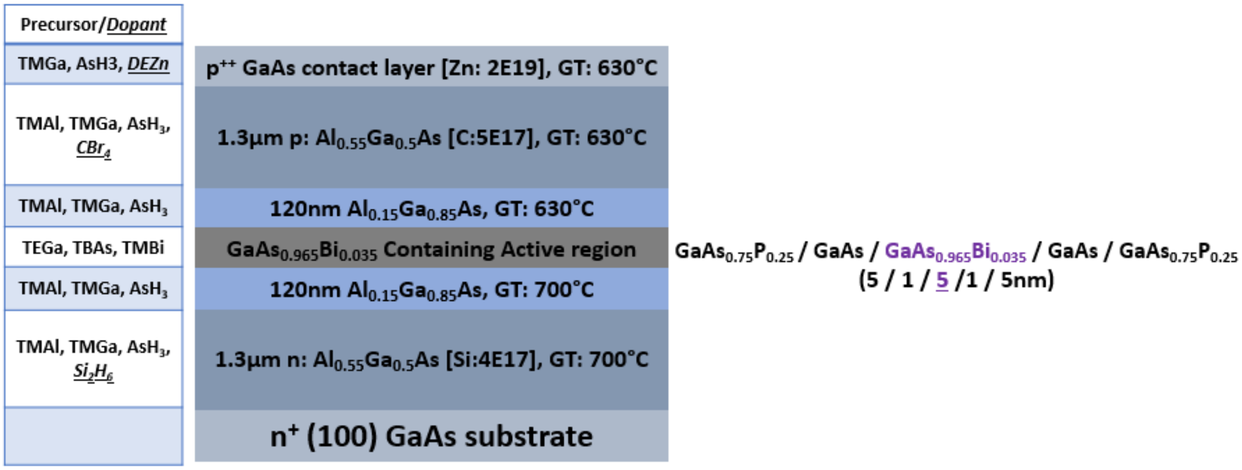

Fig. 4-24 *Complete laser diode structure with structural details employing 5nm thick SQW. The growth temperature is denoted as GT. 1nm thick GaAs interlayers were inserted between* $GaAs_{0.75}P_{0.25}$ *and* $GaAs_{0.975}Bi_{0.035}$

The laser diode employing a 5 nm thick SQW was designed to have an optical confinement factor of ~2%. After the structure growth on a full 2”-diameter GaAs substrate, the wafer was cleaved into multiple pieces. Each piece was subjected to an additional *in situ* annealing in the OMVPE reactor under AsH_3 and H_2 for various times (30, 60, 90, and 120min) at 630°C for the systematic study of the impact of the post growth thermal annealing on the device performance.

After annealing, A HAADF-STEM analysis was carried out on the device annealed for 120 min, as shown in Fig. 4-25, in order to investigate the Bi distribution as well as to expose the presence of any Bi-rich precipitates that have been observed in a prior study [26]. Bi-containing precipitates may lead to a higher internal optical loss due to a large absorption coefficient in the near IR spectral regime.

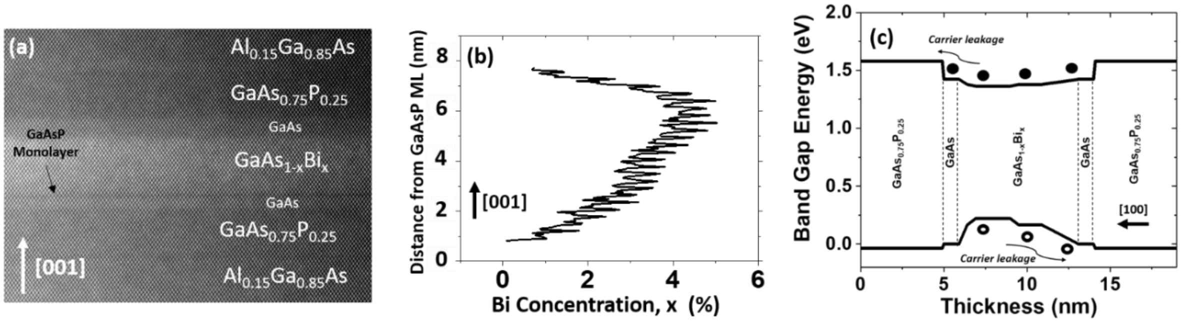

Fig. 4-25 *(a) Z-contrast STEM image of the laser device annealed for 120min at 630℃, showing the Bi containing SQW with $GaAs_{0.75}P_{0.25}$ barrier, GaAs interlayer and GaAsP monolayer. (b) Corresponding Bi concentration profile deduced from the intensity measurement where the background signal was subtracted by applying a linear fit to the GaAs within the GaAs1-xBix SQW. (c) Corresponding schematic band diagram derived from the measured Bi concentration profile assuming VBO of 15meV/%Bi and CBO of 55meV/%Bi at GaAs1-xBix/GaAs heterojunctions from ref 12.*

As shown in Fig. 4-25. (a), no evidence of Bi-related metallic precipitates, which are commonly observed in the annealed $GaAs_{1-z}Bi_z$, was found [41], most likely due to the lower annealing temperature employed in this work. The upper limit of the Bi cluster density is estimated to be ~1.3×10^3 /μm^3. A profile of Bi concentration across the $GaAs_{1-z}Bi_z$ layer was deduced from the STEM image intensity for which the background signal was subtracted by applying a linear fit to the GaAs within the $GaAs_{1-z}Bi_z$ SQW. This profile revealed a graded Bi concentration across the QW, as shown in Fig. 4-25. (b). This is likely a result of the high TMBi/V ratio employed in the growth. A similar inhomogeneity in both Bi distribution and background C concentration was observed in a prior report [32] from the a $GaAs_{1-x}Bi_x$ film grown with high TMBi/V ratio and the continuous feed of III/V precursors. The increasing Bi concentration profile in the growth direction is ascribed to the segregated Bi during the QW growth, which blocks the incorporation sites of both C and Ga while forming a Bi reservoir at the growth front, resulting in a higher Bi incorporation at the upper part of the QW. It is worthwhile noting that similar profiles were reported from the indium-segregated $In_xGa_{1-x}As/GaAs$ and $In_xGa_{1-x}N/GaN$ QW structures [48-49]. Fig. 4-25 (c) presents the schematic band diagram based on the Bi concentration profile that was from the STEM analysis. Such a graded Bi concentration will locally confine carriers within the thin region with high Bi concentration, although significant carrier leakage may occur from the lower Bi composition region of the QW under excessive band-filling at high carrier injection (Fig. 4-25 (c)). It is also worthwhile mentioning that the appearance of the intensity dip at the lower GaAsBi/GaAs interface may indicate formation of a very thin GaAsP layer during the cool-down step after GaAs growth at 630°C. The adsorption of P on the surface during the GaP/GaAs growth has been identified as a challenge for producing an abrupt interface between the two layers [31]. During the growth, the P precursor is expected to be present in the growth chamber even after the GaAsP layer growth. Since the P distribution coefficient has been observed to enhance greatly with decreasing temperature [32], a small amount of residual P may result in a considerable amount of P adsorption on the surface at the cool-down step, leading to its incorporation as a GaAsP monolayer.

Both electroluminescence (EL) and light output vs. current input (PI) were measured from both annealed (30 min) and as-grown laser diode devices employing $GaAs_{0.965}Bi_{0.035}/GaAs_{0.8}P_{0.2}$ active region, as shown in Fig. 4-26, which exhibit conventional threshold current (I_{th}) behavior and the narrowed full-width-half-max (FWHM) above the threshold current. However, the amount of reduction (6 vs 5.2 kA/cm^2) in the threshold current density (J_{th}) was not as significant as that observed from the devices with lower GaBi mole fraction (z=2.5%) within the $GaAs_{1-z}Bi_z$ active region, which was discussed in the prior section.

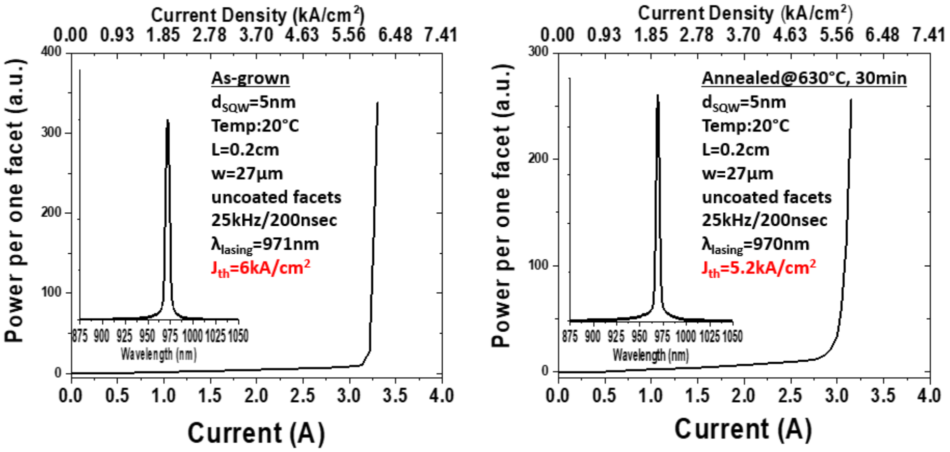

(a) (b)

Fig. 4-26 *(a) PI and the spectrum (inset) of as-grown laser diode device employing* $GaAs_{0.965}Bi_{0.035}/GaAs_{0.75}P_{0.25}$*, (b) PI and the spectrum (inset) of annealed laser diode device employing* $GaAs_{0.965}Bi_{0.035}/GaAs_{0.75}P_{0.25}$

While the devices annealed for 30 min exhibit both improved PL intensity, which was measured before device fabrication, and J_{th}, the J_{th} values from the devices annealed longer than 90 min are higher than that of the as-grown devices although the PL intensities are comparable to each other, as shown in Fig. 4-27 (a).

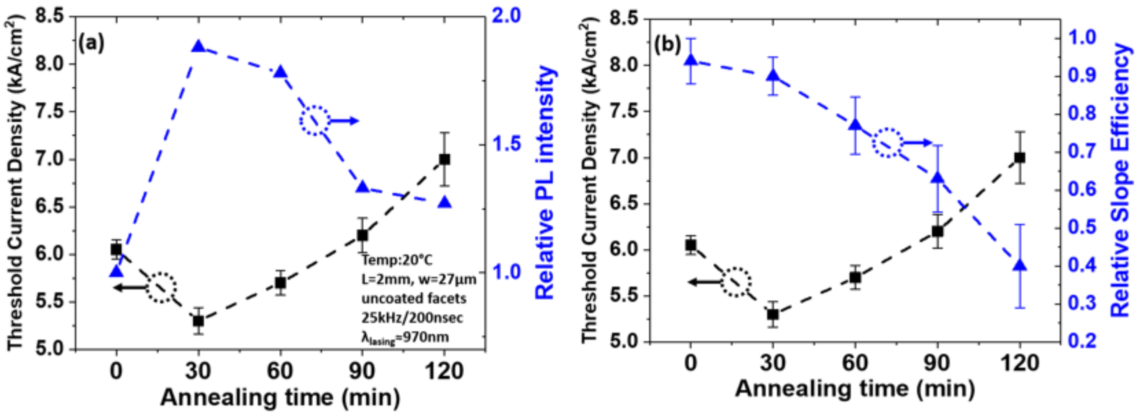

Fig. 4-27 *(a) The change in threshold current density and PL intensity as a function of annealing time where the PL intensities were normalized by that of as-grown (Annealing time=0sec). (b) The change in threshold current density and slope efficiency as a function of annealing time where the slope efficiencies were normalized by that (66mW/A) of as-grown (Annealing time=0sec). The dashed lines are for guiding eyes.*

Furthermore, a gradual decrease in the slope efficiency was observed as the annealing time increases, as plotted in Fig. 4-27 (b), which does not follow the trend of either J_{th} or PL intensity. In general, a reduction in slope efficiency indicates either a reduction in the internal differential efficiency (η_0^d) and/or increase in the internal loss (α_i), assuming a constant mirror loss, as expressed in the equation (1) below.

$$\eta_{Ext}^d = 2\eta_{slope}[\frac{q\lambda_{\text{lasing}}}{\text{hc}}] = \eta_0^d \frac{\alpha_m}{\alpha_m + <\alpha_i>} \qquad (4.7)$$

where $\eta_{\text{Ext}}^{\text{d}}$ is external differential quantum efficiency, $\eta_{\text{Slope}}$is slope efficiency, q is electronic charge (1.6×10^{-19}C), h is Planck's constant (6.63×10^{-34} J·s), c is speed of light, and α_m ismirror loss ($\alpha_m=(1/L_{cav})\ln(1/R)$) (R=0.3 for GaAs).

The internal differential efficiency (η_0^d) can be expressed by a product of the differential injection efficiency (η_i^d), which is a fraction of current entering QW above laser threshold resulting in the total recombination current (which includes both radiative and non-radiative recombination), and the differential radiative efficiency (η_r^d), which is the fraction of the current entering QW above threshold which results in radiative recombination [50] as discussed in Chapter 3.

$$\eta_0^d = \eta_i^d \eta_r^d \tag{4.8}$$

η_0^d can be less than unity, if the Fermi level does not fully pin above the laser threshold, which is evidenced by non-clamping of the carrier density, implying the terms, η_i^d and/or η_r^d, can be less than unity [50]. In particular, this incomplete carrier clamping above the threshold current from the $GaAs_{0.0978}Bi_{0.022}$ QW active region laser has been reported [18, 51], as shown in Fig 4-28.

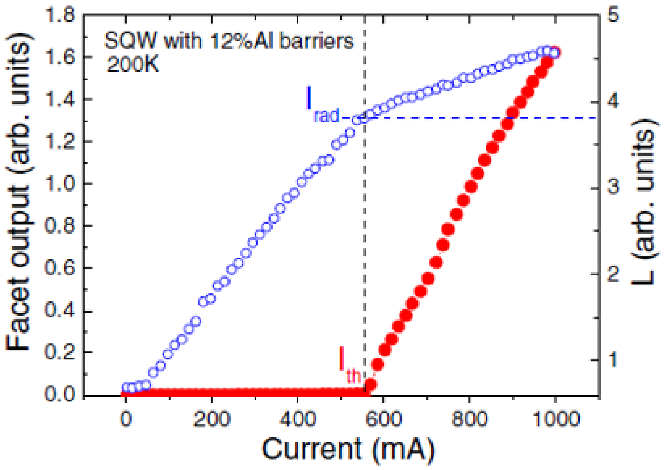

Fig. 4-28 *Light output from the laser facet and integrated spontaneous emission intensity (open circles) versus current density for $GaAs_{0.978}Bi_{0.022}$ SQW device, showing the carrier non-clamping above J_{th} (after reference 18)*

In evaluating high performance III-V based QW lasers, η_r^d is generally assumed to be unity above laser threshold and therefore, η_0^d is equal to η_i^d. Furthermore, η_i^d is often assumed to be same as the injection efficiency at threshold (η_{inj}) and the extracted η_0^d value from cavity length analysis (CLA), which was discussed in Chapter 3, is then used to obtain the transparency current density (J_{tr}). This common practice does not apply to the present structures since η_i^d can be very different from η_0^d [50], resulting in an inaccurate J_{tr} as discussed in Chapter 3. Nevertheless, CLA can still be used to extract the internal loss (α_i), internal differential quantum efficiency (η_0^d), modal material gain (Γg_{0J}), and the ratio of J_{tr}/η_{inj}, provided precautions are taken to avoid extraction of data when carrier unclamping is significant.

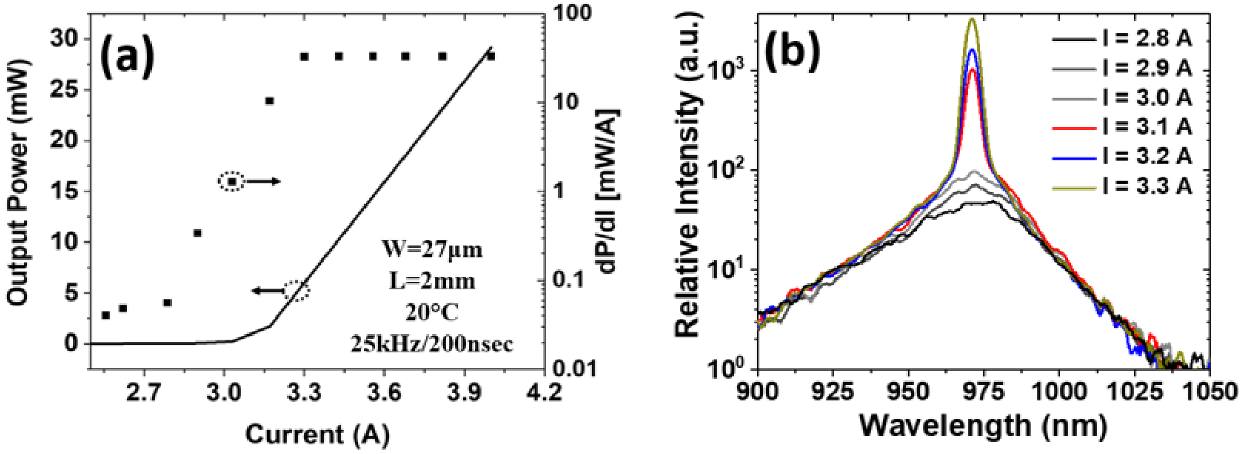

Fig. 4-29 *output power-current (PI) characteristics from a facet of as-grown* $GaAs_{0.965}Bi_{0.035}$ */* $GaAs_{0.75}P_{0.25}$ *SQW laser and the slope efficiency (*$\eta_{slope}=dP/dI$*), (b) Measured optical spectra at various driving currents*

The measured output power-current characteristics (PI) from the as-grown $GaAs_{0.965}Bi_{0.035}$ / $GaAs_{0.75}P_{0.25}$ SQW laser, shown in Fig. 4-29 (a), exhibits a soft "turn-on" behavior near J_{th}, which is not typical for conventional active region QW lasers. This soft turn-on behavior is attributed to the non-pinning of the carrier density within the active region at current injection levels just above threshold. It is noted that the measured spectrum within the region of changing slope efficiency ($\eta_{slope} = \frac{dP}{dI}$) near the threshold exhibits typical characteristics of stimulated emission such as increased intensity as well as narrowed full-width-half-max (FWHM) as shown in Fig 4-29(b). This soft turn-on in the PI characteristics can cause a significant error in extracting η_{slope}, especially near the threshold. For instance, it was observed that η_{slope}, shown in Fig 4-29 (a), levels out at driving current higher than 3.3 A, while a coherent light output via stimulated emission was already observed at 3.1 A. Therefore, only the “saturated” η_{slope} value, taken well above laser threshold were used in the CLA study to calculate the external differential quantum efficiency, η_{Ext}^{d}. It is noted that the driving current dependent EL spectra, shown in Fig 4-29 (b), shows the saturation of the broad spontaneous emission near the narrow lasing peaks at λ_{lasing} = 971nm for the injection currents higher than 3.1 A. This saturation of spontaneous emission implies carrier density within the active region after the laser threshold is rather small. Nevertheless, employing only the “saturated” η_{slope} values is expected to minimize errors due to the possibility of partial unclamping of the carrier density in the active region. Therefore, CLA was performed using the devices with the cavity length of 0.2, 0.25, and 0.3 cm.

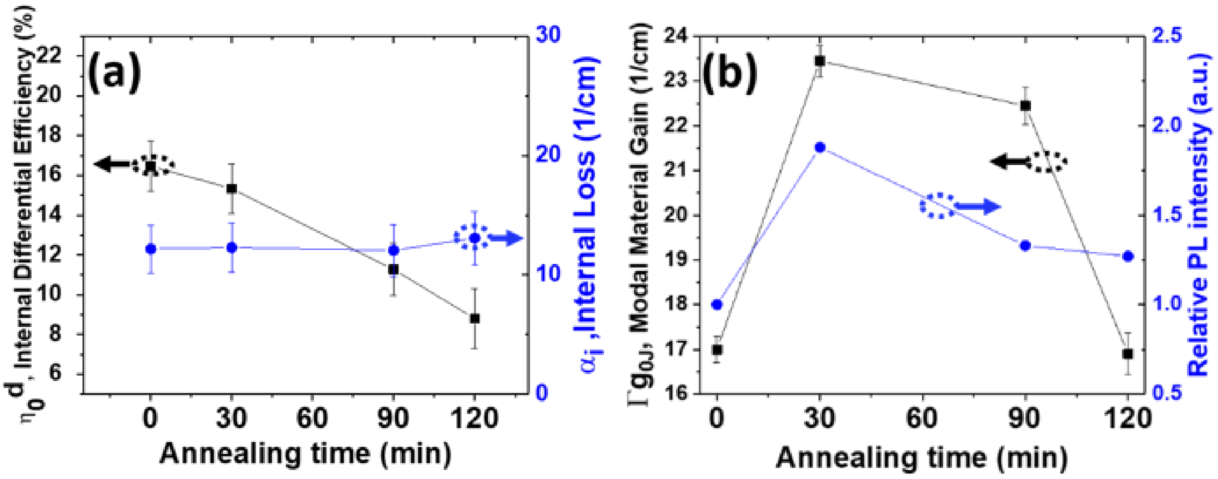

Fig. 4-30 *(a) Extracted internal differential efficiency (η_0^d), and internal loss (α_i), shown in black and blue dots, by CLA from devices annealed for various length, (b) The change in the modal material gain (Γg_{0J}) extracted by CLA and measured PL intensity from the laser material obtained before fabrication of ridge waveguide laser devices.*

The extracted internal differential efficiencies (η_0^d) and internal loss (α_i) by CLA as a function of annealing time is shown in Fig. 4-30 (a), where a gradual decrease in η_0^d was observed while α_i remained nearly constant as the annealing time increases. It must be noted that the overall η_0^d values were significantly lower, while α_i values are higher than those typically observed in high performance InGaAs QW lasers with similar emission wavelengths [51]. These low η_0^d values are partially ascribed to strong carrier leakage resulting from the graded Bi concentration within the $GaAs_{0.965}Bi_{0.035}$ QW, which has been observed by Z-contrast scanning transmission electron microscopic (STEM) analysis Fig. 4-25 (a). Well above laser threshold, where carrier pinning is assumed to occur, the η_r^d values will be close to unity as the stimulated recombination rate is orders of faster than non-radiative and spontaneous recombination rates [50]. Therefore, the degradation of the η_0^d after the post-growth thermal annealing most likely corresponds to a reduction in the differential injection efficiency, η_i^d.

It was observed that the change in modal material gain (Γg_{0J}) follows the same trends as the variation in the PL intensity with varying annealing time, that are measured at room temperature before the device processing for ridge waveguide lasers, as shown in Fig. 4-30 (b). The highest Γg_{0J} value (23.4 cm^{-1}) was found after annealing for 30 min, which corresponds to the material gain of g_{0J} = 1170 cm^{-1}. This value is still lower than that obtained from $GaAs_{0.982}Bi_{0.018}$ SQW laser (g_{0J} = 1500 cm^{-1}) by segmented contact method [52], most likely due to higher Bi concentration and graded Bi profile in the QW employed in our study. In spite of the lower material gain, our investigation demonstrates that there exists an optimum annealing point, which leads to an improved material gain. The extracted α_i values (11-14 cm^{-1}) reported in this letter are in good agreement with the reported value (10-15 cm^{-1}) [51]. Nevertheless, these α_i values are significantly higher than that of the reported high performance strained InGaAs QW lasers [51, 53]. These high α_i values can be ascribed to free carrier absorption [54-55], which results from very high carrier densities within the active region associated with high laser threshold current densities and therefore, high transparency current densities of the devices.

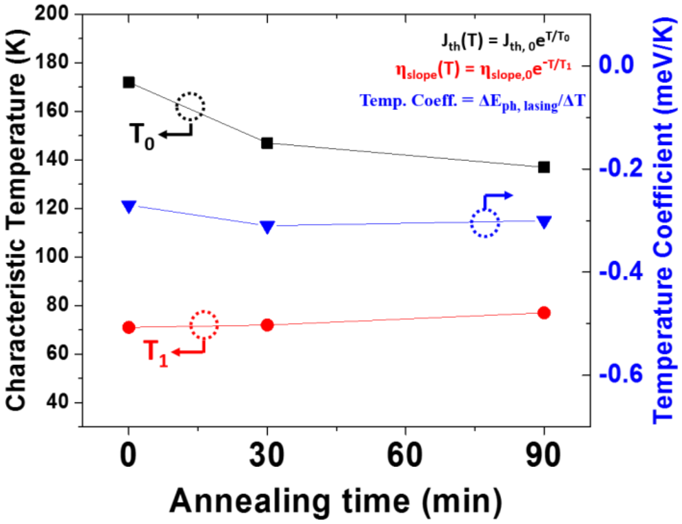

Fig. 4-31 *Summary of the change in the characteristic temperatures, T_0 (black square) and T_1 (red circle) and the temperature coefficient (blue triangle) of the lasing wavelength as a function of annealing time, measured from 283K to 323K. The fitting equations are shown at the upper right corner. The solid lines are for guiding eyes.*

Fig. 4-31 summarize the characteristic temperature coefficients of threshold current and slope efficiency, T_0 and T_1, and the temperature coefficient of emission wavelength, as a function of the annealing temperature. A gradual decrease in T_0 values from 172K (as-grown) to 137K (annealed for 90min) was observed as the annealing time increases, which is higher than the reported value (T_0 ~ 100K) from $GaAs_{0.978}Bi_{0.022}$ SQW laser within a similar measurement temperature range [18]. These higher T_0 values can possibly reflect a higher density of non-radiative recombination centers, similar to that observed in prior studies of InGaAsN QW lasers [56]. The measured T_1 values remained nearly constant as 71K (as-grown) and 77K (annealed for 90min). These T_1 values are quite low compared to conventional high performance strained InGaAs QW lasers operating in this wavelength region [57], which typically exhibit a T_1 value more than a factor of two to three over the T_0 value. This observation also indicates a significant degree of the carrier leakage from the active region [42], which may be correlated to the graded Bi profile investigated by STEM analysis. The temperature coefficient of the lasing photon energy also remained practically constant, near -0.3meV/K, which is similar to the reported value (-0.32meV) from the $GaAs_{0.956}Bi_{0.044}$ SQW laser, measured up to 180K [18]. It is smaller, however, than that of typical high performance strained InGaAs QW lasers emitting at a similar lasing photon energy (~0.42meV/K) [44].

In order to further investigate the impact of the number of QW on the the internal and external device parameters, the laser diode structure employing $GaAs_{0.965}Bi_{0.035}$ double quantum well (DQW) active region was grown as shown in Fig. 4-32, and subsequently characterized.

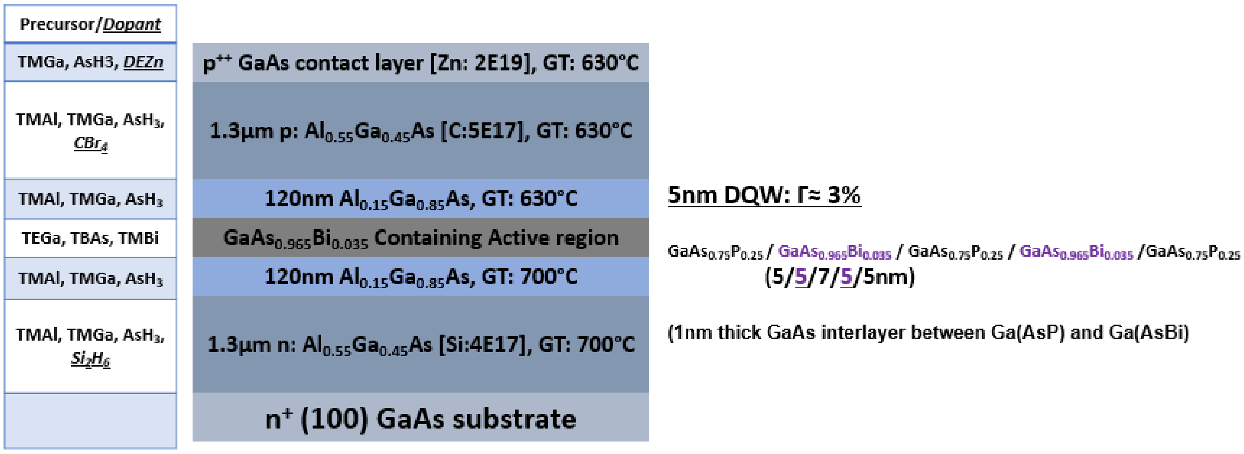

Fig. 4-32 *Complete laser diode structure with structural details employing $GaAs_{0.975}Bi_{0.035}$ DQW. The growth temperature is denoted as GT. 1nm thick GaAs interlayers were inserted between $GaAs_{0.75}P_{0.25}$ and $GaAs_{0.975}Bi_{0.035}$, and the transverse optical confinement factor (Γ) was designed to be ~3%.*

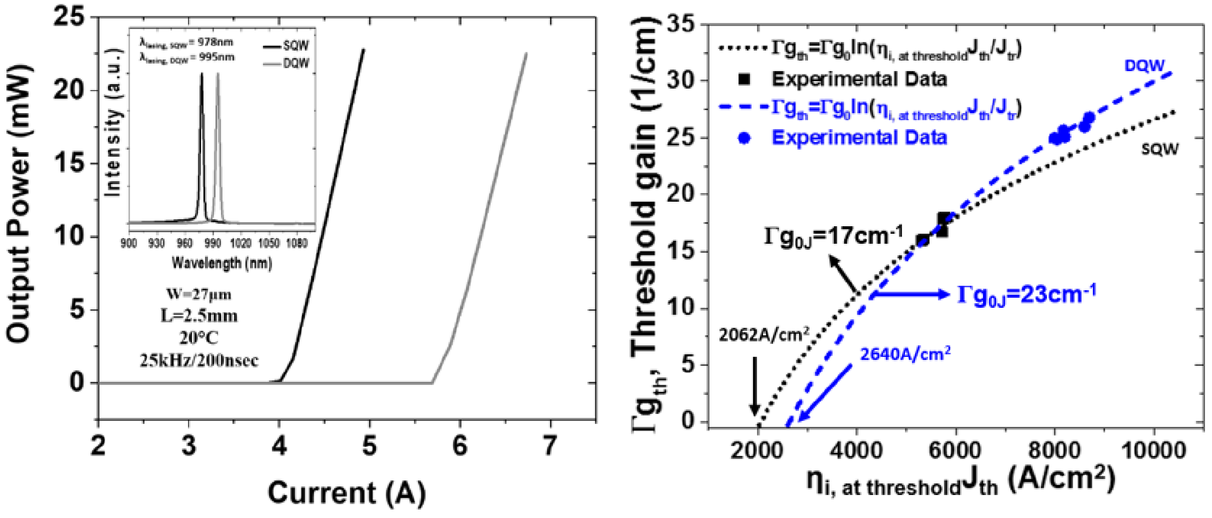

(a) **(b)**

Fig. 4-33 *(a) Output power-current (PI) characteristics from a facet of as-grown* $GaAs_{0.965}Bi_{0.035}$ */* $GaAs_{0.75}P_{0.25}$ *SQW (black) and DQW (gray) laser. Inset shows spectra. (b) Fitted gain curve using the relation* $J_{th} = \frac{J_{tr}}{\eta_{i\_at\ threshold}} \exp\left(\frac{\Gamma g_{th}}{\Gamma g_0}\right)$.

Fig. 4-33 (a). presents the PI characteristics of both SQW and DQW $GaAs_{0.965}Bi_{0.035}$ / $GaAs_{0.75}P_{0.25}$ devices, which are schematically drawn in Fig. 4-28. The shorter wavelength (978nm) of the SQW device can be explained by the more extensive carrier band-filling effect at higher current injection per QW. Shown in Fig. 4-33 (b) is the gain curve fitted in the relation $J_{th} = \frac{J_{tr}}{\eta_{i\_at\ threshold}} \exp\left(\frac{\Gamma g_{th}}{\Gamma g_0}\right)$, which was discussed in Chapter 3. The extracted internal parameters including internal differential quantum efficiency (η_0^d), internal loss parameter (α_i) and modal material gain (Γg_{0J}) from $GaAs_{0.965}Bi_{0.035}$ / $GaAs_{0.75}P_{0.25}$ SQW and DQW laser diodes are summarized in Table 4-9 below.

Table 4-9 Summary of extracted internal device parameters by CLA from SQW and DQW $GaAs_{0.965}Bi_{0.035}$ / $GaAs_{0.75}P_{0.25}$ devices

Device	**Internal differential quantum efficiency, η_0^d**	**Internal Loss, α_i [cm^{-1}]**	**Modal Material Gain, Γg_{0J} [cm^{-1}]**
SQW	16.5	12	17
DQW	19.8	21	23

It must be noted that an increase in α_i by a factor of 2 was observed from DQW devices, although they also exhibited an improved η_0^d and Γg_{0J}, respectively. The increased modal material gain (Γg_{0J}) of DQW devices corresponds to the increase in the optical confinement factor (Γ) by a factor of 1.5 (Γ_{SQW}=2% vs. Γ_{DQW}=3%). The increase in α_i possibly reflects higher free carrier absorption due to a higher injected carrier density within the increased volume of the active region for the DQW devices, as well as possible increased scattering losses at the larger number of interfaces within the DQW active region [54-55,58]. The physical origin of the increased α_i is a subject requiring further investigation.

4. 8. Conclusion

A novel $GaAs_{1-z}Bi_z$ laser structure employing Al-free $GaAs_{1-y}P_y$ QW barriers for achieving both electron confinement in the conduction band and strain balancing was investigated. Supported by DFT calculations, $GaAs_{1-y}P_y$was found to be an effective barrier material for electron confinement in the $GaAs_{1-z}Bi_z$ QW with comparable band offsets to those obtained from employing $Al_xGa_{1-x}As$ (x<0.2) barrier material. The optimum thickness of $GaAs_{1-y}P_y$ barriers for strain compensation was found based on the zero-stress criteria for a given Bi mole fraction in $GaAs_{1-z}Bi_z$ alloy. It was shown that both *in situ* and *ex situ* material characterization including HR-XRD, RT-PL, and *in situ* optical reflectance measurements are useful in optimizing the MOVPE of $GaAs_{1-z}Bi_z$ MQW and SQW and DQW laser diodes. $GaAs_{0.975}Bi_{0.025}/GaAs_{0.8}P_{0.2}$ SQW active region lasers exhibited a reduction in J_{th} after a post-growth *in situ* thermal annealing. These improved characteristics most likely result from a reduction in the point defects concentration as point defects and Bi-related defects can act as non-radiative recombination centers. $GaAs_{0.975}Bi_{0.025}/GaAs$ SQW active region lasers structure show excessive carrier band-filling and thermionic leakage at room temperature associated with a low conduction band offset, resulting in lasing emission at a higher transition energy. These experimental results suggest the use of tensile-strained $GaAs_{0.8}P_{0.2}$ can enable both strain-balancing and electron and hole confinements within the QW.

A systematic investigation was carried out on the impacts of the post-growth *in situ* thermal annealing by using $GaAs_{0.965}Bi_{0.035}$ SQW lasers grown by OMVPE. A gradual decrease in the laser slope efficiency was observed as the annealing time increased, while the maximum PL intensity as well as the lowest threshold current density were obtained after the annealing for 30 min at 630°C. STEM analysis indicates inhomogeneous Bi distribution within the SQW that is most likely due to the high TMBi/V gas phase ratio used in this work. This inhomogeneity resulted in the graded Bi profile, which might have led to the increased carrier leakage under excessive band filling conditions. The strong temperature sensitivity of the slope efficiency also implies a high degree of the quantum well carrier leakage. These observations indicate that a uniform Bi profile within the QW and the suppression of carrier leakage by employing higher bandgap materials (i.e., higher P-content GaAsP) are the critical factors for improving the dilute bismide-based device performance.

In addition, the variation of the internal and external device parameters, as a function of annealing condition, was investigated from as-grown and annealed single quantum well laser diodes employing $GaAs_{0.965}Bi_{0.035}$ / $GaAs_{0.75}P_{0.25}$ active region by means of CLA. While the internal loss, albeit significantly higher than that of conventional high performance III-V semiconductor lasers, remained relatively unchanged, the observed overall internal differential quantum efficiencies degraded with increasing annealing time. We attributed the decreasing internal differential quantum efficiency to a decreasing differential injection efficiency as annealing time increases, although this is a subject of our ongoing investigation. Also, the change in the extracted peak modal gain after annealing followed the same trends as the variation in the photoluminescence intensity, which demonstrates that an optimal post-growth thermal annealing can improve the radiative properties of the material. Cavity length analysis, carried out from as-grown single quantum well and double quantum well devices, revealed higher internal differential quantum efficiency and peak modal gain, although increased internal loss by a factor of two for the DQW devices was observed, likely due to the enhanced free carrier absorption within the larger active volume. Low internal differential quantum efficiency values obtained throughout this study strongly suggest the growth optimization for achieving a uniform Bi distribution in $GaAs_{1-x}Bi_x$ QWs, together with an optimized heterostructure employing high bandgap materials, is imperative to realize high performance $GaAs_{1-x}Bi_x$ QW based lasers. In addition, investigation of these internal device parameters by the other extraction techniques such as segmented contact method will be necessary to quantify any errors originating from CLA measurements due to the possibility of an unclamped carrier concentration above laser threshold. Nevertheless, the approaches presented in this chapter offer a pathway to realize high performance GaAsBi-based laser diodes grown by MOVPE as shown in the reported threshold current density (Fig. 4-34) as a function of GaBi mole fraction in the $GaAs_{1-z}Bi_z$ active region.

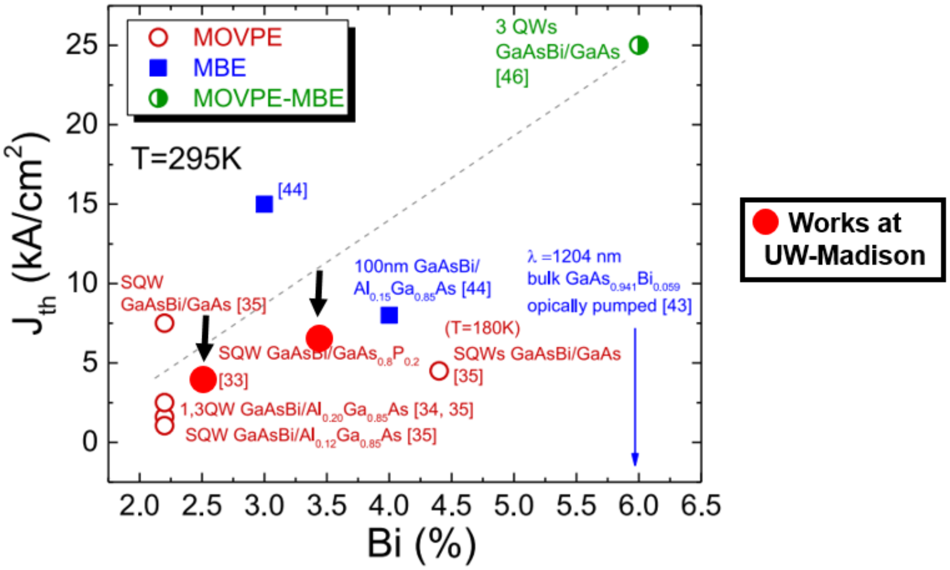

Fig. 4-34 *Threshold current density for GaAsBi based lasers as a function of Bi composition (after reference [59])*

Reference

[1] Broderick, Christopher A., Muhammad Usman, and Eoin P. O'Reilly. "Derivation of 12-and 14-band k·p Hamiltonians for dilute bismide and bismide-nitride semiconductors." *Semiconductor Science and Technology* 28.12 (2013): 125025.

[2] Francoeur, S., et al. "Band gap of GaAs 1− x Bi x, 0< x< 3.6%." *Applied physics letters* 82.22 (2003): 3874-3876.

[3] Oe, Kunishige, and Hiroshi Okamoto. "New semiconductor alloy GaAs1-xBix grown by metal organic vapor phase epitaxy." *Japanese journal of applied physics* 37.11A (1998): L1283.

[4] Madouri, D., Boukra, A., Zaoui, A., and Ferhat, M. 2008. *Computational Materials Science*, *43*(4), 818-822.

[5] Sweeney, S. J., Batool, Z., Hild, K., Jin, S. R., and Hosea, T. J. C. 2011. In *Transparent Optical Networks (ICTON), 2011 13th International Conference on* (pp. 1-4). IEEE.

[6] Broderick, Christopher A., et al. "Band engineering in dilute nitride and bismide semiconductor lasers." *Semiconductor Science and Technology* 27.9 (2012): 094011.

[7] Achour, H., Louhibi, S., Amrani, B., Tebboune, A., and Sekkal, N. 2008. *Superlattices and Microstructures*, *44*(2), 223-229.

[8] Alberi, K., et al. "Valence-band anticrossing in mismatched III-V semiconductor alloys." *Physical review B* 75.4 (2007): 045203.

[9] Alberi, Kirstin, et al. "Valence band anticrossing in $GaBi_xAs_{1-x}$." *Applied Physics Letters* 91.5 (2007): 051909.

[10] Linhart, W. M., and R. Kudrawiec. "Temperature dependence of band gaps in dilute bismides." *Semiconductor Science and Technology* 33.7 (2018): 073001.

[11] Broderick, Christopher A., Muhammad Usman, and Eoin P. O'Reilly. "Derivation of 12-and 14-band k·p Hamiltonians for dilute bismide and bismide-nitride semiconductors." *Semiconductor Science and Technology* 28.12 (2013): 125025.

[12] Usman, Muhammad, et al. "Impact of alloy disorder on the band structure of compressively strained $GaBi_xAs_{1-x}$." *Physical Review B* 87.11 (2013): 115104.

[13] Sweeney, S. J., et al. "The effect of temperature dependent processes on the performance of 1.5-μm compressively strained InGaAs (P) MQW semiconductor diode lasers." *IEEE Photonics Technology Letters* 10.8 (1998): 1076-1078.

[14] Gönül, B., and M. Oduncuoğlu. "A theoretical comparison of the pressure dependence of the threshold current of phosphorus-, aluminium-and nitrogen-based 1.3 µm lasers." *Semiconductor science and technology* 19.1 (2003): 23.

[15] Ludewig, P., et al. "Electrical injection Ga(AsBi)/(AlGa) As single quantum well laser." *Applied Physics Letters* 102.24 (2013): 242115.

[16] Fuyuki, T., Yoshida, K., Yoshioka, and R., Yoshimoto, M. 2014. *Applied Physics Express*, *7*(8), 082101.

[17] Butkute, R., Geižutis, A., Pačebutas, V., Čechavičius, B., Bukauskas, V., Kundrotas, R., Ludewig, P., and Krotkus, A. 2014 *Electronics Letters*, *50*(16), 1155-1157.

[18] Marko, I. P., et al. "Physical properties and optimization of GaBiAs/(Al) GaAs based near-infrared laser diodes grown by MOVPE with up to 4.4% Bi." *Journal of Physics D: Applied Physics* 47.34 (2014): 345103.

[19] Kim, H., et al. "Strain-compensated $GaAs_{1-y}P_y/GaAs_{1-z}Bi_z/GaAs_{1-y}P_y$ quantum wells for laser applications." *Semiconductor Science and Technology* 30.9 (2015): 094011.

[20] Al-Allak, Haider M., and Stewart J. Clark. "Valence-band offset of the lattice-matched β−FeSi 2 (100)/Si (001) heterostructure." *Physical Review B* 63.3 (2001): 033311.

[21] Forghani, Kamran, et al. "$GaAs_{1-y-z}P_yBi_z$, an alternative reduced band gap alloy system lattice-matched to GaAs." *Applied Physics Letters* 105.11 (2014): 111101.

[22] Yaguchi, Hiroyuki, et al. "Photoreflectance study of GaAs/GaAsP strained-barrier quantum well structures." *Japanese journal of applied physics* 32.1S (1993): 544.

[23] Ekins-Daukes, N. J., K. Kawaguchi, and J. Zhang. "Strain-balanced criteria for multiple quantum well structures and its signature in X-ray rocking curves." *Crystal Growth & Design* 2.4 (2002): 287-292.

[24] Tixier, S., et al. "Molecular beam epitaxy growth of GaAs 1− x Bi x." *Applied physics letters* 82.14 (2003): 2245-2247.

[25] Luo, Guangfu, et al. "Understanding and reducing deleterious defects in the metastable alloy GaAsBi." *NPG Asia Materials* 9.1 (2017): e345.

[26] Forghani, K., Guan, Y., Wood, A., Babock, S., Mawst, L. and Kuech, T.F., 2015. *Chemical Vapor Deposition*, *21*(7-8-9), pp.166-175.

[27] Kaminska, M., Weber, E.R., Liliental-Weber, Z., Leon, R. and Rek, Z.U., 1989.. *Journal of Vacuum Science & Technology B*, *7*(4), pp.710-713.

[28] Fushimi, H. and Wada, K., 1997. *IEEE Transactions on Electron Devices*, *44*(11), pp.1996-2001.

[29] Jacobsen, Heather, et al. "Ab initio study of the strain dependent thermodynamics of Bi doping in GaAs." *Physical Review B* 86.8 (2012): 085207.

[30] Kim, H., Forghani, K., Guan, Y., Kim, K., Wood, A.W., Lee, J., Babcock, S.E., Kuech, T.F. and Mawst, L.J.,. *Journal of Crystal Growth* 452 (2016) 276–280

[31] Ludewig, P., et al. "MOVPE growth of Ga (AsBi)/GaAs multi quantum well structures." *Journal of Crystal Growth* 370 (2013): 186-190.

[32] P. Ludewig, Z. L. Bushell, L. Nattermann, N. Knaub, W. Stolz, and K. Volz Journal of Crystal Growth 396 (2014) 95–99

[33] Ludewig, P., et al. "Growth of Ga (AsBi) on GaAs by continuous flow MOVPE." *Journal of Crystal Growth* 396 (2014): 95-99.

[34] Volz, K., et al. "Optimization of annealing conditions of (GaIn)(NAs) for solar cell applications." *Journal of Crystal Growth* 310.7-9 (2008): 2222-2228.

[35] Kim, T. W., et al. "Impact of thermal annealing on bulk InGaAsSbN materials grown by metalorganic vapor phase epitaxy." *Applied Physics Letters* 104.5 (2014): 051915.

[36] Mohmad, Abdul Rahman, et al. "Effects of rapid thermal annealing on GaAs1-xBix alloys." *Applied Physics Letters* 101.1 (2012): 012106.

[37] Grant, Perry C., et al. "Rapid thermal annealing effect on GaAsBi/GaAs single quantum wells grown by molecular beam epitaxy." *Journal of Vacuum Science & Technology B, Nanotechnology and Microelectronics: Materials, Processing, Measurement, and Phenomena* 32.2 (2014): 02C119.

[38] Mazzucato, S., et al. "Reduction of defect density by rapid thermal annealing in GaAsBi studied by time-resolved photoluminescence." *Semiconductor Science and Technology* 28.2 (2013): 022001.

[39] Chine, Z., et al. "Photoreflectance and photoluminescence study of annealing effects on GaAsBi layers grown by metalorganic vapor phase epitaxy." *Semiconductor Science and Technology* 25.6 (2010): 065009.

[40] Kim, H., et al. "Impact of in-situ annealing on dilute-bismide materials and its application to photovoltaics." *Journal of Crystal Growth* 452 (2016): 276-280.

[41] Wood, Adam W., et al. "Annealing-induced precipitate formation behavior in MOVPE-grown $GaAs_{1-x}Bi_x$ explored by atom probe tomography and HAADF-STEM." *Nanotechnology* 28.21 (2017): 215704.]

[42] Tansu, Nelson, and Luke J. Mawst. "Current injection efficiency of InGaAsN quantum-well lasers." *Journal of applied physics* 97.5 (2005): 054502.

[43] Fuyuki, Takuma, et al. "Electrically pumped room-temperature operation of GaAs1− xBix laser diodes with low-temperature dependence of oscillation wavelength." *Applied Physics Express* 7.8 (2014): 082101.

[44] Klopf, F., J. P. Reithmaier, and A. Forchel. "Highly efficient GaInAs/(Al) GaAs quantum-dot lasers based on a single active layer versus 980 nm high-power quantum-well lasers." *Applied Physics Letters* 77.10 (2000): 1419-1421.

[45] Buckers, Christina, et al. "Microscopic modeling of quantum well gain media for VECSEL applications." *IEEE Journal of Selected Topics in Quantum Electronics* 15.3 (2009): 984-992.

[46] Yoshida, Junichi, et al. "Temperature dependence of $GaAs_{1-x}Bi_x$ band gap studied by photoreflectance spectroscopy." *Japanese journal of applied physics* 42.2R (2003): 371.

[47] Fujii, H., Toprasertpong, K., Wang, Y., Watanabe, K., Sugiyama, M. and Nakano, Y., 2014. 100-period, 1.23-eV bandgap InGaAs/GaAsP quantum wells for high-efficiency GaAs solar cells: toward current-matched Ge-based tandem cells. *Progress in Photovoltaics: Research and Applications*, *22*(7), pp.784-795.

[48] Yu, Haiping, Christine Roberts, and Ray Murray. "Influence of indium segregation on the emission from InGaAs/GaAs quantum wells." *Applied physics letters* 66.17 (1995): 2253-2255..

[49] Dussaigne, A., et al. "In surface segregation in InGaN/GaN quantum wells." *Journal of crystal growth* 251.1-4 (2003): 471-475.

[50] Smowton, Peter Michael, and Peter Blood. "Fermi level pinning and differential efficiency in GaInP quantum well laser diodes." *Applied physics letters* 70.9 (1997): 1073-1075.

[51] Wang, J., Smith, B., Xie, X., Wang, X. and Burnham, G.T., “High-efficiency diode lasers at high output power”. *Applied physics letters*, 1999, *74*(11), pp.1525-1527

[52] Marko, Igor P., et al. "Optical gain in GaAsBi/GaAs quantum well diode lasers." *Scientific reports* 6 (2016): 28863.

[53] Buda, M., Hay, J., Tan, H.H., Wong-Leung, J. and Jagadish, C., “Low loss, thin p-clad 980-nm InGaAs semiconductor laser diodes with an asymmetric structure design”. *IEEE journal of quantum electronics*, 2003, *39*(5), pp.625-633

[54] Asryan, L.V. and Luryi, S., ”Effect of internal optical loss on threshold characteristics of semiconductor lasers with a quantum-confined active region", *IEEE journal of quantum electronics*, 2004, *40*(7), pp.833-843.

[55] D. Z. Garbuzov, A. V. Ovchinnikov, N. A. Pikhtin, Z. N. Sokolova,I. S. Tarasov, and V. B. Khalfin, “Experimental and theoretical investigations of singularities of the threshold and power characteristics of InGaAsP/InP separate-confinement double-heterostructure lasers (λ=1.3μm), ”Sov. Phys. Semicond., 1991vol. 25, no. 5, pp. 560–564

[56] Tansu, Nelson, and Luke J. Mawst. "Temperature sensitivity of 1300-nm InGaAsN quantum-well lasers." *IEEE Photonics Technology Letters* 14.8 (2002): 1052-1054..

[57] Tansu, Nelson, and Luke J. Mawst. "Low-threshold strain-compensated InGaAs (λ= 1.19-1.31 μm) quantum-well lasers." *IEEE Photonics Technology Letters* 14.4 (2002): 444-446..

[58] Hayakawa, T., Wada, M., Yamanaka, F., Asano, H., Kuniyasu, T., Ohgoh, T. and Fukunaga, T., “Effects of broad-waveguide structure in 0.8 μm high-power InGaAsP/InGaP/AlGaAs lasers” *Applied physics letters*, 1999, *75*(13), pp.1839-1841.

[59] Marko, Igor P., and Stephen J. Sweeney. "Progress toward III–V bismide alloys for near-and midinfrared laser diodes." *IEEE Journal of Selected Topics in Quantum Electronics* 23.6 (2017): 1-12.

Chapter 5. Patterned QD Active Region Laser Diodes

5. 1. Introduction

Semiconductor laser diodes (LD) employing quantum dot (QD) active regions have attracted attention due to the theoretical predictions: ultra-low threshold current density and low device temperature sensitivity originated from the delta-function-like density of states and small active volume [1, 2]. However, while high performance devices have been realized employing QD active regions formed by self-assembly under the Stranski-Krastanov (SK) growth mode, the realization of all the predicted advantages of ideal QDs has remained challenging. Key successes of SK QD lasers include ultra-low threshold current density diode lasers extending the emission into the 1.3μm wavelength region [3-8] on GaAs substrates or 1.55 μm wavelength region [9-12] on InP substrates. The self-assembly growth mode requires a highly compressively strained material and careful optimization of growth interruptions to minimize the randomness of the QD size and distribution. For many commonly used material systems, such as compressively strained InGaAs QDs on GaAs or InP, SK QD formation leads to an inherent wetting layer formation [13], which has been identified as an underlying cause for the low optical gain and high temperature sensitivity in the LD as a result of the thermally activated carrier leakage out of the QDs into the wetting layers [14-16]. Also, the large and typically bi-modal distribution in the QD sizes leads to a large inhomogeneous broadening in the optical gain spectrum [17]. By contrast, nanopatterning and selective area epitaxy (SAE) offer a more controllable pathway for QD formation, allowing the QD size to be decoupled from the strain state of the material, leading to the formation of wetting layer-free QDs (i.e. full three-dimensional nano-confinement). To date, various methods have been successfully employed to fabricate such wetting layer-free semiconductor based nanostructures, including interferometric optical lithography [18], x-ray lithography [19], atomic force microscopy based lithography [20], electron beam lithography [21-25], scanning tunnelling microscopy (STM) [25] and self-organized anodic aluminium oxide membranes [26]. Among these techniques, the LDs employing the QDs formed by e-beam lithography have successfully demonstrated low threshold current density lasing at room temperature although the QD sizes were relatively large (~100nm) [21]. Also, while electron beam lithography allows for precise control over the location and geometry of the nano-patterns, the lengthy fabrication time makes it less desirable for high-volume, large-scale device application. Challenges also remain for the other nanopatterning techniques such as enhancing resolution, reducing processing time and simplifying processes for reduced cost in semiconductor device applications. An alternate approach to the QD formation by nanopatterning is the utilization of block copolymers combined with SAE by MOVPE. Fabrication of various nanostructures using block copolymer thin films has been studied and is known as block copolymer lithography [27-32]. Periodic dense arrays of a nanosized hole pattern can be achieved using cylinder-forming block copolymers with a high degree of pore-size uniformity through spin-coating processes and pattern transfer procedures, which is applicable to large areas at low cost [31]. In prior studies, very uniform GaAs and InAs arrays with densities as high as ~10^{11} cm^{-2} have been demonstrated by BCP lithography and SAE [31-33]. In addition, lasing at low temperature (~20K) with relatively high threshold hold current density (~1.94kA/cm^2) from the highly dense InGaAsP(1.15Q) / $In_{0.53}Ga_{0.47}As$ / InGaAsP(1.15Q) (2/2/2 nm) QDs, lattice-matched to the InP substrate, has been demonstrated by employing BCP lithography [32]. However, a continuing challenge for selective QD growth includes reducing process-induced damages at the QD–substrate interface, which can act as non-radiative recombination centers and reduce the radiative efficiency of the QDs [35]. The prior studies indicated *in-situ* HCl etching prior to MOCVD growth of the QDs can result in an improved photoluminescence intensity, but the process was not yet optimized for device fabrication [36]. Here, the impact of *in situ* etching, by CBr_4 prior to the QD growth on either GaAs or InP substrate, was investigated by utilizing PL measurement and evaluating the laser diode performance. In addition, an $In_{0.1}Ga_{0.9}As$ QW placed near a wetting layer-free InAs QD active region allows for enhanced carrier injection into the QDs, elucidating the potential role of the inherent QW-like wetting layer in the conventional QD active region grown by SK growth mode. Also, a high density $In_{0.8}Ga_{0.2}As$ QD active region ($5{\sim}6 \times 10^{10} cm^{-2}$) laser on InP was demonstrated.

5. 2. Nanopatterning by block copolymer lithography

The diblock copolymer lithography has been a subject of an intensive research for the formation of semiconductor-based nanostructures by utilizing simple spin-on process followed by successive baking and chemical treatment [27-32]. Diblock copolymer lithography is based on the microphase separation of two immiscible polymer blocks A and B covalently bonded at one end. This microphase separation is promoted by thermal annealing at relatively low temperatures above the glass transition temperature of the polymer for an extended period of time. The morphology resulting from this microphase separation is dependent upon the relative chain lengths of the two blocks. Therefore, the different degree of symmetry in the relative chain lengths can lead to the various types of nanopatterns such as spherical, cylindrical, gyroid, and lamellar phase [37]. However, when these diblock copolymers are spin-coated to form a thin film over a large area of a substrate, one polymer block preferentially tends to wet the substrate surface, which results in the alternating polymer layers parallel to the substrate surface, owing to the surface energies. This problem can be avoided by employing a treatment with a random copolymer, called neutral layer, or “brush” layer, which consists of monomers from the two blocks [38]. Therefore, the diblock copolymer lithography on a semiconductor substrate is initiated with the spin-on process of this brush layer.

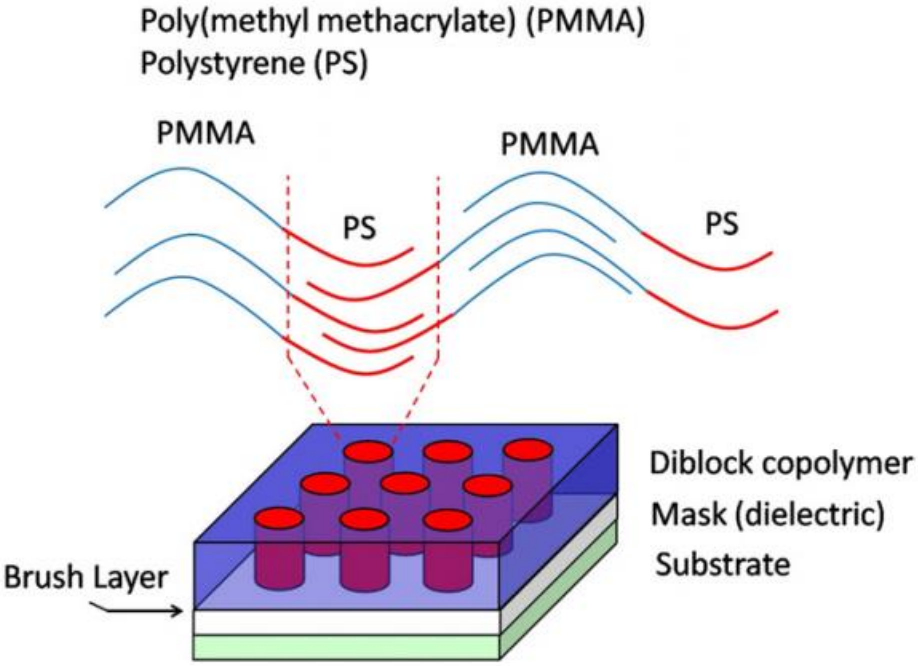

Fig. 5-1 *A schematic representation of a phase separated diblock copolymer film on a semiconductor substrate, forming cylindrical shaped PMMA within the PS matrix (after reference [35])*

Fig. 5-1 shows a schematic diagram illustrating the microphase separation of a diblock copolymer film consisting of cylindrical shaped poly(methyl methacrylate) (PMMA) within polystyrene (PS) matrix, designated as PS-b-PMMA, which was exclusively used for nanopatterning in this chapter. This PS-b-PMMA is spin-coated after the spin-on process for the neutral brush layer (PS-r-PMMA diluted in toluene: styrene fraction of 0.57) followed by the subsequent thermal anneal in a vacuum oven at ~160°C. Then, the spin-coated PS-b-PMMA is again annealed at 220°C for ~4 hours, whose morphology resulting from the microphase separation is shown in Fig. 5-2 (a). By selectively removing one of the blocks of the diblock copolymer, the morphology of this diblock copolymer is practically utilized as a mask for the formation of nanostructures on the underlying semiconductor. This can be realized by exposing the PS-b-PMMA polymer thin film using ultraviolet (UV)-irradiation, as shown in Fig. 5-2 (b), and then selectively removing the PMMA through chemical etching by acetic acid.

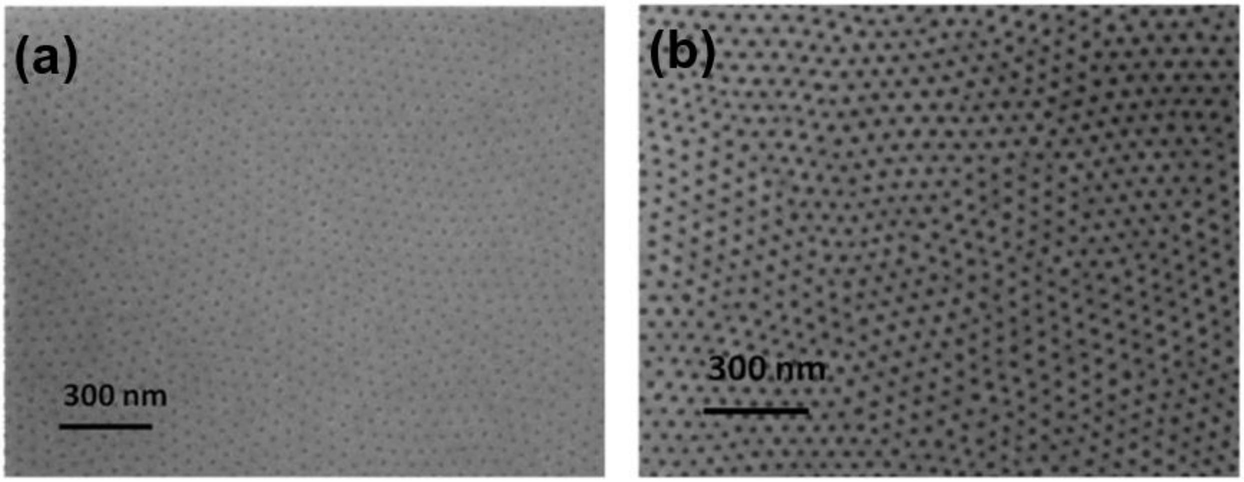

Fig. 5-2 *Top-view SEM images of PS-b-PMMA cylinder-forming diblock copolymer prepared on SiO2/GaAs (a) post-thermal anneal and (b) after UV-irradiation (after reference [35])*

UV exposure on the whole area degrades the PMMA block by breaking the polymer chains and cross-links the PS at the same time. The PMMA block composing the cylindrical domains can be removed by the UV irradiation (wavelength 254 nm, 1 J cm^{-2}) and acetic acid development. After removing the UV-exposed PMMA block, the remaining PS forms the patterned template. The removal of the PMMA block provides a nano-sized hole pattern throughout the entire film thickness, which can then be transferred into the underlying dielectric layer using the selective CF_4-based plasma etching by reactive ion etching process. After the pattern transfer, the remaining block copolymer mask on the dielectric film can be entirely removed by O_2 plasma. Finally, HCl or NH_4OH-based solutions are used to remove any native oxide and plasma damage on the substrate surface of the bottom of the hole. After these wet chemical treatments, the selective area epitaxy of semiconductor material within the holes is carried out by MOVPE process.

5. 3. $In_{0.3}Ga_{0.7}As$ QD active region on GaAs substrate with *in situ* etching by CBr_4

5. 3. 1. Establishment of optimal *in situ* etching condition

The crystal growth was carried out at 100 torr in a 3x2” close-coupled showerhead MOVPE reactor using the conventional precursors including trimethyl indium (TMIn), trimethyl gallium (TMGa), trimethyl aluminium (TMAl) and AsH_3, with purified H_2 as a carrier gas. Growth rates and *in-situ* etching rates were established on planar layers prior to QD studies. For the *in-situ* etching, CBr_4 was used under the arsine and hydrogen ambience. Although the *in-situ* etching of III-V semiconductors using CBr_4 has been reported by Arakawa *et al* [39], studies are needed regarding the application of such *in-situ* etching processes for the semiconductor nanostructure regrowth. Therefore, an optimum *in-situ* etching condition, which yields a controllable etching rate applicable for the nanostructure regrowth, was established from planar structures, consisting of $Al_{0.4}Ga_{0.6}As$ and GaAs layers grown on a GaAs substrate, by employing real-time optical reflectance monitoring by Laytec’s EpiTT™. *in situ* monitoring of the GaAs etch rate by CBr_4 has been accomplished by using a monitor wafer where $Al_{0.4}Ga_{0.6}As$ and GaAs layers were grown, and the optical reflectance from the wavelength of 633nm. The large difference in refractive index of $Al_{0.4}Ga_{0.6}As$ and GaAs provides for a measurable optical reflectance signal that can be used to determine the GaAs etch rate in near real time.

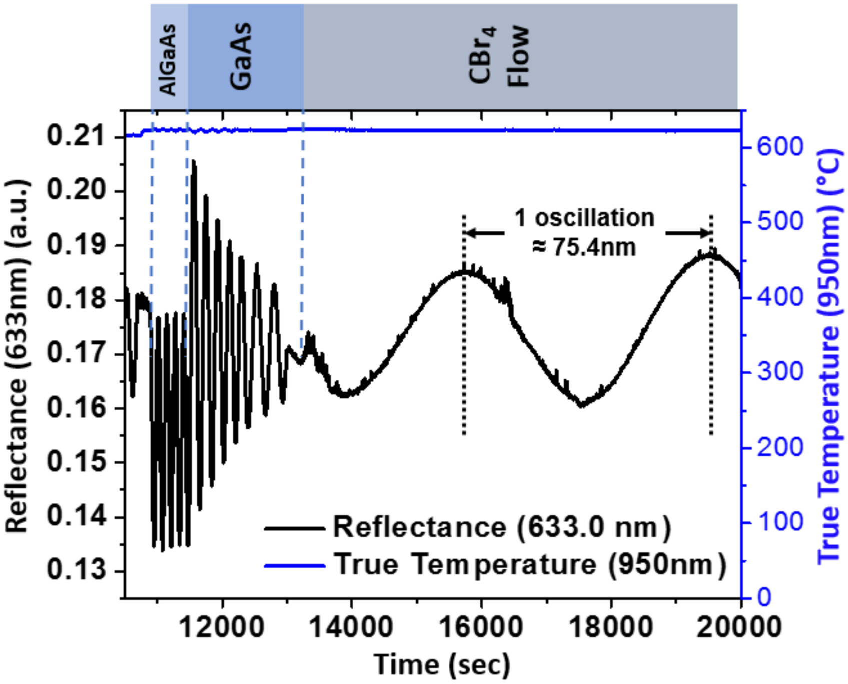

Fig. 5-3 *in situ optical reflectance showing* $Al_{0.4}Ga_{0.6}As$ *and GaAs growths and in situ etching with* CBr_4*. The etching rate was determined to be 0.33Å/sec.*

To illustrate the *in situ* optical reflectance monitoring technique, Fig. 5-3 shows the optical reflectance of $Al_{0.4}Ga_{0.6}As$ and GaAs growths on the monitor wafer followed by the *in situ* etching with CBr_4. For evaluation, at least one complete period of the optical reflectance signal was used to fit and determine the *in situ* etching rate, as discussed in Chapter 2. The *in situ* etching condition is summarized in the Table 5-1.

Table 5-1. Established in-situ etching condition used for the QD growth

Reactor Pressure (Torr)	**Carrier Gas (slm)**	**CBr_4 (µmol/min)**	**AsH_3 (µmol/min)**	**Etch Rate (Å/sec)**
100	**8.4**	**3.3**	**1800**	**0.33**

5. 3. 2. Impact of *in situ* etching on the luminescence properties of $In_{0.3}Ga_{0.7}As$ QDs

The impact of *in situ* etching on the luminescence properties were investigated by either photoluminescence measurement at room temperature (RT-PL) or by the characterization of the laser diodes employing the $In_{0.3}Ga_{0.7}As$ QD active region. First, for the evaluation of the effect of *in situ* etching on the RT-PL, the samples employing $In_{0.3}Ga_{0.7}As$ QDs were prepared as schematically shown in Fig. 5-4. For systematic comparison study, the pre-determined *in situ* etching condition was applied prior to the growth of $In_{0.3}Ga_{0.7}As$ QDs for 0, 30, 60, 90, and 120 sec, respectively.

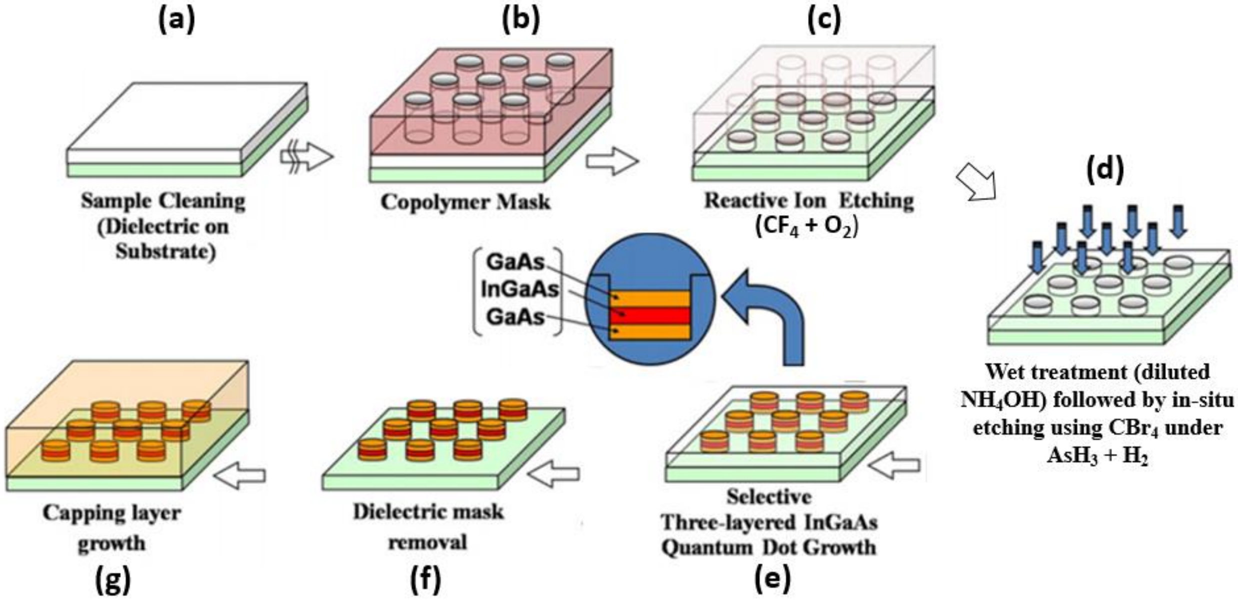

Fig. 5-4 *Schematic representation of the diblock copolymer lithography and transfer to a dielectric mask for the subsequent growth of the QDs; (a) Sample cleaning and PECVD SiNx deposition; (b) BCP lithography; (c) RIE to transfer the nanopattern from BCP to* SiN_x *using* CF_4 *plasma and subsequent BCP removal by* O_2 *plasma; (d) wet treatment and in-situ* CBr_4 *etching; (e) SAE in the MOVPE reactor; (f)* SiN_x *removal by the 6:1 BOE; (g) Capping layer regrowth by MOVPE*

Then, GaAs/$In_{0.3}Ga_{0.7}As$/GaAs (3/3/3nm) layered QDs were selectively grown. The 200nm thick GaAs buffer layer was grown on semi-insulating nominally singular (001) GaAs substrate in order to achieve an atomically abrupt and flat surface. Then, 20nm-thick SiN_x was deposited by plasma-enhanced chemical vapor deposition (PECVD). After the SiN_x deposition, BCP lithography was carried out, utilizing cylinder-forming PS-*b*-PMMA (PS: Polystyrene, PMMA: Poly (methyl methacrylate)), as described in the previous section. The nanopatterns formed by BCP lithography was transferred into the underlying SiN_x layer using CF_4 plasma by RIE process to etch the underlying SiN_x. The remaining PS was completely removed by an O_2 plasma. Prior to loading the sample into the MOVPE reactor for *in situ* etching and QD regrowth, a brief wet treatment using NH_4OH:DI = 1:10 mixture (in volume ratio) was carried out for 20 sec to remove the native oxide as well as any remaining organic contaminations. After loading the sample in the MOVPE reactor, the temperature was ramped up to 625℃ under AsH_3, *in-situ* etching using CBr_4 was carried out under AsH_3 for various times based on the pre-determined *in-situ* etching condition. Then, the temperature was ramped down to 580℃, and GaAs/$In_{0.3}Ga_{0.7}As$/GaAs (3/4/3nm) layered QDs were selectively grown on the SiN_x template. After the growth of the QDs, the samples were taken out of the MOVPE reactor and SiN_x template was removed by the 6:1 buffered oxide etchant. After the removal of SiNx hardmask, QDs were imaged using a LEO 1550 VP (JEOL) field-emission scanning electron microscope (SEM), in order to investigate the effect of the *in-situ* etching on the morphology of the QDs.

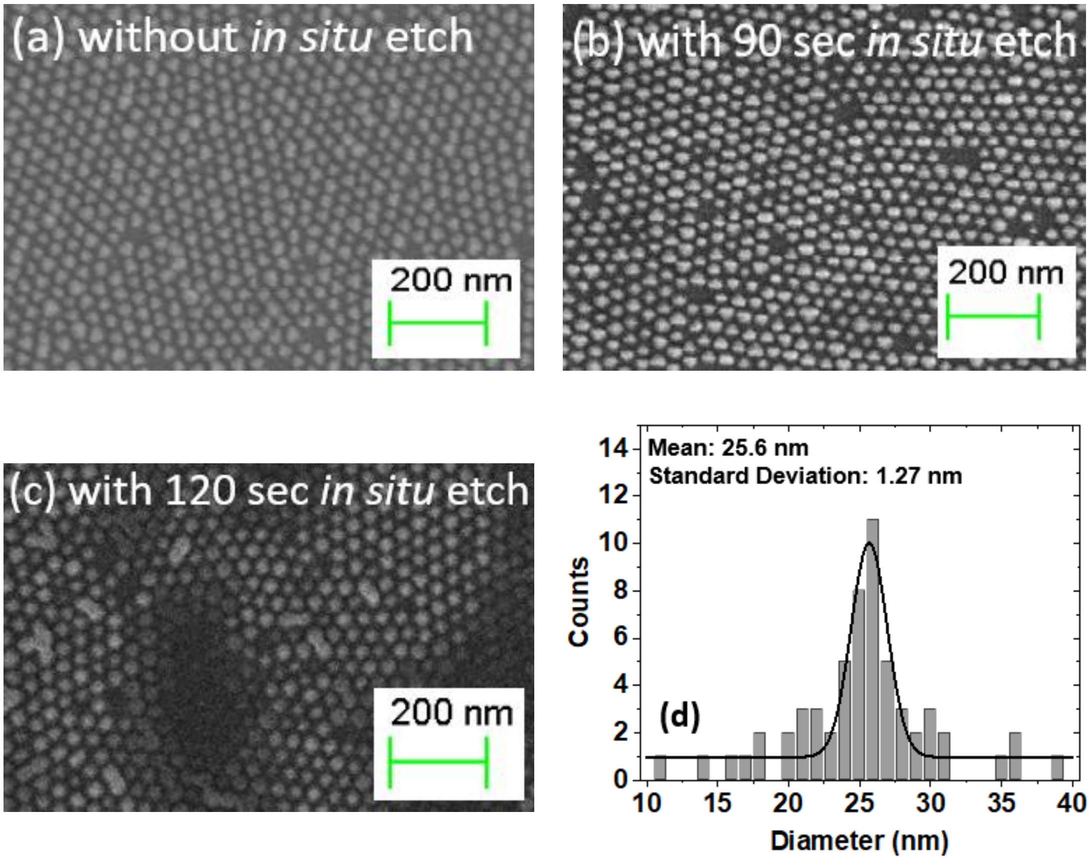

Fig. 5-5 *Top view SEM images of the QDs after SiNx hardmask removal; (a) without CBr4 in situ etching; (b) with 90sec of CBr4 in situ etching (~3nm of etching); (c) with 120sec of CBr4 in situ etching (~4nm of etching), (d) QD size distribution for the sample grown after 90sec of* CBr_4 *in situ etching*

Fig. 5-5 shows the top view SEM images of the QDs taken after SiN_x hardmask removal, which were subjected to different *in situ* etching times. It was observed that when the etching time exceeds 120sec, significant undercutting and etch pits were formed under the SiN_x hardmask, resulting in the large non-uniformity in the QD sizes. Also, shown in Figure 5-5 (d) is the QD size distribution taken from the QDs grown after 90 sec of *in situ* etching within a limited area $(400 \times 400nm^2)$ where the distribution is fitted in normal distribution with a mean value of 25.6

nm and the standard deviation of 1.27 nm. In addition, Also the areal QD density was estimated to be near $8 \times 10^{10} cm^{-2}$. The measured QD size distribution indicates uniform QDs in size can be successfully grown on the SiNx template defined by the BCP lithography and with CBr$_4$ *in situ* etching treatment.

Room Temperature PL (RT-PL) measurements were performed after growing 200nm-thick GaAs capping layer on the In$_{0.3}$Ga$_{0.7}$As QDs with varying *in situ* etching time, using the frequency doubled continuous wave Nd:YAG laser at the excitation wavelength of 532nm, 300g/mm grating monochromator, and cooled InGaAs detector.

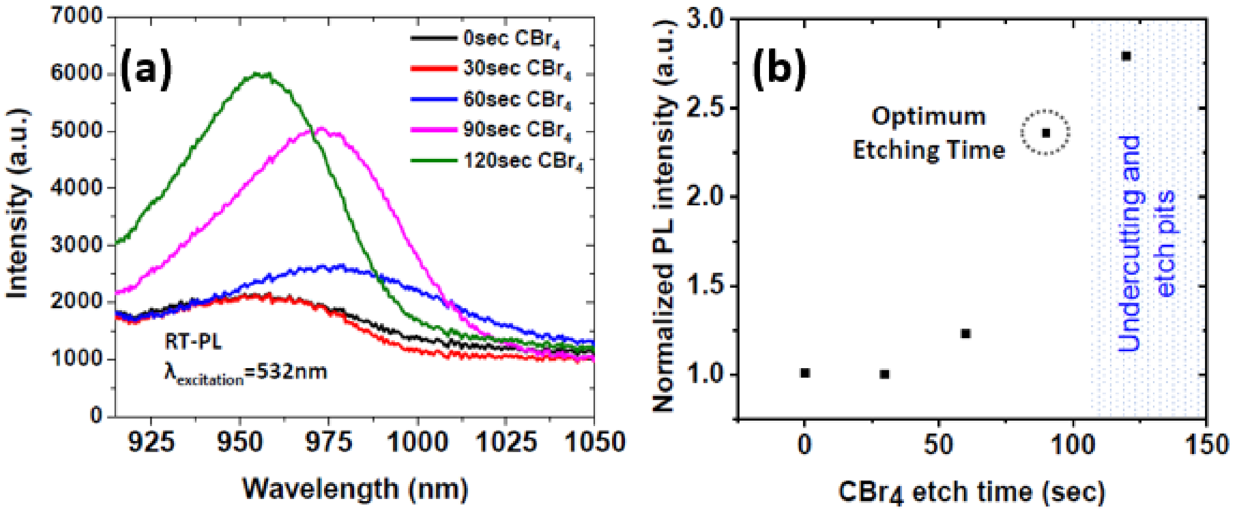

Fig. 5-6 *(a) RT-PL Spectrum; (b) Variation in the RT-PL intensities normalized by the intensity from the QD without in situ etching as a function of in situ etching time*

As shown in the Figure 5-6 (a), the RT-PL measurements from the QDs that underwent various *in situ* etching time indicates significant increase in the radiative efficiency, evidenced by the change in the PL intensity, as a longer etching time is employed. This significant increase in the PL intensity suggests that the *in situ* etching employing CBr$_4$ can be effective removing the non-radiative defects introduced during the sample preparation. However, as observed by the top view SEMs in Fig. 5-5, there exists a window of *in situ* etching, in which no apparent undercutting and etch pits are formed while maintaining the improved luminescence. Therefore, 90sec of *in situ* etching, under the condition summarized in Table 5-1, was chosen as an optimal condition for the device study. On the other hand, a relatively broad full width at half maximum (FWHM) in the PL spectrum, as large as 93meV, was also observed, suggesting the presence of inhomogeneous broadening on the nanopatterned QDs even though narrow distribution in QD diameter was achieved (Fig. 5-5 (d)). Therefore, this inhomogeneous broadening in the emission linewidth was correlated to both the QD height distribution investigated by atomic force microscopy measurement and the simulated emission wavelength by NEXTNANO^3 software package shown in Fig. 5-7, assuming a square-shaped quantum box geometry for simplicity.

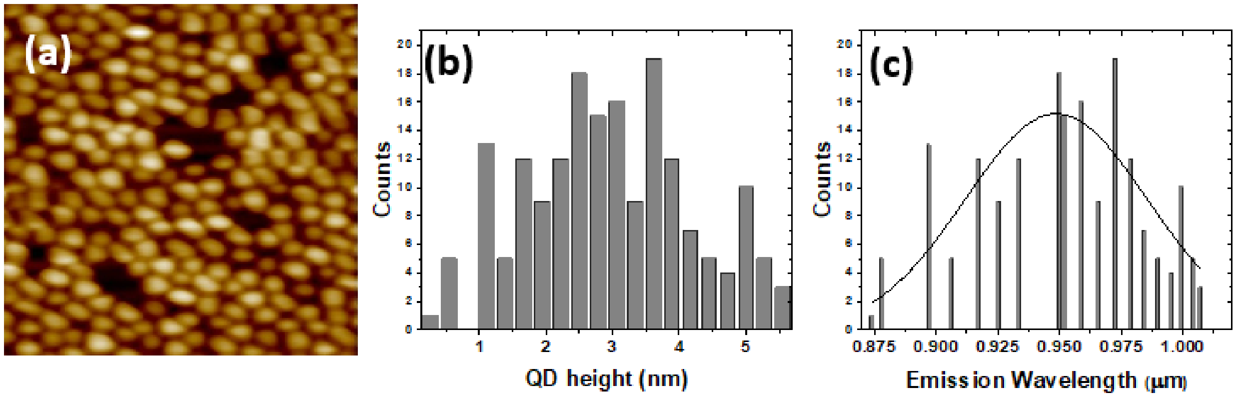

Fig. 5-7 *(a)* $500 \times 500nm^2$*Atomic force microscopic image; (b) Estimated* $In_{0.3}Ga_{0.7}As$ *QD height distribution from AFM measurement; and (c) simulated emission wavelengths from the QD height distribution from AFM measurements*

The distribution of the simulated emission wavelengths and the subsequent fitting to the normal distribution, shown in Fig. 5-7 (c), reveals a good correlation with the measured FWHM in the PL measurement (100meV by simulation vs. 93meV by PL measurement). This inhomogeneous broadening is believed to be originating from the variation of the SiN_x opening size, which, in turn, results in the local variation of the growth rate in each opening by the growth rate enhancement in the selective area epitaxy. Therefore, this result suggests a further optimization in the pattern transfer process is necessary in order to achieve a narrow emission linewidth

After finding optimized *in-situ* etching time at the fixed CBr_4/AsH_3 and temperature, two sets of LD structures employing a QD active region have been grown, as schematically shown in Fig. 5-8, with the growth parameters summarized in Table 5-2.

.

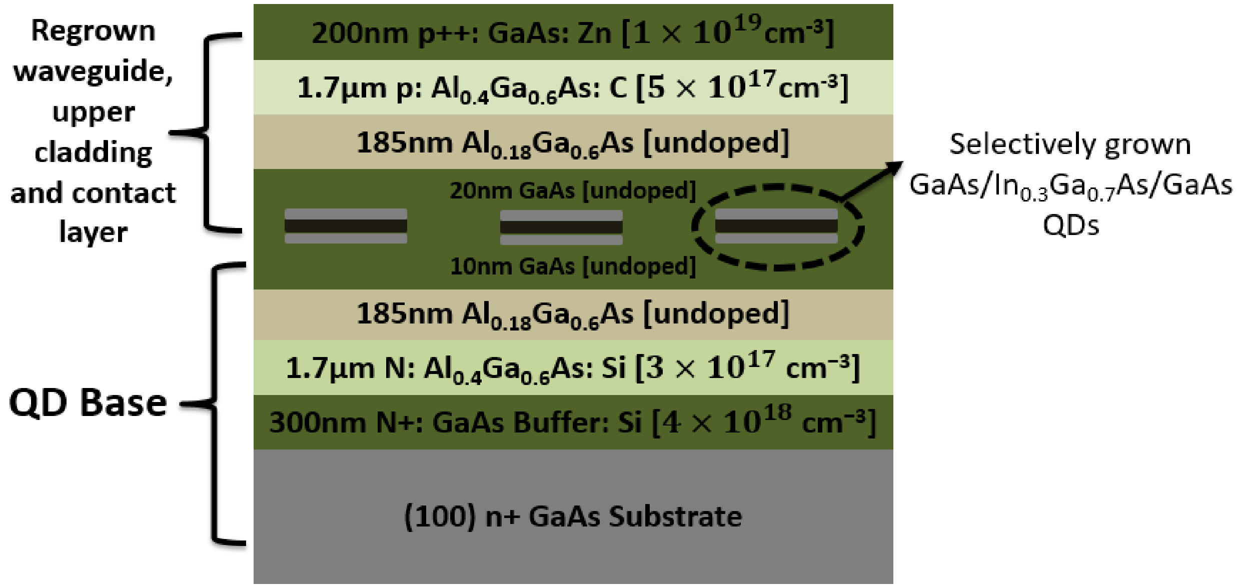

Fig. 5-8 *Structure details of the complete LD device employing QD active region. The lower device layers, indicated as "QD Base", were grown at 700*℃ *while the upper device layers over the QDs were grown at 625*℃*.*

Table 5-2. Growth Parameters used for the complete LD structure

Material	**Growth Temp. [℃]**	**TMGa [μmol/min]**	**Total III [μmol/min]**	**V/III Ratio**
n- GaAs buffer	700	55	55	70
$Al_yGa_{1-y}As$ (Lower part, y=0.18 or 0.4)	700	55	66 or 88	44 or 58
GaAs	580	55	41	76
$Al_yGa_{1-y}As$ (Upper part, , y=0.18 or 0.4)	625	55	66 or 88	44 or 58
p^{++} GaAs cap	625	55	55	35

Fig. 5-8 shows the complete LD structure investigated in this study. Diethyl zinc (DEZn) and CBr_4 were used for p-doping in GaAs and $Al_{0.4}Ga_{0.6}As$, respectively, while Si_2H_6 was used for the n-doping in GaAs and $Al_{0.4}Ga_{0.6}As$ layers. As a control sample, Dev A underwent 15sec of *in situ* etching (etching depth: ~0.5nm), while the optimized sample, Dev B, have gone through 90sec of *in situ* etching (etching depth: ~3nm). The specific details of both samples are summarized in Table 5-3.

Table 5-3. in-situ etching condition used for the QD growth

Sample	***in situ* etching depth**	**x in $In_xGa_{1-x}As$ QD**	**Thickness of $In_xGa_{1-x}As$**
Dev A (unoptimized)	0.5nm	0.3	2.5nm
Dev B (optimized)	3nm	0.3	3.5nm

After the complete laser structure growth, wet etching using H_3PO_4:H_2O_2:H_2O = 3:1:20 was carried out to form the etched ridge waveguide structure, using a patterned photoresist mask. 200nm-thick SiN_x was deposited by plasma-enhanced chemical vapor deposition for the electrical passivation. The wafer was subsequently thinned down to 150μm. Contact layers consisting of

Ti/Pt/Au (25/50/300nm) were e-beam evaporated on the top surface to form the ohmic contact to p+ GaAs. Contact to the n-type region was made to the backside of the wafer using a Ni/AuGe/Ni/Au (5/100/35/200nm) contact metallurgy. The contact metals were alloyed at 400°C for 30 sec using Rapid Thermal Annealing (RTA). Devices were measured *as-cleaved* (*i.e.* no facet coatings) at room temperature and 80K under pulsed current operation. The electroluminescence (EL) data was collected using a grating diffractometer and Si photodetector while the output power from one facet were measured using InGaAs photodiode.

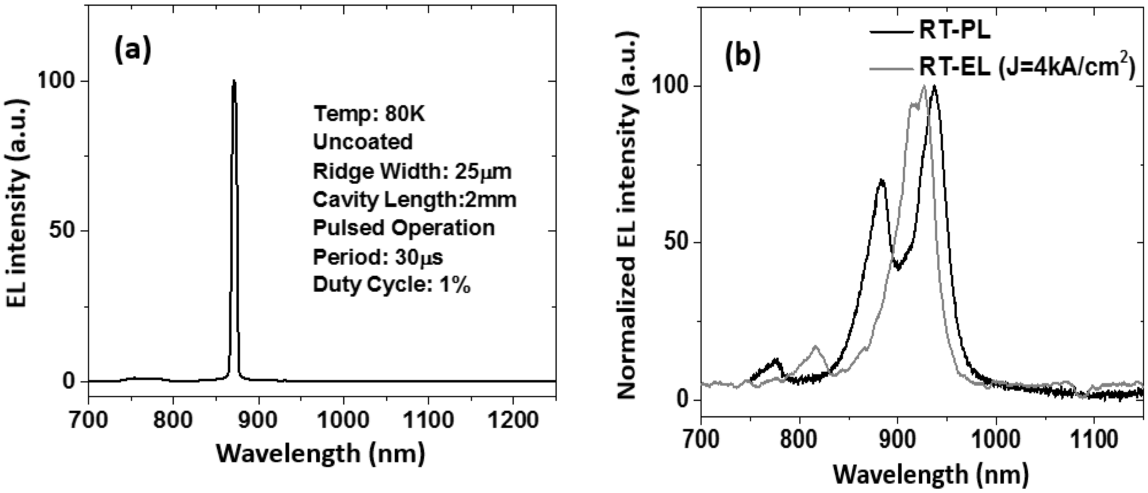

Fig. 5-9 *(a) Spectrum of Dev A at the onset of the lasing; (b) PL and EL measured at RT showing a good correlation*

Fig. 5-9 (a) shows the spectrum of the Dev A at the onset of lasing at 80K at the current drive of 1.8A, which is equivalent to the 3.4 kA/cm^2 in the threshold current density for the cavity length of 2mm. It is worthwhile mentioning that the bandgap energy of GaAs at 80K is 1.507eV (or equivalently 820nm) [40]. Therefore, it can be rationalized that the observed lasing wavelength of 880nm is from the QD emission. Shown in Fig. 5-9 (b) are the PL and EL measured at room temperature showing a good correlation. The FWHM of the PL at RT from this specific QD active region was measured as 52meV, which is less than those (~93meV) shown in Fig. 5-6, presumably owing to the improved uniformity in the SiN_x opening size , but still significantly larger than the reported FWHM value (~30meV) from the SK mode grown QDs by MOVPE [41].

The STEM investigation reveals no extended structural defects within the QD active region of the Dev A over a limited field of view (Fig. 5-10).

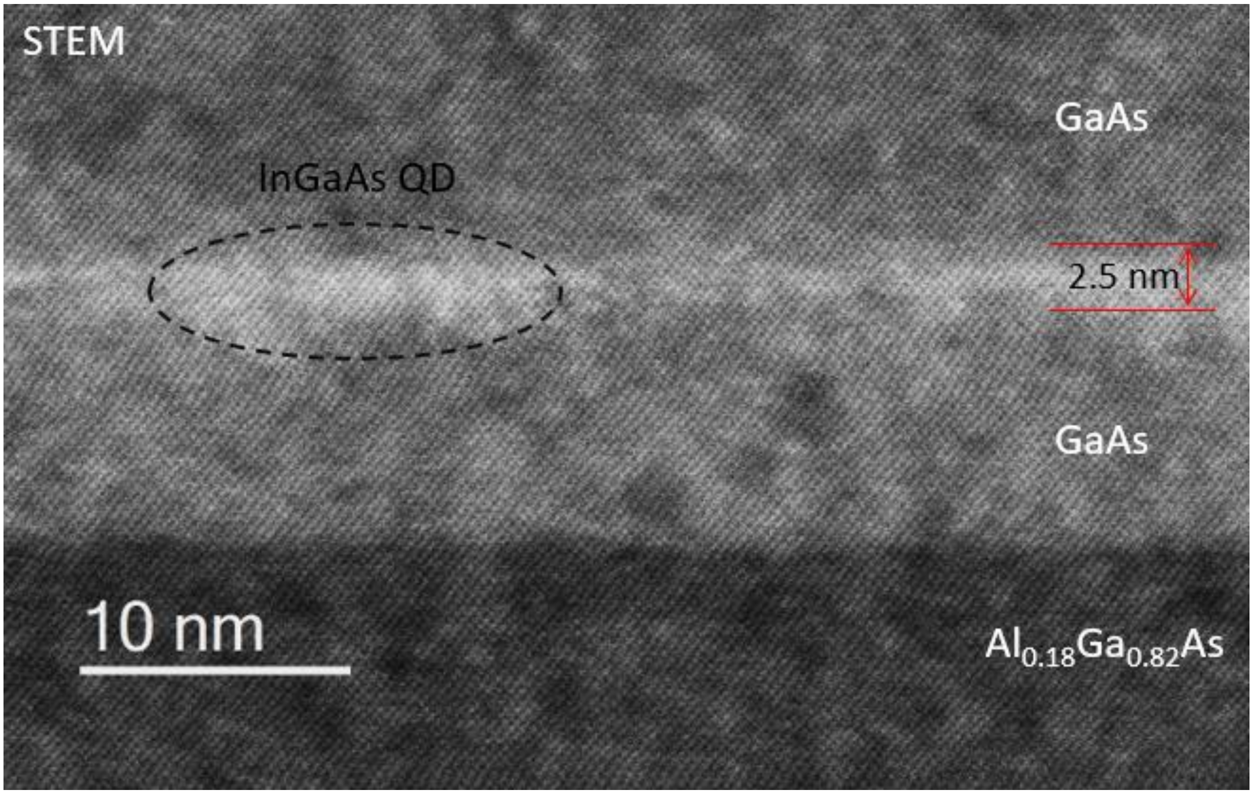

***Fig. 5-10** STEM image showing no extended structural defects within the QD active region of the Dev A over a limited field of view*

By contrast, the Dev B, with *in situ* etching carried out under the optimized condition, exhibits much reduced J_{th} (385A/cm^2 vs. 3.4kA/cm^2 from Dev A) at the same cavity length (L=2mm), indicating the number of the non-radiative recombination centers within the QD active region was significantly reduced compared to that of Dev A (Fig. 5-11 (a)). Also, the threshold current densities (J_{th}) of 1.3, 2 and 3-mm long devices agree well with the expected behaviour, i.e., the higher J_{th} was obtained from the shorter cavity devices due to the higher mirror loss and the relatively low optical gain. However, 5mm long devices show the inconsistency in J_{th}, which is under investigation, although it is possibly a result of non-uniformity in QD density and non-radiative defects.

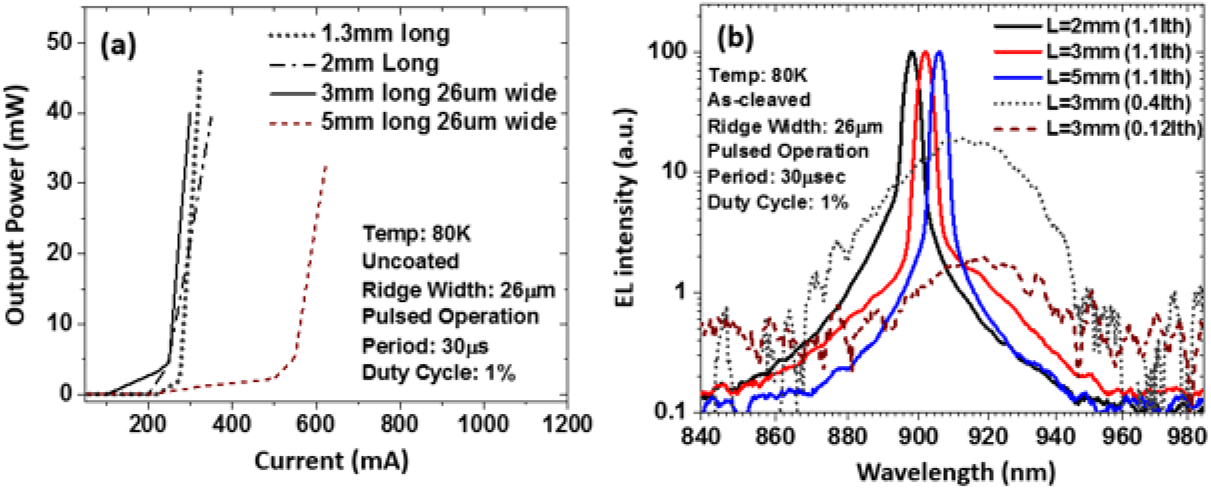

Fig. 5-11 *(a) Current-output power characteristics for various cavity length devices from Dev B; (b) Electroluminescence spectra from various cavity length devices.*

The measured spectrum from devices with different cavity lengths (Fig 5-11 (b)) indicates a spectral peak position shift of the lasing wavelength, most likely due to the state-filling [42]. Also, the spectral difference between the lasing wavelength (λ_{lasing}=902nm at I=1.1I_{th}) and the peak wavelength at low current injection (I=0.12I_{th}) may indicate lasing occurs on a QD excited state transition. On the other hand, at room temperature, the lasing from the $In_{0.3}Ga_{0.7}As$ QDs was not observed as shown in Fig. 5-12, which indicates low optical gain in the QD active region at room temperature as well as gain saturation, although the lasing emission (880nm) from the GaAs surrounding the QDs was observed.

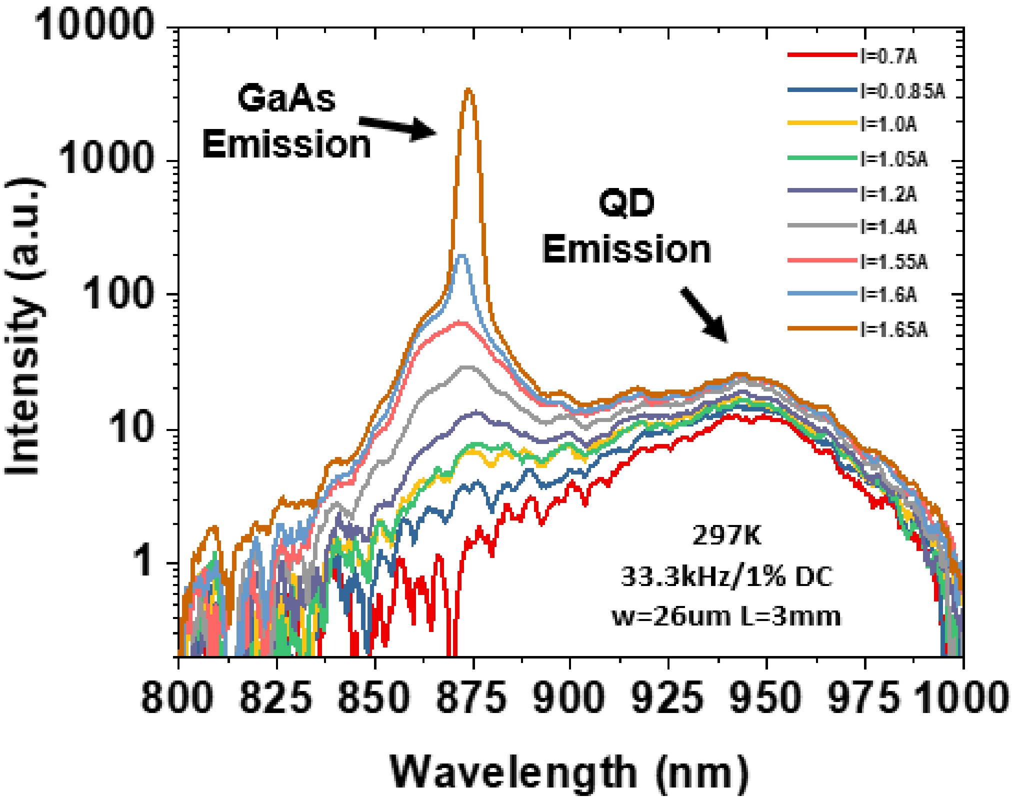

Fig. 5-12 *Electroluminescence spectra at room temperature from Dev B (L_{cav}=3mm)*

This result also implies that it is necessary to improve the carrier capture by dots at room temperature since the lasing emission from the surround GaAs suggests a majority of carriers leak out of the InGaAs QDs. Therefore, in order to enhance the carrier capture by the QDs, the following approaches were employed: SAE of lower bandgap InAs QDs and creating a carrier collecting layer adjacent to the InAs QDs, which will be discussed in the next section.

5. 4. InAs QD active region on GaAs substrate with carrier collecting layer

In the previous section, the use of CBr_4 *in situ* etching prior to the selective area MOVPE of the $In_{0.3}Ga_{0.7}As$ QD growths was shown to reduce the processing-related damage as evidenced by an enhanced luminescent intensity of the grown QDs and an improved device performance at an operating temperature of 80K. In that prior study, a significant degree of carrier leakage at room temperature from the $In_{0.3}Ga_{0.7}As$ QDs as well as poor carrier injection efficiency into the QDs were identified as possible issues that prevented lasing at room temperature. In order to further enhance the carrier collection efficiency by tightening the carrier confinement, i.e., deeper potential profile, InAs QDs was employed and investigated in this section, in contrast to the $In_{0.3}Ga_{0.7}As$ QDs. Furthermore, it is shown that InAs QDs, grown within the nanopatterns defined by the BCP lithography, lead to lasing at room temperature, although their thickness exceeds its critical thickness calculated by the force balance model [43]. It has been shown that dot-in-a-well (DWELL) structures exhibit an improved carrier capture by the QDs [44-45], although the role of inherent wetting layer in the carrier injection has remained vague. Here, we report that an $In_{0.1}Ga_{0.9}As$ QW placed near a wetting layer-free InAs QD active region allows for enhanced carrier injection into the QDs, leading to room temperature (RT) lasing. Further improvement in the fabrication process and design of the carrier collection layer is required to achieve lower threshold current densities.

The epitaxial growth was performed in a 3x2” close-coupled showerhead MOVPE reactor using the conventional metalorganic and hydride sources such as trimethyl indium (TMIn), trimethyl gallium (TMGa), trimethyl aluminium (TMAl), arsine (AsH_3), disilane (Si_2H_6), carbon tetrabromide (CBr_4), and diethylzinc (DEZn), with ultra-pure H_2 as a carrier gas at 100 Torr.

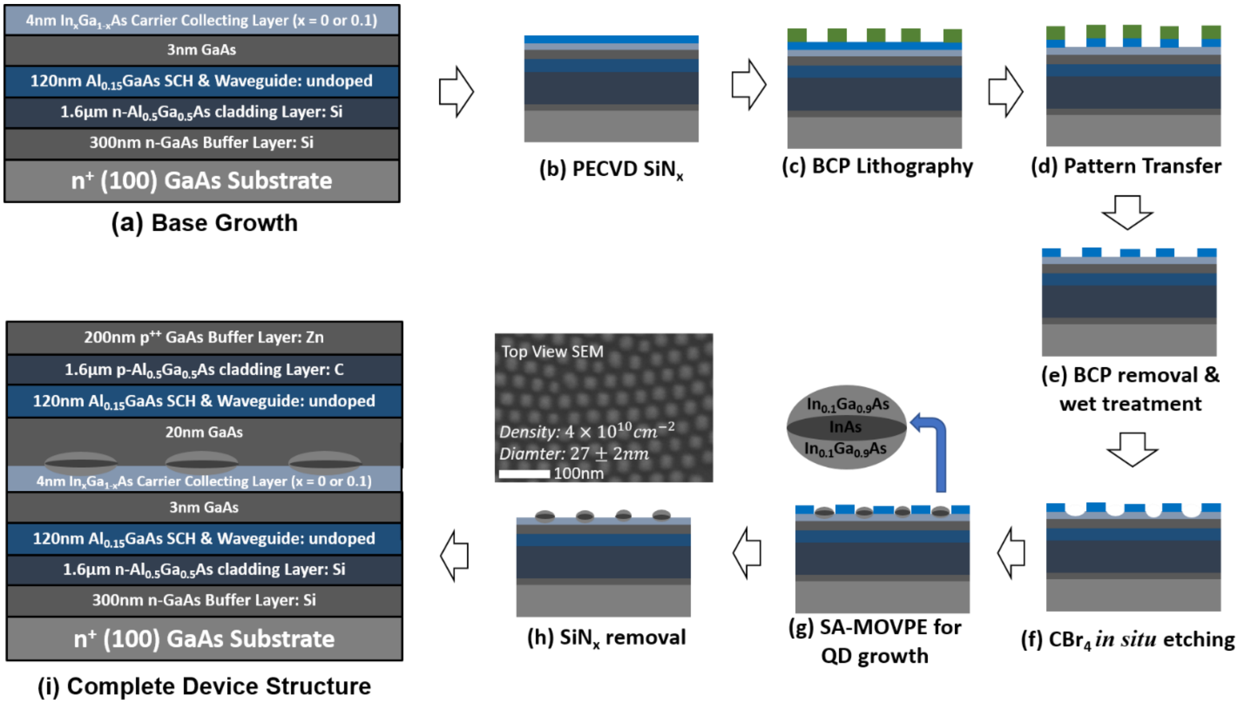

Fig. 5-13 *Schematic representation of the simplified procedure for the QD formation by BCP lithography and subsequent SA-MOVPE of the QD growth for laser active region; (a) Base growth to form lower parts of LD; (b)* SiN_x *deposition by plasma enhanced chemical vapor deposition; (c) Diblock copolymer (BCP) lithography ; (d) pattern transfer onto* SiN_x *'hard' mask by reactive ion etching using* O_2 *and* CF_4 *plasma; (e) BCP removal by* O_2 *plasma and subsequent wet treatment using 1:20 (*$NH_4OH:H_2O$*) solution; (f)* CBr_4 *in situ etching in MOVPE reactor; (g) SA-MOVPE for the growth of InAs QDs; (h)* SiN_x *removal by the 6:1 BOE; (i) Regrowth to complete the LD structure*

The procedure to form the QD active region within a laser structure is schematically presented in Fig. 5-13, using the SiN_x nanopatterns defined by BCP lithography. In order to investigate the effect of the carrier collecting layer, two types of the base structure *with* and *without* an $In_{0.1}Ga_{0.9}As$ QW were grown (Fig. 5-13 (a)). Then, the same pattern transfer process was utilized as described in the previous section. After loading the sample in the MOVPE reactor, the temperature was ramped up to 625℃ under AsH_3 for 3 min, and *in-situ* etching using carbon tetrabromide (CBr_4)

was carried out at the reactor pressure of 100 Torr under AsH_3 and hydrogen (AsH_3 partial pressure of 4.5×10^{-3} Torr) for 70 sec with CBr_4/AsH_3 molar flow ratio of 2.2×10^{-3} (Fig. 5-13 (f)). The temperature was subsequently ramped down to 580℃, and $In_{0.1}Ga_{0.9}As$ / InAs / $In_{0.1}Ga_{0.9}As$ layered QDs were selectively grown on the SiN_x nanopattern (Fig. 5-13(g)). InAs QDs with varying thickness (1.5 ~ 3 nm) were grown by independent growth and process runs on the identical base with $In_{0.1}Ga_{0.9}As$ carrier collecting layer as well, to investigate the influence of the InAs thickness in the device performance. 6:1 buffered oxide etchant was used to remove the SiNx template after the SA-MOVPE of QDs. (Fig. 1(h)). After the removal of SiN_x hard mask, QDs were imaged using a LEO 1550 VP (JEOL) field-emission scanning electron microscope (SEM), which revealed the areal QD density of $\sim 5\times 10^{10} cm^{-2}$ and the average QD diameter of 27 nm. The upper device structures were regrown at the growth temperature of 625℃ and the pressure of 100 Torr., after immediately transferring the sample into the MOVPE reactor (Fig. 5-13 (i)). Table 1 summarizes the growth condition for each layer.

Table 5-4. Growth Parameters used for the complete LD structure employing InAs QDs

Material	**Growth Temp. [℃]**	**TMGa [μmol/min]**	**Total III [μmol/min]**	**V/III Ratio**
n- GaAs buffer	700	55	55	70
$Al_yGa_{1-y}As$ (Lower part, y=0.15 or 0.5)	700	55	66 or 81	55 or 68
$In_xGa_{1-x}As$ (x=0.1 or 1)	580	0 or 27	8.2 or 41	76 or 380
$Al_yGa_{1-y}As$ (Upper part, y=0.15 or 0.5)	625	55	66 or 81	55 or 68
p^{++} GaAs cap	625	55	55	35

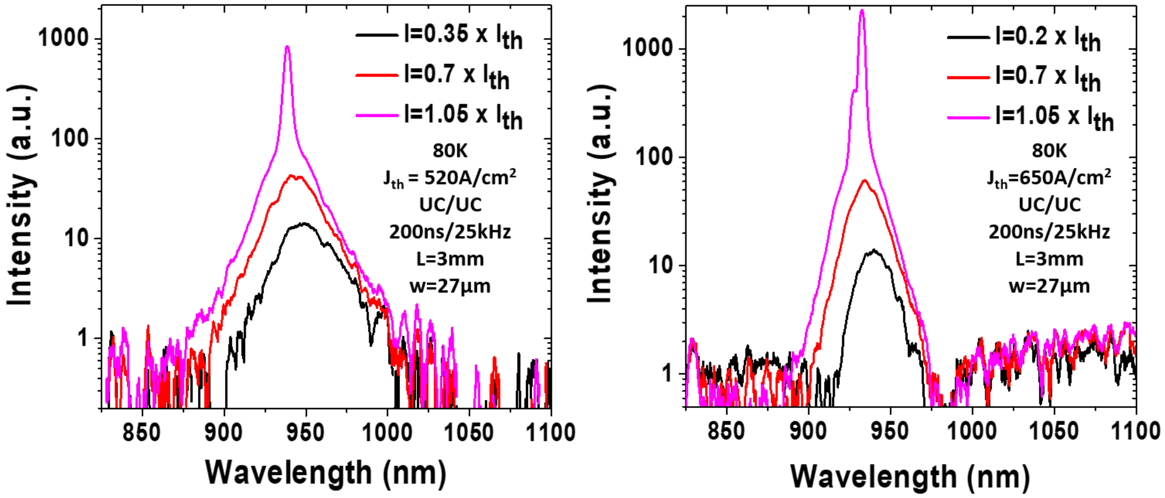

Fig. 5-14 *Electroluminescence spectra at 80K measured from (a) device without* $In_{0.1}Ga_{0.9}As$ *carrier collecting layer adjacent to 2 nm-thick InAs QDs, and (b) device with* $In_{0.1}Ga_{0.9}As$ *carrier collecting layer adjacent to 2 nm-thick InAs QDs*

Fig. 5-14 shows the EL spectra from the devices employing 2 nm thick InAs QD active region grown *with* and *without* the $In_{0.1}Ga_{0.9}As$ carrier collecting layer, respectively at the heat sink temperature of 80K. Lasing was observed from both types of devices at a similar wavelength (~930 nm), indicating the laser transition originates from the QD active region, not from the carrier collecting layer. Even at cryogenic temperature (80K), the observed threshold current densities were rather high, which can be ascribed to the relatively low optical confinement factor originated from a thin InAs QD thickness (~2 nm) together with possibly a high non-radiative defect density, which most likely was not completely eliminated even after the *in situ* etching. By contrast, typical $In_xGa_{1-x}As$ QD thickness employed for high performance QD lasers grown by SK growth mode are ranging from 5 to 10 nm [46 - 48].

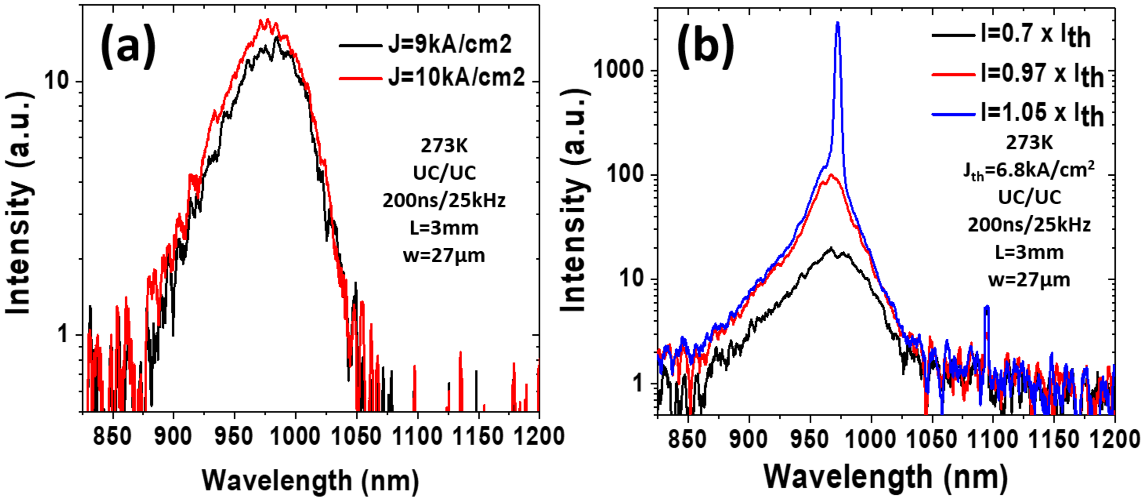

Fig. 5-15 *Electroluminescence spectra at 297K measured from (a) device without In$_{0.1}$Ga$_{0.9}$As carrier collecting layer adjacent to 2nm-thick InAs QDs, and (b) device with In$_{0.1}$Ga$_{0.9}$As carrier collecting layer adjacent to 2nm-thick InAs QDs*

The EL spectra measured at room temperature from both types of devices are shown in Fig. 5-15. While the device without In$_{0.1}$Ga$_{0.9}$As carrier collecting QW, surrounding the 2 nm thick InAs QD, did not lase up to the current limit, the device with the In$_{0.1}$Ga$_{0.9}$As QW showed lasing emission at a threshold current density of 6.8 kA/cm^2. In addition, at high driving current, increment in the current from 9 kA/cm^2 to 10 kA/cm^2, did not result in a substantial increase in the EL intensity for the device without the In$_{0.1}$Ga$_{0.9}$As carrier collecting layer which indicated a poor carrier injection efficiency into the QDs. This result implies that the existence of the carrier collecting layer adjacent to the QDs within the active region leads to improved carrier capture by the QDs and an enhanced optical gain, near room temperature. It is also noteworthy that a shoulder spectral peak near the lasing peak is present at either 80K or 293K (λ_{lasing}=930 nm at 80K and λ_{lasing}=974 nm at 293K) from the device employing the carrier collecting layer, most likely due to higher energy transitions of the electronically coupled QDs with the underlying QW carrier collecting layer.

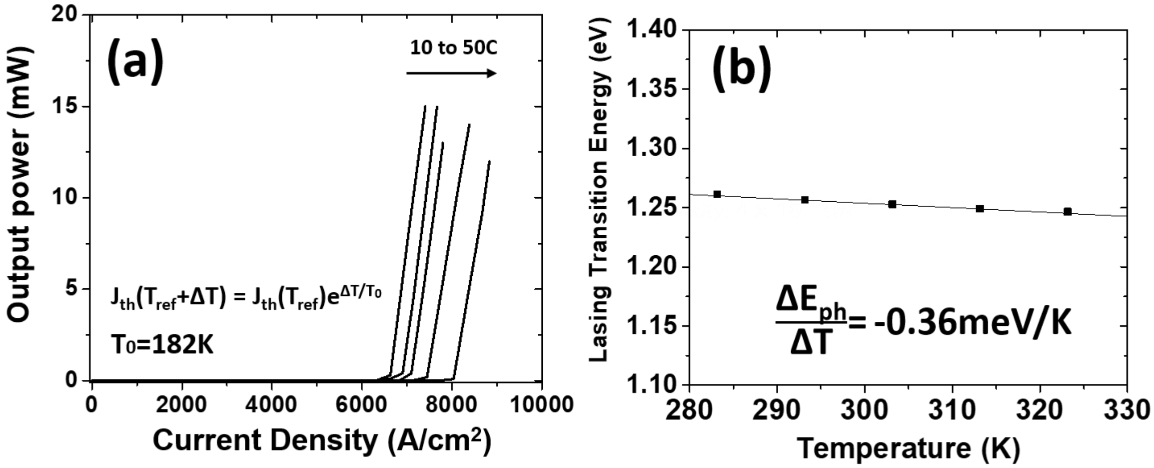

Fig. 5-16 *(a) Output Power vs. injected current density as a function of temperature from the device with* $In_{0.1}Ga_{0.9}As$ *carrier collecting layer adjacent to 2 nm-thick InAs QDs, and (b) The temperature sensitivity in the lasing transition energy*

Characteristic temperatures were measured from the devices employing 2 nm thick InAs with the $In_{0.1}Ga_{0.9}As$ carrier collecting layer around the QDs as shown in Fig. 5-16 (a). The measured T_0 (182K) was greater than the reported T_0 values from undoped InAs QD lasers [49-51], which most likely reflects a high degree of non-radiative recombination, dominating the threshold current density [52]. On the other hand, the measured T_1 (88.5K) was lower than that of conventional high performance strained InGaAs QW lasers operating in this wavelength region [53], which typically exhibit a higher T_1 value than the T_0 by a factor of two or three. This observation also indicates a significant degree of the carrier leakage in the active region [54]. The temperature sensitivity in the lasing transition energy, shown in Fig. 5-16 (b), was measured as -0.36 meV/K, which is lower than the reported value (-0.434 meV/K) from a QW laser emitting a similar wavelength [55], which can be attributed to a relatively flat gain profile of a QD laser [56].

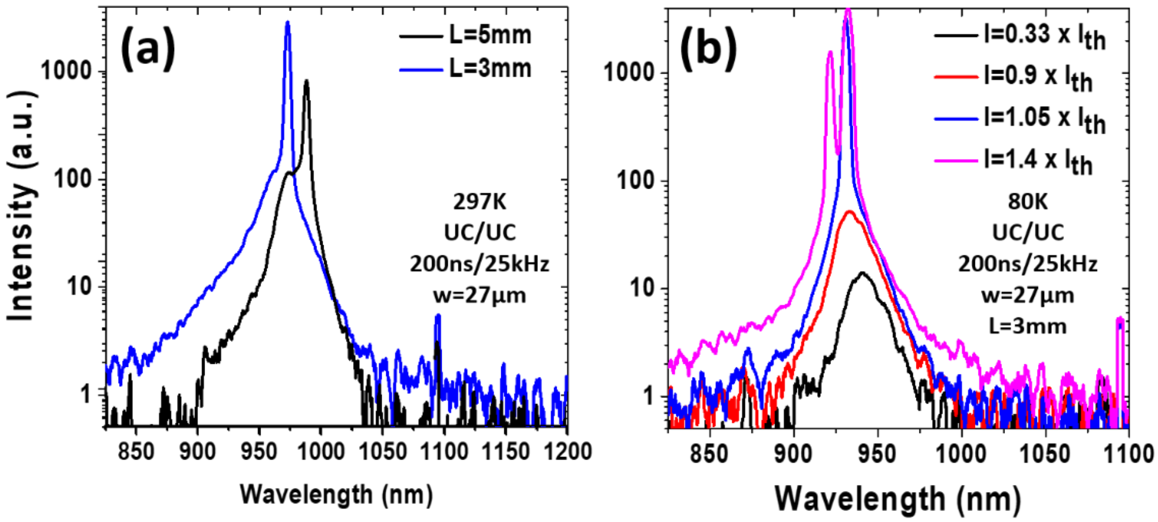

Fig. 5-17 *(a) EL spectrum measured at 297K from different cavity length devices (L=3 and 5mm), (b) EL spectrum measured at 80K as a function of electrical injection.*

A shorter lasing wavelength (974 nm) was observed from the shorter cavity (L=3 mm) lengths, in comparison to that (985 nm) of a longer cavity length (L=5 mm), as shown in Fig. 5-17 (a). This change can be ascribed to a pronounced state-filling of the QD active region [42]. In addition, the occurrence of the lasing emission from a higher energy state, in Fig. 5-17 (b), at a higher driving current and the saturation of the EL intensity from the lowest energy level can possibly be explained by the ground-state gain saturation [58].

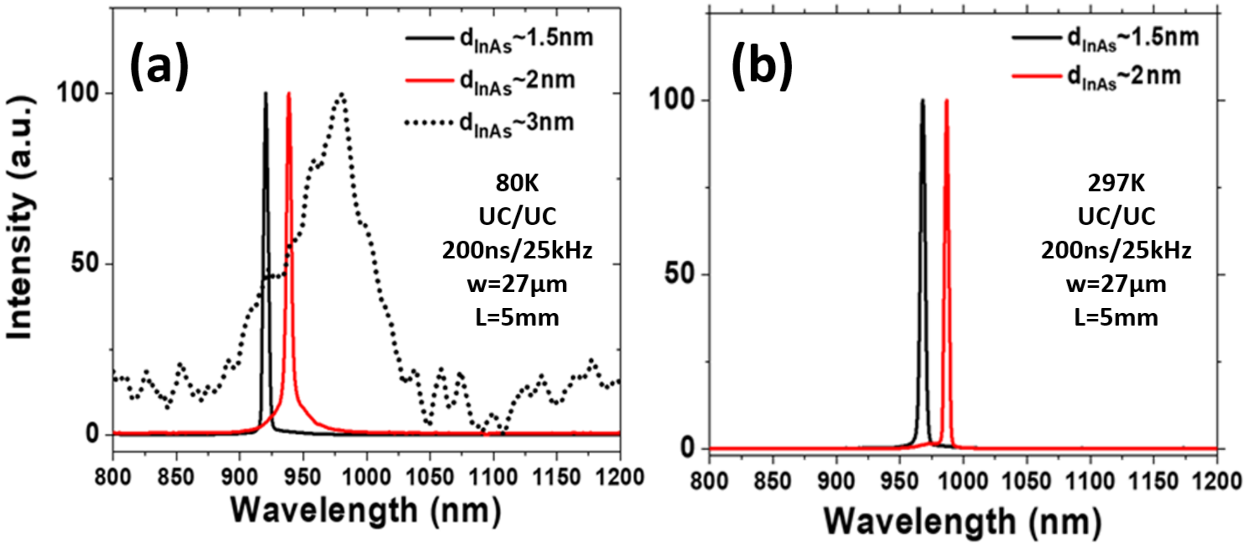

Fig. 5-18 *(a) EL spectrum measured at 80K from devices employing varying InAs QD thickness grown with* $In_{0.1}Ga_{0.9}As$ *carrier collecting layer, (b) EL spectrum measured at 297K from devices employing varying InAs QD thickness grown with* $In_{0.1}Ga_{0.9}As$ *carrier collecting layer*

To study the dependence of QD thickness on device performance, LD devices employing the active regions with various InAs QD thickness from (~1.5 nm to 3 nm) were grown on the base, which employed the $In_{0.1}Ga_{0.9}As$ carrier collecting layer. As shown in Fig. 5-18 (a), laser emission was observed from devices employing ~1.5 nm-thick and ~2 nm-thick InAs QD active region with the emission wavelength of 920nm (J_{th}=1.21 kA/cm^2) and 938nm (J_{th}=0.55 kA/cm^2), respectively, at 80K. The reduced threshold current density observed from the structure with ~2 nm thick-InAs QDs, in comparison with that containing ~1.5 nm-thick QDs, is ascribed to the higher optical confinement factor. In addition, the difference in the lasing emission wavelength reflects the change in the quantum confinement within the QDs resulting from the varying thickness. On the other hand, no lasing was observed from the device employing 3 nm-thick InAs QDs, while a broad spontaneous emission was measured at a high current injection (J~10 kA/cm^2), which is attributed to the onset of the strain relaxation within InAs QDs. The critical thickness of pseudomorphic InAs grown on GaAs substrate is calculated to be ~1 nm by the force balance model [43], which is thinner than the InAs QD thickness employed throughout this study. In practice, this theoretical critical thickness can be increased by kinetically inhibiting strain relaxation, usually by employing a low growth temperature. Nevertheless, we have shown that InAs QDs, grown within the nanopatterns, results in lasing at room temperature, even if their thickness exceeds its critical thickness calculated by the force balance model [43]

Fig. 5-18 (b) presents the EL spectrum, measured at 297K, from two devices employing ~1.5 nm-thick and ~2 nm-thick InAs QD active regions, where the lasing emission was observed at J_{th}=11.2 kA/cm (λ_{lasing}= 962 nm) for 1.5nm-thick InAs QD active region and at J_{th}=6.5 kA/cm^2 (λ_{lasing}= 985 nm) for the 2nm-thick InAs QD active region. These observed emission wavelengths are in good agreement with the calculated wavelength by NEXTNANO^3 software package utilizing 8-band k•p calculation for a quantum box geometry, as summarized in table 2.

Table 5-5 Summary of external device parameters including J_{th}, measured lasing wavelength, and calculated lasing wavelength by 8-band k•p calculation, assuming no lateral quantum confinement effect

d_{InAs}	J_{th} (297K)	λ_{lasing} (297K) (Measured)	λ_{lasing} (297K) (Calculated)
1.5 nm	11.2 kA/cm^2	962 nm	968 nm
2 nm	6.5 kA/cm^2	985 nm	1008 nm

It must be noted that the photoluminescence emission peak at room temperature from a calibration sample employing the 4 nm-thick $In_{0.1}Ga_{0.9}As$ QW, which is identical to the carrier collection layer used in this study, was near 920 nm. These results demonstrate that employing a carrier collection layer enables RT laser operation although the J_{th} values are significantly higher than those of conventional high-performance SK QD active region laser [46-51]. The higher J_{th} reflects both a lower optical confinement factor (i.e., low modal gain) and possibly a high non-radiative defect density within the active region. Further improvements in the QD active region gain are required to significantly lower threshold current densities. Strain compensation may allow for the selective growth of thicker InAs QDs to increase the optical confinement factor. More effective methods to reduce the defects within the active region are also needed to reduce the carrier loss from non-radiative defects.

The room temperature operation of LDs employing QD active regions defined by BCP lithography and SA-MOVPE are demonstrated. It was shown that a carrier collecting layer, 4 nm thick $In_{0.1}Ga_{0.9}As$ QW, surrounding the QDs helps enhance carrier capture by the QDs, evidenced by the comparison study between the device structures *with* and *without* the carrier collecting layer. The QD active region lasers exhibited ground state gain saturation, pronounced band-filling effects, and the temperature insensitivity in the lasing wavelength. The relatively high J_{th} values (6.5~11.2 kA/cm^2) observed are attributed to the high non-radiative defect density, which is reflected by a high T_0 value. Reducing these non-radiative defects, most likely introduced during the pattern-transfer process, is a key issue that needs to be addressed. Further optimization in *in situ* etching and increasing the optical confinement factor is needed to enhance the active region gain. In order to further understand the fundamental carrier recombination and loss process of the selectively grown QD active region, additional studies are needed to extract internal device parameters including the material gain parameter and internal loss, by employing a multi-segment contact method [59].

5. 5. $In_{0.8}Ga_{0.2}As$ QD active region on InP substrate with carrier collecting layer

5. 5. 1. Application of nanopatterned QD active region to InP substrate

The InAs-based QD lasers, grown by Stranski-Krastanov (SK) growth mode, emitting near telecom O-band (1.3 μm) have been well-established over the last two decades, demonstrating very low threshold current densities (J_{th}), high output power, and long-term reliability on various types of substrates such as GaAs, Ge, and Si [3-12]. On the other hand, the growth of isotropic InAs QD formation on InP substrates for achieving the emission wavelength near the telecom C-band (1.55 μm) still remains quite challenging, because of the smaller driving force for the nucleation of InAs QDs, stemming from the smaller lattice mismatch on InP [60-61] as shown in Table 5-6.

Table 5-6 Lattice mismatch of InAs between GaAs substrate and InP substrate

Substrate	**GaAs**	**InP**
InAs Lattice mismatch	7.2%	3.2%

This smaller lattice mismatch often results in the broken quantum wire-like structure, which leads to spectral and polarization dependency of the modal gain on the cavity orientation of the edge emitting device structure [60-61]. As an alternative to SK QDs, QDs can be formed in a more controllable fashion by employing nanopatterning and the subsequent MOVPE process, by which the QD formation is decoupled from the strain state of the material. This process leads to the formation of dense arrays of wetting-layer-free QDs, although the challenges stemming from surface state formation and efficient carrier injection into the QDs have remained problematic issues, as discussed in the previous sections. Therefore, *in situ* etching for III-V alloys lattice-matched to InP substrate was investigated in this section, which was used prior to the selective area epitaxy of QDs on InP. Laser diodes employing a single stack $In_{0.8}Ga_{0.2}As$ QD active region formed by block copolymer (BCP) lithography and selective growth on InP substrates operate at room temperature (RT) with relatively low threshold current densities.

5. 5. 2. *in situ* etching for InGaAs, AlInAs and InP using CBr_4

Crystal growth for the QD formation as well as for *in situ* etching were carried out in a vertical chamber OMVPE reactor equipped with a close-coupled showerhead gas delivery system, using H_2 as a carrier gas. Trimethyl-indium (TMIn), trimethyl-gallium (TMGa), trimethyl-aluminium (TMAl), arsine (AsH_3) and phosphine (PH_3) were used as In, Ga, Al, As, and P precursors, respectively. In the previous section, the effectiveness on *in situ* etching by CBr_4, prior to the $In_xGa_{1-x}As$ QD growth on GaAs substrates, was demonstrated where an enhanced RT-PL intensity and an improved performance were observed from the QD lasers. In order to apply *in situ* etching to InP-based material system, such as $Al_xIn_yGa_{1-x-y}As$ or InP, we have carried out a set of *in situ* etching experiments to estimate the etch rate as well as the surface smoothness, in a similar manner to the methodology in the previous section, which employed a real-time optical reflectance monitoring system. A series of *in situ* etching experiments using CBr_4 were carried out on $Al_{0.48}In_{0.52}As$, $In_{0.53}Ga_{0.47}As$ (AlInAs and InGaAs thereafter) and InP under a H_2+VH_3 (V being either P or As) partial pressure and at a fixed temperature of 585℃. In order to obtain a sharp contrast in the real-time optical reflectance from the sample surface, these experiments were initiated with the growth of ~500 nm-thick lattice-matched AlInGaAs (E_g ~ 1.03 eV) layer on planar (100) InP substrate, after which AlInAs, InGaAs or InP were grown, and CBr_4 under H_2 + VH_3 ambient was subsequently flown for *in situ* etching.

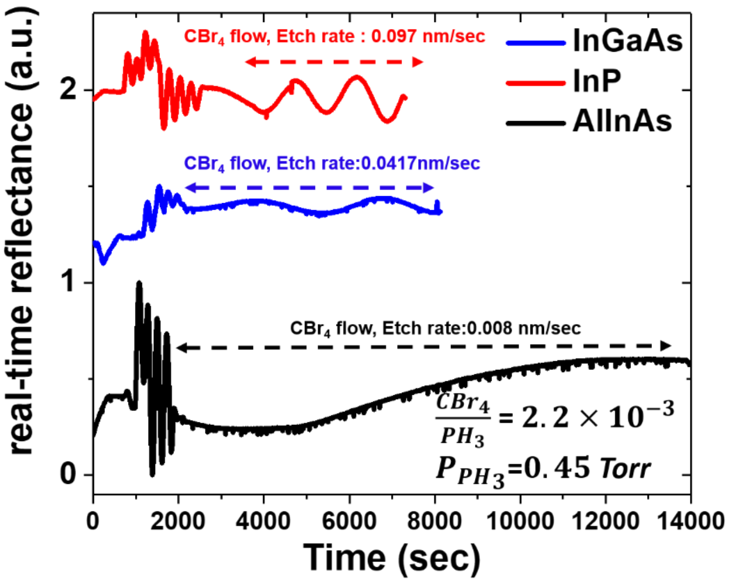

Fig. 5-19 *Real-time reflectance measured from InGaAs, AlInAs, and InP under the* PH_3+H_2 *ambience at 585 ℃. A fixed* CBr_4/PH_3 *molar flow ratio of* 2.2×10^{-3} *with a* PH_3 *partial pressure of 0.45 Torr was used.*

All samples which have gone through *in situ* etching under PH_3+H_2 ambience exhibited mirror-like smooth surface morphology, as evidenced by no apparent degradation in the measured reflectance, although the *in situ* etch rate of AlInAs was significantly slower than that of either InGaAs or InP. Our finding also indicates an excellent etching selectivity can be achieved by *in situ* etching as summarized in Table 5-7, which can be potentially useful for structures requiring an AlInAs etch-stop layer.

Table 5-7. in situ etching selectivity under PH_3 ***overpressure (0.45 Torr)***

Material	**InP/AlInAs**	**InGaAs/AlInAs**	**InP/InGaAs**
Etching Selectivity	12.13	5.21	2.33

Another set of *in situ* etching experiments has been carried out under AsH_3+H_2 ambience, in order to find an optimized in situ etching condition, especially for InGaAs, as shown in Fig. 5-20, below.

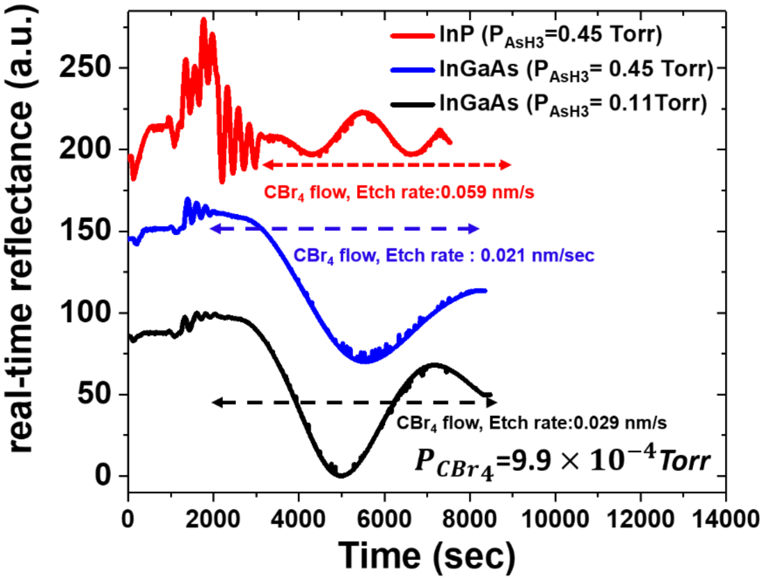

Fig. 5-20 *Real-time reflectance measured from InGaAs and InP under the AsH_3+H_2 ambience at 585* ℃. *A fixed CBr_4 partial pressure of* 9.9×10^{-4} *Torr was used while varying AsH_3 overpressure.*

In contrast to the previous observation, a gradual decrease in the average *in situ* reflectance was observed from InGaAs, regardless of the amount of AsH_3 overpressure, and samples exhibited a hazy surface morphology. On the other hand, the InP, *in situ* etched under AsH_3 overpressure, exhibited a mirror-like surface morphology, without a measurable drop in the reflectance. The etching selectivity for InP/InGaAs at AsH_3 overpressure of 0.45 *Torr* was 2.81.

The etching selectivity obtained for InP/InGaAs under the same amount of either AsH_3 or PH_3 overpressure were similar, while the etch rate of InP obtained under PH_3 overpressure was 1.6 times faster than that under AsH_3 overpressure. The *in situ* etching process is similar to the inverse process of hydride vapor phase epitaxy (HVPE), which utilizes the halogen transport, as shown below [39].

$$\text{III-V (solid)} + \text{HBr (gas)} + \text{VH}_3\text{ (gas)} \rightarrow \text{VH}_3\text{ (gas)} + \text{III-Br (gas)} + \text{H}_2\text{ (gas)}$$

Bromine radicals are thermally decomposed from CBr_4 within the OMVPE reactor, resulting in a HBr compound, which will react with the surface of the solid phase III-V. Then, with group III species present, the bromine radicals will form a volatile III-Br species. The remaining group V species will be removed from the surface only after forming volatile VH_3 hydrides at the etching temperature of 585℃. It is known that the thermal decomposition efficiency of AsH_3 is higher than that of PH_3 at this temperature [62], implying there will be more As atoms on the surface, which can possibly lead to the observed slower *in situ* etching rate when AsH_3 is used as the ambient hydride. At elevated temperatures, AsH_3 is a conventional ambient hydride gas for the solid phase III-As alloy to prevent As-dissociation. Likewise, the conventional ambient hydride for P-terminating species, such as InP in this case, is PH_3. However, we observe a mirror-like surface morphology only for the InGaAs *in situ* etched under PH_3 overpressure, while a relatively poor (hazy) surface morphology was observed from the InGaAs after *in situ* etching under an AsH_3 overpressure. While the chemical mechanism has not been identified, the degree of inequality in the vapor pressure between In-Br and Ga-Br under either AsH_3 or PH_3 overpressure can be possibly responsible for this observation.

The results of the *in situ* etching experiments carried out on AlInAs, InGaAs, and InP indicate that either InGaAs or InP under PH_3 overpressure is a suitable condition for the *in situ* etching to remove the processing-related damages prior to the selective area epitaxy for the QD on the nanopatterns defined by BCP. It is noteworthy that InP is known to have a low surface recombination velocity [63]. Therefore, utilizing the etching selectivity of InP/InGaAs under PH_3 ambient (2.33), we have used a 3 nm thick InP layer as a sacrificial layer, which was removed by the CBr_4 *in situ* etching prior to the QD selective growth.

5. 5. 3. Characteristics of $In_{0.8}Ga_{0.2}As$ QD active region laser

After establishing *in situ* etching conditions, the base material, forming the lower part of the complete laser structure, was prepared, as schematically represented in Fig. 5-21 (a).

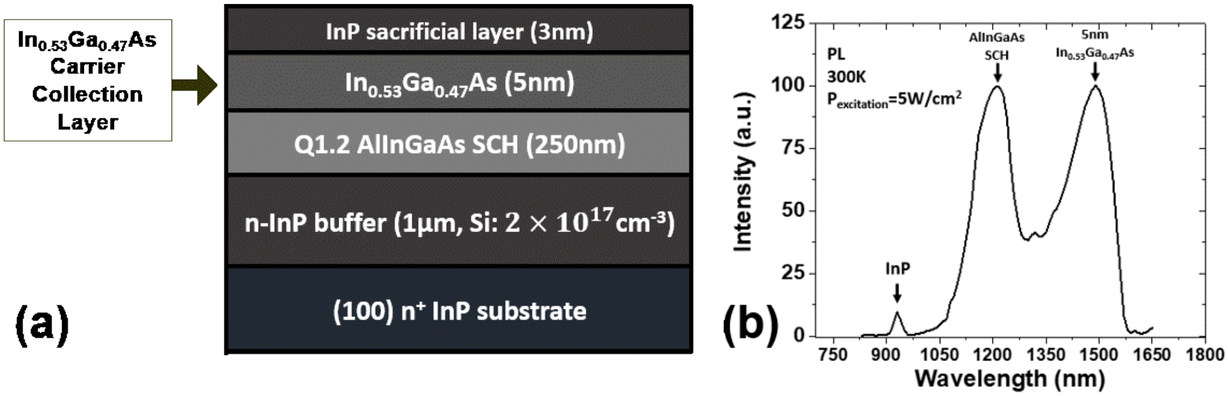

Fig. 5-21 *(a) Schematic of the base material, which forms the lower part of the complete laser structure, (b) Photoluminescence (PL) spectrum measured from the base material*

In the previous section, an enhanced carrier capture by QDs by employing a carrier collecting layer, placed adjacent to the QDs was demonstrated. Therefore, we have employed 5 nm thick InGaAs carrier collecting layer beneath the 3nm thick InP sacrificial layer, which will be removed prior to the QD growth by *in situ* etching. (Fig. 5-21 (a)). The measurement of photoluminescence (PL) from this base material, shown in Fig 5-21 (b), reveals that the emission near 1480 nm is due to the 5 nm thick InGaAs carrier collection layer.

Then, 20nm-thick SiN_x was deposited by plasma-enhanced chemical vapor deposition (PECVD) on the base material. Afterward, the BCP lithography and the subsequent pattern-transfer process were performed as described in the previous section, in order to form nanopatterns on SiN_x hardmask. Prior to loading the pattern-transferred sample into the OMVPE reactor for *in situ* etching and QD regrowth, a brief wet treatment using HCl:DI = 1:3 mixture (in volume ratio) was carried out for 20 sec to remove the native oxide. After loading the sample in the MOVPE reactor, the temperature was ramped up to 585 ℃ under PH_3 for 3 min, and *in-situ* etching using carbon tetrabromide (CBr_4) was initiated at the reactor pressure of 100 Torr under PH_3 and hydrogen (PH_3 partial pressure of 0.45 *Torr*) for 45 sec with CBr_4/PH_3 molar flow ratio of 2.2×10^{-3}. Then, the selective area epitaxy was carried out on the SiN_x template for the formation of $In_{0.53}Ga_{0.47}As$ / $In_{0.8}Ga_{0.2}As$ / $In_{0.53}Ga_{0.47}As$ (2/4/2 nm) layered QDs

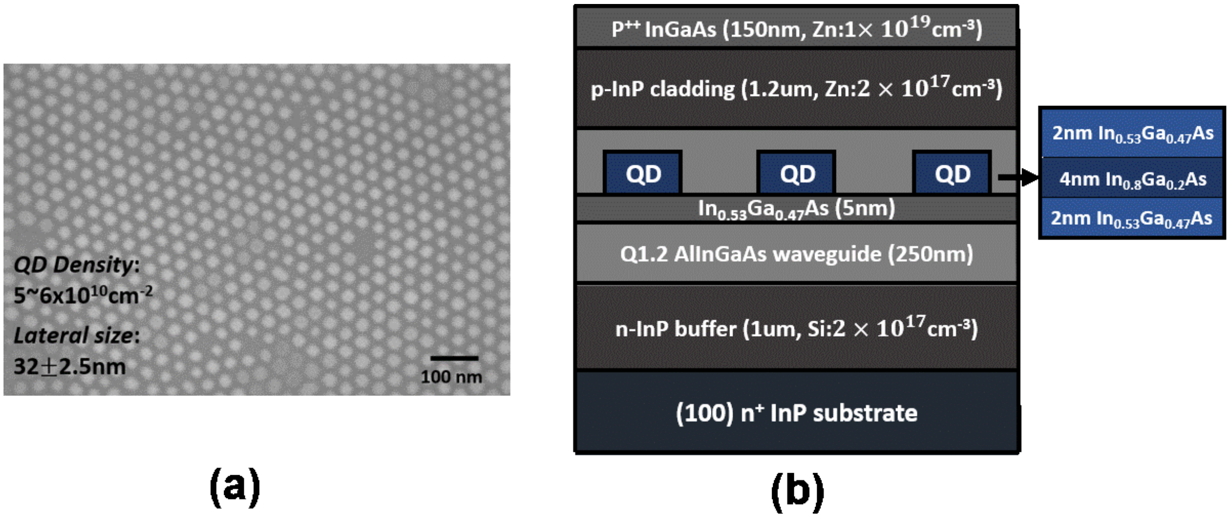

Fig. 5-22 *(a) Top-view scanning electron microscopic image taken after the selective area epitaxy for QD growth and the subsequent removal of SiNx hardmask, (b) Schematic of the complete laser structure, which forms the lower part of the complete laser structure,*

After the growth of the QDs, the samples were taken out of the OMVPE reactor and SiN_x template was removed by the 6:1 buffered oxide etchant. After the removal of SiN_x hardmask, QDs were imaged using a LEO 1550 VP (JEOL) field-emission scanning electron microscope (SEM), which revealed the QD density of $5\sim6\times 10^{10}\ cm^{-2}$ and the average QD diameter of 32 nm, as shown in Fig 5-22 (a). Then, the remaining InP was removed by *in situ* etching, and upper device structures were regrown at the growth temperature of 605 ℃ and the pressure of 100 Torr, after immediately transferring the sample into the MOVPE reactor (Fig. 5-22(b)). Table 5-8 summarizes the growth parameters used for the growth of the complete laser structure.

Table 5-8 Growth Parameters used for the complete LD structure

Material	**Growth Temp. [℃]**	**TMIn [µmol/min]**	**TMGa [µmol/min]**	**V/III Ratio**
InP	605	52	-	54
$In_{0.53}Ga_{0.47}As$	585/605	32.2	27.3	49
$In_{0.8}Ga_{0.2}As$	585	32.2	1.89	85
AlInGaAs (E_g ~1.03eV)	605	32.2	13.5	102

25µm-wide ridge waveguide lasers were fabricated by the standard photolithography technique and the subsequent wet etching using H_3PO_4:H_2O_2:H_2O = 1:1:8 mixture for InGaAs p^+ contact layer and H_3PO_4:HCl = 3:1 mixture for InP upper cladding layer, respectively. 200 nm thick PECVD SiN_x was used for the electrical passivation. The wafer was subsequently thinned down to 150µm. Ti/Pt/Au (25nm/30nm/300nm) and AuGe/Ni/Au (100nm/25nm/200nm) were e-beam evaporated on p^+ InGaAs contact layer and n^+ InP substrate side, respectively, to form contact electrodes. Then, these contact electrodes were alloyed at 375°C for 30 sec by rapid thermal annealing (RTA) to form the ohmic contact. Devices were measured *as-cleaved* (i.e. no facet coatings) from 10 to 50 ℃ under pulsed current operation. The cavity lengths tested were 0.1, 0.2 and 0.4 cm. The electroluminescence (EL) data was collected using an optical spectrum analyzer (OSA) while the output power from one facet were measured using an InGaAs photodiode in conjunction with an integrating sphere.

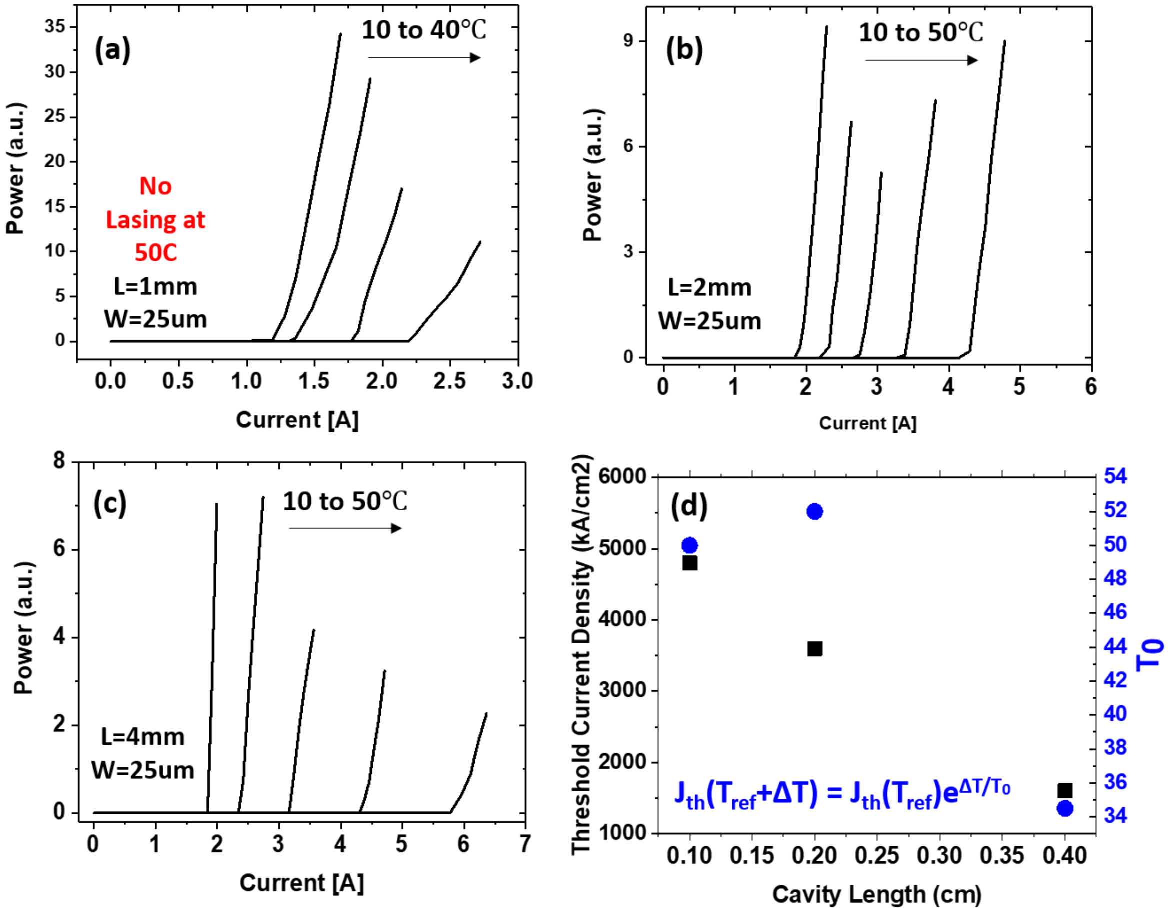

Fig. 5-23 *(a) Output power vs. current (PI) for 1mm-long QD device where no lasing was observed at 50℃, (b) Output power vs. current (PI) for 2mm-long QD device, (c) Output power vs. current (PI) for 4mm-long QD device, (d) summary of threshold current density at heat sink temperature of 10℃ and the characteristic temperature as a function of cavity length*

Shown in Fig. 5-23 are the output power vs. input current characteristics under pulsed operation (pulse width:200 nsec, duty cycle: 0.5%) for the devices with varying cavity length at the heat sink temperature from 10 to 50°C. A dramatic reduction in J_{th} was observed as the cavity length increases (J_{th}~1.6kA/cm^2, L=4mm) at the heat sink temperature of 10°C. The J_{th} at the infinite cavity length, which was extrapolated from J_{th} values for either 1mm-long and 2mm-long devices, is found to be 2.4 kA/cm^2 that is significantly larger than the obtained J_{th}~1.6kA/cm^2 from the 4mm-long device. This observation most likely reflects the relatively low optical modal gain, originating from either a low optical confinement factor or low material gain, from the single layer QD active region. In addition, a rapid reduction in the characteristic temperature (T_0) was also observed for the longest cavity length (L=4mm) devices. This observation is in a good agreement with the trend reported previously from devices employing a single layer of InAs QDs surrounded by an InGaAs QW grown on GaAs substrate, which was ascribed to the larger density of QD excited states (ES) leading to a higher J_{th} at shorter cavity lengths [51]. Nevertheless, the obtained J_{th} was comparable with that from the SK-mode grown single-layer InAs QD lasers emitting the similar wavelength (3.5 kA/cm^2, pulsed (this work) vs. 2.75 kA/cm^2, CW [64]) at the same cavity length (L=2mm).

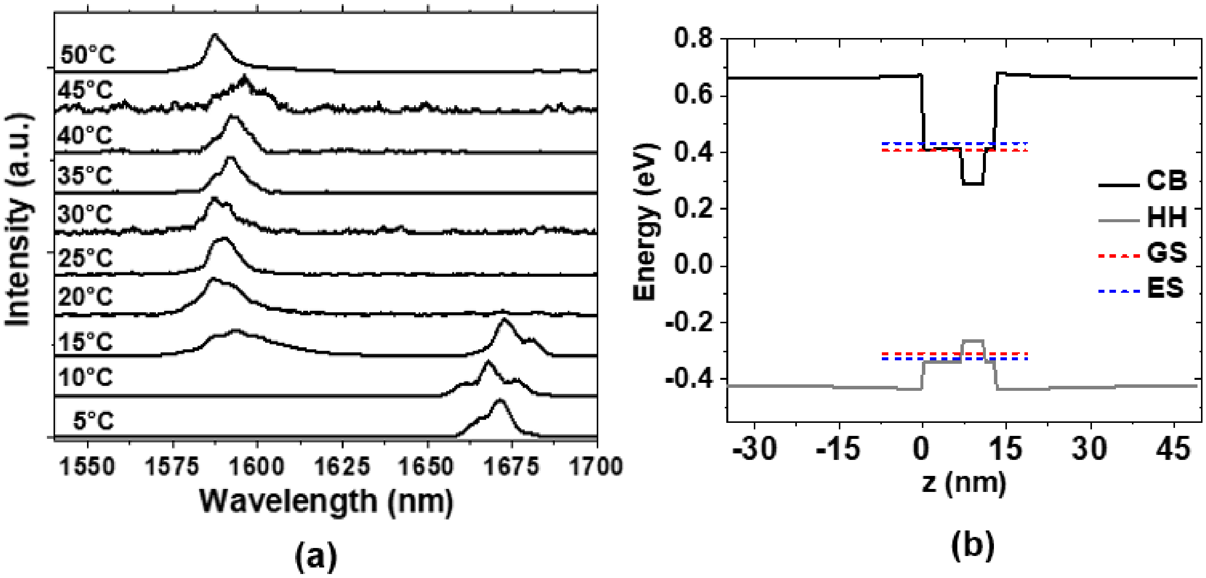

Fig. 5-24 *(a) Lasing spectra at the injection current of ~1.3*I_{th} *as a function of heat sink temperature from 4mm long* $In_{0.8}Ga_{0.2}As$ *QD laser, and (b) calculated band diagram and transition energy at 283K where the conduction band edge of the conduction band, heavy hole band are denoted as CB and HH respectively*

Presented in Fig. 5-24 (a) is the EL spectra from the 4mm-long QD device measured at I~1.3Ith while varying heat sink temperature from 5 to 50°C. At 15~20°C, the 4mm-long devices exhibit a sudden drop in the lasing wavelength from 1.67µm to 1.59µm, most likely due to a pronounced band-filling effect [42]. The calculated transition energies at 283K of the target structure, shown in Fig. 5-24. (b), correspond to GS: 0.717eV (1.73 µm) and the ES: 0.761 eV (1.63 µm), which was carried out by constructing the 3-dimensional QD structure using a commercial Schrodinger/Poisson solver [57]. In order to further verify the origin of the discrepancy between simulated and observed wavelength, a further investigation involving either tunneling electron microscopy or atom probe tomography is necessary to better quantify the compositional and shape profiles of the QDs.

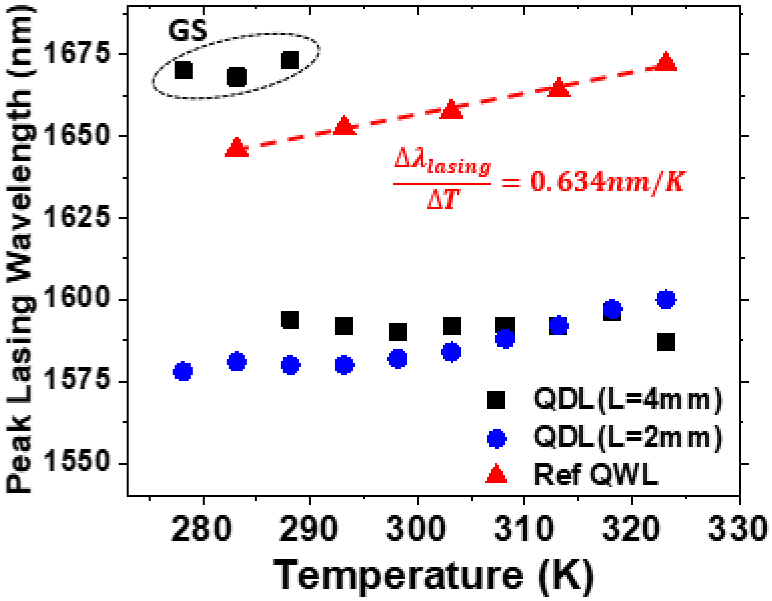

***Fig. 5-25** Summary of peak lasing wavelengths as a function of heat sink temperature*

Fig. 5-25 shows the variation in the peak lasing wavelengths from the 2-mm long and 4mm-long QD devices, as well as a reference 3-QW laser (3x $In_{0.65}Ga_{0.35}As$/AlInGaAs (7.5/15 nm) emitting similar lasing wavelength. The primary lasing transition for the 4mm-long QD devices is dominated by the ground-state (GS) QD transition, emitting at 1.67µm, while 2mm-long QD devices exhibit lasing at 1.56µm, which is most likely originating from an excited state (ES) transition. The 2-mm long and 4mm-long QD devices show a relatively low sensitivity in the lasing wavelength from 10 °C to 25 °C and 15 °C to 50 °C, respectively, although they are most likely from the ES transition. Similarly, a weak temperature dependency in the lasing wavelength (0.09nm/K) was reported from a single layer SK mode grown InAs QD laser on InP substrate emitting near 1.7 µm [65]. For reference, a conventional 3-QW laser (3x $In_{0.65}Ga_{0.35}As$/AlInGaAs (7.5/15 nm)) emitting at a similar wavelength exhibits a monotonic increase in the lasing wavelength with temperature coefficient ($\Delta\lambda_{lasing}/\Delta T$) of 0.634 nm/K. This observation suggests that an additional optimization in the active region heterostructure is necessary to improve the carrier injection efficiency into the GS, which can be possibly realized by employing tunnel injection scheme [66]. It is noteworthy that the overlapping spectral features between QD excited state and the electronic state of the carrier collection layer make it difficult to determine the exact origin of the higher energy laser emission. However, the observed low temperature sensitivity in the laser wavelength further substantiates that the higher energy spectral features correlate with that expected from the QD state transition. Therefore, spectral gain measurement and loss extraction via segmented contact method are necessary, in order to further understand the carrier dynamics in either GS or ES.

5. 6. Conclusion

LDs employing $In_{0.3}Ga_{0.7}As$ QD active regions defined by BCP lithography and subsequent SAE were demonstrated. It was shown that removing the processing-related damage prior to the QD growth is one of the key issues that needs to be addressed. In presented work, the effectiveness of *in situ* CBr_4 etching prior to the growth of $In_{0.3}Ga_{0.7}As$ QDs on either GaAs substrate by SAE has been demonstrated. It was observed that an improved radiative efficiency of the $In_{0.3}Ga_{0.7}As$ QDs can be achievable as a result of the reduced non-radiative centers through well controlled *in situ* etching by using CBr_4 while maintaining the template for the QD regrowth, as evidenced by either RT-PL measurements or an improved device performance, i.e., much reduced J_{th}, at 80K was obtained from the LD employing QDs that underwent the optimum *in situ* etching condition prior to QD deposition, compared to the device grown with unoptimized *in situ* etching condition. However, this $In_{0.3}Ga_{0.7}As$ QD active region exhibited a significant carrier leakage and gain saturation at room temperature.

In order to enhance the carrier capture by the QD active region at room temperature, a carrier collecting layer, 4 nm thick $In_{0.1}Ga_{0.9}As$ QW, was employed in close proximity to InAs QDs active region. This InAs QD active region laser with a carrier collecting layer operated at room temperature while exhibiting ground state gain saturation, pronounced band-filling effects, and the temperature insensitivity in the lasing wavelength. The relatively high J_{th} values (6.5~11.2 kA/cm^2) observed are attributed to the high non-radiative defect density, which is reflected by a high T_0 value.

Finally, a single layered $In_{0.8}Ga_{0.2}As$ QD active region laser devices on InP substrate was demonstrated, by selective area epitaxy utilizing nanopatterns formed by BCP lithography. In order to remove processing related damages, which acts as non-radiative centres, controllable *in situ* etching condition was investigated, going through a series of experiments varying ambient hydride overpressure as well as varying the target material. It was found that depending on the types of ambient hydride as well as the target material, it is possible to achieve an excellent *in situ* etching selectivity, which can be utilized for the complete removal of a sacrificial layer, i.e., a thin InP layer, in the future work. In addition, a single layered $In_{0.8}Ga_{0.2}As$ QD active region laser devices exhibited a dramatic reduction in J_{th}, which reflects a low optical gain as well as a sudden drop in T_0, which was ascribed to the larger density of the QD excited states. While the lasing wavelength insensitivity was observed from longer cavity QD devices, in comparison with the reference QW device, within a temperature range, the shorter cavity devices showed the lasing emission from the exited state. Further optimization in the device structure is necessary to achieve an enhanced carrier injection into the ground state. Also, the gain and loss extraction by segmented contact method is needed in order to understand the fundamental carrier transport and recombination process within the $In_{0.8}Ga_{0.2}As$ QD active region laser devices.

Reference

[1] M. Asada, Y. Miyamoto, and Y. Suematsu, “Gain and the threshold of three-dimensional quantum-box lasers,” *IEEE J. Quantum Electron.*, Vol.2 QE-22, pp. 1915-1921, Sept. 1986

[2] Arakawa, Y., and Hiroyuki Sakaki. "Multidimensional quantum well laser and temperature dependence of its threshold current." *Applied Physics Letters* 40.11 (1982): 939-941.

[3] Bimberg, Dieter, et al. "Quantum dot lasers: breakthrough in optoelectronics." *Thin Solid Films* 367.1-2 (2000): 235-249.

[4] Ledentsov, Nikolai N., et al. "Quantum-dot heterostructure lasers." *IEEE Journal of Selected Topics in Quantum Electronics* 6.3 (2000): 439-451.

[5] Liu, G. T., et al. "The influence of quantum-well composition on the performance of quantum dot lasers using InAs-InGaAs dots-in-a-well (DWELL) structures." *IEEE Journal of Quantum Electronics* 36.11 (2000): 1272-1279.

[6] Ledentsov, N. N. "Long-wavelength quantum-dot lasers on GaAs substrates: from media to device concepts." *IEEE journal of selected topics in quantum electronics* 8.5 (2002): 1015-1024.

[7] Sellers, I. R., et al. "1.3μm InAs/GaAs multilayer quantum-dot laser with extremely low room-temperature threshold current density." *Electronics Letters* 40.22 (2004): 1412-1413.

[8] Deppe, Dennis G., et al. "Quantum dot laser diode with low threshold and low internal loss." *Electronics Letters* 45.1 (2009): 54-56.

[9] Seravalli, L., et al. "1.59 μm room temperature emission from metamorphic In As∕In Ga As quantum dots grown on GaAs substrates." *Applied Physics Letters* 92.21 (2008): 213104.

[10] Liu, H. Y., et al. "1.55 μm InAs quantum dots grown on a GaAs substrate using a GaAsSb metamorphic buffer layer." *Applied Physics Letters* 92.11 (2008): 111906..

[11] Mi, Zetian, and Pallab Bhattacharya. "Pseudomorphic and metamorphic quantum dot heterostructures for long-wavelength lasers on GaAs and Si." *IEEE Journal of selected topics in quantum electronics* 14.4 (2008): 1171-1179..

[12] Ledentsov, N. N., et al. "MBE-grown metamorphic lasers for applications at telecom wavelengths." *Journal of Crystal Growth* 301 (2007): 914-922.)

[13] Matthews, Daniel Richard, et al. "Experimental investigation of the effect of wetting-layer states on the gain–current characteristic of quantum-dot lasers." *Applied Physics Letters* 81.26 (2002): 4904-4906.

[14] Heitz, R., et al. "Excited states and energy relaxation in stacked InAs/GaAs quantum dots." *Physical Review B* 57.15 (1998): 9050.

[15] Matthews, Daniel Richard, et al. "Experimental investigation of the effect of wetting-layer states on the gain–current characteristic of quantum-dot lasers." *Applied Physics Letters* 81.26 (2002): 4904-4906.

[16] Colombo, D., et al. "Efficient room temperature carrier trapping in quantum dots by tailoring the wetting layer." *Journal of applied physics* 94.10 (2003): 6513-6517.

[17] Asryan, L. V., and R. A. Suris. "Inhomogeneous line broadening and the threshold current density of a semiconductor quantum dot laser."*Semiconductor science and technology* 11.4 (1996): 554.

[18] Birudavolu, S., et al. "Selective area growth of InAs quantum dots formed on a patterned GaAs substrate." *Applied physics letters* 85.12 (2004): 2337-2339.

[19] Warren, A. C., et al. "Fabrication of sub-100-nm linewidth periodic structures for study of quantum effects from interference and confinement in Si inversion layers." *Journal of Vacuum Science & Technology B: Microelectronics Processing and Phenomena* 4.1 (1986): 365-368.

[20] Luscher, S., et al. "Quantum wires and quantum dots defined by lithography with an atomic force microscope." *Microelectronics Journal* 33.4 (2002): 319-321.

[21] Elarde, V. C., A. C. Bryce, and J. J. Coleman. "High performance laser with nanopatterned active layer by selective area epitaxy." *Electronics Letters* 41.20 (2005): 1122-1124.

[22] Chithrani, D., et al. "Optical spectroscopy of single InAs/InP quantum dots around λ= 1.55 μm." *Physica E: Low-dimensional Systems and Nanostructures* 21.2-4 (2004): 290-294.

[23] Nakamura, Y., et al. "Regular array of InGaAs quantum dots with 100-nm-periodicity formed on patterned GaAs substrates." *Physica E: Low-dimensional Systems and Nanostructures* 21.2-4 (2004): 551-554.

[24] Lee, H. S., et al. "Selective area wavelength tuning of InAs/GaAs quantum dots obtained by TiO 2 and SiO 2 layer patterning." *Applied Physics Letters* 94.16 (2009): 161906.

[25] Kohmoto, Shigeru, et al. "Site-controlled self-organization of individual InAs quantum dots by scanning tunneling probe-assisted nanolithography." *Applied physics letters* 75.22 (1999): 3488-3490.

[26] Liang, Jianyu, et al. "A growth pathway for highly ordered quantum dot arrays." *Applied physics letters* 85.24 (2004): 5974-5976.

[27] Park, Miri, et al. "Block copolymer lithography: periodic arrays of~ 1011 holes in 1 square centimeter." *Science* 276.5317 (1997): 1401-1404..

[28] Liu, Guojun, et al. "Thin films with densely, regularly packed nanochannels: preparation, characterization, and applications." *Chemistry of materials* 11.8 (1999): 2233-2240.

[29] Sidorenko, Alexander, et al. "Ordered reactive nanomembranes/nanotemplates from thin films of block copolymer supramolecular assembly." *Journal of the American Chemical Society* 125.40 (2003): 12211-12216..

[30] Xiao, Shuaigang, et al. "Graphoepitaxy of cylinder-forming block copolymers for use as templates to pattern magnetic metal dot arrays." *Nanotechnology* 16.7 (2005): S324..

[31] Li, R. R., et al. "Dense arrays of ordered GaAs nanostructures by selective area growth on substrates patterned by block copolymer lithography." *Applied Physics Letters* 76.13 (2000): 1689-1691.

[32] Mawst, Luke, et al. *OPTO (*pp. 759716-759716). International Society for Optics and Photonics (2010)

[33] Alizadeh, Azar, et al. "Epitaxial growth of 20 nm InAs and GaAs quantum dots on GaAs through block copolymer templated SiO 2 masks." *Journal of Applied Physics* 105.5 (2009): 054305.

[34] Wang, Hao, et al. "Distribution control of 1.55 μm InAs quantum dots down to small numbers on truncated InP pyramids grown by selective area metal organic vapor phase epitaxy." *Applied Physics Letters* 94.14 (2009): 143103.

[35] Kuech, Thomas F., and Luke J. Mawst. "Nanofabrication of III–V semiconductors employing diblock copolymer lithography." *Journal of Physics D: Applied Physics* 43.18 (2010): 183001.

[36] Park, Joo Hyung, et al. "Nanoscale selective growth and optical characteristics of quantum dots on III-V substrates prepared by diblock copolymer nanopatterning." *Journal of Nanophotonics* 3.1 (2009): 031604.

[37] Guarini, K. W., et al. "Nanoscale patterning using self-assembled polymers for semiconductor applications." *Journal of Vacuum Science & Technology B: Microelectronics and Nanometer Structures Processing, Measurement, and Phenomena* 19.6 (2001): 2784-2788.

[38] Mansky, P., et al. "Controlling polymer-surface interactions with random copolymer brushes." *Science* 275.5305 (1997): 1458-1460.

[39] Arakawa, Satoshi, Mitsumasa Itoh, and Akihiko Kasukawa. "In-situ etching of semiconductor with CBr4 in metalorganic chemical vapor deposition (MOCVD) reactor." *Japanese journal of applied physics* 41.2S (2002): 1076.

[40] Blakemore, J. S. "Semiconducting and other major properties of gallium arsenide." *Journal of Applied Physics* 53.10 (1982): R123-R181.

[41] Passaseo, A., et al. "Wavelength control from 1.25 to 1.4 μm in $In_xGa_{1-x}As$ quantum dot structures grown by metal organic chemical vapor deposition." *Applied Physics Letters* 78.10 (2001): 1382-1384.

[42] Mirin, R., A. Gossard, and J. Bowers. "Room temperature lasing from InGaAs quantum dots." *Electronics Letters* 32.18 (1996): 1732-1734.

[43] J. W. Matthews, A. E. Blakeslee, S. Mader, "Use of misfit strain to remove dislocations from epitaxial thin films", Thin Solid Films, vol. 33, pp. 253, 1976

[44] G. T. Liu, A. Stintz, H. Li, K. J. Malloy, L. F. Lester, "Extremely low room-temperature threshold current density diode lasers using InAs dots in InGaAs quantum well", Electron. Lett., vol. 35, pp. 1163-1165, 1999

[45] G. Park, D. L. Huffaker, Z. Zou, O. B. Shchekin, D. G. Deppe, " Temperature dependence of lasing characteristics for long wavelength (1.3 μm) GaAs-based quantum dot lasers ", IEEE Photon. Technol. Lett., vol. 11, pp. 301-303, 1999.

[46] G. Park, D. L. Huffaker, Z. Zou, O. B. Shchekin, D. G. Deppe, " Temperature dependence of lasing characteristics for long wavelength (1.3 μm) GaAs-based quantum dot lasers ", IEEE Photon. Technol. Lett., vol. 11, pp. 301-303, 1999.

[47] V. M. Ustinov, N. A, Maleev, A. E. Zhukov, A. R. Kovsh, A. Y. Egorov, A. V. Lunev, B. V. Volovik, I. L. Krestnikov, Y. G. Musikhin, N. A. Bert, P. S. Kop’ev, “InAs/InGaAs quantum dot structures on GaAs substrates emitting at 1.3 μm”. *Appl. Phys. Lett., vol. 74, no. 19, pp. 2815, 1999*

[48] H. Shoji, K. Mukai, N. Ohtsuka, M. Sugawara, T. Uchida, H. Ishikawa, "Lasing at three-dimensionally quantum-confined sublevel of self-organized $In_{0.5}Ga_{0.5}As$ quantum dots by current injection ", IEEE Photon. Technol. Lett., vol. 7, pp. 1385-1387, Dec. 1995.

[49] Y. Qiu, P. Gogna, S. Forouhar, A. Stintz, L. F. Lester, " High-performance InAs quantum-dot lasers near 1.3 µm ", Appl. Phys. Lett., vol. 79, no. 22, pp. 3570-3572, Nov. 2001

[50] H.-Y. Liu, B. Xu, Y.-Q. Wei, D. Ding, J.-J. Qian, Q. Han, J.-B. Liang, Z.-G. Wang, "High-power and long-lifetime InAs/GaAs quantum-dot laser at 1080 nm", Appl. Phys. Lett., vol. 79, pp. 2868-2870, 2001.

[51] L. F. Lester, A. Stintz, H. Li, T. C. Newell, E. A. Pease, B. A. Fuchs, K. J. Malloy, " Optical characteristics of 1.24- muhboxm InAs quantum-dot laser diodes ", IEEE Photon. Technol. Lett., vol. 11, pp. 931-933, Aug. 1999.

[52] N. Tansu, L. J. Mawst, "Temperature sensitivity of 1300-nm InGaAsN quantum-well lasers", IEEE Photon. Technol. Lett., vol. 14, pp. 1052-1054, Aug. 2002.

[53] N. Tansu, L. J. Mawst, " Low-threshold strain-compensated InGaAs(N) (λ=1.19−1.31µm) quantum-well lasers ", IEEE Photon. Technol. Lett., vol. 14, pp. 444-446, Apr. 2002

[54] N. Tansu, L. J. Mawst, "Current injection efficiency of 1300-nm InGaAsN quantum-well lasers", J. Appl. Phys., vol. 97, pp. 2523-2525, Mar. 2005

[55] F. Klopf, J. P. Reithmaier, A. Forchel, "Highly efficient GaInAs/(Al)GaAs quantum-dot lasers based on a single active layer versus 980 nm high-power quantum-well lasers", Appl. Phys. Lett., vol. 77, pp. 1419-1421, Sept. 2000

[56] F. Klopf, S. Deubert, J. P. Reithmaier, A. Forchel, "Correlation between the gain profile and the temperature-induced shift in wavelength of quantum-dot lasers", Appl. Phys. Lett., vol. 81, pp. 217-219, 2002.

[57] The nextnano^3 software package can be downloaded from www.nextnano.de

[58] L. V. Asryan, R. A. Suris, "Inhomogeneous line broadening and the threshold current density of a semiconductor quantum dot laser", Semicond. Sci. Technol., vol. 11, pp. 554, 1996

[59] P. Blood, G. M. Lewis, P. M. Smowton, H. Summers, J. Thomson, J. Lutti, "Characterization of semiconductor laser gain media by the segmented contact method", IEEE J. Sel. Topics Quantum Electron., vol. 9, no. 5, pp. 1275-1282, Sep./Oct. 2003

[60] C. Gilfert, et al. "High gain 1.55 µm diode lasers based on InAs quantum dot like active regions." *Applied Physics Letters* 98.20 (2011): 201102.

[61] A. A. Ukhanov, et al. "Orientation dependence of the optical properties in InAs quantum-dash lasers on InP." *Applied physics letters* 81.6 (2002): 981-983.

[62] A. S. Jordan, et al. "Thermodynamic analysis of AsH3 and PH3 decomposition including subhydrides." *Journal of Vacuum Science & Technology A: Vacuum, Surfaces, and Films* 12.1 (1994): 204-215.

[63] C. A. Hoffman, et al. "Study of surface recombination in GaAs and InP by picosecond optical techniques." *Journal of Applied Physics* 51.3 (1980): 1603-1604.

[64] Kotani, Junji, et al. "First demonstration of single-layer InAs/InP (100) quantum-dot laser: continuous wave, room temperature, ground state." *Electronics letters* 45.25 (2009): 1317-1318.

[65] Qiu, Yueming, et al. "Lasing characteristics of InAs quantum-dot lasers on (001) InP substrate." Applied physics letters 83.9 (2003): 1704-1706.

[65] Bauer, Sven, Vitalii Sichkovskyi, and Johann Peter Reithmaier. "Growth and optical characteristics of InAs quantum dot structures with tunnel injection quantum wells for 1.55 µm high-speed lasers." *Journal of Crystal Growth* 491 (2018): 20-25.

Chapter 6. Future works

6. 1. Wavelength extension of dilute-bismide-based QW active region laser

6. 1. 1. Higher Bi incorporation in $GaAs_{1-z}Bi_z$ QW active region

In chapter 4, the growth and device characteristics of the $GaAs_{1-z}Bi_z$ QW active region was presented where the higher Bi incorporation was found with decreasing growth temperature. In order to realize the predicted potential advantages of the $GaAs_{1-z}Bi_z$ QW active region, *i.e.*, $E_g < \Delta_{so}$ to suppress CHSH Auger process, the incorporation Bi as high as 10% is necessary. However, a further reduction in the growth temperature to achieve this high GaBi mole fraction may not be a practical approach for the optoelectronic device application, as the $GaAs_{1-z}Bi_z$ in dilution regime (Bi% < 4%) is already grown at a substantially low growth temperature near 400 °C. It was shown that the $GaAs_{1-z}Bi_z$ material grown in this temperature (~400 °C) range possesses the degraded luminescence properties, due to significantly high density of incorporated carbon, point defects, and related defect complexes, as shown in Fig. 4-8, in the prior chapter.

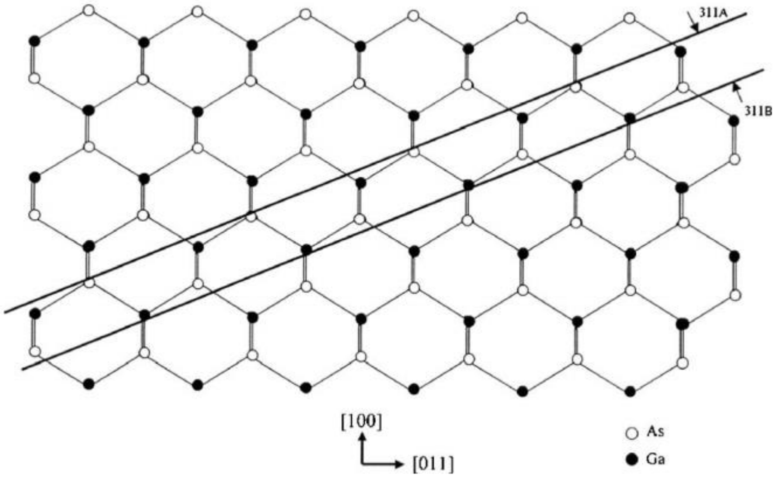

Fig. 6-1 *A schematic illustration of (311) planes of GaAs (After reference [1])*

On the other hand, the use of high index plane (311) GaAs substrate may offer a pathway for enhancing Bi incorporation within $GaAs_{1-z}Bi_z$ QW active region while minimizing the growth temperature reduction. The (311) surface exhibits (100) terraces and (111) step-edge atoms. For (311)B plane, (100)-like Ga atoms and (111)B-like As atoms are present on the surface. As a result, (311)B substrate has been frequently used to obtain the desired structural/optical properties within the epitaxial layer such as an improved InAs QD areal density [2] and a higher N incorporation within GaAsN film [3]. In addition, an enhanced incorporation of Bi within the bulk $GaAs_{1-z}Bi_z$ film on (311)B GaAs substrate was reported in a prior study [4], while this material was grown by solid-source MBE. Therefore, a preliminary study has been carried out for achieving a higher Bi incorporation within $GaAs_{1-z}Bi_z$ QW on either (001) or (311)B substrate by MOVPE in this work.

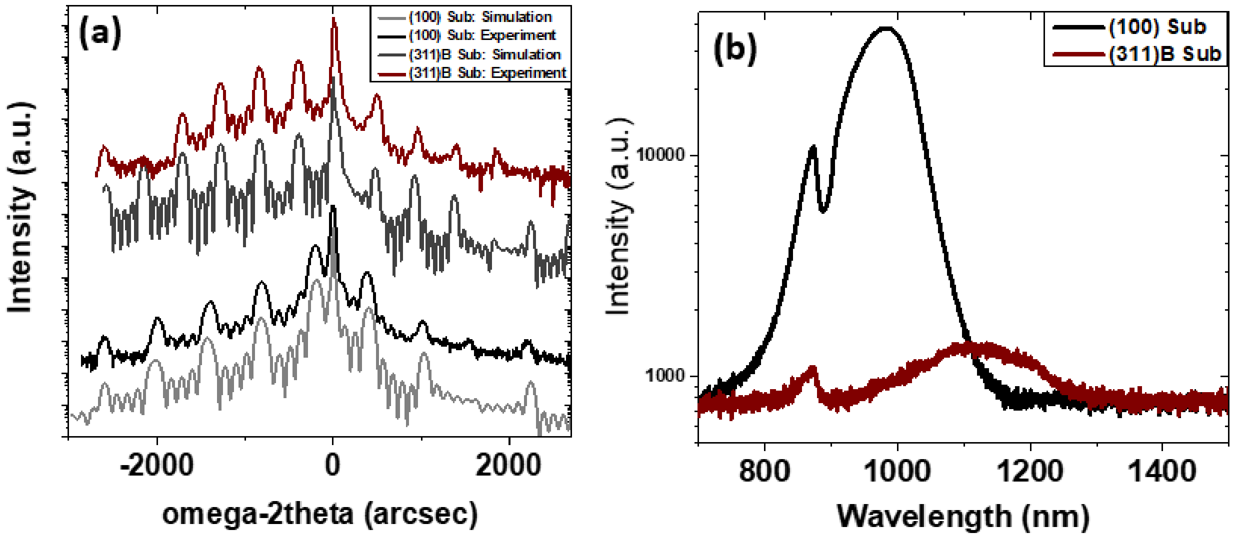

Fig. 6-2 *(a) HR-XRD spectra of the 5-period $GaAs_{1-z}Bi_z/GaAs$ MQW grown on either (100) or (311)B substrate, and (b) PL spectra taken at room temperature from the 5-period $GaAs_{1-z}Bi_z$ /GaAs MQW*

Fig. 6-2 (a) presents the HR-XRD spectra around (004) or (311) GaAs reflection taken from 5-period $GaAs_{1-z}Bi_z$/GaAs MQW grown on either (001) or (311)B GaAs substrates under the same growth condition summarized in Table 5-1.

Table 6-1 Summary of growth parameters

Material	Pressure [Torr]	Growth Temp.	TEGa [µmol/min]	TMBi/V	V/III
$GaAs_{1-z}Bi_z$	**50**	**440 °C**	**122**	**0.036**	**1.41**
GaAs	**100**	**625°C**	**TMGa and AsH3 used**	**-**	**65**

Assuming a GaBi zincblende lattice constant of 0.633nm [5], the GaBi mole fractions of each sample was found by performing the XRD dynamic simulations at a point of best fit to the experimental HR-XRD data shown in Fig. 6-2 (a). The structural details of each sample derived from the XRD simulations are summarized in Table 2.

Table 6-2 Structure Details and $GaAs_{1-z}Bi_z$ growth rate on a different crystallographic plane

Crystallographic Plane	Structure Details from the HR-XRD dynamic simulation	$GaAs_{1-z}Bi_z$ Growth Rate [nm/sec]	PL Peak Position [eV]
(001)	**5x $GaAs_{0.974}Bi_{0.026}$/GaAs (8/23m)**	**0.089**	**1.265**
(311)B	**5x $GaAs_{0.936}Bi_{0.064}$/GaAs (10.5/30nm)**	**0.117**	**1.083**

A higher GaBi mole fraction (z=6.4%) within this $GaAs_{1-z}Bi_z$ film was identified as (311)B GaAs substrate was employed, in comparison to z=2.6% grown on (001) GaAs substrate. This higher Bi incorporation is evidenced by the PL spectra taken at room temperature, as shown in Fig. 6-2 (b). The sample grown on (311)B GaAs substrate exhibits the PL peak position of 1145 nm, or equivalently 1.083eV, while that grown on (001) shows the PL peak position of 980 nm (1.265eV). Also, an enhanced growth rate (0.089 vs. 0.117 nm/sec) of $GaAs_{1-z}Bi_z$ was observed on (311)B GaAs substrate.

Post growth thermal annealing within the MOVPE reactor under AsH_3/H_2 ambient was performed for 30 min at 630°C for this 5-period $GaAs_{0.936}Bi_{0.064}/GaAs$ MQW grown on (311)B GaAs substrate.

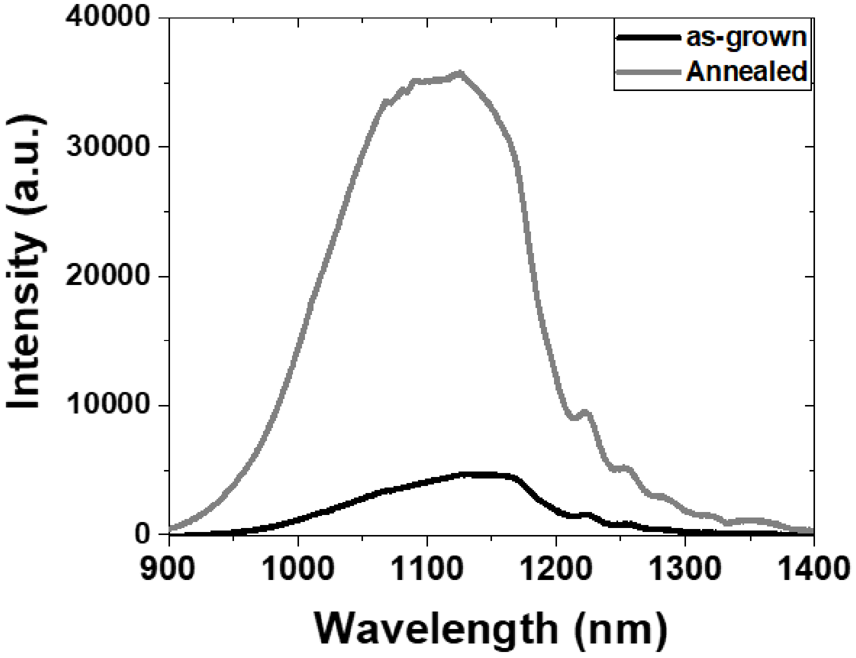

Fig. 6-3 *Photoluminescence spectra from 5-period $GaAs_{0.936}Bi_{0.064}/GaAs$ MQW grown on (311)B before and after in situ annealing under AsH_3/H_2 ambient at 630°C for 30 min*

Shown in Fig. 6-2 are the PL spectra from 5-period $GaAs_{0.936}Bi_{0.064}/GaAs$ MQW sample, grown on (311)B GaAs substrate, before and after *in situ* annealing under AsH_3/H_2 ambient at 630°C for

30 min. 7-fold increase in the PL intensity was observed after the post-growth *in situ* annealing, indicating a substantial increase in the radiative efficiency within the $GaAs_{0.936}Bi_{0.064}$ QWs. However, the FWHM in the PL linewidth was as broad as 189 meV, which is significantly larger than 95 meV from the $GaAs_{0.974}Bi_{0.026}$ QWs. This broader FWHM potentially indicates the presence of nonhomogeneous Bi distribution [6] and/or abundant localized states [7]. Therefore, further improvement in improving the emission linewidth is necessary.

Nevertheless, the presented preliminary study on the use of (311)B substrate holds the potential for realizing a higher Bi concentration ($z \geq 10\%$) within $GaAs_{1-z}Bi_z$ QW active region while minimizing the reduction in the growth temperature, although further optimization processes in the growth parameter and the post-growth thermal annealing condition are necessary.

6. 1. 2. Novel Heterostructure employing $GaAs_{1-z}Bi_z$ QW for wavelength extension

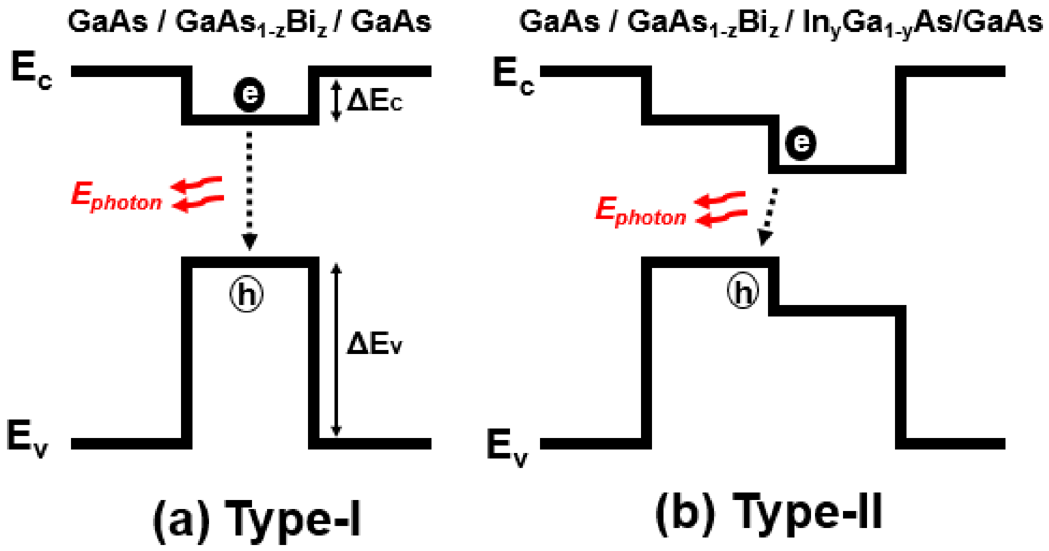

Fig. 6-4 *Schematic band diagram for (a) Type-I band-to-band transition, and (b) Type-II band-to-band transition*

Until now, the type-I band-to-band transition, schematically shown in Fig. 6-4 (a), has been investigated and discussed. In type-I heterostructure, the narrow bandgap active region is enclosed by wide band gap materials, resulting in both electron and hole pairs to be confined within the same narrow band gap region, and thus leading to the radiative recombination process by vertical transition. On the other hand, type-II heterostructure consists of two different narrow band gap materials, which are enclosed by wide band gap materials, as represented in Fig. 6-5 (b). In this type of heterostructure, electrons and holes are separately confined in the close proximity, which results in the diagonal transition for the radiative recombination process.

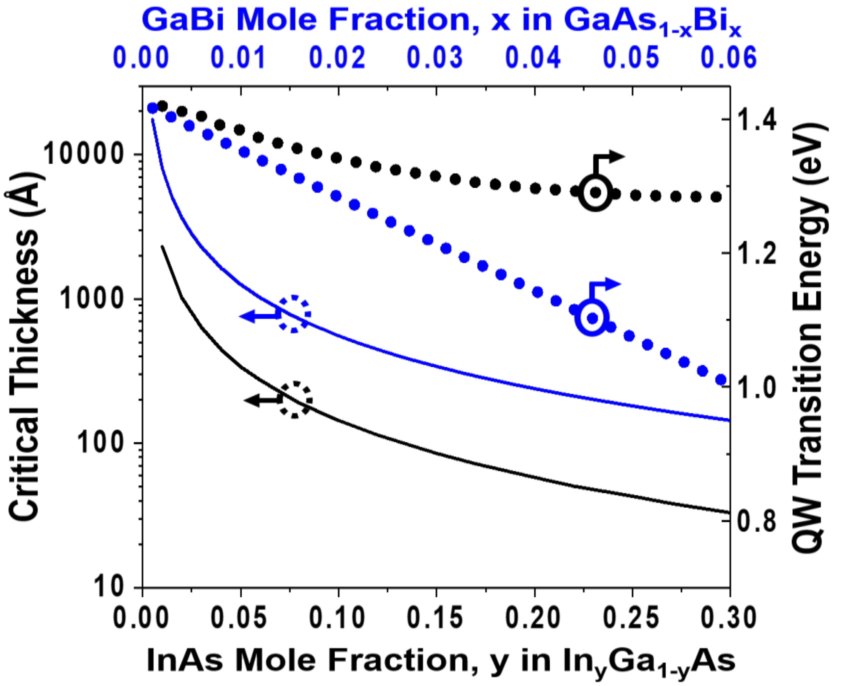

Fig. 6-5 *The critical thickness of the compressively-strained* $GaAs_{1-x}Bi_{x}$ *(Blue) and* $In_yGa_{1-y}As$ *QWs (Black) grown on GaAs and the corresponding transition energy of single quantum well (QW) at their critical thickness by force balance model [8]. The transition energies of the* $In_yGa_{1-y}As$ *QWs were calculated by 8 band k•p model.*

Type-II based heterostructure has been successfully used for the emission of an extended emission wavelength near telecom O-band, that is not accessible by the conventional type-I heterostructure, by employing InGaAs/GaAsSb system on GaAs substrate [9-11]. However, the similar lattice constant of InAs (6.058Å) and GaSb (6.095Å) and the subsequent heavy biaxial compressive strain by both InGaAs and GaAsSb QWs, when grown on GaAs substrate, have limited the versatile heteroepitaxial design, while requiring a careful optimization in the epitaxial growth process in order to avoid the strain relaxation.

In chapter 4, the origin of band gap reduction in $GaAs_{1-z}Bi_z$ has been discussed and explained within the framework of the valance band anti-crossing model, which leads to a large valence band offset (~55meV/%Bi) and a relatively small conduction band offset (~15meV/%Bi) at the $GaAs_{1-z}Bi_z$/GaAs heterojunction [12]. Furthermore, the less degree of biaxial strain by $GaAs_{1-z}Bi_z$, in comparison to those of InGaAs and GaAsSb QWs at the same emission wavelength, makes it a suitable candidate for the narrow band gap material in the type II-heterostructure, as schematically shown in Fig. 6-5.

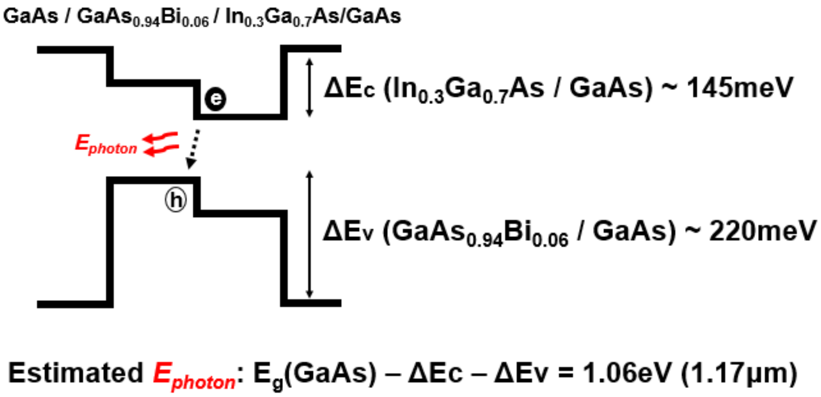

Fig. 6-6 *Schematic band diagram for GaAs/$GaAs_{0.94}Bi_{0.06}$/$In_{0.3}Ga_{0.7}As$/GaAs type-II QW heterostructure with the estimated emission energy of 1.06eV (1.17μm)*

Fig. 6-6 represents the schematic band diagram for GaAs/$GaAs_{0.94}Bi_{0.06}$/$In_{0.3}Ga_{0.7}As$/GaAs type II QW heterostructure with the estimated emission wavelength of 1.17 µm. The preliminary study was also performed as shown in Fig. 6-7, on (001) GaAs substrate. In order to achieve a relatively high GaBi mole fraction of 6%, the growth temperature was reduced to 400 °C with further reduced V/III ratio of 0.74, as summarized in table 6-3.

Table 6-3. Summary of growth parameters

Material	Pressure [Torr]	Growth Temp.	TEGa [µmol/min]	TMBi/V	V/III
$GaAs_{0.94}Bi_{0.06}$	**50**	**400 °C**	**186**	**0.055**	**0.74**
$In_{0.3}Ga_{0.7}As$	**100**	**500°C**	**65**	**TMIn/III=0.13**	**123**

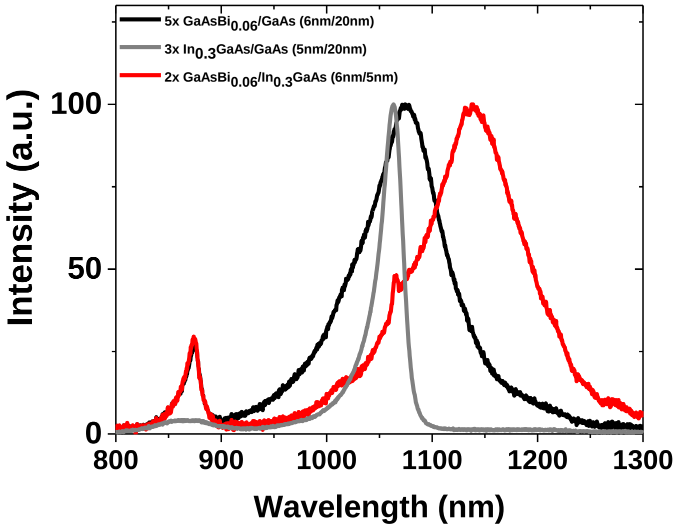

Fig. 6-7 *Normalized photoluminescence spectra from 5-period $GaAs_{0.06}Bi_{0.06}$/GaAs MQW, 3-period $In_{0.3}Ga_{0.7}As$ MQW, and 2-period $GaAs_{0.06}Bi_{0.06}$/ $In_{0.3}Ga_{0.7}As$/GaAs MQW structure*

A clear evidence of the extended wavelength (1.15 µm) from the type II QW heterostructure (2-period $GaAs_{0.06}Bi_{0.06}$/ $In_{0.3}Ga_{0.7}As$/GaAs MQW structure) was observed, in comparison to those from the type I heterostructure, which exhibited the emission wavelength near 1.05 and 1.07 µm, respectively. This observed emission wavelength is in good agreement with the estimated emission wavelength (1.17µm). However, a relatively broad FWHM in the PL linewidth (126meV) was observed, which was similar to that from 5-period $GaAs_{0.06}Bi_{0.06}$/GaAs MQW. Therefore, a further investigation is necessary to reduce this PL linewidth for the application to the laser diode active region, in addition to a careful optimization in the growth parameter and the post-growth annealing condition. Also, in order to increase the electron and hole wavefunction overlap for the enhanced recombination probability, employing a "W-type" type-II heterostructure [10] is a subject of the future work.

6. 2. QD active region utilizing nanopatterns defined by BCP lithography

6. 2. 1. Alternative pathway to form QD active region

So far, we have investigated utilizing nanopatterns and subsequent selective area epitaxy to form QD active region. However, in this process, more than one regrowth steps are inevitable for the growth of a complete full laser structure, as schematically represented in Fig. 5-13.

In particular, the post-processing after the selective area epitaxy of the QDs can possibly affect the luminescent properties of the selectively grown QDs, as they are exposed in the air, forming a native oxide layer around the QDs. The formation of native oxide on the surface of III-V semiconductor is known to result in a significant surface states [13], possibly leading to poorer quantum luminescent efficiency. In addition, residual external impurities remaining on the surface during the SiN_x removal process can also cause a substantial reduction in the minority carrier lifetime. Furthermore, the complexity in the growth of the full laser structure can be a practical limiting factor due to its higher fabrication cost originating from multiple regrowth steps.

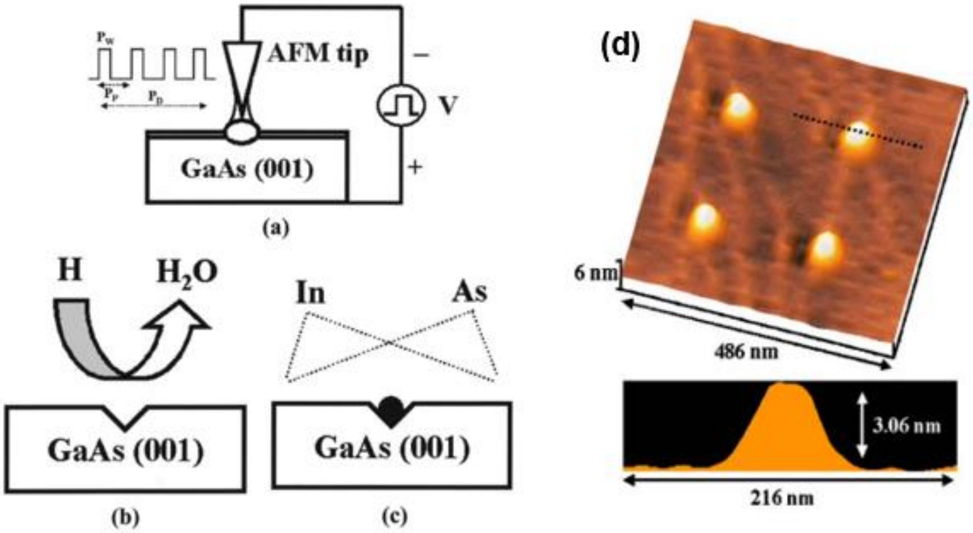

Fig. 6-8 *The schematic illustration of the experimental procedures for (a) the formation of the nano-oxide dots on GaAs (001) surface by AFM tip-induced oxidation, (b) subsequent removal of a nano-oxide dots and native oxide layer by atomic hydrogen irradiation, (c) the deposition of InAs QDs on the nanoholes by droplet epitaxy method, and (d) the AFM image with a cross sectional profile for the InAs QDs (after reference [15])*

On the other hand, a prior study has demonstrated the formation of the ordered InAs QD array on nanoholes defined by AFM lithography [14-15], as shown in Fig. 6-8. Similarly, dense nanoholes on the InP surface can be possibly formed, utilizing BCP lithography and subsequent wet etching processes, as shown in Fig. 6-9.

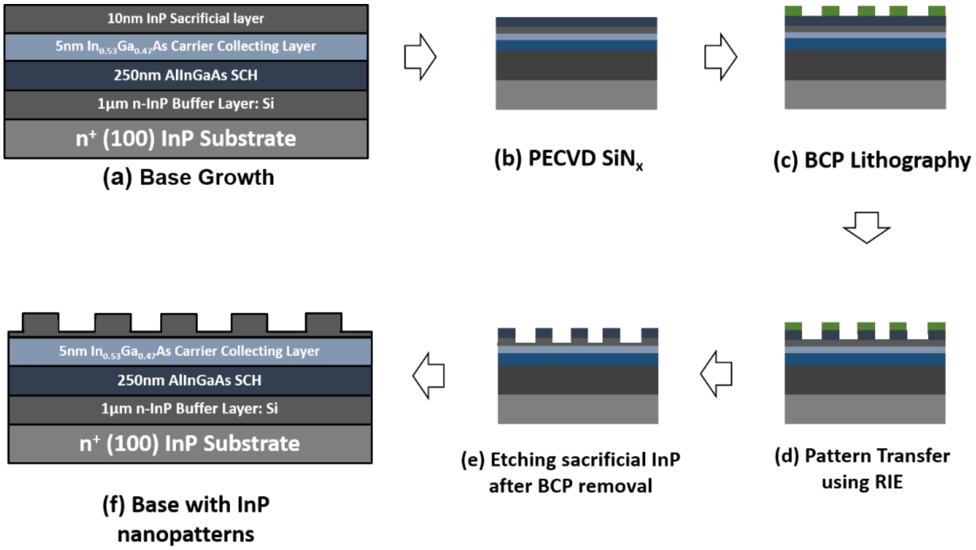

Fig. 6-9 *Schematic representation of the simplified procedure for the formation of InP nanoholes defined by BCP lithography*

As a preliminary study, the nanoholes on the 10nm thick InP sacrificial layer was formed with SiN_x hardmask, using an etchant of HCl:DI water (1:3 in volume ratio) for 45 sec. After forming InP nanoholes, the remaining SiN_x hardmask was removed by using buffered oxide etchant (1:6).

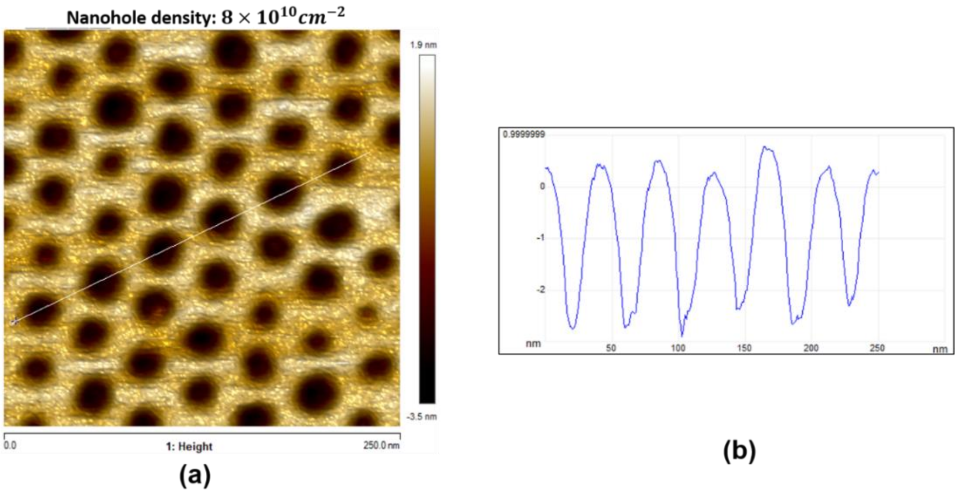

Fig. 6-10 *(a) Atomic Force Microscopic image of the formed nanoholes defined by BCP lithography, and (b) the line scan showing an average etching depth of ~3 nm.*

As shown in Fig. 6-10, a dense array of nanoholes (density: ~ $8 \times 10^{10} cm^{-2}$) were obtained with the average etching depth of ~3 nm. These nanoholes could be potentially used for the formation of the QD active region without the need for an additional regrowth for the complete laser structure after the SiN_x removal.

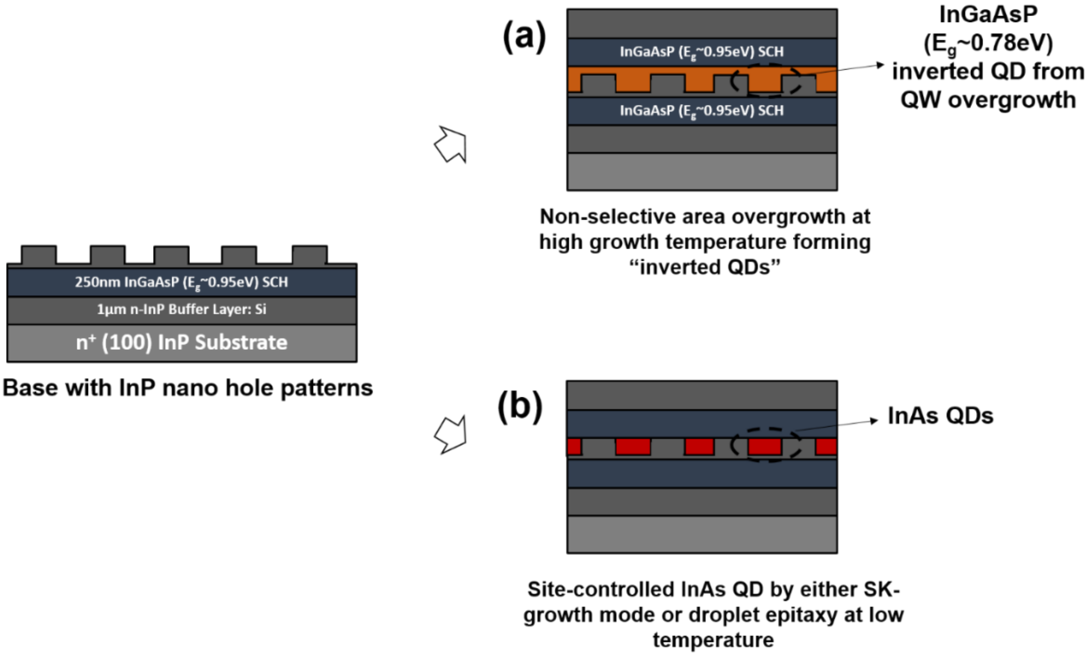

Fig. 6-11 *Schematics for the formation of QD active region on the nanoholes by (a) non-selective QW overgrowth, and, (b) site-controlled InAs QDs by either SK-growth mode or droplet-epitaxy.*

Fig. 6-11 schematically represents the possible methods for forming QDs on these InP nanoholes without the need for the additional regrowth for the upper device structures including the upper cladding layer and contact layer. By employing a relatively high MOVPE growth temperature near 600 °C and the subsequent self-planarization process, it will be possible to perform non-selective QW growth, which will, in turn, eventually form "inverted" QD structure, as shown in Fig. 6-11 (a). The strain state of this overgrown quantum well can be either lattice-matched, tensile-strained, or compressively strained, if its thickness is thinner the critical thickness.

In addition, these nanohole patterns on InP can allows for the site-controlled InAs QDs by either SK growth mode [16] or droplet epitaxy [14-15]. In particular, the vertical alignment of the SK mode grown QDs within the multi-stacked QD layers has been observed in prior studies [17-18], as shown in Fig. 6-12, which was attributed to the strain field created by the underlying QDs grown on GaAs substrate.

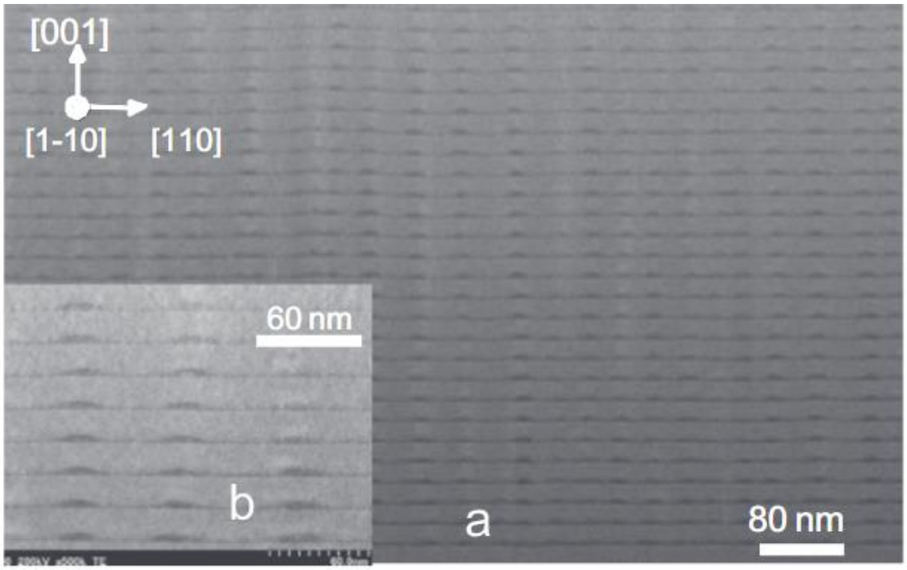

Fig. 6-12 *STEM images of (a) 30-stack QD layers grown by SK growth mode on GaAs substrate and (b) an extended image of their top portion showing the vertical alignment of the QDs (after reference [17])*

This vertical alignment of QDs can be applied to the approaches presented in Fig. 6-12 (b) in order to achieve a higher optical modal gain from the QD active region. Therefore, the possible future work includes implementing these QD growths scheme on the nanohole patterns, particularly on InP substrate. In addition, in order to form a more uniform nanohole patterns by isotropic wet etching, a modification on the nanopatterns on BCP can be achieved by adjusting PS/PMMA ratio, and the resulting BCP pattern, as shown in Fig. 6-13, which exhibited a larger diameter (~50 nm vs. ~20 nm in the conventional BCP pattern) as well as a longer hole-to-hole distance (~50nm vs. ~25 nm in the conventional BCP pattern), although further optimization is necessary to improve uniformity in the hole size and spacing.

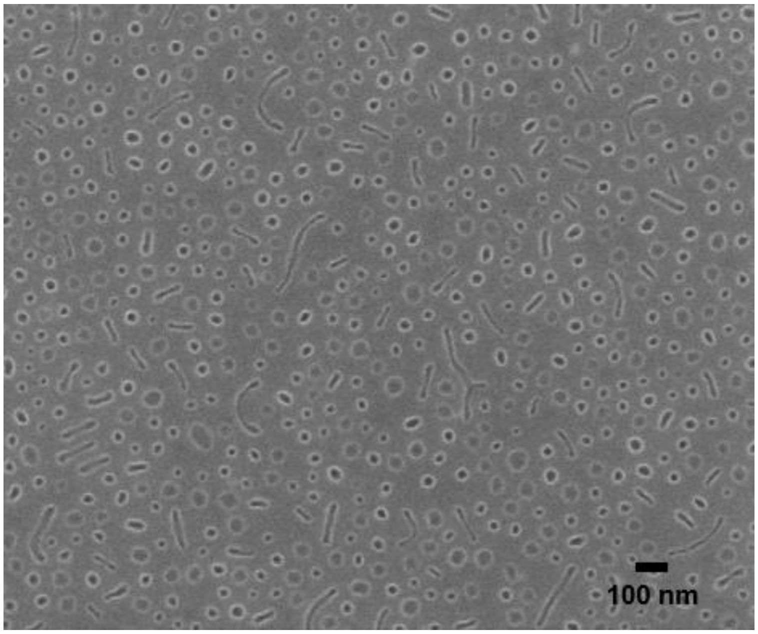

Fig. 6-13 *Alternative BCP mask for the formation of nanoholes by wet etching*

6. 2. 2. Extraction of internal device parameters of the QD lasers

It has been contended that the conventional cavity length analysis, which is often used to measure the internal parameters such as transparency current, material gain, internal quantum efficiency, and internal optical loss, should not be applied for the QD active region lasers due to the non-pinning of the fermi-level above the laser threshold [19]. Therefore, in order to further understand the fundamental carrier recombination mechanism and loss process of the selectively grown QD active region, additional measurements are needed to extract internal device parameters including the material gain parameter and internal loss, which can be realized by employing a multi-segment contact method (MSCM) [20]. For these measurements, a test set-up was established to measure amplified spontaneous emission from the single pass, multi-segment devices where each segment is electrically isolated, as shown in Fig 6-14. An InGaP single QW laser (λ_{lasing} ~ 636 nm) material grown on GaAs substrate was used to test and check the integrity of this established measurement condition.

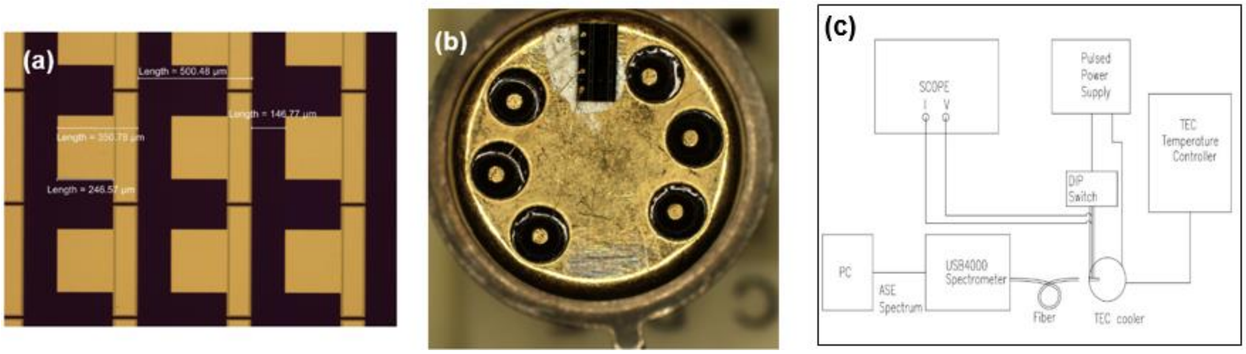

Fig. 6-14 *(a) Top-view optical image of the fabricated wafer for the multi-segment contact method, (b) packaged device on TO-can, (c) schematic diagram of the measurement set-up where the packaged device is positioned on the TEC cooler.*

The measurement of amplified spontaneous emission from the multi-segment devices offers a pathway to measure internal optical loss itself by beer's law, net gain spectra (subsequently internal optical loss), material gain and the transparency current density, as shown in Fig. 6-15. In addition, overall radiative efficiency (η_r) of the QD active region can be obtained, which is important to understand the statistical carrier recombination mechanism, involved in the spontaneous emission process. These obtained internal parameters were in a good agreement with the obtained results by the conventional cavity length analysis (CLA), as shown in table 6-4.

Table 6-4. Comparison of the extracted internal device parameters by either MSCM or CLA

	Multi-segment measurement	Cavity Length Analysis
Γg_{0J} (cm^{-1})	21.3	22.69
J_{tr}, (A/cm^2)	212	186
α_i (cm^{-1})	2.2	1.97
η_r	0.16	

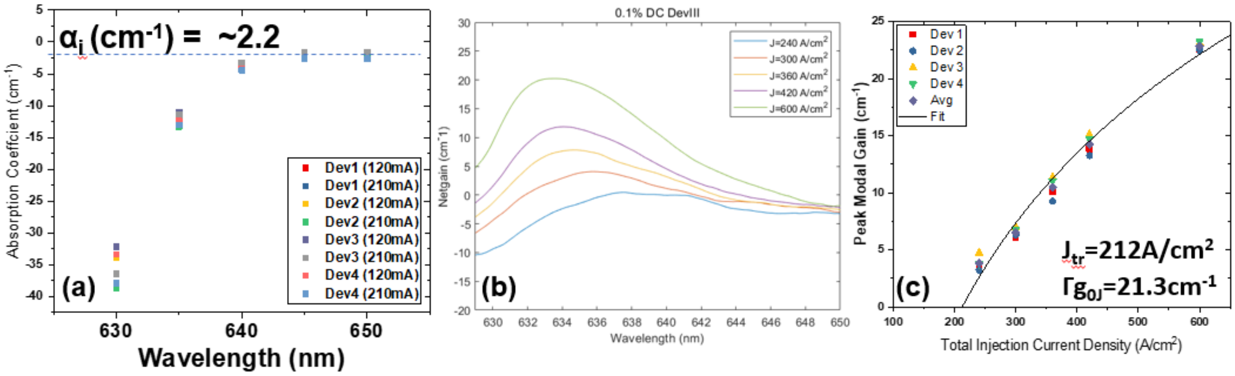

Fig. 6-15 *(a) The loss measurement obtained by independently pumping each segment and by applying beer's law (b) Net gain spectra at different pumping level, (c) Peak modal gain vs. total injection current where the logarithmic fitting enables to obtain the transparency current density (J_{tr}) and material gain (Γg_{0J})*

Therefore, the measurement of these internal parameters of the InP-based selectively grown QD active region lasers, using this multi-segment gain measurement technique, will be a subject of the future work.

Reference

[1] Li, Y., and M. Niewczas. "Strain relaxation in (100) and (311) Ga P⁄ GaAs thin films." *Journal of applied physics* 101.6 (2007): 064910.

[2] Saito, Hideaki, Kenichi Nishi, and Sigeo Sugou. "Ground-state lasing at room temperature in long-wavelength InAs quantum-dot lasers on InP (311) B substrates." *Applied Physics Letters* 78.3 (2001): 267-269.

[3] Han, Xiuxun, et al. "N incorporation and optical properties of GaAsN epilayers on (3 1 1) A/B GaAs substrates." *Journal of Physics D: Applied Physics* 44.1 (2010): 015402.

[4] Henini, M., et al. "Molecular beam epitaxy of GaBiAs on (311) B GaAs substrates." *Applied Physics Letters* 91.25 (2007): 251909.

[5] Tixier, S., et al. "Molecular beam epitaxy growth of GaAs 1− x Bi x." *Applied physics letters* 82.14 (2003): 2245-2247.

[6] Mohmad, Abdul Rahman, et al. "Bismuth concentration inhomogeneity in GaAsBi bulk and quantum well structures." *Semiconductor Science and Technology* 30.9 (2015): 094018.

[7] Yan, Bing, et al. "Bismuth-induced band-tail states in GaAsBi probed by photoluminescence." *Applied Physics Letters* 114.5 (2019): 052104.

[8] Matthews, J. W., and A. E. Blakeslee. "Defects in epitaxial multilayers: I. Misfit dislocations." *Journal of Crystal growth* 27 (1974): 118-125.

[9] Ryu, Sang-Wan, and P. D. Dapkus. "Optical characterization and determination of conduction band offset of type-II GaAsSb/InGaAs QW." *Semiconductor science and technology* 19.12 (2004): 1369.

[10] Yeh, J-Y., et al. "Long wavelength emission of InGaAsN⁄ GaAsSb type II “W” quantum wells." *Applied physics letters* 88.5 (2006): 051115.

[11] Fuchs, C., et al. "High-temperature operation of electrical injection type-II (GaIn) As/Ga (AsSb)/(GaIn) As “W”-quantum well lasers emitting at 1.3 µm." *Scientific reports* 8.1 (2018): 1-6.

[12] Usman, Muhammad, et al. "Impact of alloy disorder on the band structure of compressively strained $GaBi_xAs_{1-x}$." *Physical Review B* 87.11 (2013): 115104.

[13] Speckbacher, Maximilian, et al. "Direct measurements of Fermi level pinning at the surface of intrinsically n-type InGaAs nanowires." *Nano letters* 16.8 (2016): 5135-5142.

[14] Koguchi, Nobuyuki. "Toward the fabrication of site-controlled III-V compound semiconductor quantum dots by droplet epitaxy." *J Korean Physical Society* 45 (2004): 650-655.

[15] Kim, Jong Su, Mitsuo Kawabe, and Nobuyuki Koguchi. "Ordering of high-quality InAs quantum dots on defect-free nanoholes." *Applied physics letters* 88.7 (2006): 072107.

[16] Kohmoto, Shigeru, et al. "Site-controlled self-organization of InAs quantum dots." *Materials Science and Engineering: B* 88.2-3 (2002): 292-297.

[17] Sugaya, T., et al. "Multi-stacked quantum dot solar cells fabricated by intermittent deposition of InGaAs." *Solar energy materials and Solar cells* 95.1 (2011): 163-166.

[18] Sugiyama, Yoshihiro, et al. "Stacked InAs self-assembled quantum dots on (001) GaAs grown by molecular beam epitaxy." *Japanese journal of applied physics* 35.2S (1996): 1320.

[19] Blood, Peter. "Quantum efficiency of quantum dot lasers." *IEEE Journal of Selected Topics in Quantum Electronics* 23.6 (2017): 1-8.

[20] P. Blood, et al. "Characterization of semiconductor laser gain media by the segmented contact method." *IEEE Journal of Selected Topics in Quantum Electronics* 9.5 (2003): 1275-1282.

7. Appendix

7. 1. Device processing flow for segmented-contact device

i. **Clean sample with aceton/IPA/DI water**

ii. **1st Lithography to form a ridge (If using NH_4OH or H_2SO4 based wet etchant, SiN_x is used as a hard mask)**

Side view

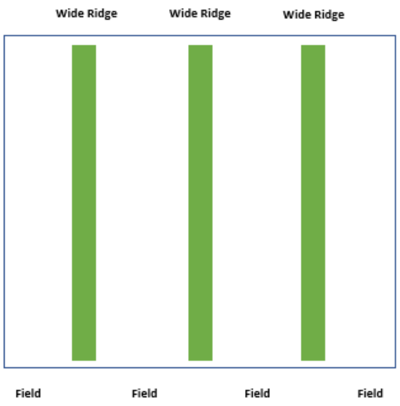

Top-view

iii. **Wet/plasma etch with either the photoresist (PR) mask or hard mask**

iv. **Removal of photoresist by aceton/IPA/DI, followed by O_2 plasma ashing**

v. **Deposition of SiN_x as a hard mask (~100nm-thick)**

vi. **2nd Lithography to segmentation**

Side view

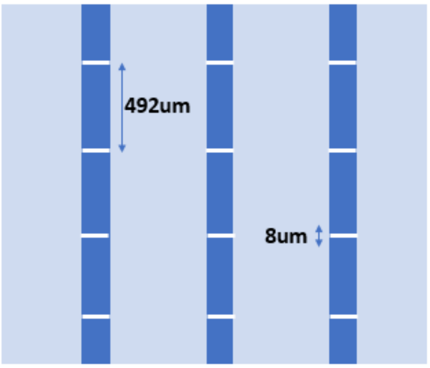

Top-view

vii. **Plasma etch to open the isolation area (CF_4+ O_2 based plasma)**

viii. Removal of photoresist by aceton/IPA/DI, followed by O_2 plasma ashing

ix. Shallow wet or plasma etch for the segmentation, targeting the entire removal of the contact layer and a part of cladding layer, which needs to be shallow enough not to interfere waveguiding

x. Removal of SiN_x as a hard mask by buffered oxide etchant (6:1)

xi. Deposition of SiN_x for electrical passivation (~200nm-thick)

xii. 3rd Lithography to open the contact window

Side view

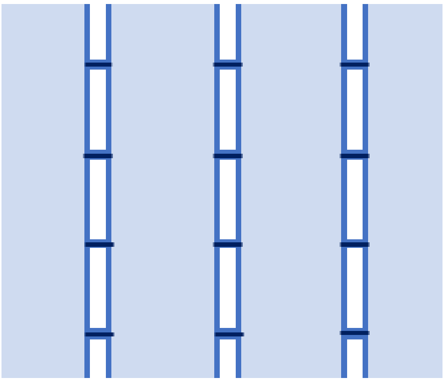

Top-view

xiii. Plasma etch to open the contact window (CF_4+ O_2 based plasma)

xiv. Removal of photoresist by aceton/IPA/DI, followed by O_2 plasma ashing

xv. 4th Lithography for front metal lift-off using a negative photoresist

xvi. Native oxide removal (HCl:DI water = 1:30 in volume ratio)

xvii. Front metal deposition by e-beam evaporation (typically Ti/Pt/Au)

Side view

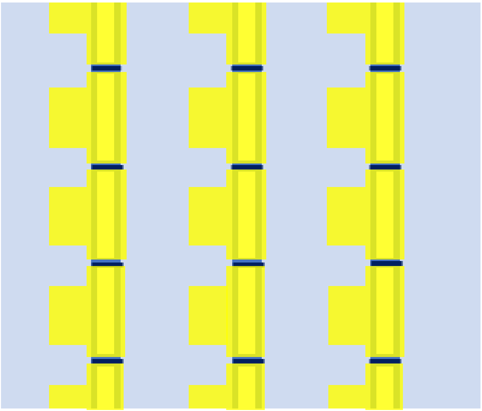

Top-view

xviii. **Lift-off (Typically by soaking the sample in 1165 for more than 3 hours followed by a short ultrasonification with aceton, IPA, and DI water and O_2 plasma ashing)**

xix. **Backside lapping (until the substrate thickness of 100 ~ 150 μm)**

xx. **Soaking the lapped sample in hot aceton for more than 30min, followed by O2 plasma ashing on the backside of the substrate**

xxi. **Backside metal deposition (typically AuGe/Ni/Au)**

xxii. **Rapid thermal annealing for alloyed contact formation**

xxiii. **Device packaging**

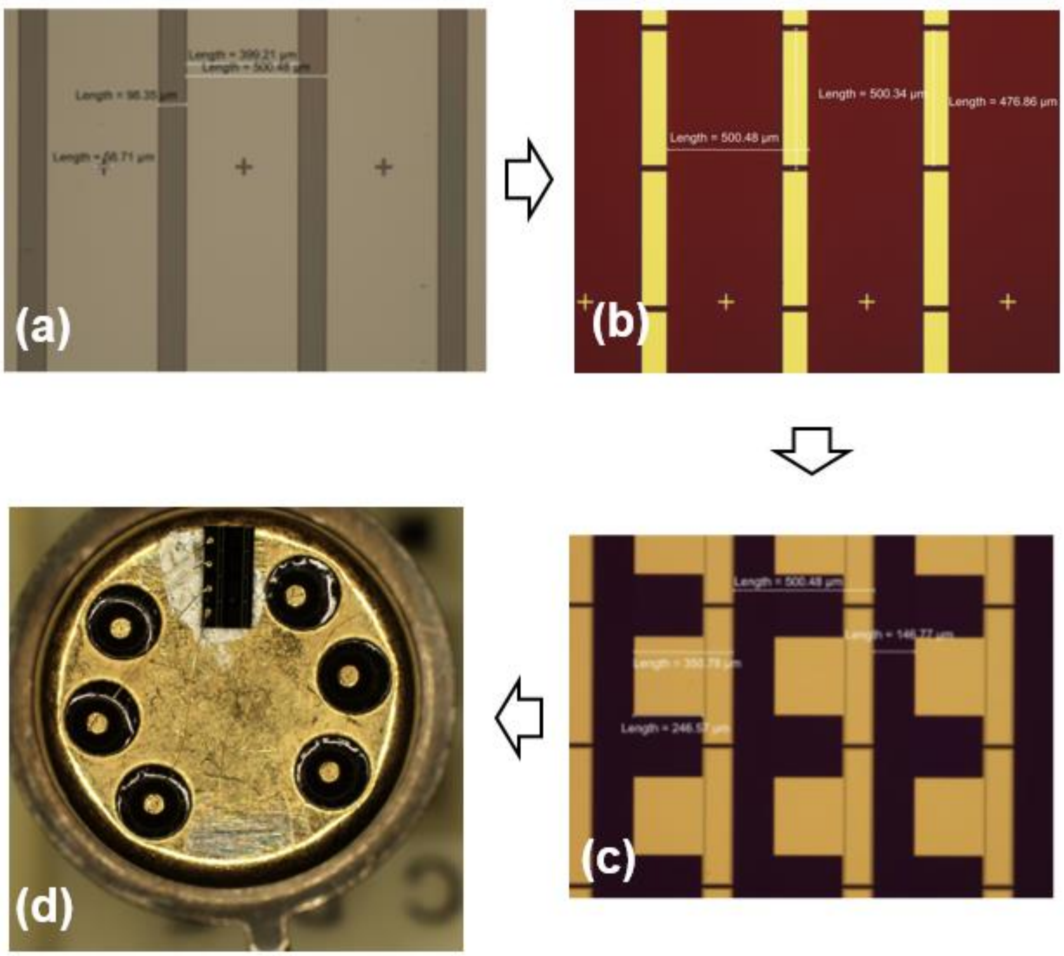

Fig. 7-1 *(a) Wide ridge formation by standard photolithography by wet etching (b) Segmentation by etching & electrical isolation by SiNx & contact window opening (c) Contact metal deposition by metal evaporation and lift-off and (d) Device package on TO-can for independent pumping on each segment*

7. 2. Device processing flow for lateral side contact device

i. Clean sample with aceton/IPA/DI water

ii. 1st Lithography to form a ridge (If using NH_4OH or H_2SO4 based wet etchant, SiN_x is used as a hard mask)

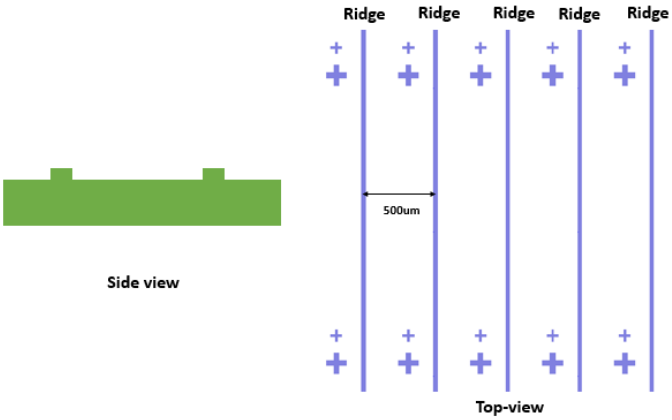

iii. Wet/plasma etch with either the photoresist (PR) mask or hard mask

iv. Removal of photoresist by aceton/IPA/DI, followed by O_2 plasma ashing

v. Deposition of SiN_x as a hard mask and electrical passivation (~200nm-thick)

vi. 2nd Lithography to etch through contact layer, upper cladding layer, waveguide layer, active region, and lower cladding layer

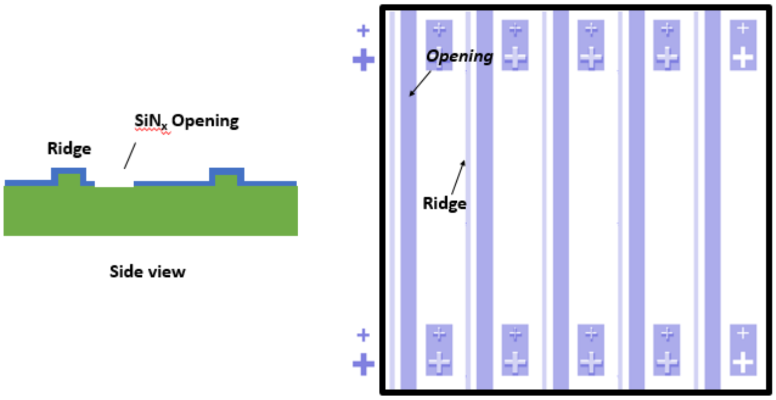

vii. Plasma etch to open the lateral contact area (CF_4+ O_2 based plasma)

viii. Removal of photoresist by aceton/IPA/DI, followed by O_2 plasma ashing

ix. Wet/plasma etch with the hard mask, to etch through contact layer, upper cladding layer, waveguide layer, active region, and lower cladding layer.

x. 3rd Lithography for lateral metal contact lift-off using a negative photoresist

xi. Native oxide removal (HCl:DI water = 1:30 in volume ratio)

xii. E-beam metal deposition on the substrate side (typically AuGe/Ni/Au)

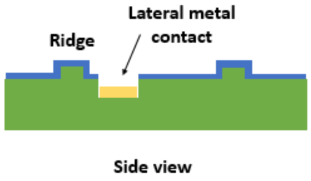

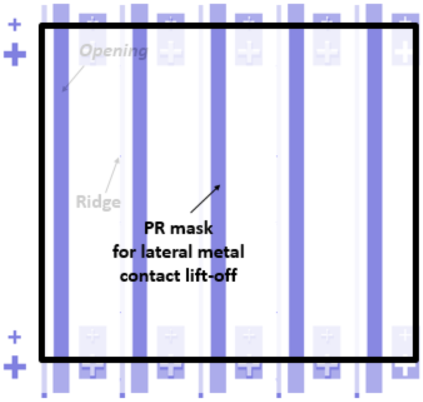

xiii. Lift-off off (Typically by soaking the sample in 1165 for more than 3 hours followed by a short ultrasonification with aceton, IPA, and DI water and O_2 plasma ashing)

xiv. by O_2 plasma ashing

xv. 4th Lithography for contact window opening on the top epi-layer

xvi. Plasma etch to open the top contact area (CF_4+ O_2 based plasma)

xvii. Removal of photoresist by aceton/IPA/DI, followed by O_2 plasma ashing

xviii. 5th lithography for top contact metal contact lift-off using a negative photoresist

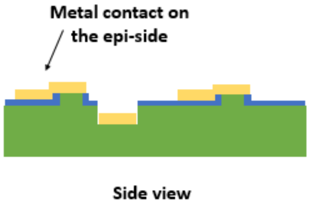

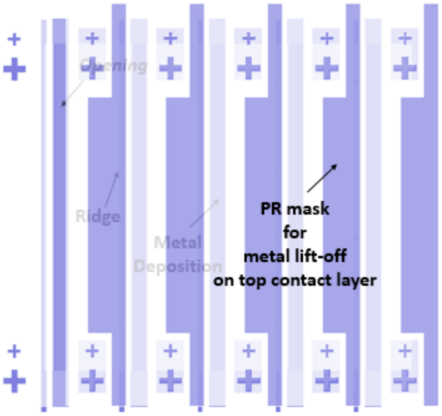

xix. E-beam metal deposition on the substrate side (typically Ti/Pt/Au)

xx. Native oxide removal (HCl:DI water = 1:3 in volume ratio)

xxi. Lift-off (Typically by soaking the sample in 1165 for more than 3 hours followed by a short ultrasonification with aceton, IPA, and DI water and O$_2$ plasma ashing)

xxii. Rapid thermal annealing for alloyed contact formation

xxiii. Backside lapping (until the substrate thickness of 100 ~ 150 μm)

xxiv. Soaking the lapped sample in hot aceton (~75°C for more than 30 min, followed by O2 plasma ashing on the backside of the substrate

xxv. Device packaging

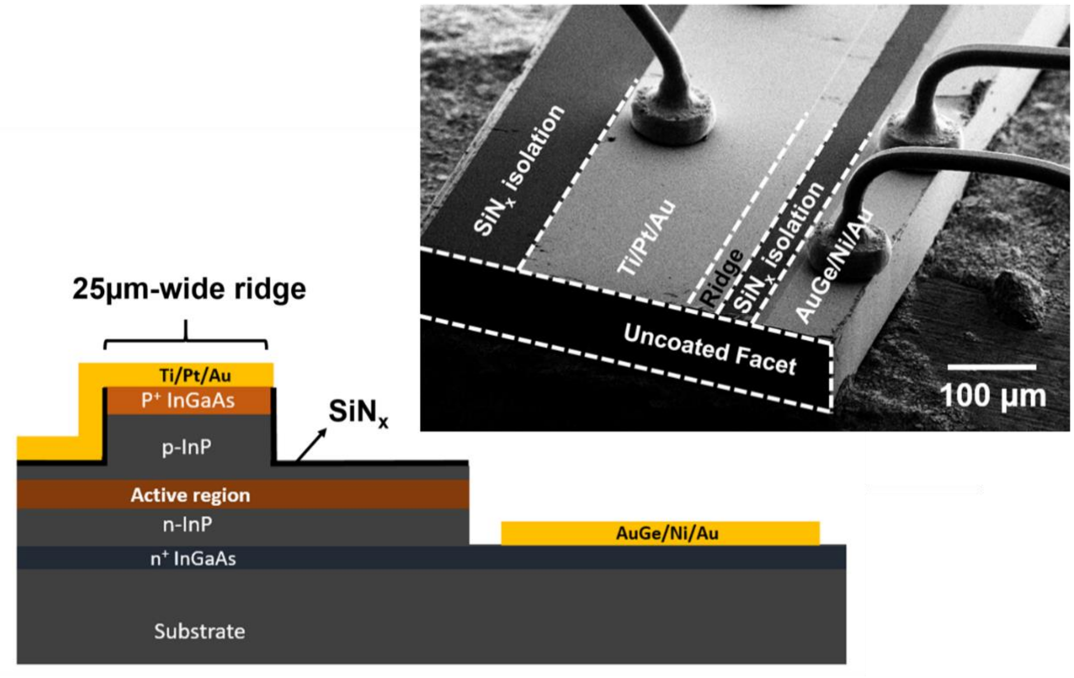

Fig. 7-2 *Schematic view of cross section and top-view SEM of fabricated and packaged device structure*

7.3. Peer-reviewed publications

1. W. Sun*, **H. Kim***, L. J. Mawst, N. Tansu. "Interplay of GaAsP Barrier and Strain Compensation in InGaAs Quantum Well at Near-Critical Thickness.", *Journal of Crystal Growth* 531 (2019): 125381. (** Equally contributed*)

2. **H. Kim**, B. Shi, Z. Lingley, Q. Li, A. Rajeev, M. Brodie, K. M. Lau, T. F. Kuech, Y. Sin, L. J. Mawst. "Electrically injected 1.64µm emitting $In_{0.65}Ga_{0.35}As$ 3-QW laser diodes grown on mismatched substrates by MOVPE", *Optics Express* 27.23 (2019): 33205-33216

3. **H. Kim**, W. Wei, T. F. Kuech, P. Gopalan, L. J. Mawst. "Impact of InGaAs carrier collection quantum well on the performance of InAs QD active region lasers fabricated by diblock copolymer lithography and selective area epitaxy", *Semiconductor Science and Technology* 34.2 (2019): 025012

4. Rajeev, B. Shi, Qiang Li, J. D. Kirch, M. Cheng, A. Tan, **H. Kim**, K. Oresick, C. Sigler, K. M. Lau, T. F. Kuech, L. J. Mawst. "III–V Superlattices on InP/Si Metamorphic Buffer Layers for λ≈4.8 µm Quantum Cascade Lasers", *physica status solidi (a)* 216.1. (2019): 1800493

5. **H. Kim**, Y. Guan, T. F. Kuech, L. J. Mawst. "Impact of Thermal Annealing on Internal Device Parameters of $GaAs_{0.965}Bi_{0.035}/GaAs_{0.75}P_{0.25}$ Quantum Well Lasers", *IET Optoelectonics*, 13.1 (2018): 12-16

6. **H. Kim**, K. Kim, Y. Guan, J. Lee, T. F. Kuech, L. J. Mawst. "Single junction solar cell employing strain compensated $GaAs_{0.965}Bi_{0.035}/GaAs_{0.75}P_{0.25}$ multiple quantum wells grown by metal organic vapor phase epitaxy", *Applied Physics Letters*, 112, (2018) 251105

7. D. Botez, J. D. Kirch, C. Boyle, K. M. Oresick, C. Sigler, **H. Kim**, B. B. Knipfer, J. H. Ryu, D. Lindberg, T. Earles, L. J. Mawst, Y. V. Flores, "High-efficiency, high-power mid-infrared quantum cascade lasers", *Optical Materials Express*, 8, 5, (2018): 1378

8. Pateras, J. Park, Y. Ahn, J. A. Tilka, M. V. Holt, **H. Kim**, L. J. Mawst, and P. G. Evans, “Dynamical scattering in coherent hard x-ray nanobeam Bragg diffraction”, *PHYSICAL REVIEW B*, 97, (2018) 235414

9. **H. Kim**, Y. Guan, S. E. Babcock, T. F. Kuech, L. J. Mawst, “Characteristics of OMVPE grown GaAsBi QW lasers and Impact of Post-Growth Thermal Annealing”, *Journal of Applied Physics*, 123, (2018) 113102

10. W. Wood, W. Chen, **H. Kim**, Y. Guan, K. Forghani, A. Anand, T.F. Kuech, L. J. Mawst, S. E. Babcock, “Annealing-Induced Precipitate Formation Behavior in MOVPE-grown GaAs$_{1-x}$Bi$_x$ Explored by Atom Probe Tomography and HAADF-STEM”, *Nanotechnology*, 28 (2017) 215704

11. **H. Kim**, Y. Guan, K. Forghani, T. F. Kuech, L. J. Mawst, “Laser Diodes Employing GaAs$_{1-x}$Bi$_x$/GaAs$_{1-y}$P$_y$ Quantum Well Active Regions”, *Semiconductor Science and Technology* 32 (2017): 07500

12. **H. Kim**, J. Choi, Z. Lingley, M. Brodie, Y. Sin, T. F. Kuech, P. Gopalan, L. J. Mawst, “Selective growth of strained (In)GaAs quantum dots on GaAs substrates employing diblock copolymer lithography nanopatterning”, *Journal of Crystal Growth*, 465, (2017) 48–54

13. J. Kirch, **H. Kim**, C. Boyle, C. C Chang, L. Mawst, D. Lindberg III, T. Earles, D. Botez, M. Helm, J. von Borany, S. Akhmadaliev, R. Böttger, C. J. Reyner, “Proton Implantation for Electrical Insulation of the InGaAs/InAlAs Superlattice Material Used in 8-15 μm-Emitting Quantum Cascade Lasers”, *Applied Physics Letter. 110*, 082102 (2017)

14. Y. Guan, K. Forghani, **H. Kim**, S. E. Babcock, L. J. Mawst, and T. F. Kuech, “Surface kinetics study of metal-organic vapor phase epitaxy of GaAs$_{1-y}$Bi$_y$ on offcut and mesa-patterned GaAs Substrates”, *Journal of Crystal Growth*, 464, (2017) 39–48

15. T. W. Kim, A. W. Wood, **H. Kim**, Y. Kim, J. J. Lee, M. Peterson, Y. Sin, S.C. Moss, T. F. Kuech, S. E. Babcock, and L. J. Mawst, “Impact of Sb incorporation on MOVPE-grown

bulk InGaAs(Sb)N films for solar cell application", *IEEE Journal of Photovoltaics* 6.6 (2016): 1673-1677

16. **H. Kim**, Y. Guan, K. Forghani, K. Kim, Y. Kim, J.J. Lee, T.F. Kuech, A. Wood, S. E. Babcock, and L. J. Mawst, "Impact of in-situ Annealing on Dilute Bismide Materials and its application to Photovoltaic Applications", *Journal of Crystal Growth* 452 (2016): 276-280

17. L. J. Mawst, T. W. Kim, **H. Kim**, Y. Kim, K. Kim, J.J. Lee, T. F. Kuech, Z. R. Lingley, S. D. Lalumondiere, Y. Sin, W. T. Lotshaw, and S. C. Moss, "Diluted-Nitride-Antimonide Materials Grown by MOVPE for Multi-Junction Solar Cell Application" ECS Transactions 66.7 (2015): 101-108

18. **H. Kim**, K. Forghani., Y. Guan, G. Luo, A. Anand, D. Morgan, T. F. Kuech, L. J. Mawst, Z. R. Lingley, B. J. Foran, Y. Sin, "Strain-Compensated GaAsP/GaAsBi/GaAsP Quantum Wells for Laser application", *Semiconductor Science and Technology* 30.9 (2015): 094011

7.4. Conference proceedings

1. (Invited) L. Mawst, A. Rajeev, **H. Kim**, J. Kirch, K. Oresick, B. Knipfer, S. Xu, D. Botez, B. Shi, Q. Li, K. M. Lau, T. F. Kuech "Quantum Cascade Laser Active Regions Grown on Lattice-mismatched substrates by OMVPE", 19th International Conference on Crystal Growth and Epitaxy (ICCGE-19) and 19th US Biennial Workshop on Organometallic Vapor Phase Epitaxy (OMVPE-19), Keystone Resort, Keystone, Colorado, USA, Jul 28 – Aug 2, 2019

2. K. Lekhal, A. Rajeev, S. Xu, **H. Kim**, O. Elleuch, T. Kuech, L. J. Mawst, "High Growth Rate $In_xGa_{1-x}As$ metamorphic buffer layers by OMVPE", 19th International Conference on Crystal Growth and Epitaxy (ICCGE-19) and 19th US Biennial Workshop on Organometallic Vapor Phase Epitaxy (OMVPE-19), Keystone Resort, Keystone, Colorado, USA, Jul 28 – Aug 2, 2019

3. **(Invited) H. Kim**, W. Wei, P. Gopalan, T. F. Kuech, L. J. Mawst, "$In_{0.8}Ga_{0.2}As$ QD active region (λ~1.65μm) laser diodes grown by block copolymer lithography and selective area OMVPE", 19th International Conference on Crystal Growth and Epitaxy (ICCGE-19) and 19th US Biennial Workshop on Organometallic Vapor Phase Epitaxy (OMVPE-19), Keystone Resort, Keystone, Colorado, USA, Jul 28 – Aug 2, 2019

4. **H. Kim**, B. Shi, Z. Lingley, Q. Li, A. Rajeev, M. Brodie, K. M. Lau, T. F. Kuech, Y. Sin, L. J. Mawst, "Electrically Injected 1.64μm emitting $In_{0.65}Ga_{0.35}As$ 3-QW laser diodes grown on mismatched substrates by MOVPE", Compound Semiconductor Week 2019 (CSW2019), Nara Kasugano International Forum, Nara, Japan, May 19 – 23, 2019

5. (Invited) L. J. Mawst, C. Sigler, J. D. Kirch, C. Boyle, K. Oresick, **H. Kim**, D. F. Lindberg III, T. L. Earles, D. Botez, "High-Power MOCVD-Grown Quantum Cascade Laser", IEEE Photonics Conference (IPC), Reston, VA, USA, Sept 30 – Oct 4, 2018

6. **H. Kim**, W. Wei, P. Gopalan, T. F. Kuech, L. J. Mawst, "Quantum Dot Laser Diodes emitting 1.57~1.67μm at room temperature grown by Block Copolymer Lithography and

Selective Area MOCVD", 26th International Semiconductor Laser Conference, Hilton Santa Fe Historic Plaza, Santa Fe, New Mexico, USA, Sept 16-19, 2018

7. B. Knipfer, C. Sigler, C. Boyle, J. D. Kirch, K. Oresick, **H. Kim**, D. Botez, L. J. Mawst, N. Becher, M. Farzaneh, D. F. Lindberg III, T. Earles, "Failure Analysis of High-Power (One-Watt) Room-Temperature Continuous Wave MOCVD Quantum Cascade Lasers", 26th International Semiconductor Laser Conference, Hilton Santa Fe Historic Plaza, Santa Fe, New Mexico, USA, Sept 16-19, 2018

8. **H. Kim**, W. Wei, T. F. Kuech, P. Gopalan and L. J. Mawst, "Room temperature Lasing from Selective Area MOVPE of InAs Quantum Dots on GaAs fabricated by block-copolymer lithography", 19th International Conference on Metal Organic Vapor Phase Epitaxy, Nara Kasugano International Forum, Nara, Japan, June 3-8, 2018

9. W. Sun, **H. Kim**, L. J. Mawst, and N. Tansu, "Strain relaxation and compensation in InGaAs quantum wells at near critical thickness", 19th International Conference on Metal Organic Vapor Phase Epitaxy, Nara Kasugano International Forum, Nara, Japan, June 3-8, 2018

10. M. Dwyer, **H. Kim**, L. Mawst, D. van der Weide, "Double-uniform Schottky diode nonlinear transmission line generating sub-picosecond transients", IEEE Radio and Wireless Symposium (RWS), Anaheim, CA, Jan 14-17, 2018

11. **H. Kim**, W. Wei, T. F. Kuech, P. Gopalan and L. J. Mawst, "Room Temperature Operation of InAs Quantum Dot lasers Formed by Diblock-Copolymer Lithography and Selective Area MOCVD", IEEE Photonics Conference (IPC), Orlando, FL, USA, Oct 1-5, 2017

12. **H. Kim**, L. J. Mawst, Y. Guan, S.E. Babcock T. F. Kuech "Characteristics of Ga(AsP)/Ga(AsBi)/Ga(AsP) Quantum Well Active Region Lasers Grown by MOVPE" 21st American Conference on Crystal Growth and Epitaxy (ACCGE-21) and 18th U.S. Biennial Workshop on Organometallic Vapor Phase Epitaxy (OMVPE-18), Santa Fe, NM, USA, July 30- August 4, 2017.

13. L. J. Mawst, **H. Kim**, Y. Guan, S.E. Babcock T. F. Kuech "Characteristics of Ga(AsP) / Ga(AsBi) / Ga(AsP) Quantum Well Active Region Lasers Grown by MOVPE" 8th International Workshop on Bi-containing Semiconductors: Growth, Properties, and Devices, Marburg, Germany, July 23-26, 2017

14. (Invited) D. Botez, J. D. Kirch, C.C. Chang, C. Boyle, **H. Kim**, K. M. Oresick, C. Sigler, L. J Mawst, M. Jo, J. C. Shin, D. G. Kim, D. F. Lindberg III, T. L. Earles, "High internal differential efficiency midinfrared quantum cascade lasers", SPIE Photonic West Opto, San Francisco, CA, USA, Jan 28 – Fab 2, 2017

15. **H. Kim**, Y. Guan, K. Forghani, T. F. Kuech and L. J. Mawst, "Strain-Compensated Ga(AsP)/Ga(AsBi)/Ga(AsP) Quantum Well Active Region Lasers" SPIE Photonic West Opto, San Francisco, CA, USA, Jan 28 – Fab 2, 2017

16. **H. Kim**, J. Choi, T. F. Kuech, P. Gopalan and L. J. Mawst, "Selective MOCVD growth of strained (In) GaAs quantum dot active region laser diode on GaAs substrates employing diblock copolymer lithograph", IEEE Photonics Conference (IPC), Waikoloa, HI, USA, Oct 2-6, 2016

17. (Invited) L. J. Mawst, **H. Kim**, Y. Guan, K. Forghani, and T. F. Kuech, "Ga(AsBi)/Ga(AsP) Quantum Well Lasers Grown by MOCVD", IEEE Photonics Conference (IPC), Waikoloa, HI, USA, Oct 2-6, 2016

18. **H. Kim**, Y. Guan, K. Forghani, T. F. Kuech and L. J. Mawst, "Strain-Compensated Ga(AsP)/Ga(AsBi)/Ga(AsP) Quantum Well Active Region Lasers" 7th International Workshop on Bi-containing Semiconductors: Growth, Properties, and Devices, Shanghai, People's Republic of China, July 24-27, 2016

19. **H. Kim**, A. Wood, W. Chen, Y. Guan, K. Forghani, T. F. Kuech, S. E. Babcock and L. J. Mawst, "Atom Probe Tomography and Transmission Electron Microscope Analysis of Bi Precipitate within annealed Ga(AsBi) alloy" 7th International Workshop on Bi-containing Semiconductors: Growth, Properties, and Devices, Shanghai, People's Republic of China, July 24-27, 2016

20. (Poster) M. H. Jo, **H. Kim**, J. Choi, H. Kim, J. Hwang, D. G. Kim, P. Gopalan, J. C. Shin and L. J Mawst, “Selective-Area MOVPE Growth of the Ternary III-V Nanowires Employing PS/PMMA Diblock Copolymer Nanopatterning”, 18th International Conference on Metal Organic Vapor Phase Epitaxy, San Diego, CA, USA, July 10-15, 2016

21. **H. Kim**, J. Choi, Z. R. Lingley, M. Brodie, Y Sin, T. F. Kuech, P. Gopalan and L. J. Mawst, “Selective Growth of Strained (In)GaAs Quantum Dots on GaAs Substrates Employing Diblock Copolymer Lithography Nanopatterning”, 18th International Conference on Metal Organic Vapor Phase Epitaxy, San Diego, CA, USA, July 10-15, 2016

22. Y. Guan, **H. Kim**, S. E. Babcock, L. J. Mawst and T. F. Kuech, “Surface Step-Dependent Incorporation for $GaAs_{1-x}Bi_x$ during Metal Organic Vapor Phase Epitaxy”, 18th International Conference on Metal Organic Vapor Phase Epitaxy, San Diego, CA, USA, July 10-15, 2016

23. W. Chen, A. Wood, **H. Kim**, K. Forghani, Y. Guan, L. J. Mawst, T. F. Kuech and S. E. Babcock, “Atom Probe Tomography Study of Bi Precipitation during Annealing of Metastable $GaAs_{1-x}Bi_x$ Solid Solution” 18th International Conference on Metal Organic Vapor Phase Epitaxy, San Diego, CA, USA, July 10-15, 2016

24. M. R. Laskar, D. H. K. Jackson, K. Forghani, **H. Kim**, and T. F. Kuech, “Epitaxial Growth of Two-dimensional Layered Semiconductors” 20th American Conference on Crystal Growth and Epitaxy (ACCGE-20) and 17th U.S. Biennial Workshop on Organometallic Vapor Phase Epitaxy (OMVPE-17) and The Second 2D Electron Material Symposium, Big Sky, MT, USA, August 2-7, 2015.

25. **H. Kim**, K. Forghani, Y. Guan, Y. Kim, K. Kim, J. Lee, T. F. Kuech, and L. J. Mawst, “Impact of in-situ Annealing on Dilute Bismide Materials and its Application to Solar Cell” 20th American Conference on Crystal Growth and Epitaxy (ACCGE-20) and 17th U.S. Biennial Workshop on Organometallic Vapor Phase Epitaxy (OMVPE-17) and The Second 2D Electron Material Symposium, Big Sky, MT, USA, August 2-7, 2015.

26. **H. Kim**, K. Forghani, Y. Guan, Y. Kim, K. Kim, J. Lee, T. F. Kuech, and L. J. Mawst, "Impact of in-situ Annealing on Dilute Bismide Materials and its Application to Optoelectronic Devices" 6th International Workshop on Bismuth-Containing Semiconductor, Madison, WI, USA, July 19-22, 2015.

27. Y. Sin, Z. Lingley, M. Peterson, M. Brodie, S. C. Moss, T. W. Kim, **H. Kim**, Y. Guan, K. Forghani, and L. J. Mawst, "Time-resolved PL and TEM studies of MOVPE-grown bulk dilute nitride and bismide quantum well heterostructure" SPIE OPTO. International Society for Optics and Phtonics, 2015

28. L. J. Mawst, K. Forghani, Y. Guan, A. Anand, **H. Kim**, T. Kim, A. Wood, S. Babcock, T. F. Kuech, Z. R. Lingley, S. D. LaLumondiere, Y. Sin, W. T. Lotshaw, and S. C. Moss "Strain-Compensated GaAsP/GaAsBi(P)/GaAsP Quantum Wells for Laser Applications", 5th International Workshop on Bismuth-Containing Semiconductor, Cork, Ireland, July 20-23, 2014